

**Metal-Organic Framework-Spherical Carbon Composites
for Heterogeneous Catalysis in Continuous Flow**

Anthony Griffiths

Submitted in accordance with the requirements for the degree of
Doctor of Philosophy

School of Chemical and Process Engineering

March 2024

The candidate confirms that the work submitted is his own, except where work which has formed part of jointly authored publications has been included. The contribution of the candidate and the other authors to this work has been explicitly indicated below. The candidate confirms that appropriate credit has been given within the thesis where reference has been made to the work of others.

This copy has been supplied on the understanding that it is copyright material and that no quotation from the thesis may be published without proper acknowledgement.

The right of Anthony Griffiths to be identified as Author of this work has been asserted by Anthony Griffiths in accordance with the Copyright, Designs and Patents Act 1988

Chapter 3 and Chapter 4 are based on work from a jointly authored publication:

- **A. Griffiths**, S. L. Boyall, P. Müller, J. P. Harrington, A. M. Sobolewska, W. R. Reynolds, R. A. Bourne, K. J. Wu, S. M. Collins, M. Muldowney and T. W. Chamberlain. "*MOF-based heterogeneous catalysis in continuous flow via incorporation onto polymer based spherical activated carbon supports*". *Nanoscale*, 2023, **15**, 17910-17921

AG performed the experiments, interpreted the data and drafted the original manuscript. Expert help with continuous flow experiments and data was supplied by Sarah Boyall and Pia Müller, and by John Harrington for electron microscopy. Thomas Chamberlain conceived the original idea, secured funding to perform the research and supervised the experiments and data analysis with Kejun Wu (flow experiments), Sean Collins (MOF characterisation) and Richard Bourne (continuous flow experiments) at the University of Leeds and the Industrial team at Sterling Pharma Solutions; Anna Sobolewska, William Reynolds and Mark Muldowney (API related heterogeneous catalysis).

Other published or submitted work not discussed in this thesis include:

- S. Doherty, J. G. Knight, H. Y. Alharbi, R. Paterson, C. Wills, C. Dixon, L. Siller, T. W. Chamberlain, **A. Griffiths**, S. M. Collins, K. J. Wu, S. D. Simmonds, R. A. Bourne, K. R. J. Lovelock, J. Seymour. "*Efficient Hydrolytic Hydrogen Evolution from Sodium Borohydride Catalysed by Polymer*

Immobilized Ionic Liquid-Stabilized Platinum Nanoparticles". *ChemCatChem*, 2022, **14**(4), e202101752.

- R. Paterson, A. A. Alharbi, C. Wills, C. Dixon, L. Siller, T. W. Chamberlain, **A. Griffiths**, S. M. Collins, K. J. Wu, M. D. Simmons, R. A. Bourne, K. R. J. Lovelock, J. Seymour, J. G. Knight, S. Doherty. "Heteroatom Modified Polymer Immobilized Ionic Liquid Stabilized Ruthenium Nanoparticles: Efficient Catalysts for the Hydrolytic Evolution of Hydrogen from Sodium Borohydride". *Molecular Catalysis*, 2022, **528**, 112476.
- S. Doherty, J. G. Knight, T. Backhouse, T. S. T. Tran, R. Paterson, F. Stahl, H. Y. Alharbi, T. W. Chamberlain, R. A. Bourne, R. Stones, **A. Griffiths**, J. P. White, Z. Aslam, C. Hardacre, H. Daly, J. Hart, R. H. Temperton, J. N. O'Shea, N. H. Rees. "Highly efficient and selective aqueous phase hydrogenation of aryl ketones, aldehydes, furfural and levulinic acid and its ethyl ester catalyzed by phosphine oxide-decorated polymer immobilized ionic liquid-stabilized ruthenium nanoparticles". *Catalysis Science & Technology*, 2022, **12**, 3549-3567.
- S. Doherty, R. Paterson, L. E. Fahy, E. Acra, C. Dixon, C. Wills, H. Yan, **A. Griffiths**, S. M. Collins, K. J. Wu, R. A. Bourne, T. W. Chamberlain, J. G. Knight. "Amine-Modified Polyionic Liquid Supports Enhance the Efficacy of PdNPs for the Catalytic Hydrogenation of CO₂ to Formate". *Chem. Commun*, 2023, 59, 13470-13473.
- S. Doherty, J. G. Knight, A. A. Alharbi, C. Wills, T. W. Chamberlain, R. A. Bourne, **A. Griffiths**, S. M. Collins, K. J. Wu, P. Mueller. "Amino-Modified Polymer Immobilized Ionic Liquid Stabilized Ruthenium Nanoparticles: Efficient and Selective Catalysts for the Partial and Complete Reduction of Quinolines". *ChemCatChem* 2023, **15**(11), e202300418.
- R. Paterson, H. Y. Alharbi, C. Wills, T. W. Chamberlain, R. A. Bourne, **A. Griffiths**, S.M. Collins, K. J. Wu, M. D. Simmons, R. Menzel, A. F. Massey, J. G. Knight, S. Doherty. "Highly efficient and selective partial reduction of nitroarenes to N-arylhydroxylamines catalysed by phosphine oxide-decorated polymer immobilized ionic liquid stabilized ruthenium nanoparticles". *Journal of Catalysis*, 2023, **417**, 74-88.
- S. L. Boyall, P. Berman, **A. Griffiths**, A. Massey, T. Dixon, T. Shaw, J. Millera, J. P. White, R. Menzel, K. Leslie, G. Clemens, F. L. Muller, R. A. Bourne, T.

W. Chamberlain. "*Palladium Nanoparticle Deposition on Spherical Carbon Supports for Heterogeneous Catalysis in Continuous Flow*". *Catalysis Science and Technology*. 2024, **14**, 2563-2573.

Acknowledgements

I would firstly like to thank Thomas Chamberlain for his unwavering support and guidance throughout this project. Thank you for keeping me motivated during the more challenging periods of this project and for the stellar advice you have given me throughout, I will carry a lot of it forward with me. Thank you to Sean Collins for your invaluable input throughout the course of this project as well as the detailed feedback on my writing - you have helped me to elevate my writing ability hugely. Another thank you to Kejun Wu for your help throughout this project and for attending my progress meetings from China for the past two years despite it being much later (and basically past my bedtime) where you are.

I would also like to thank the supervisory team at Sterling Pharma (Mark Muldowney, Will Reynolds and Anna Sobolewska) for their guidance throughout this project and for making me feel incredibly welcome during my visits (and for putting me up in nice hotels). Thank you to those involved with M2P (Elaine Martin, Angela Morrison, John Blacker, David Harbottle, Nicole Hondow, Andy Brown, Robert Hammond) for the opportunity to be part of such an exciting CDT and thanks to the rest of M2P cohort 1.

I would like to acknowledge Chris Pask for providing PXRD training and Faye Esat for the acquisition of PXRD data presented in Chapter 3 of this thesis. Adrian Cunliffe and Karine Alves Thorne for TGA training. Benjamin Douglas for N₂ adsorption and DLS training. Alex Kulak for SEM-EDX sample preparation and data collection. John Harrington for FIB-SEM-EDX sample preparation and data collection. Andrew Britton for XPS sample preparation and data collection and Alex Massey for XPS data interpretation. Simon Lloyd and Karine Alves Thorne for AAS training. Saba Saifoori and Wei Pin Goh for Instron 5566 (crush testing) training. Oliver Kershaw and Mark Howard for NMR training. Mary Bayana, Pia Müller and Brendan Hall for help with GC method development. Pia Müller and Adam Clayton for help choosing an appropriate DoE design. Pia Müller and Sarah Boyall for helping to design the flow system and general help with flow experimentation. William Reynolds, Anna Sobolewska and Mark Muldowney at Sterling Pharma Solutions Ltd. for help with flow reactions. Jeanine Williams for help with HPLC method development and running of samples. Thank you also to

Rose Montgomery Danagher (MChem student) who obtained some of the results presented in this thesis (Chapter 5).

I would like to thank everyone in office 2.07 (Alex, Bence, Sean, Rachel, Xiangyi, Tom M, Jamie, Han). Alex, thank you for providing entertainment and humour throughout. Thank you to iPRD members (Brendan, Tom D, Mary, Tom S, Adam, Ricardo, Nisha, Holly, Connor) and others elsewhere (Gerome, James, Dan, Megan, Mae, Oisín).

I would also like to thank my parents (Liz and Paul) for their endless support and for always providing an environment conducive to learning. Thanks to my sixth form chemistry teacher, Mr Bryan, whose excellent teaching (some 8/9 years ago) is largely the reason for why I did not drop A-level chemistry (when I was adamant I was going to) and also demanded an acknowledgment on any future PhD thesis.

Abstract

The optimisation of heterogeneous catalysis in continuous flow has the potential to deliver significant benefits to fine chemical manufacturing. However, many promising industrial heterogeneous catalyst candidates, such as metal-organic frameworks (MOFs), exist as powders which are unsuitable for use in flow reactors. This thesis explores an approach to exploiting MOFs for heterogeneous catalysis in continuous flow by combining them with scalable, industrially implementable polymer-based spherical activated carbon (PBSAC) supports. A novel heterogeneous catalyst consisting of the Lewis acidic MOF MIL-100(Sc) immobilised onto PBSAC spheres, termed MIL-100(Sc)@PBSAC, was developed and studied in continuous flow.

Firstly, following in-depth characterisation (i.e. PXRD, TGA, FT-IR, N₂ adsorption, SEM-EDX, DLS and XPS), the Lewis acidic catalytic properties of MIL-100(Sc) (in powder form) towards an industrially important reaction (intramolecular cyclisation of citronellal) were studied via design-of-experiments (DoE) and kinetic modelling approaches (Chapter 2). Statistically significant DoE models were generated when studying the initial rate and catalytic efficiency. Upon kinetic model generation, a Langmuir-Hinshelwood mechanism was found to adequately describe the reaction mechanism. Next, novel MIL-100(Sc)@PBSAC composites were reproducibly synthesised by a reflux approach and thoroughly characterised (i.e. FIB-SEM-EDX, PXRD, N₂ adsorption, TGA, AAS, XPS, DLS and crush testing) (Chapter 3). MIL-100(Sc) was found to reside primarily in the pores and cracks on the surface of PBSAC spheres. The MIL-100(Sc)@PBSAC composite was then successfully applied in continuous flow for industrially relevant Lewis acid-catalysed reactions, including both intramolecular cyclisation of citronellal and cannabidiol synthesis (Chapter 4). Finally, initial work regarding the development of a new catalytic system, Cu@UiO-67-BPY@PBSAC, incorporating a postsynthetic modification step, for application in 3-phase (liquid-solid-gas) continuous flow heterogeneous catalysis, is discussed (Chapter 5).

Overall, this research demonstrates the potential for MOF-based heterogeneous catalysis in continuous flow for fine chemical synthesis. Adding a new dimension in the form of MOF@PBSAC composites to the broader trend from catalysis in

batch to catalysis in flow, this work outlines a generalisable approach to exploit the versatility of MOF- and other coordination polymer-based catalysts in continuous manufacturing.

Table of Contents

Acknowledgements	5
Abstract	7
Table of Contents	9
List of Abbreviations	13
List of Figures	17
List of Schemes	28
List of Tables	29
Chapter 1 Introduction	33
1.1 Fine chemical production.....	33
1.1.1 Batch to continuous fine chemical manufacture.....	33
1.1.2 Heterogeneous catalysis.....	35
1.1.3 Reaction optimisation.....	41
1.2 Metal-organic frameworks (MOFs)	51
1.2.1 The MIL-100 series of MOFs	53
1.2.2 MOF-based catalysis	59
1.2.3 MOF-based heterogeneous catalysis in continuous flow	67
1.3 Polymer-based spherical activated carbon (PBSAC)	72
1.3.1 Activated carbon	72
1.3.2 PBSACs as catalyst supports in continuous flow	73
1.3.3 PBSACs as supports for MOFs.....	76
1.4 Research aim	77
Chapter 2 Exploring the catalytic activity of MIL-100(Sc) by in-depth characterisation, design-of-experiments and kinetic modelling	80
2.1 Introduction.....	80
Part A	83
2.2 Synthesis and characterisation of MIL-100(Sc).....	83
2.2.1 Synthesis of MIL-100(Sc).....	83
2.2.2 Activation of MIL-100(Sc).....	86
2.2.3 Stoichiometry of MIL-100(Sc)	93
2.2.4 Textural properties of MIL-100(Sc)	98
2.2.5 MIL-100(Sc) particle size distribution, morphology and composition	99
2.2.6 Estimating interior vs. exterior catalyst site ratio	103
2.2.7 Probing surface structure by XPS	110
2.3 Conclusion: Part A.....	111

Part B	111
2.4 Catalytic activity studies into MIL-100(Sc)	111
2.4.1 The intramolecular cyclisation of citronellal	113
2.4.2 Design-of-experiments (DoE)	120
2.5 Kinetic model development	138
2.5.1 Homogeneous catalyst: scandium triflate	139
2.5.2 Heterogeneous Catalyst: MIL-100(Sc)	145
2.6 Conclusion: Part B	152
2.7 Conclusions of the chapter	153
2.8 Appendices	154
Chapter 3 Development of a novel metal-organic framework catalyst suitable for continuous flow operations	160
3.1 Introduction	160
3.2 Synthesis of MIL-100(Sc)@PBSAC composites	161
3.2.1 Solvothermal synthesis	164
3.2.2 Reflux synthesis of MIL-100(Sc)	167
3.3 Characterisation of MIL-100(Sc)@PBSAC	171
3.3.1 Studying the synthesis of MIL-100(Sc)@PBSAC	171
3.3.2 Studying porosity	175
3.3.3 Studying thermal stability, composition and metal loading	177
3.3.4 Studying the surface structure	181
3.3.5 Mechanical and physical properties for flow chemistry	186
3.4 Conclusions of the chapter	188
3.5 Appendices	189
Chapter 4 Studying the catalytic activity of MIL-100(Sc)@PBSAC composites in batch and continuous flow	190
4.1 Introduction	190
4.2 Catalytic activity of MIL-100(Sc)@PBSAC in batch	194
4.2.1 Reusability testing	194
4.2.2 Effect of stirring rate	195
4.3 Catalytic activity of MIL-100(Sc)@PBSAC in continuous flow	196
4.3.1 Studying residence time distribution	198
4.3.2 The intramolecular cyclisation of (±)-citronellal	201
4.3.3 Cannabidiol (CBD) and cannabidiol-methyl ester (CBD-ME) synthesis	227
4.4 Conclusions of the chapter	238

4.5 Appendices.....	240
4.5.1 Calculation of reaction metrics.....	240
4.5.2 HPLC chromatograms from methyl olivetolate and <i>p</i> -menthadienol coupling showing peaks at <i>t</i> = 2.2 mins and 2.7 mins (see section 4.3.3.2).....	241
4.5.3 NMR of methyl olivetolate and <i>p</i> -menthadienol reaction (see section 4.3.3.2).....	242
Chapter 5 Conclusions and Future Work.....	243
5.1 Conclusions.....	243
5.2 Designing a new MOF@PBSAC system: preliminary work.....	245
5.2.1 Synthesising Cu@UiO-67-BPY and Cu@UiO-67-BPY@PBSAC	247
5.2.2 Preliminary catalytic activity testing.....	249
5.2.3 Conclusion and next steps.....	250
5.3 Future work	251
5.3.1 Routes to or requirements for scale-up.....	251
5.3.2 Generalising to other reactions	254
5.3.3 Further technique/method development across research.....	256
Chapter 6 Experimental.....	258
6.1 Characterisation	258
6.1.1 Powder X-ray diffraction (PXRD)	258
6.1.2 Thermogravimetric analysis (TGA)	258
6.1.3 FT-IR spectroscopy.....	258
6.1.4 N ₂ adsorption (BET).....	258
6.1.5 Scanning electron microscopy-energy dispersive X-ray analysis (SEM-EDX)	259
6.1.6 Focused ion beam-scanning electron microscopy-energy dispersive X-ray analysis (FIB-SEM-EDX)	260
6.1.7 Dynamic light scattering (DLS)	260
6.1.8 X-ray photoelectron spectroscopy (XPS).....	260
6.1.9 Atomic absorption spectroscopy (AAS).....	261
6.1.10 Crush testing.....	261
6.1.11 Nuclear magnetic resonance (NMR) spectroscopy.....	261
6.1.12 Gas chromatography (GC).....	261
6.1.13 High-performance liquid chromatography (HPLC)	266
6.2 Chapter 2 procedures.....	268

6.2.1 Reagents and materials	268
6.2.2 Solvothermal synthesis of MIL-100(Sc)	269
6.2.3 Optimising MIL-100(Sc) drying temperature study.....	269
6.2.4 Molecular modelling.....	269
6.2.5 Design-of-experiments (DoE)	269
6.2.6 Kinetic experiments with scandium triflate for kinetic model	270
6.2.7 Kinetic modelling.....	270
6.3 Chapter 3 procedures.....	271
6.3.1 Reagents and materials	271
6.3.2 Solvothermal synthesis of MIL-100(Sc)@PBSAC composites	271
6.3.3 Reflux synthesis of MIL-100(Sc)@PBSAC composites	271
6.3.4 Testing MIL-100(Sc)@PBSAC catalytic activity.....	272
6.3.5 Confirming trimesic acid adsorption.....	272
6.4 Chapter 4 procedures.....	272
6.4.1 Reagents and materials	273
6.4.2 Reusability testing of MIL-100(Sc)@PBSAC composites	273
6.4.3 Stirring rate experiment.....	273
6.4.4 Flow system setup	274
6.4.5 Residence time distribution (RTD) determination: pulse test	275
6.4.6 (±)-Citronellal cyclisation in continuous flow	275
6.4.7 Cannabidiol (CBD) and cannabidiol-methyl ester (CBD-ME) synthesis	277
6.5 Future work procedures.....	278
6.5.1 Synthesis of Cu@UiO-67-BPY	278
6.5.2 Synthesis of Cu@UiO-67-BPY@PBSAC.....	279
6.5.3 Epoxidation of cyclohexene with Cu@UiO-67-BPY@PBSAC	279
References.....	280

List of Abbreviations

AAS	Atomic absorption spectroscopy
AC	Activated carbon
API	Active pharmaceutical ingredient
BET	Brett-Emmett-Teller
BJH	Barrett-Joyner-Halenda
BPR	Back pressure regulator
bpy	2,2'-bipyridine-5,5-dicarboxylic acid
BTC	Benzene-1,3,5-tricarboxylate
CBD	Cannabidiol
CBD-ME	Cannabidiol-methyl ester
CCD	Central composite design
Cit:Sc ratio	Citronellal:scandium molar ratio
cm	Centimetre
cm ³	Centimetre cubed
d	Diameter
DCM	Dichloromethane
DFPs	Defunctionalisation products
d _H	Hydrodynamic diameter
DLS	Dynamic light scattering
DMF	N,N-dimethylformamide
DoE	Design-of-experiments
D _p	Particle diameter
D _t	Reactor tube diameter
E _a	Activation energy
EDX	Energy dispersive X-ray

eV	Electronvolt
FDA	US Food and Drug Administration
FFD	Full factorial design
FIB	Focused-ion beam
FIB-SEM-EDX	Focused-ion beam-scanning electron microscopy-energy dispersive X-ray
g	Gram
GC	Gas chromatography
GSK	GlaxoSmithKline
HPLC	High performance liquid chromatography
hr	Hour
ID	Internal diameter
IR	Infrared
ISP	Isopulegol
ISPs	Isopulegols
k	Rate constant
kJ	Kilojoule
kV	Kilovolt
LH	Langmuir-Hinshelwood
m	Metre
M	Molarity
mg	Milligram
MIL	Materials of Institute Lavoisier
mL	Millilitre
mM	Millimolar
mmol	Millimole
MOF	Metal-organic framework

mol	Mole
MPa	Megapascals
NMR	Nuclear magnetic resonance
NP	Nanoparticle
OD	Outer diameter
OH	Hydroxide
OVAT	One-variable-at-a-time
PBR	Packed-bed reactor
PBSAC	Polymer-based spherical activated carbon
ppm	Parts-per-million
PSD	Particle size distribution
PSM	Post synthetic modification
PXRD	Powder X-ray diffraction
RSM	Response surface methodology
RTD	Residence time distribution
Sc	Scandium
Sc(OTf) ₃	Scandium triflate
SEM	Scanning electron microscopy
SEM-EDX	Scanning electron microscopy-energy X-ray
SSQ	Sum of squares
STY	Space-time yield
TBR	Trickle-bed reactor
TGA	Thermogravimetric analysis
THC	Tetrahydrocannabinol
TOF	Turnover frequency
TON	Turnover number
UiO	University of Oslo

UV	Ultraviolet
wt	Weight
XPS	X-ray photoelectron spectroscopy
μL	Microlitre
μm	Micrometre

List of Figures

- Figure 1: APIs in some of the FDA approved pharmaceuticals that exploit continuous manufacturing. N.B. Orkambi is a combination of two APIs.....35
- Figure 2: a) Contribution of catalytic processes to chemical industry, b) contribution of heterogeneous catalysis in comparison to other catalytic processes (2018). Figure reproduced with permission.¹⁶36
- Figure 3: Schematic of four common strategies used to heterogenise homogeneous catalysts, namely adsorption, encapsulation, covalent tethering and electrostatic interactions. Figure modified with permission.²⁷37
- Figure 4: Four types of flow synthesis as classified by Kobayashi and colleagues. Figure modified with permission.⁴⁹40
- Figure 5: Schematic representation of three main types of reactors used for heterogeneous catalysis in flow, namely a packed-bed, monolith and wall-coated reactor. The arrows indicate the direction of flow through the reactor. Figure modified with permission.⁵⁷41
- Figure 6: Left: OVAT method for studying chemical reaction space. Right: DoE method for studying chemical reaction space. Each orange circle represents an experiment.42
- Figure 7: 2-level 3-factor FFD DoE carried out in this work consisting of 11 experiments: 8 corner-point experiments and 3 replicate experiments in the centre.43
- Figure 8: a) Continuous flow acid-catalysed esterification of fumaric acid to monomethyl fumarate or dimethyl fumarate in the presence of methanol studied using a DoE by Vigo and colleagues.⁶⁷ b) Response surface generated following the DoE showing % of dimethyl fumarate as a function of residence time (Rt) and temperature (T). Yellow illustrates lower % of dimethyl fumarate (i.e. $\approx 85 - 88\%$), green intermediary illustrates intermediary percentages of dimethyl fumarate (i.e. $\approx 88 - 96\%$) and blue indicates higher percentages of dimethyl fumarate (i.e. $> 96\%$). Figure reproduced with permission.⁶⁷44
- Figure 9: Response surface plot of anisole conversion after a) 1 hour of reaction b) 5 hours of reaction in the DoE. Figure reproduced with permission.⁶⁸46
- Figure 10: Reaction between catechol and glyoxylic acid catalysed by Al_2O_3 to produce 3,4-dihydroxymandelic acid, a step in the synthesis of vanillin and its derivatives.....47
- Figure 11: Contour plot generated by Lapkin *et al.*⁶⁰ using data obtained from the DoE carried out by Minisci *et al.*⁶⁹ to show selectivity towards 3,4-dihydroxymandelic acid for the reaction between catechol and glyoxylic acid using an aluminium oxide catalyst. Figure reproduced with permission.....47

Figure 12: Reaction network used by Claus and colleagues to model the one-pot transformation of citronellal to menthols using a Ru/H-BEA catalyst. Figure reproduced with permission.⁷⁶	49
Figure 13: Number of publications per year when searching ‘metal-organic framework’ on Web of Science from 2001 to 2022.....	52
Figure 14: a) Common examples of secondary building units in MOFs. From left to right: MIL-100/101(Fe), Cu₃(BTC)₂, MOF-5 (coordinatively unsaturated sites shown by dotted circles) b) Common examples of linkers in MOFs. From left to right: 2-methylimidazole, terephthalic acid, trimesic acid and 4,4',4'',4'''-(1,3,6,8-Pyrenetetrayl)tetrabenzoic acid linkers.....	52
Figure 15: Structure of MIL-100(M) MOFs. Trimesic acid linkers are coordinated to M₃O trimer units (note that coordinatively unsaturated sites are illustrated by circles) giving rise to supertetrahedron units and small and large cages.....	54
Figure 16: Coordinatively unsaturated sites situated on nodes of MIL-100 MOFs allowing them to serve as Lewis acid catalysts.....	55
Figure 17: Top: Scheme of Friedel-Crafts reaction carried out by Ferey and colleagues. Conversion of benzyl chloride following Friedel-Crafts reaction with benzene to produce diphenylmethane. Figure reproduced with permission.¹⁰⁵	55
Figure 18: Reaction between benzaldehyde and glycol carried out by Zhu <i>et al.</i>¹¹⁴	56
Figure 19: Performance of different MIL-100 MOFs in a study carried out by Čejka and colleagues. Figures reproduced with permission.¹²³ ...	57
Figure 20: Carbonyl-ene reaction of α-methylstyrene with ethyl trifluoropyruvate. The conversion after 6 hours is shown for the mixed-metal MIL-100 MOFs (square: MIL-100(Sc, Al), circle: MIL-100(Sc, Fe), triangle: MIL-100(Sc, Cr), diamond: MIL-100(Sc, Fe)XS and upside down triangle: MIL-100(Sc, Fe)XS where XS means that an excess of metal was used in the synthesis than stoichiometrically required). Figure modified with permission.¹²⁰	59
Figure 21: Percentage of MOF publications for catalysis applications every year from 2001 to 2022. This was calculated by dividing the number of publications every year when searching for ‘metal-organic framework catalyst’ Web of Science by ‘metal-organic framework’.....	60
Figure 22: Different types of MOF catalysts. MOF-based catalysts include catalysis by the metal nodes, by functional linker molecules and by the introduction of guest species into the framework. Figure reproduced with permission.¹²⁷	60
Figure 23: Response surface contours obtained for biodiesel production (oleic acid and ethanol reaction) with a heteropolyanion-based ionic liquid MIL-100(Fe) catalyst using RSM. Figure reproduced with permission.¹³⁴	63

Figure 24: Contour plots obtained in the DoE study of endo- to exo-Dicyclopentadiene using UiO-66 as a catalyst. Figure reproduced with permission ¹³⁵	64
Figure 25: a) Epoxide carbonylation in continuous flow carried out by Sanford and colleagues using a range of different MOF species. b- c) Initial testing of catalysts over 5 hours time-on-stream. d) 24 hour stability study carried out with MIL-100(Sc). Figures b-d reproduced with permission. ¹²⁵	69
Figure 26: a) Diels-alder reaction between 1,4-benzoquinone and cyclohexa-1,3,-diene. b) Epoxide ring-opening reaction between styrene oxide and aniline. c) Friedel-crafts reaction between 2-methoxynaphthalene and acetic anhydride.	69
Figure 27: Schematic representation of activated carbon. Figure reproduced with permission. ¹⁸⁴	72
Figure 28: Optical image of PBSAC spheres.....	73
Figure 29: Light microscope image of Pd/PBSAC before (left) and after (right) use in 100 hour hydrodechloriantion reaction. Figure reproduced with permission. ¹⁹⁰	74
Figure 30: a-b) Reduction of 1-methoxy-4-nitrobenzene tested in continuous flow using Pd@PBSAC catalyst in GSK's pilot plant equipment, a stable catalytic activity was observed over 6 hours. c- d) Deprotection of N-benzyl-4-methoxyaniline tested in continuous flow, over 10 hours minimal loss in conversion was observed. Figures b and d reproduced with permission. ³²	75
Figure 31: Typical PXRD pattern of the product obtained following solvothermal synthesis (purple) and the simulated powder pattern of isostructural MIL-100(Cr) (red) for comparison. ¹⁰⁶	86
Figure 32: MIL-100(Sc) powder before (a) or after (b) drying under vacuum overnight at 150 °C. A colour change from white to orange was observed.	87
Figure 33: PXRD pattern of MIL-100(Sc) after being subjected to different drying temperatures: 150 °C under vacuum overnight (black), 150 °C for 90 mins (purple) and simulated pattern of MIL-100(Cr) (red).	88
Figure 34: Typical TGA plot obtained for MIL-100(Sc) showing % weight change (purple) and first derivative weight change (red) with increasing temperature for MIL-100(Sc) dried at 150 °C for 90 mins. Samples were heated from room temperature at 10 °C min ⁻¹ in flowing air. Arrows illustrate relevant Y-axis for data.	89
Figure 35: Images of samples that were submitted to different drying conditions and the colour change that was observed.	91
Figure 36: TGA profiles of different drying conditions employed for MIL-100(Sc) powder.....	92
Figure 37: FT-IR spectrum of activated MIL-100(Sc) in this work (washed with water and ethanol, stirred in methanol for 24 hours and dried at 150 °C for 1.5 hours) between 500 - 4000 cm ⁻¹	94

Figure 38: TGA plot showing how stoichiometry of MIL-100(Sc) was determined using the 'dry' mass of MIL-100(Sc) at 380 °C and the residual mass following framework decomposition at approximately 580 °C.	96
Figure 39: N ₂ adsorption and desorption isotherm of MIL-100(Sc) obtained at -196 °C.	99
Figure 40: a-c) SEM image of MIL-100(Sc) particles. d) Histogram of average particle diameter (nm) for 75 particles. e) Cumulative average particle diameter (nm) of the 75 particles sized.....	100
Figure 41: a) SEM image where EDX map was obtained. b-d) O K α , C K α and Sc K α EDX map, respectively. e) Spot where EDX spectrum was obtained and f) resultant EDX spectrum. Note that large Si K α peak arises from the silicon wafer the sample was dispersed on.....	101
Figure 42: Mastersizer 3000 unit (middle) equipped with a Hydro MV automated wet dispersion unit (right).....	102
Figure 43: Diameter of a spherical particle (left) and diameter of a cubic particle (right).....	105
Figure 44: A hypothetical MIL-100(Sc) particle 204 nm in diameter consisting of cubic unit cells with 816 scandium units with a unit cell parameter of 74.52 Å. Such a particle was calculated to contain 20517 unit cells. Note: relative lengths in the illustration are not to scale.....	106
Figure 45: In a hypothetical reaction involving 100 mg of completely dry MIL-100(Sc) which was completely monodisperse, comprising 204 nm particles, it was calculated that 2.67×10^{13} particles were present.....	107
Figure 46: Relationship between % of sites located on the exterior of MIL-100(Sc) vs. particle diameter.	109
Figure 47: a) XPS spectra of MIL-100(Sc) showing O 1s, Sc 2s, Sc 2p and C 1s peaks respectively. b) C1s region of the spectrum which was deconvoluted to give three peaks at peaking at 284.8, 287.2 and 289.9 eV - these correspond to the C-C, C-O and C=O bonds respectively. c) Sc 2p region of the spectrum. d) Sc 2s region of the spectrum.....	110
Figure 48: Intramolecular cyclisation of citronellal catalysed by Lewis acids forms four isopulegol isomers.	114
Figure 49: a) Citronellal molecule and related dimensions. b) Isopulegol molecule and related dimensions. c) Anticlockwise: Supertetrahedron unit of MIL-100(M), small cage, large cage and unit cell of MIL-100(M). Structures of MIL-100(M) are based on a defect-free structure with a stoichiometry of [M ₃ O(BTC) ₂ X.].....	119
Figure 50: 2-level 3-factor FFD DoE carried out in this work consisting of 11 experiments: 8 corner-point experiments and 3 replicate experiments in the centre. Repeat of Figure 7.	120

Figure 51: Concentration profiles of (\pm)-citronellal and (\pm)-isopulegol isomers (left), conversion, selectivity to (\pm)-isopulegols and (\pm)-isopulegol (right).	124
Figure 52: a) Left: Untransformed histogram in saturated model, right: log transformed histogram. b) Left: Saturated coefficient plot of untransformed model with all terms shown. Right: Unsaturated coefficient plot of log transformed model with terms removed to give best validation metrics. c) Left: Validation metrics of the saturated, unrefined model. Right: Highest validation metrics of final unsaturated and log transformed model.....	126
Figure 53: Significant and non-significant model terms in the coefficient plot.....	127
Figure 54: a-b) Interaction plot from the final initial rate DoE model for Ratio*Conc interaction term.	128
Figure 55: Contour plot generated which shows the initial rate as a function of the variables studied.....	129
Figure 56: Surface plot of initial rate at 110 °C highlighting the difference in initial rate values observed for the experiments in the DoE.....	130
Figure 57: For TOF a) Left: Untransformed histogram in saturated model, right: log transformed histogram. b) Left: Saturated coefficient plot of untransformed model with all terms shown. Right: Unsaturated coefficient plot of log transformed model with terms removed to give best validation metrics. c) Left: Validation metrics of the saturated, unrefined model. Right: Validation metrics of final unsaturated and log transformed model.	130
Figure 58: Contour plot generated which shows the TOF as a function of the variables studied.....	132
Figure 59: Surface plot of TOF at 110 °C showing the variation in values that were predicted by the model.....	133
Figure 60: Plot of optimised data points outputted by MODDE software. A Pareto front (red points) was identified illustrating the trade-off upon attempting to maximise these conditions.....	133
Figure 61: Contour plot of initial rate and TOF with optimised conditions outputted by MODDE shown by target icon (temperature: \approx 110 °C, citronellal concentration: 0.75 M, citronellal:scandium molar ratio: 8.2).	134
Figure 62: For selectivity towards (\pm)-isopulegols a) Left: Untransformed histogram in saturated model, right: negative log transformed histogram. b) Left: Saturated coefficient plot of untransformed model with all terms shown. Right: Saturated coefficient plot of negative log transformed model with terms removed to give best validation metrics. c) Left: Validation metrics of the saturated, unrefined model. Right: Validation metrics of the negative log transformed and saturated model.....	135

Figure 63: For diastereoselectivity a) Untransformed histogram in saturated model. b) Left: Saturated coefficient plot of untransformed model with all terms shown. c) Left: Validation metrics of the saturated, unrefined model.....	137
Figure 64: The kinetic experiments carried out in the model (5 mol % Sc(OTf) ₃ , 0.1 M (±)-citronellal, DCM) at -20 °C, -30 °C and -40 °C and model fit. For each species, the model fits the experimental data well.....	144
Figure 65: The DoE experiments (1, 2 and 4) that were used to test the fit of the model fit.	147
Figure 66: a): The DoE experiments (1, 2 and 4) that were used to test the model fit and the subsequent model fit of the kinetic model based on LH kinetics. b) A first-order exponential decay curve was fitted to the same DoE experiments (1, 2 and 4) showing an improved fit. ...	151
Figure 67: a) Image of material formed following in-situ solvothermal approach. b) Powder X-ray diffraction patterns of simulated MIL-100(Cr) (red) and MIL-100(Sc)@PBSAC material prepared by in-situ solvothermal synthesis (blue).	165
Figure 68: Synthetic procedure of MIL-100(Sc)@PBSAC composites carried out in this work.	167
Figure 69: Visual appearance of MIL-100(Sc)@PBSAC (image) was unchanged from as received PBSAC spheres.	168
Figure 70: a) TGA profile of PBSAC-trimesic acid control sample. There is a small weight loss beginning at approximately 300 °C corresponding to the thermal decomposition of adsorbed trimesic acid. b) TGA profile of trimesic acid. Thermal decomposition begins to occur at approximately 300 °C. Figures reproduced with permission. ³⁰⁰	172
Figure 71: An assessment of the repeatability of synthesis of MIL-100(Sc)@PBSAC composites over 24 batches. The intramolecular cyclisation of (±)-citronellal was used as the model reaction, with the yield after 2 hours of reaction. Conditions: 0.1 M (±)-citronellal, toluene, 110 °C, 65 mg catalyst.	173
Figure 72: a-b) Powder X-ray diffraction patterns of MIL-100(Sc) simulated by adjusting the unit cell parameter of MIL-100(Cr) to 74.518 Å (red), MIL-100(Sc) synthesized by reflux (green), MIL-100(Sc)@PBSAC composites (blue) and PBSAC spheres (control) (yellow). N.B. The data presented in (b) is identical to (a) but displays narrower y-axis and x-axis ranges to enable clearer MIL-100(Sc) peak visualisation. Figures reproduced with permission. ³⁰⁰	174
Figure 73: N ₂ adsorption/desorption isotherms of PBSAC (yellow), MIL-100(Sc)@PBSAC (blue) and MIL-100(Sc) (green). The adsorption isotherm is represented by filled points whilst the desorption isotherm is represented by hollow points. Figure reproduced with permission. ³⁰⁰	175

- Figure 74: Plot of BJH desorption differential pore volume vs. pore width for PBSAC (yellow), MIL-100(Sc)@PBSAC (blue) and MIL-100(Sc) (green). Figure reproduced with permission.³⁰⁰177**
- Figure 75: a) TGA profiles of PBSAC (yellow), MIL-100(Sc)@PBSAC (green) and MIL 100(Sc) (blue) in flowing air. b) TGA derivative weight loss plot for PBSAC (yellow), MIL-100(Sc)@PBSAC (green) and MIL-100(Sc) (blue). MIL-100(Sc) and MIL-100(Sc)@PBSAC decomposition begins at a similar temperature (≈ 380 °C). Figures reproduced with permission.³⁰⁰178**
- Figure 76: a) TGA profile of PBSAC spheres showing the dry mass (≈ 515 °C) and residual mass following framework decomposition at ≈ 740 °C. b) TGA profile of MIL-100(Sc)@PBSAC showing the dry mass (≈ 380 °C) and residual mass following framework decomposition at ≈ 700 °C. c) TGA profile of MIL-100(Sc) showing the dry mass (≈ 380 °C) and residual mass following framework decomposition at ≈ 580 °C. Figures reproduced with permission.³⁰⁰179**
- Figure 77: a-c) SEM images of a PBSAC bead showing; a) the whole bead and (b-c) a crack located on surface of a PBSAC bead. d) EDX spectrum of PBSAC sphere. Figures reproduced with permission.³⁰⁰181**
- Figure 78: a) SEM image of MIL-100(Sc)@PBSAC composite sphere. b-d) Magnified SEM images of the surface of a MIL-100(Sc)@PBSAC sphere illustrating the cracks and scratches on the surface with MIL-100(Sc) present inside of these cracks. e) SEM image of a MIL-100(Sc)@PBSAC sphere with the region where EDX spectra was obtained is highlighted. f) Resultant EDX spectra of this region. Figures a, c and f reproduced with permission.³⁰⁰182**
- Figure 79: Magnified SEM image of the surface of a MIL-100(Sc)@PBSAC sphere illustrating the cracks and scratches on the surface with MIL-100(Sc) present inside of these cracks and position where EDX map was acquired. b) Sc $K\alpha$ EDX map of the surface of a MIL-100(Sc)@PBSAC sphere. c) EDX line scan location across a crack on the surface of a MIL-100(Sc)@PBSAC sphere indicated by the yellow line in the inset image and subsequent scandium $K\alpha$ counts across a crack on the surface of MIL-100(Sc)@PBSAC as a function of the distance. Figure a reproduced with permission.³⁰⁰..183**
- Figure 80: a) SEM image showing a 10 μm FIB cross-section to show the surface crack of a MIL 100(Sc)@PBSAC sphere. (b-d) O $K\alpha$, C $K\alpha$ and Sc $K\alpha$ EDX map respectively of the etched sample. Figures reproduced with permission.³⁰⁰184**
- Figure 81: a) Survey of as received PBSAC showing O 1s and C 1s peaks respectively. b) C1s region of the spectrum which was deconvoluted to give three peaks reach maxima at 284.8, 285.7 and 289.9 eV - these correspond to the C-C, C-O and C=O bonds respectively.185**

- Figure 82: a) Survey of MIL-100(Sc)@PBSAC showing O 1s, Sc 2p/N 1s and C 1s peaks respectively. b) C1s region of the spectrum which was deconvoluted to give three peaks peaking at 284.9, 285.8 and 289.9 eV - these correspond to the C-C, C-O and C=O bonds respectively. c) Sc 2p region of spectrum with three peaks. The first correspond to the 2p_{3/2} and 2p_{1/2} at 403.1 and 407.6 eV respectively. The third peak, at 399.9 eV, was assigned to N 1s.....185**
- Figure 83: The apparatus used to test the crush strength of MIL-100(Sc)@PBSAC and PBSAC spheres. Particles were placed in a stage and a piston was moved towards the spheres at a constant force until the sphere was crushed.....187**
- Figure 84: Volume distribution of PBSAC spheres obtained from Mastersizer 3000 laser diffraction analysis. Figure reproduced with permission.³⁰⁰188**
- Figure 85: PXRD pattern of loose powdered MIL-100(Sc) (green) that was formed in the reaction vessel during MIL-100(Sc)@PBSAC synthesis compared with the simulated pattern of MIL-100(Sc). Figure reproduced with permission.³⁰⁰189**
- Figure 86: Reusability testing of MIL-100(Sc)@PBSAC composites in batch. Conditions: 0.09 M Citronellal, toluene, 110 °C, 1 hour, 150 mg catalyst. Catalyst reactivated by soaking in methanol for 24 hours and dried by blowing nitrogen over the catalyst.....195**
- Figure 87: Effect of stirring rate and observed catalytic activity. Conditions: 0.08 M (±)-citronellal, 110 °C, toluene, 150 mg catalyst.196**
- Figure 88: a) Flow setup used in this work. MIL-100(Sc)@PBSAC composites were packed inside a vertically placed stainless steel packed-bed reactor heated using an aluminium heating block, heating coils and a Eurotherm temperature controller. A HPLC pump was used to pump reagents to the reactor through PTFE tubing and system pressure was maintained using a back pressure regulator (BPR) (75 psi) (not shown). Samples were collected at the tubing outlet. b-d) Packed-bed reactor used for flow reactions b) with and c) without connectors attached and d) aerial view. Figures reproduced with permission.³⁰⁰197**
- Figure 89: Plot of normalised residence time distribution (E(Θ)) vs. residence time at each flow rate studied.....199**
- Figure 90: Continuous flow study carried out by Murzin and colleagues for the cyclisation of citronellal catalysed by different extrudates containing 30% wt. bentonite binder and zeolites a) H-β-25, b) H-β-150, and c) H-Y-5.1. Conversion of citronellal is shown by filled points whilst mass balance is shown by unfilled points over 150 minutes time-on-stream. Deactivation is visible in all three studies. Conditions: 35 °C, 10 bar argon, 0.4 mL/min, 0.086 M citronellal, 1 g catalyst. Figure a-c reproduced with permission.³¹⁵203**

Figure 91: a) Concentration vs. time plots for (\pm)-citronellal and four (\pm)-isopulegol isomers that are produced in the reaction over the 9 hours time-on-stream at 0.25 mL/min. b) Conversion, yield and selectivity to (\pm)-isopulegol vs. time plot for the 9 hours time-on-stream.....	205
Figure 92: TON, TOF and productivity of the reaction for the formation of (\pm)-isopulegols vs. time over the 9 hours time-on-stream.	208
Figure 93: a-c) SEM image of MIL-100(Sc)@PBSAC composite sphere after 26 hours-on-stream. The surface of the particle appears unchanged to MIL-100(Sc)@PBSAC spheres that have not been used for a reaction. c) SEM image of a MIL-100(Sc)@PBSAC sphere with the region where EDX spectra was obtained highlighted. d) Resultant EDX spectra of this region. Figures reproduced with permission. ³⁰⁰	210
Figure 94: TGA profile and 1st derivative of MIL-100(Sc)@PBSAC composite a) before 26 hour reaction at 0.25 mL/min b) after 26 hour reaction at 0.25 mL/min.....	211
Figure 95: a) Conversion and b) Yield (of (\pm)-isopulegols) plots for flow experiments carried out at 0.25, 0.5, 1 and 1.5 mL/min. N.B. Data at 0.25 mL/min are same from section 4.3.2.1.	213
Figure 96: (\pm)-Isopulegols mass balance as a function of time in the flow experiments for the flow rate experiments conducted at 0.25, 0.5, 1.0 and 1.5 mL/min.....	216
Figure 97: Normalised yield values after 1 hour of reaction versus the number of residence volumes for at the flow rates studied.	217
Figure 98: Waxy material that was observed to form at the reactor connection.....	218
Figure 99: ¹ H NMR (CDCl ₃) of waxy material that was observed to form suggesting that it was hydrocarbon-based. Peak at 7.3 ppm corresponds to CHCl ₃ solvent peak.	218
Figure 100: Toluene wash step after 24 hours in the flow reaction at 0.5 mL/min. Toluene was flowed through for 2 hours at 2 mL/min, 110 °C. No improvements in conversion or yield were observed.....	219
Figure 101: Conversion and yield vs. time data in the stability studies at 0.5 mL/min (0.23 M (\pm)-citronellal, 80 °C, CHCl ₃ , 0.5 mL/min) for 3.5 hours of time-on-stream then. NB: the quantities of (\pm)-citronellal and MIL-100(Sc)@PBSAC used in this reaction were scaled-down to preserve materials.	221
Figure 102: Depiction of replacement of (\pm)-citronellal molecule coordinated to Sc ³⁺ site of MIL-100(Sc) node by methanol molecule.	222
Figure 103: Conversion and yield vs. time data in the stability studies in methanol (0.5 mL/min, 0.2 M (\pm)-citronellal, 100 °C, 500 mg MIL-100(Sc)@PBSAC) for 4 hours.....	223

Figure 104: Methanol wash flow experiment that was carried out. After 4 hours of reaction (0.4 M (\pm)-citronellal, 1 g (\pm)-citronellal, 0.5 mL/min, 110 °C), the catalytic activity was partially regenerated by flowing methanol through the system (2 mL/min, 60 mins, 110 °C).	224
Figure 105: TGA profile and 1st derivative of MIL-100(Sc)@PBSAC composite a) after methanol wash experiment.	225
Figure 106: Left to right: Cannabidiol (CBD), the active ingredient in Epidolex®, Δ^9 -THC, known as Dronabinol in a pharmaceutical context, the active ingredient in Marinol® and Syndros® and Nabilone, a synthetic cannabinoid and active ingredient in Cesamet®.	227
Figure 107: Coupling between methyl olivetolate and <i>p</i> -menthadienol to produce CBD-methyl ester catalysed by MIL-100(Sc)@PBSAC composites in continuous flow studied in this research.	230
Figure 108: Coupling between olivetol and <i>p</i> -menthadienol to produce CBD catalysed by MIL-100(Sc)@PBSAC composites in continuous flow studied in this research.	234
Figure 109: Δ^9 -THC and other THC isomers Δ^8 -THC, Δ^8 - <i>iso</i> -THC and $\Delta^{4(8)}$ - <i>iso</i> -THC that may have formed. These compounds were observed by Kappe <i>et al.</i> ³⁴⁶ upon studying THC formation in continuous flow.	237
Figure 110: a) Zr ₆ cluster in UiO- MOFs with connectivity to one 4,4-biphenyldicarboxylic acid linker in UiO-67 MOFs shown. b) Linkers in UiO-66, UiO-67 and UiO-67-BPY MOFs respectively. Left to right: 1,4-dicarboxylic acid, 4,4-biphenyldicarboxylic acid and 2,2'-bipyridine-5,5'-dicarboxylic acid.	245
Figure 111: a) Cu@UiO-67-BPY prepared by Luan <i>et al.</i> ³⁵¹ and used as a catalyst for the selective oxidation of alcohols and the aerobic epoxidation of alcohols. b) One reaction studied by Luan <i>et al.</i> ³⁵¹ namely the aerobic epoxidation of cyclohexene catalysed by CuCl ₂ -UiO-67-BPY.....	246
Figure 112: a) TGA of UiO-67-BPY@PBSAC (green) and PBSAC (yellow). b) PXRD of UiO-67-BPY (simulated) (blue), Cu@UiO-67-BPY (red) Cu@UiO-67-BPY@PBSAC (green) and PBSAC (yellow).	248
Figure 113: a-d) SEM images of Cu@UiO-67-BPY@PBSAC. e-f) EDX spot and subsequent spectrum obtained for Cu@UiO-67-BPY@PBSAC.	249
Figure 114: SEM images used to obtain particle size distribution with line profiles for each particle that was sized shown.....	259
Figure 115: Calibration curve of (\pm)-citronellal and response factor (slope). Internal standard used was n-decane. Figure reproduced with permission. ³⁰⁰	262
Figure 116: Calibration curve of isopulegol and response factor (slope). Internal standard used was n-decane. Figure reproduced with permission. ³⁰⁰	263

Figure 117: Calibration curve of (\pm)-citronellal and response factor (slope). Internal standard used was biphenyl.	264
Figure 118: Calibration curve of isopulegol and response factor (slope). Internal standard used was biphenyl.	264
Figure 119: Calibration curve of cyclohexene and response factor (slope). Internal standard used was biphenyl.	265
Figure 120: Calibration curve of cyclohexene oxide and response factor (slope). Internal standard used was biphenyl.	266
Figure 121: Calibration curve of methyl olivetolate and response factor (slope). Internal standard used was biphenyl.	267
Figure 122: Calibration curve of CBD-methyl ester and response factor (slope). Internal standard used was biphenyl.	267
Figure 123: a) Packed-bed reactor used in this work with adapters connected. b) Packed-bed reactor used in this work without adapters connected. c) Top-view of packed-bed reactor used in this work. Figure reproduced with permission.³⁰⁰	274
Figure 124: Flow setup used in this work. Figure reproduced with permission.³⁰⁰	275

List of Schemes

- Scheme 1: Hydrogenation step conducted by Papageorgiou *et al.*⁷⁹ who developed a model to describe the kinetics of the reaction and a physical model to explore the reaction temperature profiles.....50**
- Scheme 2: Synthesis of MIL-100(Sc) carried out in this work, adopted from Wright *et al.* where precursors were added to a PTFE liner and heated solvothermally in a stainless steel autoclave at 150 °C for 48 hours.¹¹⁹85**
- Scheme 3: Proposed mechanism of citronellal cyclisation involving re-arrangement, Lewis acid catalyst coordination and cyclisation of citronellal in a concerted fashion to produce isopulegol.....118**
- Scheme 4: Scheme of (±)-citronellal cyclisation catalysed by scandium triflate.....143**
- Scheme 5: Scheme of first model that was fitted for the (±)-citronellal cyclisation catalysed by MIL-100(Sc) using experimental data from the DoE.146**
- Scheme 6: Scheme of model based on LH kinetics that was fitted for the (±)-citronellal cyclisation catalysed by MIL-100(Sc) using experimental data from the DoE. Species 3 is an adsorption complex between a (±)-citronellal molecule and MIL-100(Sc).148**
- Scheme 7: Summary of reactions studied in continuous flow using MIL-100(Sc)@PBSAC composites in this work. a) The intramolecular cyclisation of citronellal, coupling of b) olivetol or c) methyl olivetolate with *p*-menthadienol in a Friedel-Crafts reaction to produce CBD or CBD-methyl ester respectively.....193**
- Scheme 8: a) The intramolecular cyclisation of citronellal and the b) ‘protected route’ to CBD-methyl ester (see section 4.3.3 for more detail) studied using the flow system described in Figure 87.197**
- Scheme 9: The flow system used in this work in which (±)-citronellal (≈ 0.4 M in toluene) was pumped through a packed-bed reactor containing 1 g of MIL-100(Sc)@PBSAC and maintained at 110 °C...201**
- Scheme 10: Summary of reaction routes to CBD(-methyl ester) explored in this work into continuous flow. The reactions involve coupling of olivetol or methyl olivetolate with *p*-menthadienol in a Friedel-Crafts reaction.....228**

List of Tables

Table 1: Comparison of the amounts of materials produced and their subsequent E-factor in the bulk and fine chemicals industries. ^{1, 28} ...	38
Table 2: The Michael addition reactions studied by Wright <i>et al.</i> involving the use of indole-based substrates of differing sizes to observe the impact upon the catalytic activity.	58
Table 3: Summary of key literature exploring the catalytic activity of a MOF-based catalyst via DoE or RSM.	66
Table 4: Conditions employed for synthesis of MIL-100(Sc) powder in this work, based on the conditions used by Wright <i>et al.</i> ¹¹⁹	84
Table 5: Effect of drying conditions on colour and final mass of activated MIL-100(Sc).....	90
Table 6: Shows starting mass, mass just before framework decomposition (at 380 °C) and the mass present following framework decomposition (at 600 °C) of an activated MIL-100(Sc) sample in this work. These are also presented as weight percentages.....	97
Table 7: Proposed formula of MIL-100(Sc) in this work following TGA analysis compared with the literature reported formula. ¹¹⁹	97
Table 8: D10, D50, D90, span and D[3,2] values obtained for MIL-100(Sc) during light scattering analysis.....	102
Table 9: Analytical technique and the corresponding information that may be derived when estimating the number of catalytically active scandium sites located on the exterior of the framework vs the interior.	104
Table 10: Comparison of catalytic activity of MIL-100(Sc) in this work towards intramolecular cyclisation of citronellal compared to other MOFs and other popular examples of heterogeneous and homogeneous (where stated) catalysts taken from the literature....	115
Table 11: Set of variables and conditions studied in the DoE in toluene.	121
Table 12: The list of 11 experiments conducted in the 2-level 3-factor FFD DoE in this work. Note: despite being systematically tabulated, the experiments were carried out in a random order outputted by the DoE software.....	121
Table 13: Initial rate of reaction, selectivity towards (±)-isopulegols and the selectivity towards the formation of (±)-isopulegol for each experiment in the DoE.....	125
Table 14: The three sets of conditions outputted by MODDE that gave rise to the best combined initial rate and TOF values and thus gave rise to the Pareto front.	134
Table 15: Results obtained by Newman <i>et al.</i> ^{203, 264} when using scandium triflate for the intramolecular cyclisation of citronellal with DCM. ...	140

Table 16: Time and temperature dependent yields and selectivity for scandium triflate catalysed racemic citronellal cyclisation in DCM in this work. Conditions for this work: 5 mol% Sc(OTf) ₃ . 0.1 M citronellal.....	140
Table 17: Isomer-specific yields and selectivity ratios obtained in this work for the cyclisation of (±)-citronellal using scandium triflate....	141
Table 18: The reaction and subsequent activation energy determined by the kinetic model.	144
Table 19: The rate constant value outputted by Dynochem® and associated confidence interval.....	148
Table 20: The equilibrium constant value outputted by Dynochem® and associated confidence interval for the model based on LH kinetics.	149
Table 21: The rate constant value outputted by Dynochem® and associated confidence interval for the model based on LH kinetics.	150
Table 22: The reaction and subsequent activation energy determined by the kinetic model for the MIL-100(Sc) catalysed citronellal cyclisation based on LH kinetics.	152
Table 23: Mass of MIL-100(Sc) used for each experiment.....	154
Table 24: Summary of key papers showcasing the preparation of metal-organic framework-activated carbon composite materials.....	163
Table 25: Conditions employed for synthesis of powdered MIL-100(Sc) in this work, based on the conditions used by Wright <i>et al.</i> ²⁸⁶	164
Table 26: Comparison of solvothermal and reflux synthetic approaches.....	166
Table 27: Conditions employed for the reflux synthesis of MIL-100(Sc)@PBSAC in this work.....	169
Table 28: Experimental data obtained when comparing the catalytic activity of the two batches of different loadings (11.87% w/w and 5.98% w/w maximum possible loading syntheses) in the attempted synthesis of MIL-100(Sc)@PBSAC and a control sample involving as received PBSAC spheres. Conditions: 0.1 M (±)-citronellal, 110 °C, toluene, 150 mg catalyst.	171
Table 29: BET surface area, micropore volume and total pore volume of PBSAC, MIL 100(Sc) and MIL-100(Sc)@PBSAC.....	176
Table 30: D10, D50 and D90 size range of PBSAC spheres and MIL-100(Sc)@PBSAC. The tube-to-diameter (D _t /D _p) range was calculated for each size range. The crush strength of MIL-100(Sc)@PBSAC was unchanged from PBSAC spheres.....	187
Table 31: Summary of literature examples employing a MOF-based heterogeneous catalysts for liquid phase continuous flow reactions.	190

Table 32: Residence time of reactants within the filled packed-bed reactor at a given flow rate as determined by the pulse method or the volume gained upon filling with 2-propanol.	200
Table 33: Summary of research conducted regarding the continuous flow intramolecular cyclisation citronellal with heterogeneous catalysts.	201
Table 34: Average productivity and TOF values obtained for the 9 hours time-on-stream and the productivity and TON after 9 hours.	206
Table 35: Average productivity and TOF values obtained for the 9 hours time-on-stream and the productivity and TON after 9 hours.	208
Table 36: Atomic absorption spectroscopy (AAS) data of before and after 26 hours time-on-stream. An average 10.6 % loss of scandium was measured to have leached over the course of the reaction.....	209
Table 37: Flow rate studied and the resultant residence times for the packed-bed reactor used in this work.	212
Table 38: Average conversion and yield values after first 9 hours time-on-stream (at 0.25, 0.5, 1.0 mL/min) and first 5 hours time-on-stream (at 1.5 mL/min).	214
Table 39: Average productivity, TOF and STY for first 9 hours time-on-stream (0.25, 0.5, 1.0 mL/min) or 5 hours time-on-stream (1.5 mL/min) and total productivity and TON after these times.	215
Table 40: Comparison of conversion and yield obtained after 1 hour on stream when using chloroform and methanol as the reaction solvents (0.2 M citronellal, 500 mg catalyst, 0.5 mL/min).....	222
Table 41: Atomic absorption spectroscopy (AAS) data of before and after 26 hours time-on-stream. An average 3.9% loss of scandium was measured due leaching over the course of the reaction.....	225
Table 42: Batch testing of methyl olivetolate and <i>p</i> -menthadienol coupling in chlorinated solvents and using homogeneous species Sc(OTf) ₃ . Conditions: 20 mM methyl olivetolate and 22 mM or 40 mM of <i>p</i> -menthadienol, 0.5 mol % scandium loading (relative to methyl olivetolate).	231
Table 43: 20 mM methyl olivetolate, 80 mM <i>p</i> -menthadienol, 500 mg MIL-100(Sc)@PBSAC, toluene, 140 °C.	232
Table 44: Comparison of relative size of peaks at t = 2.2 and t = 2.7 minutes across experiments where different <i>p</i> -menthadienol concentrations (but identical methyl olivetolate concentrations) were employed. At lower flow rates (longer residence times), the size of these peaks appeared to depend linearly on the <i>p</i> -menthadienol concentration.....	233

Table 45: Results obtained in this work for coupling of olivetol with <i>p</i> -menthadienol using MIL-100(Sc)@PBSAC composites in a packed-bed reactor in continuous flow. Comparison is done using HPLC peak areas for all olivetol-containing species. 100 mM Olivetol, 400 mM <i>p</i> -menthadienol, Omnifit glass column (10 cm x 0.88 cm) was filled with MIL-100(Sc)@PBSAC (4.7 g).....	235
Table 46: Percentage of HPLC peak areas for peaks at t = 11.5, 13.0 and 14.2 minutes as a percentage of all peaks in HPLC chromatogram (including olivetol-containing species) for experiments listed in Table 45.	238
Table 47: Conversion of cyclohexene and yield of cyclohexene oxide after 4 hours of reaction. Conditions: 40 °C, acetonitrile (5 mL), 1 mmol cyclohexene, pivaldehyde (1.2 mmol) and 1 atm. compressed air balloon.....	250
Table 48: GC method used for off-line experiment analysis.....	262
Table 49: Temperature program used for off-line GC chromatography...	262
Table 50: GC method used for off-line experiment analysis.....	263
Table 51: Temperature program used for off-line GC chromatography...	263
Table 52: GC method used for off-line experiment analysis.....	265
Table 53: Temperature program used for off-line GC chromatography...	265
Table 54: Method parameters for HPLC analysis of methyl olivetolate and <i>p</i> -menthadienol coupling	266
Table 55: Solvent composition for HPLC analysis of methyl olivetolate and <i>p</i> -menthadienol coupling.....	267
Table 56: Method parameters for HPLC analysis of olivetol and <i>p</i> -menthadienol coupling	268
Table 57: Solvent composition for HPLC analysis of olivetol and <i>p</i> -menthadienol coupling.	268

Chapter 1 Introduction

1.1 Fine chemical production

A fine chemical may be defined as a chemical produced in limited quantities ($\approx 10 - 10^4$ tonnes y^{-1}) and worth more than \$10 kg^{-1} . These chemicals are defined by their complex molecular structure which often involves multistep organic synthesis. Fine chemicals are typically intermediates in pharmaceuticals and agrochemicals.^{1, 2} The global fine chemicals market was valued at \$155.5 billion in 2018 and is expected to reach \$219.49 billion by the end of 2024.³ The UK pharmaceutical industry, a large user of fine chemicals, is important to the national economy providing $\approx 400,000$ jobs and contributing a gross value added of \approx £15 billion to the UK economy.⁴

1.1.1 Batch to continuous fine chemical manufacture

Historically, the production of fine chemicals was typically performed in standard multipurpose equipment (e.g. stirred-tank reactors) in batch, for which sufficient infrastructure already exists, and generally involved the use of stoichiometric reagents in the liquid phase followed by product isolation and purification.^{1, 2}

The last few decades have seen the start of an industry-wide shift towards the adoption of continuous manufacturing within the fine chemical industry. If properly implemented, this shift has the potential to deliver enormous quality, efficiency and safety benefits.⁵ The implementation of such technologies has also received support from regulatory bodies such as the United States' Food and Drug Administration (FDA), which recognises continuous manufacturing as an “emerging technology that can enable modernisation of the pharmaceutical industry and deliver potential benefits to both patient and industry”.⁶ Studies have shown that perhaps 30-50% of current batch processes could be carried out continuously to deliver additional benefits.⁷ The potential benefits derived from continuous manufacturing include:^{5, 7-10}

- Enhanced process safety (due to smaller reactor volumes and enhanced heat transfer rates for reactions with large exotherms).
- Improved product quality (due to precise control of reagent addition, temperature, better mixing leading to higher yields and control of impurity formation).

- Analysis in real time via in-line analytics allows for feedback control.
- Broader process window (due to access to higher temperatures and pressures) which may lead to faster reactions.
- Opportunities for reaction automation.
- Integration of downstream processing (such as other reactor modules or analytics).
- Fewer scale-up issues.

Continuous manufacturing is not a new concept and already forms the basis of production in the petrochemical and bulk chemical industries, where production scales are much larger ($\approx 10^4 - 10^6$ tonnes y^{-1}) due to the improved efficiency of this production method over batch.^{1, 10, 11} In contrast, uptake of continuous manufacturing processes within the fine chemical industry has been slow. Fine chemicals have small production volumes and short lifecycles (because regulatory approval is uncertain, an unpredictable market and patent expiration) meaning batch processing is still preferred as it uses established technology for which sufficient infrastructure, skilled personnel, and business and regulatory processes are already in place. Despite the potential long-term benefits that could be derived from continuous manufacturing, the costs of developing this technology are high and there is a lack of expertise in the workforce to support implementation. As such, uptake has not always been a priority for companies in a highly competitive and short-term profit-driven industry. Further, due to ambitious product timelines where time-to-market is highly important, there is often no time to redesign batch processes into continuous ones.^{5, 10-13}

To date, there are just twelve US Food & Drug Administration (FDA) approved continuous manufacturing applications (three of which are semi-continuous, i.e. they combine batch and continuous processing). Figure 1 illustrates the active pharmaceutical ingredient (API) in Orkambi, Prezista, Verzenio and Daurismo all of which make use of continuous manufacturing in their production.^{5, 14} Although this number is small, the implementation of all of these processes has come within the last decade which is evidence that industry is beginning to embrace continuous manufacturing.

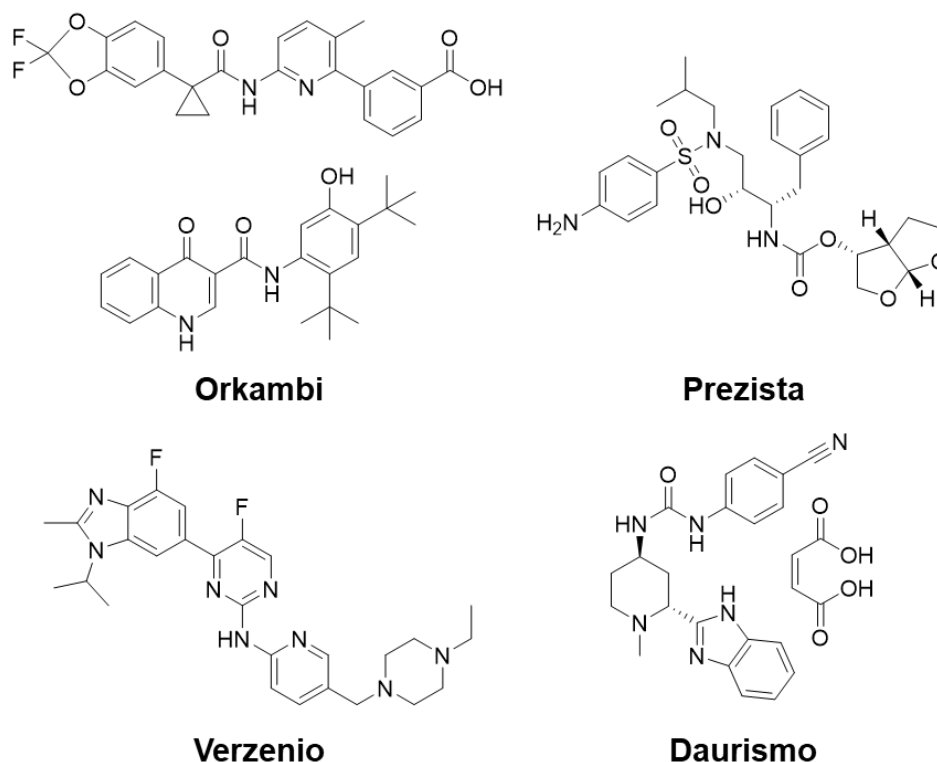


Figure 1: APIs in some of the FDA approved pharmaceuticals that exploit continuous manufacturing. N.B. Orkambi is a combination of two APIs.

1.1.2 Heterogeneous catalysis

A catalyst is a substance that increases the rate of a chemical reaction without undergoing any change itself. It does this by providing an alternative reaction pathway that has a lower activation energy.

The importance of catalysis to society is undeniable. More than 60% of chemical products and 85 - 90% of chemical processes involves use of a catalyst at some stage of their production.^{15, 16} Catalysts are involved in the production of more than \$10 trillion in goods and services of global gross domestic product (GDP) annually with a global demand exceeding \$30 billion.¹⁷

Historically, heterogeneous catalysis, where the catalyst (typically solid) exists in a different phase to the reactants/products (typically liquid/gas), has formed the basis of catalysis within the chemical industry due to the inherent economic advantages heterogeneous catalysts possess, most notably the ease of separation of the catalyst from products and subsequent reusability.¹⁸ Today it is estimated that 80% of all industrial catalytic processes use heterogeneous catalysts (Figure 2).¹⁶

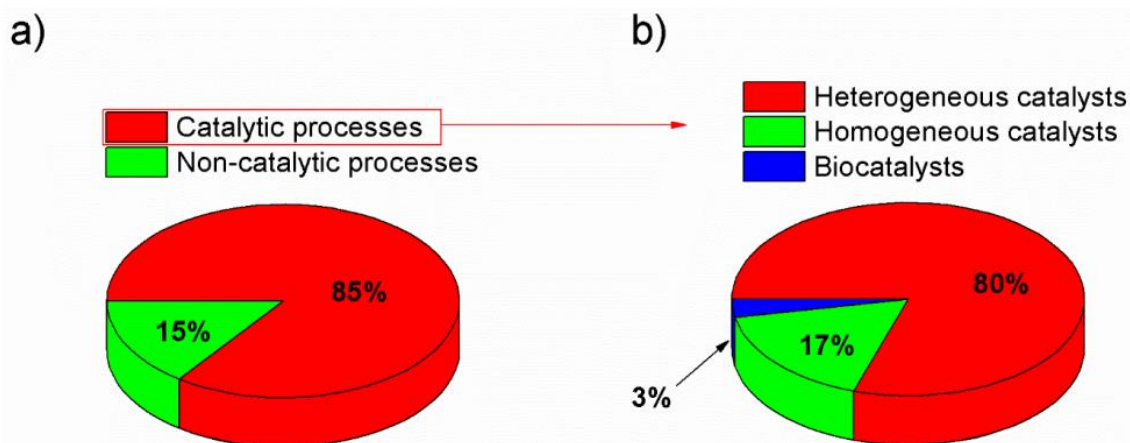


Figure 2: a) Contribution of catalytic processes to chemical industry, b) contribution of heterogeneous catalysis in comparison to other catalytic processes (2018). Figure reproduced with permission.¹⁶

The importance of heterogeneous catalysis was recognised over 100 years ago where, in 1912, Paul Sabatier won the Nobel prize in chemistry for his method of hydrogenating ethylene with hydrogen gas in the presence of finely divided nickel.¹⁹ In 1918, Fritz Haber won the Nobel prize in chemistry for the development of the Haber-Bosch process which produced ammonia at high pressures (300 bar) and temperatures (500 °C) from nitrogen and hydrogen using an iron catalyst.^{20, 21} Heterogeneous catalysis also plays a key role in a number of other industrial bulk catalytic processes, for example in the Fischer-Tropsch process used to convert carbon monoxide and hydrogen (syngas) into a range of hydrocarbons using cobalt or iron catalysts.²²

1.1.2.1 Porous and non-porous heterogeneous catalysts

Heterogeneous catalysts may be categorised as either porous or non-porous catalysts. Porous catalysts may also themselves be divided into three types: microporous (pore diameter < 2 nm), mesoporous (pore diameter 2 - 50 nm) and macroporous (pore diameter > 50 nm).²³ The main benefit of using porous catalysts is the large surface area of these materials increasing the per-volume or per-mass active catalytic area.^{17, 18} Examples of porous catalysts include zeolites, silica, alumina, zirconia, covalent-organic frameworks (COFs) and metal-organic frameworks (MOFs).^{17, 18}

Porous and non-porous heterogeneous catalysts can also be divided into bulk and supported catalysts. Catalytically active materials can serve as catalysts

themselves in a single-component form, giving bulk catalysts, or they may be supported onto a material comprising two or more components (with the catalytically active component typically present as a minor fraction) to give supported catalysts. Use of a support is primarily done to improve the dispersion of the active phase and therefore high surface area supports are desirable.¹⁸ Many of the support materials used are inert but some are also active in the catalytic process. For example, ceria supports play a role in catalytic CO oxidation when using ceria-supported platinum catalysts.²⁴ The examples of the porous catalytically active materials given above also serve as catalyst supports.^{17, 18} Activated carbon is a stable, high surface area (typically > 1000 m²/g) form of carbon that finds widespread use as a catalyst support - see section 1.3 for more discussion of the use of these materials as supports.^{18, 25} Homogeneous catalysts (i.e. catalysts existing in the same phase as the reagents, usually as a species dissolved in a liquid medium) have also been immobilised onto support materials for use as heterogeneous catalysts, with the homogeneous catalyst said to be 'heterogenised'.^{15, 17} Commonly employed strategies for the heterogenisation of homogeneous catalysts include adsorption, encapsulation, covalent tethering and exploiting electrostatic interactions (Figure 3).²⁶

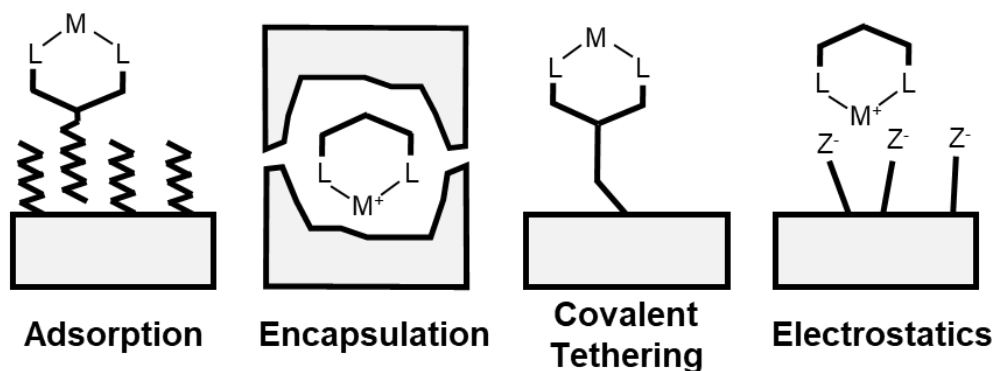


Figure 3: Schematic of four common strategies used to heterogenise homogeneous catalysts, namely adsorption, encapsulation, covalent tethering and electrostatic interactions. Figure modified with permission.²⁷

1.1.2.2 Catalysts for fine chemical production

The E-factor for a process is the kg of waste per kg of product produced. Comparison of the E-factors for bulk and fine chemicals shows that fine chemical production is much more wasteful than bulk chemical production due to the use of stoichiometric reagents coupled with multistep organic synthesis (Table 1). Because of the uncertainty regarding regulatory approval, an unpredictable

market and the expiration of patents, fine chemicals have much shorter lifecycles than bulk chemicals (as was discussed in section 1.1.1) and time-to-market carries vital importance. Thus, historically, it has been more sensible to exploit the existing stock of knowledge regarding the use of stoichiometric reagents rather than developing more efficient technologies.^{1, 2, 28, 29} In their 2016 review, Farina *et al.*³⁰ argued that the fine chemical industry does not use immobilised homogeneous catalysts due to the lower stability (via leaching of the metal), activity and selectivity thus their usage does not actually offer cost savings.

Table 1: Comparison of the amounts of materials produced and their subsequent E-factor in the bulk and fine chemicals industries.^{1, 28}

	Product tonnage	E-factor
Bulk chemicals	$10^4 - 10^6$	< 1 to 5
Fine chemicals	$10^2 - 10^4$	5 - 100
Pharmaceuticals	$10^1 - 10^3$	25 - 100

A more widespread implementation of heterogeneous catalysis in the fine chemical industry offers an efficient approach to their production, with such technologies starting to expand to the manufacture of the fine chemicals by the early 2000s.^{1, 31} In their 2021 review on heterogeneous catalysis in flow in the fine chemical industry, Luque and colleagues³¹ suggested that the use of supported metal nanoparticles, single-site molecular and single-atom catalysts for fine chemical production will become ubiquitous. GlaxoSmithKline (GSK) report that heterogeneous hydrogenations now account for 77% of their gas/liquid transformations (with 50% of these facilitated by a Raney nickel/sponge metal catalyst with the remaining catalysed by alternative metal-type catalysts).³²

1.1.2.3 Lewis acid catalysis in the fine chemical industry

A Lewis acid is a species that accepts an electron pair from a donor substrate forming a donor-acceptor adduct. This can result in an increase in the reactivity of the donor thus making Lewis acids useful reagents/catalysts in organic synthesis for a range of essential transformations such as Friedel-Crafts reactions, Diels-Alder reactions, oxidation reactions and aldol reactions.³³ Many of the conventional Lewis acids employed to catalyse these reactions (e.g. AlCl_3 , BF_3 , ZnCl_2) are homogeneous catalysts meaning that after their use for a reaction recovery is difficult.^{1, 33, 34} Furthermore, these species are often required in stoichiometric quantities (due to stronger coordination with products) thus making

them one large source of waste.^{1, 33} The development of solid Lewis acids offering inherent recyclability is an attractive solution and has been pursued. One approach has been to heterogenise these conventional species on support materials.³³ Common support materials include silica,^{35, 36} polymers,^{37, 38} alumina^{39, 40} and zeolites^{41, 42} Some solid materials also exhibit Lewis acidic catalytic properties such as alumina⁴³ and zeolites^{44, 45} - the latter are microporous solids that have found widespread application in the petrochemical industry for decades.^{46, 47} For example, zeolite ZSM-5 is used for the isomerisation of *m*-xylene to *p*-xylene.⁴⁷ A new generation of unique solid materials which possess highly tuneable structures, namely metal–organic frameworks (MOFs), have been shown to exhibit Lewis acidic catalytic properties and have future potential to be used for fine chemical synthesis - see section 1.2.1.1 for more discussion of the Lewis acidic catalytic properties of MOFs.⁴⁸

1.1.2.4 For fine chemical production in continuous flow

The use of heterogeneous catalysts for continuous flow synthesis offers a greener alternative to the traditional use of stoichiometric reagents in batch. For review articles highlighting recent developments, see references 49-52.

To highlight the benefits that can potentially be gained from using heterogeneous catalysis in continuous flow, Kobayashi *et al.*^{49, 53} classified flow synthesis systems into four types (Figure 4). Type 1: A stoichiometric reaction of A and B in a reactor which occurs by mixing in a reactor. Over the course of the reaction the concentration of reagents decreases which lowers the reactivity and unreacted reagents may be obtained with the product. Type 2: One of the reagents (B) is supported and packed into a reactor whilst the other reactant (A) is flowed through the reactor. Using excess amounts of B means the reaction easily goes to completion and the reaction mixture will contain the desired product only but overreaction may occur. Once the supported reagent is consumed the column has to be changed. Type 3: Reagents A and B are reacted in the presence of a homogeneous catalyst. After the reaction a separation step is required. Type 4: A catalytic reaction between A and B which is catalysed by a heterogeneous catalyst present in the reactor. No separation of the catalyst from the products is required and the catalyst can be re-used. If full conversion is reached then no further purification of the product is required.

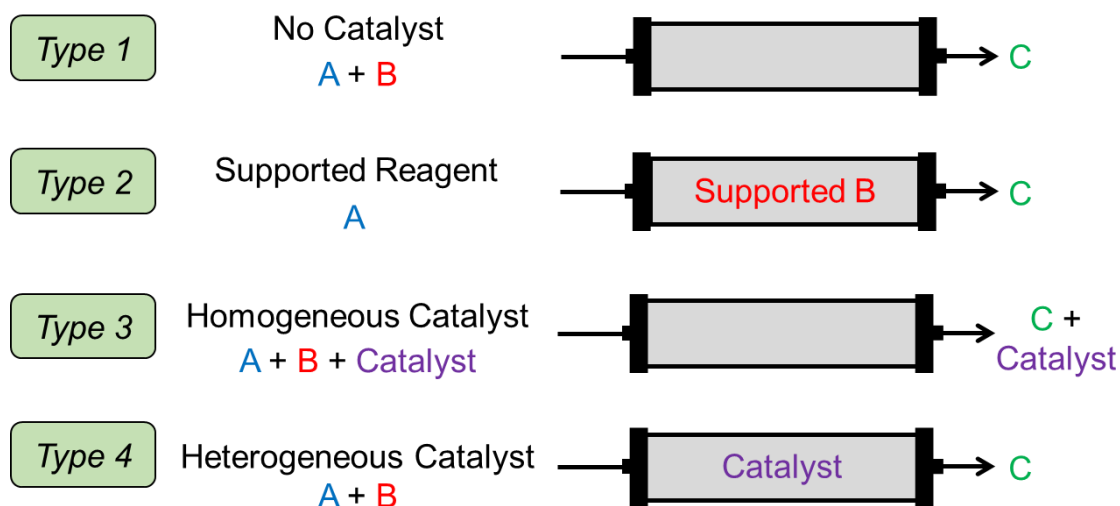


Figure 4: Four types of flow synthesis as classified by Kobayashi and colleagues. Figure modified with permission.⁴⁹

Upon consideration of the Twelve Principles of Green Chemistry,⁵⁴ Type 3 and 4 are the most preferable as they employ a catalyst leading to energy savings and waste reduction (as not employing stoichiometric reagents). The added benefit of a Type 4 system is that, in an ideal heterogeneously catalysed reaction in flow, all starting materials/reagents are consumed with only the desired product remaining after the reaction. The product stream can then be directly used in the next reaction without the need for further treatment (e.g. separation of the catalyst and workup of product streams).

In the context of a heterogeneously catalysed reaction in continuous flow, there are three main types of flow reactor (Figure 5):^{49, 55}

- packed-bed in which heterogeneous catalyst particles/powder are packed into a column and the reactants are passed through (N.B. trickle-bed reactors are a special type of packed-bed reactor).
- monolithic which is a regular or irregular network of meso- and microporous channels. The catalyst is either prepared externally and packed inside the reactor or prepared inside the reactor.
- wall-coated where the catalyst is immobilised onto the inner walls of the microreactor.

Most commercial heterogeneous reactors are based on packed-beds owing to their simple preparation and generality as the bed can simply be packed with the desired catalyst.^{49, 55} The form of the catalyst that is packed into the bed

(i.e. powder, pellet) is highly important when designing heterogeneous catalysts for use in continuous flow. In their pure form, heterogeneous catalysts typically exist as fine powders and, consequently, their direct application in flow reactors (e.g. packed-bed reactors) may in turn lead to blockages inside the reactor (via plug formation) hindering process efficiency, or worse, produce large pressure build-ups. The use of larger-sized shaped supports ($\approx > 50 \mu\text{m}$), such as monoliths, extrudates and porous beads prepared frequently from materials such as alumina, silica, polymers and carbon are used to manage these issues with the active species often anchored to the support.^{18, 32, 56}

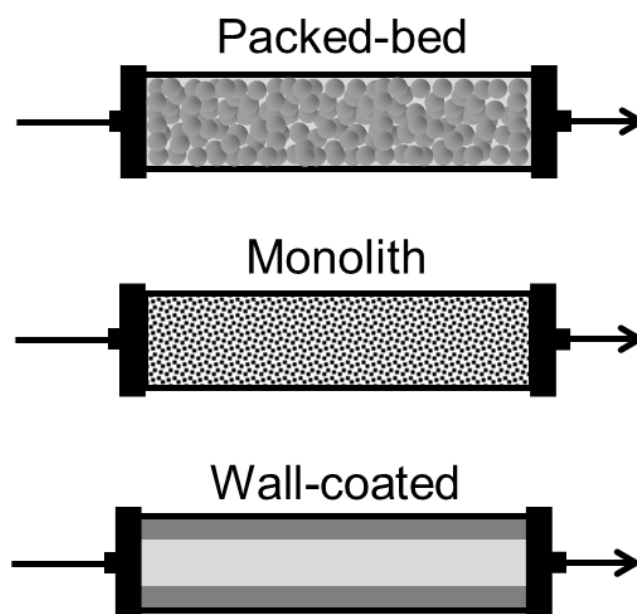


Figure 5: Schematic representation of three main types of reactors used for heterogeneous catalysis in flow, namely a packed-bed, monolith and wall-coated reactor. The arrows indicate the direction of flow through the reactor. Figure modified with permission.⁵⁷

1.1.3 Reaction optimisation

During fine chemical development, researchers make use of different tools to optimise processes, improve system understanding and lower costs. Two of these are design-of-experiments (DoE)⁵⁸⁻⁶² and kinetic modelling.^{60, 62}

1.1.3.1 Design-of-experiments (DoE)

A DoE is a powerful reaction optimisation tool, based on statistics, that has found widespread use in chemical process development for decades but is less commonly used in academia.⁵⁸⁻⁶⁰ In a DoE, multiple variables are varied simultaneously to efficiently explore the experimental space for a given reaction

(through the construction of a response surface) allowing for greater process understanding and the identification of optimised conditions when compared to other, less efficient, traditional experimental methods such as 'one variable at a time' (OVAT) approaches (Figure 6).⁶³

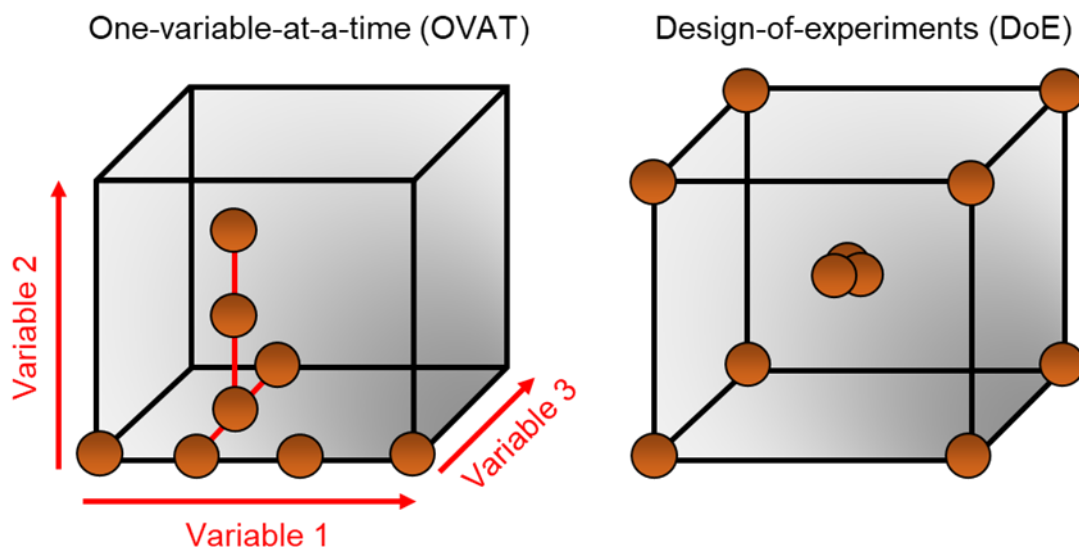


Figure 6: Left: OVAT method for studying chemical reaction space. Right: DoE method for studying chemical reaction space. Each orange circle represents an experiment.

In OVAT experimental approaches, the choice of experimental conditions is dictated by the scientific intuition of the researcher and involves fixing all variables except for one. After the best output (e.g. yield) for a given variable has been obtained, another variable is changed and optimised until the researcher believes they have reached the optimum set of conditions. Such an approach to reaction optimisation is inefficient in exploring experimental space and ignores any interactions that may exist between variables.^{60, 63, 64} In a chemical system the effect of variables upon the output that is being measured are not independent of one another which is not accounted for in OVAT approaches. Carrying out a DoE enables the researcher to understand the interactions that may exist between variables.⁶⁵

Full factorial designs (FFD) (a general example of which is illustrated on the right of Figure 6) are one common DoE design. In an FFD DoE each variable (e.g. temperature) is given a discrete level (e.g. 2 levels, -1 and +1: 70 °C and 110 °C) and experiments are conducted across all possible combinations of levels across these variables. Centre-point replicate experiments are also carried out to provide a measure of the variation of the response under identical conditions.^{65, 66}

The number of experiments in a FFD DoE is determined by Eqn. 1 where N is the number of experiments, a function of n which is the number of levels, k which is the number of factors and m which is the number of centre point replicates. A 2-level 3-factor full factorial design consists of 11 experiments: 8 corner point experiments and 3 centre point replicate experiments (Figure 7).

$$N = n^k + m \quad \text{Eqn. 1}$$

$$11 = 2^3 + 3$$

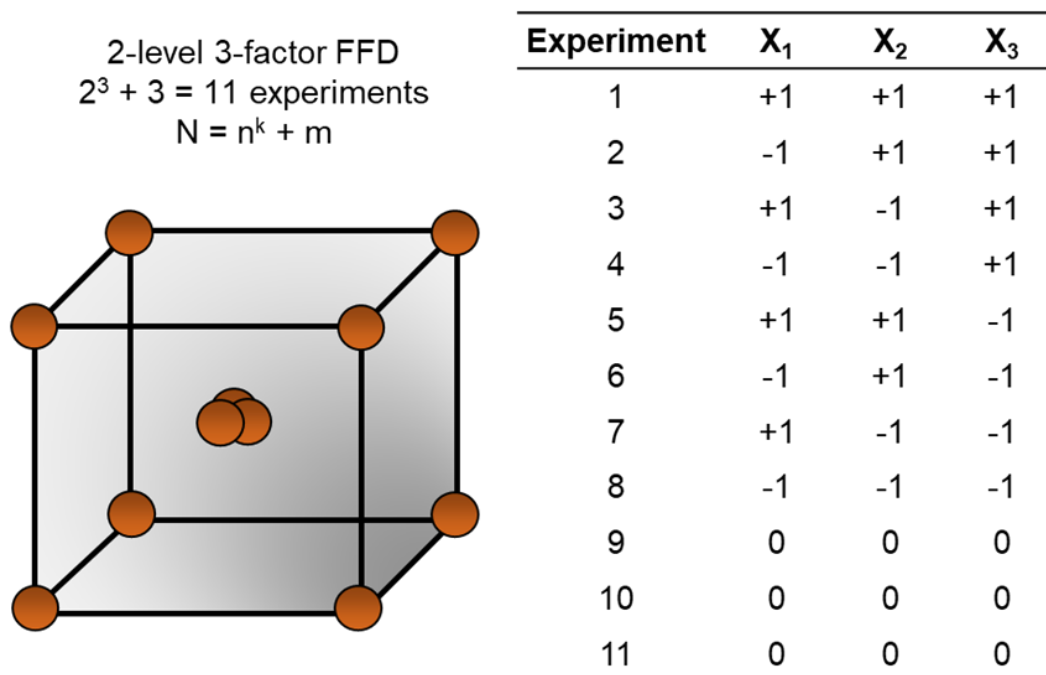


Figure 7: 2-level 3-factor FFD DoE carried out in this work consisting of 11 experiments: 8 corner-point experiments and 3 replicate experiments in the centre.

The use of a DoE has a relatively low expertise barrier-to-entry as a number of user-friendly software tools (e.g. MODDE, JMP, Design-Expert) are now available for scientists to use.⁶⁰ Review articles published highlight the utility of DoEs in fine chemical development.^{58, 59, 61}

Vigo *et al.*⁶⁷ used a DoE to optimise the synthesis of the API (and prodrug) dimethyl fumarate and corresponding active molecule monomethyl fumarate in continuous flow from fumaric acid (via an acid-catalysed esterification in the presence of methanol) using a commercial heterogeneous SiliaBond Propylsulfonic Acid (SCX-2) catalyst (Figure 8a). A central composite design (CDD), similar to a FFD but with additional axial points that enable an estimation

of curvature, was selected. This design consisted of 18 experiments (14 distinct experiments, 4 centre point replicates) where 3 variables were varied at 3 different levels. The reaction temperature (110, 120, 130 °C), residence time (10, 20, 30 minutes) and catalyst loading (50, 75, 100%) were chosen as the variables for the design.

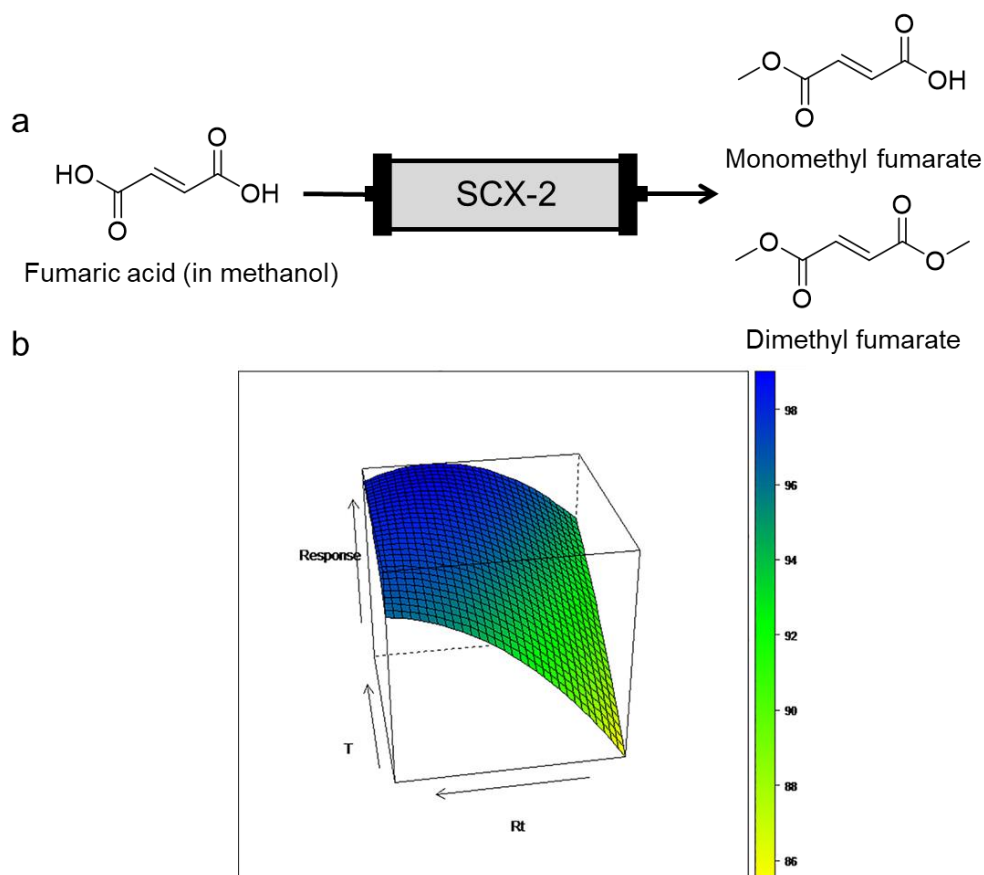


Figure 8: a) Continuous flow acid-catalysed esterification of fumaric acid to monomethyl fumarate or dimethyl fumarate in the presence of methanol studied using a DoE by Vigo and colleagues.⁶⁷ b) Response surface generated following the DoE showing % of dimethyl fumarate as a function of residence time (Rt) and temperature (T). Yellow illustrates lower % of dimethyl fumarate (i.e. $\approx 85 - 88\%$), green intermediary illustrates intermediary percentages of dimethyl fumarate (i.e. $\approx 88 - 96\%$) and blue indicates higher percentages of dimethyl fumarate (i.e. $> 96\%$). Figure reproduced with permission.⁶⁷

One of the limitations imposed by studying this system in continuous flow was the need for the reaction mixture to remain a solution throughout the whole reaction. Thus, before flowing the reaction mixture into the packed-bed containing the SCX-2 catalyst for each reaction, an initial batch reaction was carried out to partially convert the fumaric acid, which had low solubility in the reaction solvent (methanol), into the products (monomethyl fumarate and dimethyl fumarate)

which were more soluble. Following this, the partially converted reaction mixture was filtered off (to remove the catalyst) and then flowed through the packed-bed reactor at the conditions stated in the DoE. In all cases, fumaric acid was completely converted to monomethyl fumarate or dimethyl fumarate (sum of their HPLC peak areas were 100%), and so the amount of dimethyl fumarate formed was maximised. When considering conditions where a solution of 98% dimethyl fumarate was obtained, the researchers selected the sweet spot for the system to be 125 °C (15 °C lower than the temperature limit of the catalyst), a 30 minute residence time (guaranteeing good productivity for industrial production) and a catalyst loading of 63% (a good compromise to limit the amount of catalytic material used for the production). These optimised conditions were then tested where good agreement with the predicted value was measured. Figure 8b shows the response surface generated for this system; inspection shows a relatively broad combination of reaction temperatures and residence times gave rise to the desirable 98% of DMF offering the researchers some flexibility with regards to sweet spot selection.

A DoE was used by Van Grieken *et al.*⁶⁸ to identify optimal conditions when using perfluorosulfonic acid Nafion functionalised mesoporous SBA-15 silica as a catalyst for the Friedel-Crafts acylation of anisole with acetic anhydride to produce methoxy acetophenones. Methoxy acetophenones are key intermediates for the production of pharmaceuticals and fragrances. After identifying an optimum loading of the Nafion resin on SBA-15 of 13 wt.% (following the preparation of three batches of different loadings), a factorial design of experiments based on a 3² model was used to study the system with the ratio of anisole to acetic anhydride (1:1, 1:2 1:3) and the reaction temperature (100, 130, 150 °C) selected as variables.

Figure 9 illustrates the contour plots that were obtained following the DoE. A large increase in anisole conversion was observed upon increasing the reaction temperature whilst increasing the molar ratio was found to contribute to the catalytic activity to a lesser extent – this relationship is more clearly illustrated after 5 hours of reaction (Figure 9b). Deactivation of the catalyst was found to occur due to the interaction of *p*-methoxyacetophenone and other poly-acetylated products with this effect more pronounced at higher ratios of anisole:acetic anhydride (1:3) and lower temperatures (100 °C) where minimal increases in

conversion were measured between 1 and 5 hours. The best reaction conditions were identified to be at the highest temperature (150 °C) and an equimolar amount of anisole:acetic anhydride. Furthermore, comparison of the performance of the Nafion resin on SBA-15 catalyst with other sulfonic acid group-containing catalysts at the optimal conditions identified by the DoE (150 °C, equimolar ratio of anisole:acetic anhydride) showed their catalyst to be the most active.

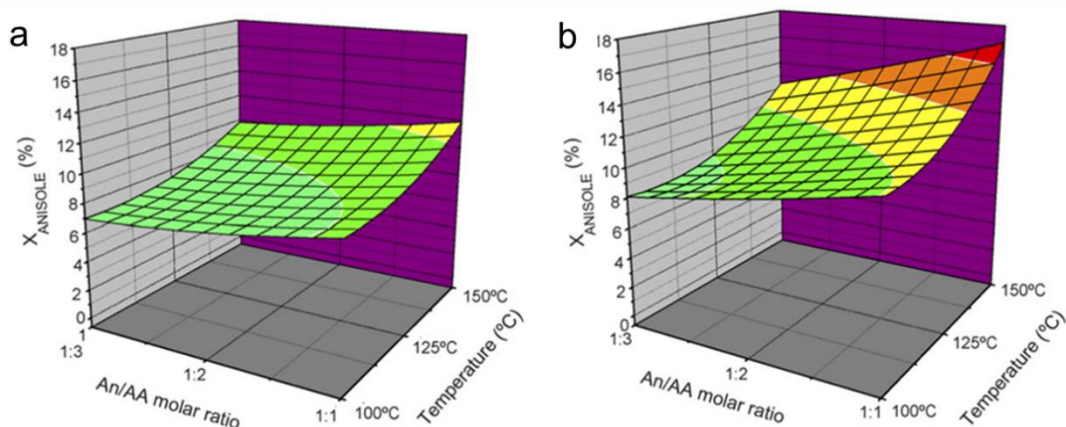


Figure 9: Response surface plot of anisole conversion after a) 1 hour of reaction b) 5 hours of reaction in the DoE. Figure reproduced with permission.⁶⁸

Overall, this DoE study formed a central part of the exploration of the catalytic activity of this material and the authors were able to deduce valuable information about the system from the results (e.g. the optimal conditions which enabled comparison with other catalysts). The results obtained in the DoE also provided interesting insight into the negative role that larger amounts of acetic anhydride had on the formation of poly-acetylated products, and thus catalyst deactivation, which are important considerations for this industrially important reaction. This work could have benefitted further, however, from studying more than two variables in the DoE to gain even further insight into the catalytic properties of this material.

Several DoE studies were exploited by Minisci et al.⁶⁹ who explored new synthetic strategies to prepare vanillin, iso-vanillin and heliotropin which are important products in the fine chemical industry. This included optimising the reaction between catechol and glyoxylic acid to give 3,4-dihydroxymandelic acid. Their initial attempts to reproduce the literature led to low selectivity and yield (< 20%) and thus a DoE was conducted to optimise the reaction conditions (Figure 10).

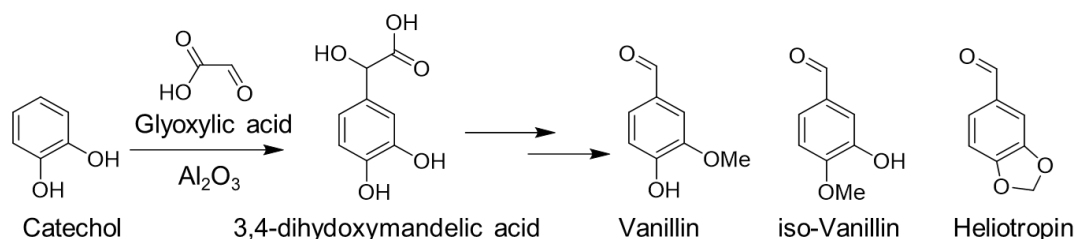


Figure 10: Reaction between catechol and glyoxylic acid catalysed by Al_2O_3 to produce 3,4-dihydroxymandelic acid, a step in the synthesis of vanillin and its derivatives.

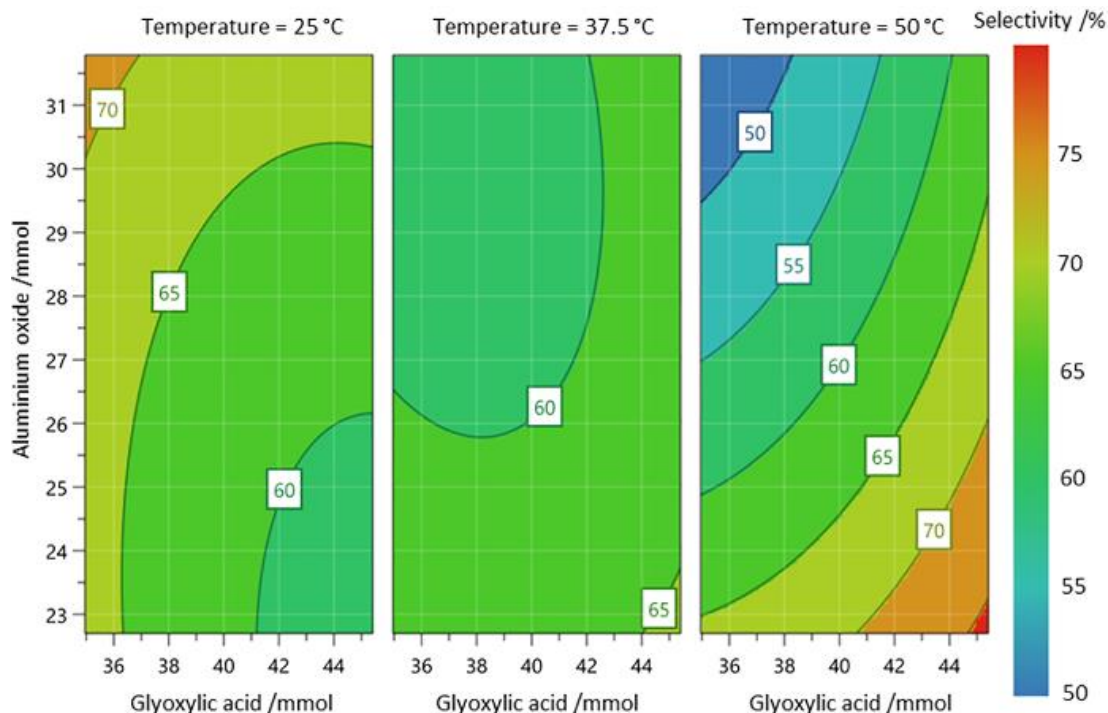


Figure 11: Contour plot generated by Lapkin *et al.*⁶⁰ using data obtained from the DoE carried out by Minisci *et al.*⁶⁹ to show selectivity towards 3,4-dihydroxymandelic acid for the reaction between catechol and glyoxylic acid using an aluminium oxide catalyst. Figure reproduced with permission.

In the first DoE, the amount of glyoxylic acid, amount of aluminium oxide, the reaction temperature and amount of NaOH were all varied in the study whilst the amount of catechol, volume of water and reaction time were all kept constant. A full factorial design consisting of 18 experiments ($2^4 + 2$) was set up but introductory experiments identified that the isolated product was much more impure when excess NaOH was used (which the authors attributed to the formation of Na salts). Given this, a second DoE was carried out with 3 variables (amount of glyoxylic acid, amount of aluminium oxide, reaction temperature) keeping the amount of NaOH added the same. The DoE identified that high

selectivity of the product could be obtained when the quantity of glyoxylic acid was in slightly more excess than catechol, a quantity fraction of 2.17 - 2.28 catechol:aluminium oxide and the temperature within 50 - 60 °C. A selectivity of 90.5% (towards 3,4-dihydroxymandelic acid) and a conversion of 78.4% was obtained. Figure 11 shows a contour plot generated by Lapkin *et al.*⁶⁰ (using the data presented by Minisci *et al.*⁶⁹) showing the selectivity towards 3,4-dihydroxymandelic acid at the different conditions studied in the DoE. This study demonstrated effective use of statistical experimental design for the optimisation of fine chemical production.

1.1.3.2 Kinetic modelling

The examples discussed illustrate that a DoE can be a powerful tool to optimise chemical reactions, however, this is only a statistical model meaning that it contains no mechanistic information about the chemical process itself. A more robust description of the process can be obtained by the development of a mechanistic model of the chemical reaction constructed from a scientific understanding of the chemical processes.^{60, 70}

When a chemical reaction occurs, the species involved follow a reaction mechanism. Using kinetic models to describe such a system can lead to important mechanistic insights (e.g. reaction pathways, activation energies, possible sources of side products) into chemical reactions. This information can help predict how a reaction will occur and make them easier to control which in turn can speed up process development and lower costs.^{60, 70, 71}

Typically, the development of kinetic models involves the collection of time series data in batch and then chemical intuition is used to propose a reaction model and obtained kinetic parameters.⁷¹ Modern advancements in computation have enabled the generation of kinetic models using software such as DynoChem,⁷² Compunetics,⁷³ Berkeley Madonna⁷⁴ and KinSim⁷⁵ as opposed to conventional approaches (i.e. manually transforming experimental data) to identifying reaction orders and kinetic parameters.⁶⁰

Claus *et al.*⁷⁶ developed a kinetic model to describe the one-pot transformation of citronellal to menthols (i.e. tandem cyclisation of citronellal to produce isopulegols and hydrogenation to produce menthols), using a Ru/H-BEA catalyst. The series of reactions is highly important from an industrial standpoint due to the

latter being one of the most heavily consumed flavour compounds worldwide (estimated 30,000 metric tonnes consumed annually) but is usually conducted over two discrete steps, as opposed to in a one-pot fashion.⁷⁷ The intramolecular cyclisation of citronellal (the first of the two steps) was used in this work to study the Lewis acidic catalytic activity of MIL-100(Sc) powder and MIL-100(Sc)@PBSAC composites, see section 2.4.1 for more discussion on this. The reaction network used by Claus *et al.*⁷⁶ to describe the system is shown in Figure 12 which includes terms that describe the formation of isopulegols, menthols and a range of other side products (i.e. dimers, defunctionalisation products (DFPs), citronellal hydrogenation products (DHC, COL, DMO)).

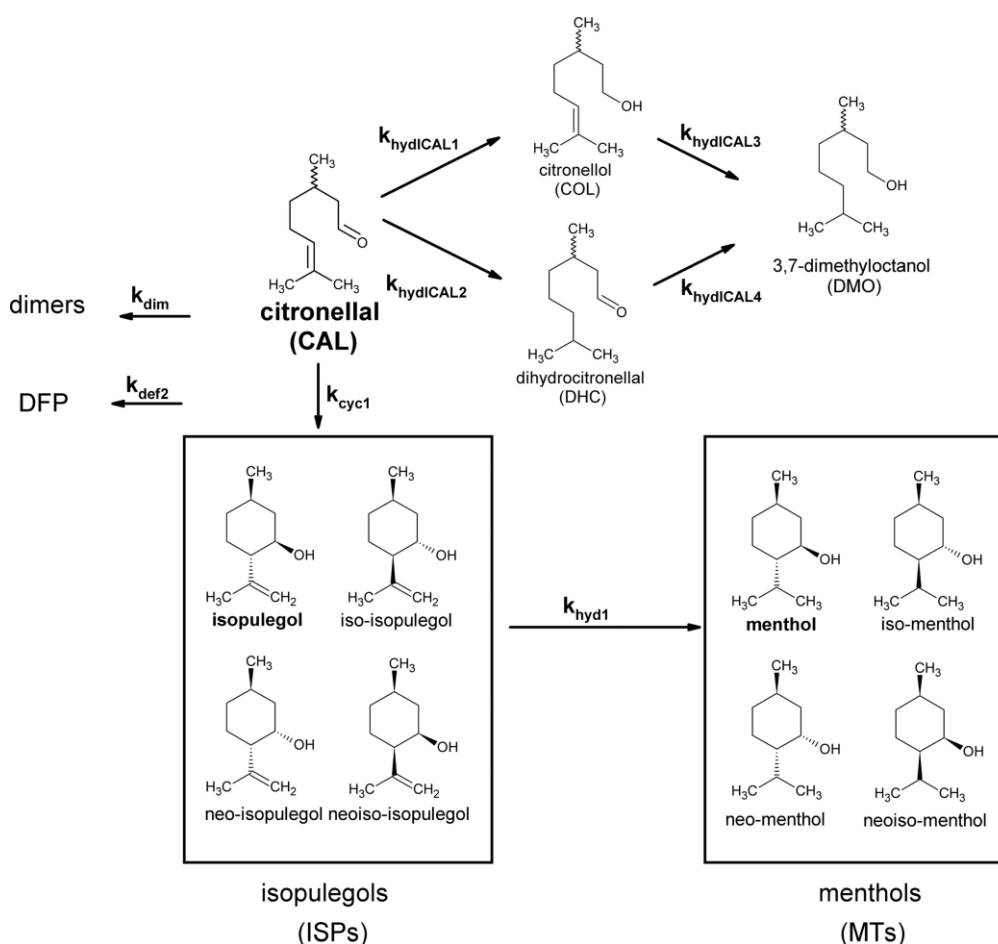
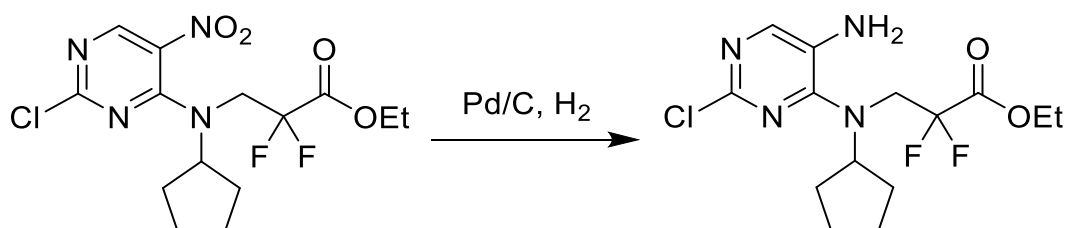


Figure 12: Reaction network used by Claus and colleagues to model the one-pot transformation of citronellal to menthols using a Ru/H-BEA catalyst. Figure reproduced with permission.⁷⁶

For the model, the authors used a Langmuir-Hinshelwood approach which is commonly employed to describe heterogeneously catalysed reactions.^{18, 78} A series of equations, containing rate constants and adsorption coefficients, to describe the reaction rates for each step in the network were generated and the

model subsequently fitted. Upon fitting the model, good agreement with the experimental data for citronellal and main products was obtained (via visual observation) and estimated values for a number of the fitted parameters (i.e. rate constants, equilibrium constants, activation energies) were outputted, with many possessing low error (< 30% relative standard error). The activation energy (E_a) of the cyclisation step was estimated to be 104 kJ mol^{-1} . The hydrogenation of citronellal, an undesirable side reaction, producing either citronellol or dihydrocitronellal possessed estimated activation energies of 72.7 kJ mol^{-1} and 79 kJ mol^{-1} , respectively, which was lower than the cyclisation step meaning that these reactions were preferred at lower temperatures. The finding of the model matched previous experimental observations in which menthol yield (meaning less hydrogenation of citronellal was occurring) increased with the temperature.

Dynochem is a user-friendly kinetic modelling software that is employed in the pharmaceutical industry during drug development.⁷⁹⁻⁸⁹ Papageorgiou *et al.*⁷⁹ used DynoChem to identify safe reaction conditions for the scale-up of a highly exothermic hydrogenation reaction with a heterogeneous Pt/C catalyst (Scheme 1). The model took into consideration the kinetics of the reaction (which was found to be best described using Langmuir-Hinshelwood (LH) kinetics) and contained a physical model where the reaction temperature profiles of the reactor over time and the maximum expected exotherm as a function of the agitation speed (or mass transfer coefficient) were successfully captured. The physical model was then validated experimentally with similar values between the predicted and experimental temperature profile over the course of the reaction as well as the maximum temperature and agitation speed was obtained.



Scheme 1: Hydrogenation step conducted by Papageorgiou *et al.*⁷⁹ who developed a model to describe the kinetics of the reaction and a physical model to explore the reaction temperature profiles.

The time series data used to construct kinetic models may be obtained using a DoE in an approach broadly known as model-based design-of-experiments (MBDoe).^{62, 87, 90-93} A combined DoE and kinetic modelling approach was

conducted by Wells *et al.*⁸⁷ in 2018 to track and kinetically model the impurities generated during the synthesis of a late phase developmental candidate. A level of one specific impurity > 0.6% in the final API drug substance meant that it would fail to meet specification. As such, control and understanding of the formation of this impurity was crucial. The DoE that was carried out, using an automated reaction screening platform, was a 3-level fractional factorial DoE which consisted of 24 experiment DoE and 8 centre point experiments. After identifying the conditions which gave the minimum formation of the impurity via the DoE, which would be sufficient to pass product specifications, the reaction mechanism was studied via kinetic modelling using DynoChem. The model that was generated was found to fit the experimental data reasonably well (via visual inspection) highlighting process understanding. Overall the researchers proposed a range of each experimental parameter to be included in the regulatory submission which gave < 0.6% of the impurity to meet specification. The kinetic model gave confidence in understanding the risks of impurity formation and enabled confirmation of the recommended process parameters.

1.2 Metal-organic frameworks (MOFs)

Metal-organic frameworks are a class of coordination polymers consisting of metal nodes (typically in the form of ions or clusters), termed secondary building units (SBUs), linked together by organic ligands typically resulting in crystalline structures that are uniform in three-dimensions. It is also worth noting that variations such as two-dimensional MOFs⁹⁴ and non-crystalline MOFs⁹⁵ (i.e. amorphous MOFs, MOF liquids, MOF glasses) also exist. MOFs are characterised by their structural diversity and large surface areas (1000 - 10,000 m²/g) owing to their porous structures (although non-porous MOFs or MOFs with inaccessible porosity also exist, for example in interpenetrated frameworks⁹⁶).^{48, 97} Some of the proposed applications of MOFs include gas storage,⁹⁸ gas separation,⁹⁹ biomedicine,¹⁰⁰ water harvesting¹⁰¹ and catalysis¹⁰². MOFs have been explored as vehicles for the capture of CO₂ in wake of the emerging climate change crisis.¹⁰³

To date, the CSD MOF subset contains approximately 120,000 crystal structures of MOFs,¹⁰⁴ with an increasing number of research articles related to MOFs published every year (Figure 13).

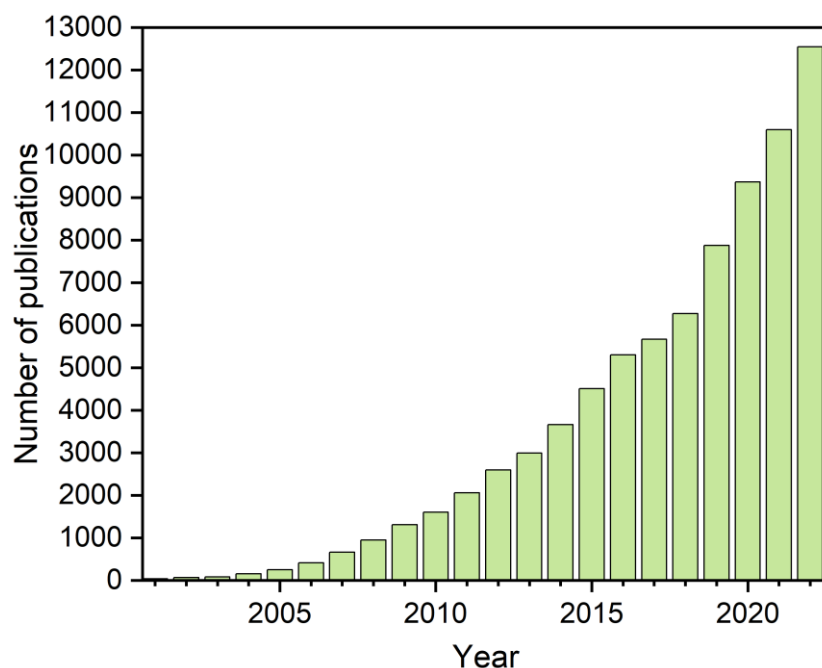


Figure 13: Number of publications per year when searching ‘metal-organic framework’ on Web of Science from 2001 to 2022.

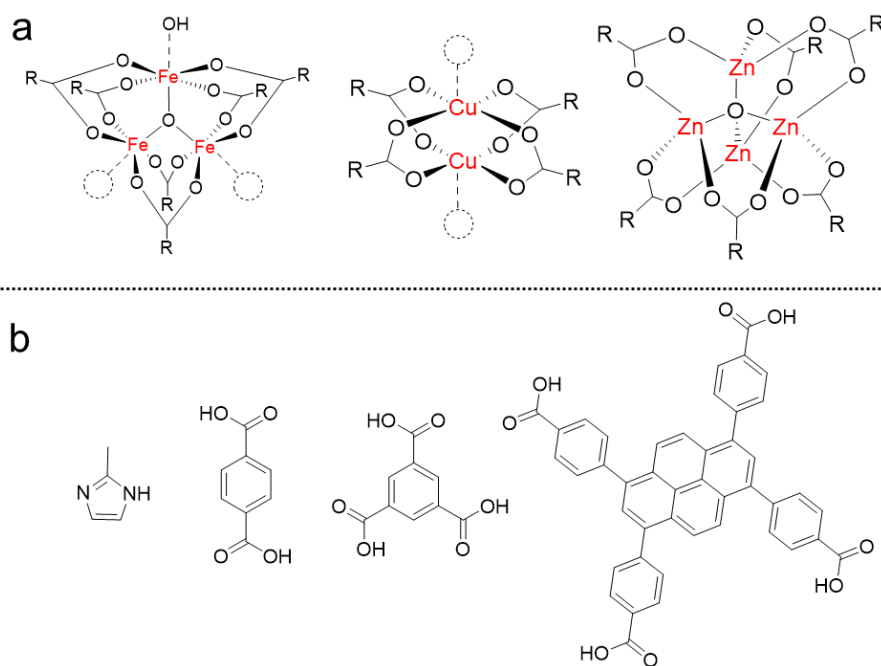


Figure 14: a) Common examples of secondary building units in MOFs. From left to right: MIL-100/101(Fe), Cu₃(BTC)₂, MOF-5 (coordinatively unsaturated sites shown by dotted circles) b) Common examples of linkers in MOFs. From left to right: 2-methylimidazole, terephthalic acid, trimesic acid and 4,4',4'',4'''-(1,3,6,8-Pyrenetetrayl)tetrabenzic acid linkers.

An attractive feature of MOFs is the enormous scope to tailor the properties of these materials by adjusting both the metal and organic units used in their

preparation. The geometry, size and functionality of the constituent parts may all be varied in order to prepare a MOF with desirable properties.⁴⁸ Some common examples of metal nodes and organic ligands in MOFs are shown in Figure 14.

1.2.1 The MIL-100 series of MOFs

The MIL-100(M) (M = Sc, Cr, Fe, Al, V) (MIL = Materials of Institute Lavoisier) series of MOFs are popular owing to their large (and permanent) porosity, high surface area and stability.¹⁰⁵⁻¹⁰⁷ Previously described as a 'star' MOF by Hai-Long *et al.*,¹⁰⁸ the commercialisation of some MIL-100 MOFs has been realised with some analogues (MIL-100(M), M = Fe, Cr, Al) now available to purchase from a range of suppliers. Similarly, amorphous Fe-BTC MOF consisting of the same metal and linker as MIL-100(Fe) is also available to purchase (under trade name Basolite F300). MIL-100(M) MOFs have been studied previously as adsorbents,¹⁰⁹ drug carriers¹¹⁰ and catalysts.¹⁰⁷

The structure of MIL-100 MOFs consists of metal trimer units, M_3O , which contain three octahedral metal ions (if fully coordinated) sharing a μ_3 -O ion. Four of these units are linked together via 1,3,5-benzenetricarboxylate (BTC, trimesate) linker molecules forming a supertetrahedron. These supertetrahedra are then further coordinated to each other via trimesate ligands resulting in the formation of small and large cages.¹¹¹ The smaller cages are ≈ 25 Å in diameter and built from rings of five supertetrahedra with windows approximately 6 Å in diameter, the larger cages are ≈ 29 Å in diameter and built from rings of five and six supertetrahedra, the latter resulting in larger-sized windows approximately 9 Å in diameter. Overall, MIL-100 MOFs possess the general formula of $[M_3O(BTC)_2X]$, where M = metal, BTC is 1,3,5-benzenetricarboxylic acid and X is a singly charged anion required to balance the positive charge of the framework. The structure is depicted in Figure 15.

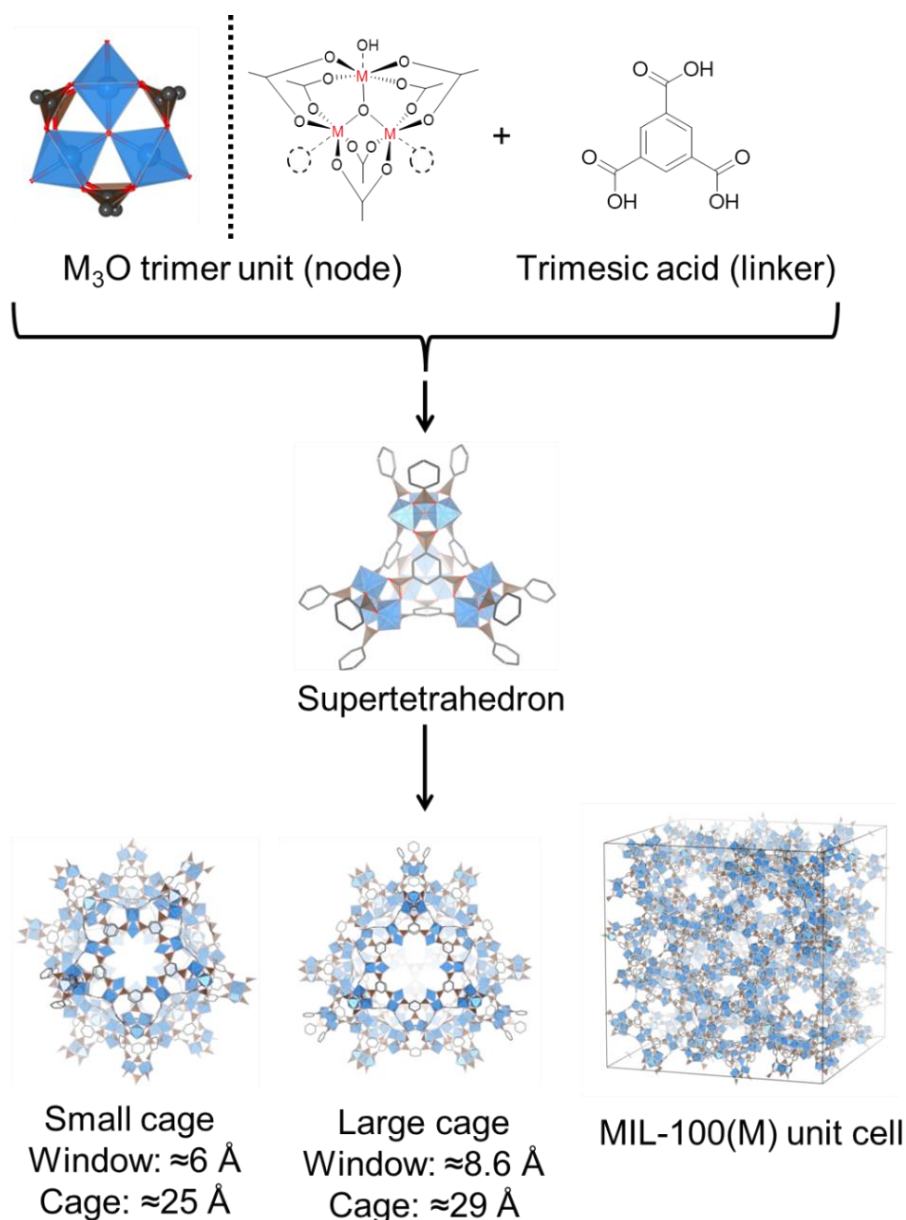


Figure 15: Structure of MIL-100(M) MOFs. Trimesic acid linkers are coordinated to M_3O trimer units (note that coordinatively unsaturated sites are illustrated by circles) giving rise to supertetrahedron units and small and large cages.

1.2.1.1 MIL-100 MOFs as Lewis acid catalysts

The activation of MIL-100(M) MOFs leads to the generation of coordinatively unsaturated metal sites on the nodes which enables them to serve as heterogeneous Lewis acid catalysts (Figure 16).¹¹² MIL-100(M) MOFs have previously been used as Lewis acid catalysts for acetalisation reactions,¹¹³⁻¹¹⁶ α -pinene oxide isomerisations,^{117, 118} carbonyl-ene reactions,^{118, 119} Friedel-Crafts reactions,^{105, 119-121} Diels-Alder reactions,¹¹⁸ imine reactions,¹¹⁹ Prins

reactions,^{122, 123} epoxide carbonation reactions^{115, 124, 125} and epoxide ring-opening reactions¹¹⁵.

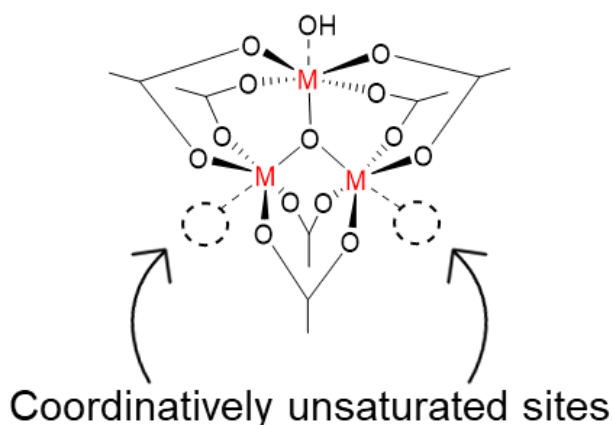


Figure 16: Coordinatively unsaturated sites situated on nodes of MIL-100 MOFs allowing them to serve as Lewis acid catalysts.

The potential for MIL-100 MOFs to serve as a Lewis acid catalyst was recognised back in 2007 by Ferey and colleagues¹⁰⁵ in which the catalytic activity of MIL-100(Fe) and MIL-100(Cr) was compared with zeolites for the Friedel-Crafts benzylation of benzene by benzyl chloride (BZC) to diphenylmethane (Figure 17). MIL-100(Fe) was found to be the most active catalyst, reaching 100% conversion after approximately 10 minutes whilst the zeolite catalysts gave conversions of between 40-55% after 5 hours. The least active species was found to be MIL-100(Cr) in which 42% conversion was obtained after 30 hours.

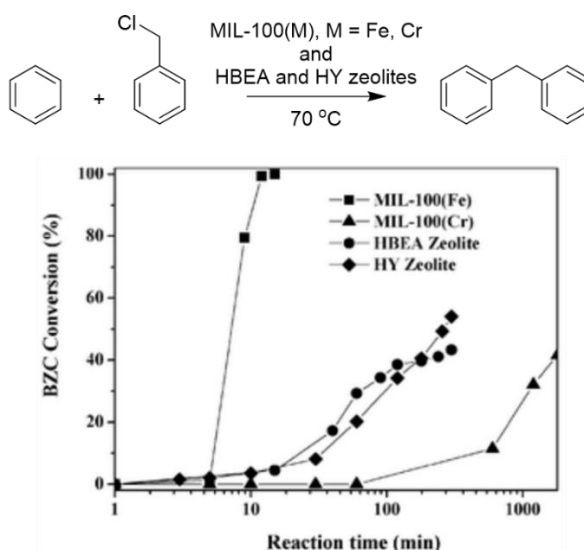


Figure 17: Top: Scheme of Friedel-Crafts reaction carried out by Ferey and colleagues. Conversion of benzyl chloride following Friedel-Crafts reaction with benzene to produce diphenylmethane. Figure reproduced with permission.¹⁰⁵

Zhu *et al.*¹¹⁴ used MIL-100(Fe) (prepared at a low temperature < 100 °C and in HF-free conditions) for the acetalisation of benzaldehyde with glycol (Figure 18). MIL-100(Fe) was found to be more catalytically active than USY and H-β zeolites reaching 85.5% yield of acetal product after 120 minutes compared to 55.8% and 49.5% respectively. The lower activity of the zeolites was attributed to the microporous nature, thus hindering the mass transfer of reactants. When compared with homogeneous catalyst iron nitrate nonahydrate the yield was found to be almost the same (85.3%) highlighting the availability of the Fe³⁺ sites in the porous MIL-100(Fe) framework. This study simply yet effectively demonstrated the high potential of MIL-100(Fe) as a Lewis acid catalyst when compared with other catalysts, both homogeneous (iron nitrate nonahydrate) and heterogeneous (USY and H-β zeolites) in nature.

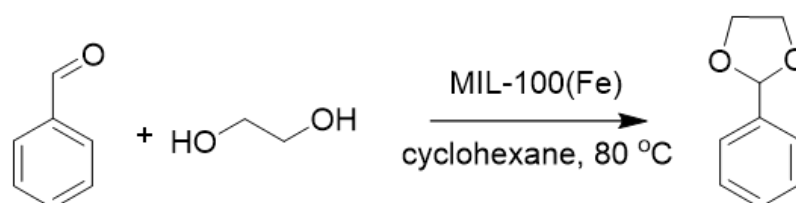


Figure 18: Reaction between benzaldehyde and glycol carried out by Zhu *et al.*¹¹⁴

A thorough study published in 2017 comparing the Lewis acidic catalytic activity of a range of MIL-100(M) MOFs (M = Al, Cr, Fe, In, Sc, V) was carried out by Čejka and colleagues.¹²³ In their study they measured the concentration of Lewis acidic sites in the MOFs using IR spectroscopy (via d₃-acetonitrile adsorption) where it was found that the number of Lewis acidic sites decreased in the order MIL-100(M) M = Sc > V > Cr > Fe > Al > In. Following assessment of the concentration of Lewis acidic sites in each MOF, the catalytic activity was studied via a Prins condensation reaction (of β-pinene and formaldehyde to form nopol) (Figure 19) where MIL-100(Sc) and MIL-100(V) outperformed the other isostructural MIL-100(M) MOFs (Figure 19a) which the authors related to the higher concentration of Lewis acid sites as evidenced by the positive correlation with the rate of reaction (Figure 19b). The yields of nopol obtained with MIL-100(Sc) and MIL-100(V) (90 and 94% respectively) were the best reported to date using a heterogeneous catalyst at the time of publishing.

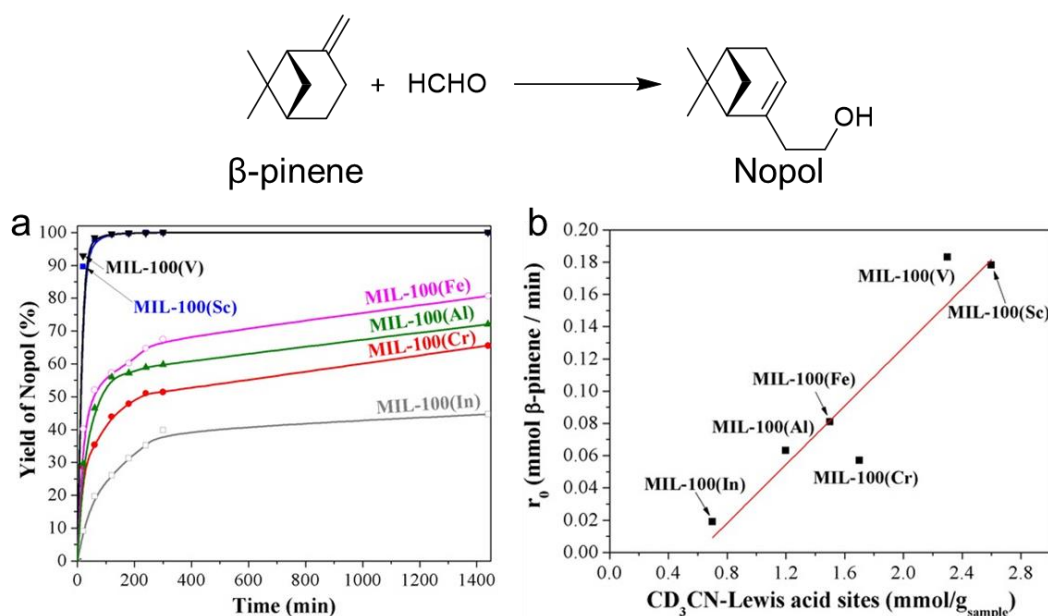


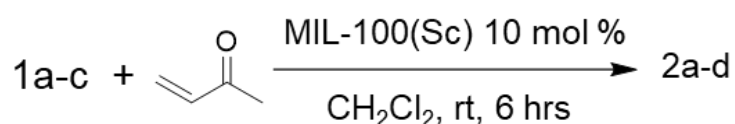
Figure 19: Performance of different MIL-100 MOFs in a study carried out by Čejka and colleagues. Figures reproduced with permission.¹²³

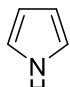
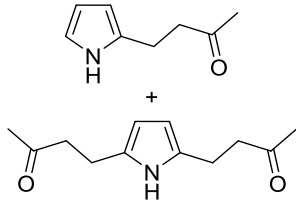
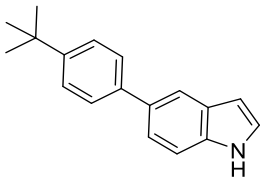
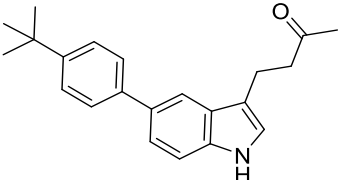
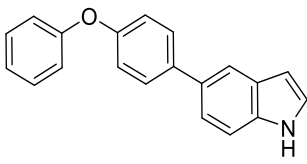
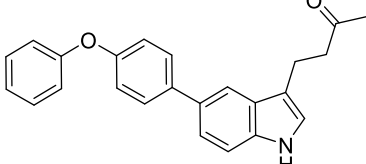
In an earlier study published in 2013, Wright and colleagues¹¹⁹ explored the catalytic performance of a range of scandium-based MOFs (i.e. MIL-100(Sc), MIL-101(Sc), MIL-88B(Sc), MIL-68(Sc), MIL-88D(Sc) and socMOF(Sc)) and compared these with other catalytically active heterogeneous zeolite/MOF species (i.e. Sc³⁺-exchanged zeolite Beta, MIL-100(Cr), MIL-101(Cr), MIL-100(Fe), HKUST-1(Cu), CPO-27(Ni) and STA-12(Ni)) for a range of organic transformations (i.e. intermolecular carbonyl-ene reactions of nucleophilic alkenes and aldehydes; Friedel–Crafts type Michael addition reactions between electron-rich heterocycles and electron-deficient alkenes and for ketimine and aldimine formation). Their results found that MIL-100(Sc), which was proven to be a heterogeneous catalyst via filtration testing, clearly outperformed all of the other catalysts whilst also demonstrating a high degree of recyclability across three cycles.

A highlight of this work was the study involving the use of indole-based structures of varying sizes for Michael addition reactions with methyl vinyl ketone (Table 2). The authors found that upon increasing the size of the indole-based molecule, thus making them bulkier (Table 2, structures 1a-c) and less able to access/leave the pores of MIL-100(Sc), via windows 5 Å and 9 Å in diameter, the amount of product formed decreased suggesting that a majority of the catalysis normally happened inside of the pores for this reaction. As a control measure, the bulkier molecules readily reacted with homogeneous catalyst scandium triflate

(Sc(OTf)₃) where such size restrictions do not exist. The low conversion for the bulkier substrates therefore led the authors to suggest that the surface of the framework provided only minor contributions to the catalysis and that some may have also happened within cages close to the surface. Whilst this study demonstrated that the catalysis was happening inside of the pores, whether catalysis occurs inside the pores for other MIL-100(M)-catalysed reactions is likely to depend on a number of factors such as how the MIL-100(M) framework was prepared and activated (leading to different properties), the reaction mechanism and the conformation.

Table 2: The Michael addition reactions studied by Wright *et al.* involving the use of indole-based substrates of differing sizes to observe the impact upon the catalytic activity.



Reactant	Product	Product (%) ^a
 1a	 2a, 2b	N/A / 89 ^b
 1b	 2c	99 / 33
 1c	 2d	84 / 24

^a of Sc(OTf)₃ / MIL-100(Sc). ^b 1:6 ratio of di- to mono- substituted product.

The superior catalytic activity of MIL-100(Sc) compared to other metals was again demonstrated by Wright *et al.* in another study¹²⁰ where mixed metal MOFs of MIL-100(Sc, M) (M = Fe, Al, Cr) in varying proportions were prepared. The catalytic activity of each material was tested using a carbonyl ene reaction with a clear dependency of the conversion on the amounts of scandium present in the

MOF (Figure 20) (the relative metal composition of the frameworks was determined using energy dispersive X-ray (EDX) analysis).

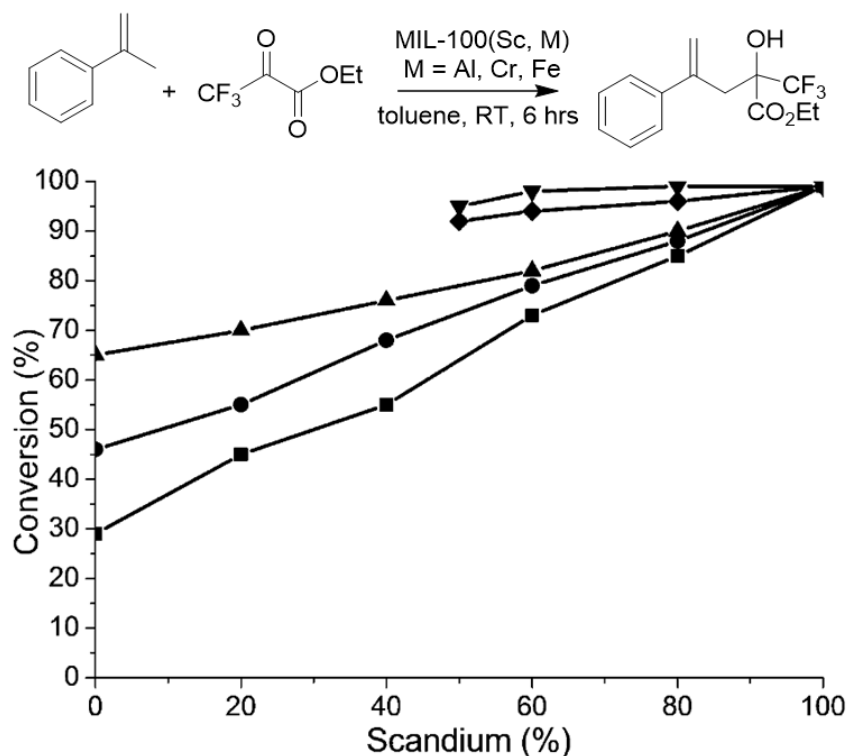


Figure 20: Carbonyl-ene reaction of α -methylstyrene with ethyl trifluoropyruvate. The conversion after 6 hours is shown for the mixed-metal MIL-100 MOFs (square: MIL-100(Sc, Al), circle: MIL-100(Sc, Fe), triangle: MIL-100(Sc, Cr), diamond: MIL-100(Sc, Fe)XS and upside down triangle: MIL-100(Sc, Fe)XS where XS means that an excess of metal was used in the synthesis than stoichiometrically required). Figure modified with permission.¹²⁰

1.2.2 MOF-based catalysis

Since research on MOFs first commenced, there has been a large increase in the number of publications involving their use as catalysts with now almost 25% of all MOF publications pertaining to this application (Figure 21). This trend highlights the recognition of the potential of these materials. In their 2020 review article, Gascon *et al.*¹²⁶ stated feeling overwhelmed by the volume and breadth of recent publications regarding MOF-based heterogeneous catalysis.

MOF-based heterogeneous catalysis can broadly be categorised into three types: catalysis by the metal node (e.g. via Lewis acidic sites on coordinatively unsaturated sites), by functional linker molecules (e.g. via the chelation of catalytically active metal ions to functionalised linkers) and by the introduction of guest species (e.g. enzymes, metal nanoparticles, metal complexes) into the

pores of the framework (Figure 22). These modes of catalysis may also be combined giving rise to multifunctional MOFs,¹²⁷ whilst the well-defined pore size or narrow pore size distribution of the MOF structure also enables size-selective reactivity to occur.¹²⁸ The versatility of these materials means that they have also been explored for electrocatalysis, photocatalysis, asymmetric catalysis and even MOF-derived catalysis. Recent review articles^{102, 126, 127, 129-131} highlight the sheer breadth of this vibrant research field.

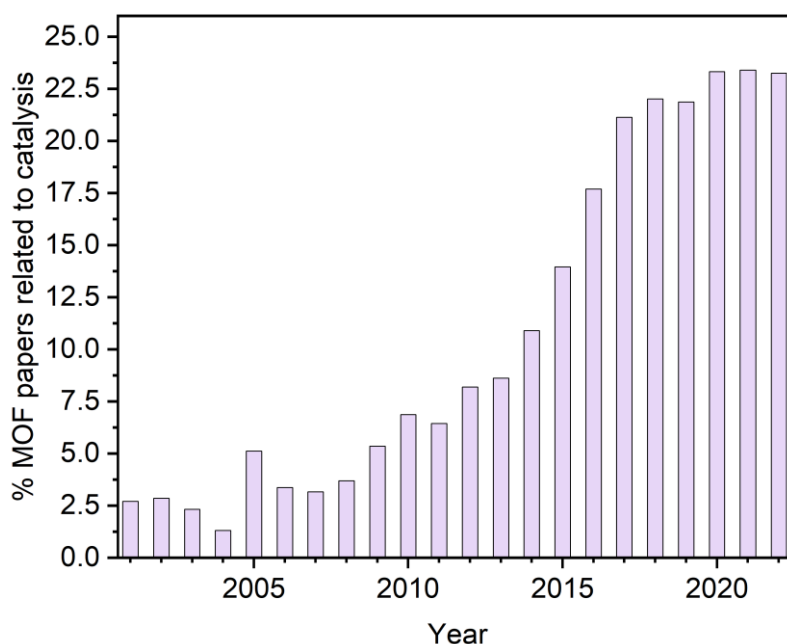


Figure 21: Percentage of MOF publications for catalysis applications every year from 2001 to 2022. This was calculated by dividing the number of publications every year when searching for ‘metal-organic framework catalyst’ Web of Science by ‘metal-organic framework’.

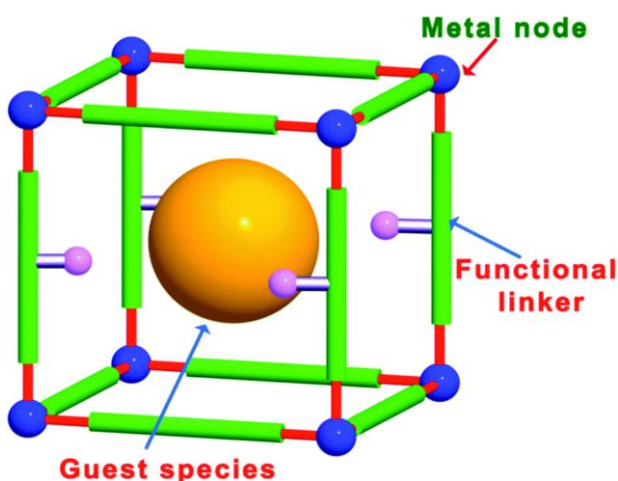


Figure 22: Different types of MOF catalysts. MOF-based catalysts include catalysis by the metal nodes, by functional linker molecules and by the introduction of guest species into the framework. Figure reproduced with permission.¹²⁷

1.2.2.1 Towards industrial implementation of MOF-based catalysis

The industrial implementation of MOF-based heterogeneous catalysis has not yet been realised in the chemical industry, however, despite the wealth of examples regarding the use of MOFs as catalysts in the literature. A number of limitations regarding the current state of the research field have been postulated.^{102, 130}

These include:

- Limited thermal and chemical stability
- Difficulties in regeneration
- Generally relatively expensive to produce on a large scale

Due to these shortcomings, it is unlikely that MOFs are going to find application in large-scale catalytic applications like fuel processing or petrochemical synthesis where high stabilities and regenerative catalysts are important (e.g. cracking of heavy petroleum requires 500 - 560 °C,¹³² whilst typical MOF thermal stability ranges from 300 – 500 °C)^{133, 102} It has instead been suggested that the best prospects are offered by using MOFs for the synthesis of fine chemicals where higher temperatures and catalytic regeneration are not explicit requirements.¹⁰²

Jiang and Jiao¹³⁰ suggested that more efforts should be directed on applications where MOFs are irreplaceable - such as in fine chemical reactions affording high chemo-, stereo- and regioselectivity. In a similar vein, Gascon *et al.*¹²⁶ postulated that the use of MOFs as catalysts may become more attractive from a commercial standpoint if MOFs can deliver properties that cannot be achieved otherwise (similar to Jiang and Jiao), particularly if they can be produced cheaply (i.e. using cheap metals, ligands and if no solvents are used in their activation).

It is plausible that in the future MOFs may find use as catalysts for fine chemical synthesis as the industry transitions away from the use of stoichiometric reagents and towards greener alternatives like heterogeneous catalysis. Further, the application of MOFs in continuous flow could provide additional benefits to fine chemical manufacture – see section 1.2.3 for more discussion of this.

1.2.2.2 Design-of-experiments (DoE) in MOF catalysis

As discussed in section 1.1.3, design-of-experiments and kinetic modelling are two tools that are frequently employed in fine chemical development. To date, there are a number of published examples regarding the use of DoE or similar,

i.e. response surface methodology (RSM), a tool based on DoE, to explore the catalytic activity of MOFs (Table 3). Such approaches offer efficient approaches to the optimisation of MOF-catalysed reactions and enable the identification of trade-offs between responses.

Liu *et al.*¹³⁴ encapsulated a heteropolyanion-based ionic liquid within the pores of MIL-100(Fe) and optimised the resultant material as a catalyst for biodiesel production (oleic acid and ethanol reaction) using RSM. A 2-level 4-factor central composite design (CCD) with a total of 30 experiments (24 distinct experiments, including 8 axial points, and 6 centre point replicates) was selected with the molar ratio of ethanol to oleic acid (2:1, 6:1, 10:1, 14:1, 18:1 mol mol⁻¹), catalyst loading (5, 10, 15, 20, 25 % wt.), reaction temperature (90, 100, 110, 120, 130 °C) and reaction time (2, 3, 4, 5, 6 hours) all varied. Response surface contours were also generated to explore the effect of different variables on the conversion (Figure 23). The molar ratio of ethanol:oleic acid was the most significant factor, with the conversion increasing significantly upon changing the ratio from 2:1 to 10:1. The esterification was reversible, thus excess ethanol was beneficial for driving the reaction. However, the addition of too much ethanol diluted the reaction mixture which is reflected in the decrease in conversion at > 10:1. Increased catalyst loadings also increased the conversion up to about 15 wt%. Above 15 wt% the authors postulated that the active sites were blocked by excess catalyst. The reaction temperature was found to not change the conversion drastically within the range that was studied, whilst the conversion was found to significantly increase from 0 - 2 hours of reaction (not shown in contour plots, Figure 23), with more moderate increases after 4 hours.

The optimum conditions were identified by RSM to be 11.36:1, 14.76% wt., 111.14 °C and 5 hours of reaction giving a predicted conversion of oleic acid of 94.75%. This was verified experimentally (at 11:1, 15% wt. 111 °C, 5 hours) where a similar conversion value was obtained (94.55%) highlighting the predictive power of these statistical tools. This RSM study optimised this reaction across a broad range of experimental space (including the study of 4 variables) in a more efficient manner than conventional OVAT experimentation. As the conversion was found to not be drastically influenced by the reaction temperature, the authors could have selected a wider temperature range, incorporating lower temperatures offering energy savings. This study was also conducted with the

sole purpose of optimising the conversion of oleic acid to produce biodiesel and thus this was the only response that was measured. This work prompts further investigations monitoring multiple responses beyond a singular optimisation to outline a more complete picture and the identification of potential trade-offs in MOF-catalysed reactions

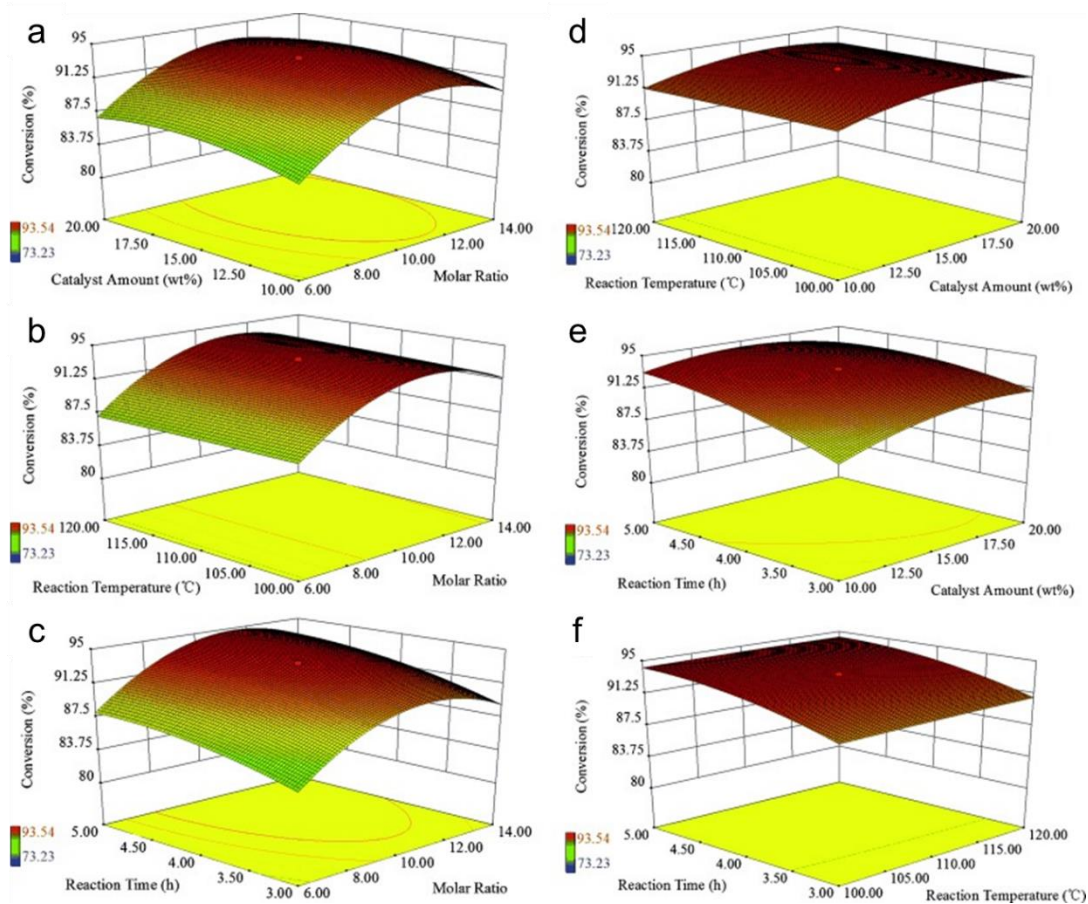


Figure 23: Response surface contours obtained for biodiesel production (oleic acid and ethanol reaction) with a heteropolyanion-based ionic liquid MIL-100(Fe) catalyst using RSM. Figure reproduced with permission.¹³⁴

Keshavarz *et al.*⁹¹ optimised the solvent-free isomerisation of endo- to exo-dicyclopentadiene using UiO-66 as the catalyst using a DoE. A central composite design (CCD) consisting of 20 experiments was selected with the yield studied as function of reaction time (2, 3.4, 5.5, 7.5, 9 hours), temperature (100, 116, 140, 164, 180 °C) and catalyst weight percentage (2, 3.6, 6, 8.4, 10% wt.). The reaction time was found to be the most significant factor and had a negative effect on the yield as longer reaction times lead to unwanted side reactions. Small decreases or increases in yield were observed upon increasing the temperature and catalyst weight percentage, respectively. The decrease in yield upon increasing the temperature was attributed to thermal oligomerisation at higher

temperatures which reduced the isomerisation efficiency whilst the increased amount of catalyst increased the number of active sites available for reaction. Figure 24 shows contour plots were generated for the data illustrating that the highest yields were obtained between 3.4 - 4.5 hours of reaction.

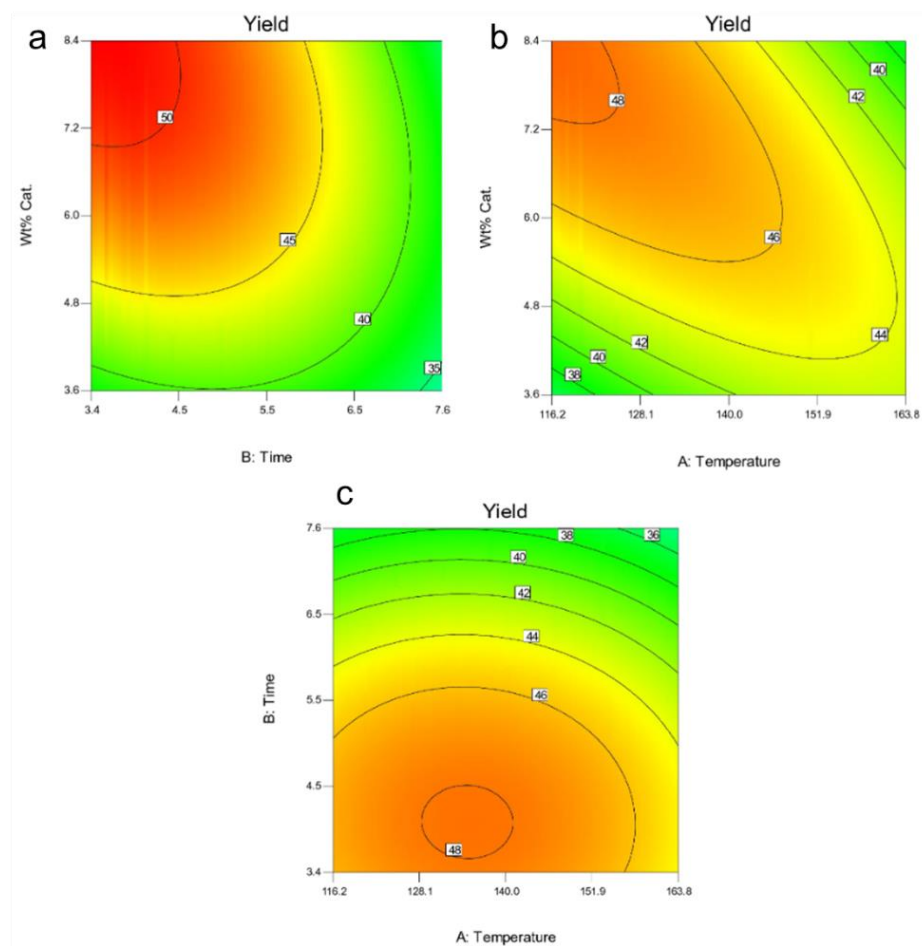


Figure 24: Contour plots obtained in the DoE study of endo- to exo-Dicyclopentadiene using UiO-66 as a catalyst. Figure reproduced with permission¹³⁵

Inspection of Figure 24 shows that, in general, lower to middle levels of temperature and reaction time and higher percentages of catalyst loading produced the greatest isomerisation yield. The highest yield (51%) was obtained at 116 °C, 3.4 hours and 8.4 wt.% with good convergence between experimental and predicted values. The optimised results obtained in the study were compared with other heterogeneous species (i.e. zeolites and MOFs) where UiO-66 gave the highest selectivity towards exo-dicyclopentadiene. The authors also reported the formation of small amounts of side-products (e.g. tricyclopentadiene, 9-methylidenetricyclo[4.2.1.12,5] decane, tetraisobutylene); thus the selectivity of the reaction (and general system understanding) could have been improved

further by developing a mechanistic understanding of the formation of these side-products. The use of model-based DoE would enable further exploration into this.

Table 3 summarises the literature to date regarding the use of DoE/RSM to study MOF-based catalysts. Examples include esterification reactions for biodiesel production,^{134, 136-140} CO₂ photoreduction,¹⁴¹ photodegradation,¹⁴¹⁻¹⁴⁶ hydrodeoxygenation¹⁴⁷ and isomerisation¹³⁵ reactions. Examples related to the catalysis of synthetic organic transformations (such as those employed in the fine chemical industry) are lacking. By more frequently studying MOF-catalysed reactions via these approaches, researchers can exploit their inherent advantages (e.g. more efficiently map experimental space, identify optimised reaction conditions, obtain knowledge of interactions that exist between variables) which could offer essential cost savings with MOFs currently limited by their relatively expensive production on large scales.¹⁰⁹

A further observation is that in each study, similar variables were typically studied: temperature, time, catalyst loading and reagent molar ratio/concentration. There are seemingly no studies exploring responses other than conversion or yield (or degradation). In chemical systems, there are a number of other important metrics that can give valuable insight into the nature of a reaction, guide conditions selection and enhance system understanding - for example the initial reaction rate and TOF. These metrics have not been reported in a study involving the use of either DoE or RSM for a MOF-catalyst to date. Deeper understanding of reaction metrics such as these, and how they may be related to each other, could in turn help guide the conditions employed to give both timely and catalytically efficient (and thus more cost effective) reactions. Additional value could be added by studying more than one response at a time allowing previously unobserved trade-offs to be identified. Beyond optimising processes, the data generated in a DoE can be used to obtain mechanistic information through the generation of kinetic models via model-based design-of-experiments (see section 1.1.3.2 for more discussion of model-based design-of-experiments).

Table 3: Summary of key literature exploring the catalytic activity of a MOF-based catalyst via DoE or RSM.

MOF	Method	Reaction	Variables	Responses	Ref
UiO-66	DoE	Isomerisation of endo- to exo-dicyclopentadiene	Temp Time Cat. Loading	Yield	135
MIL-53(Fe)	DoE	Photo-Fenton degradation of sulfamethoxazole	pH [H ₂ O ₂] Cat. Loading	Degradation	143
HSiW-UiO-66 ^a	RSM	Lauric acid with methanol for biodiesel production	Temp Time Cat. Loading	Conversion	136
IL@H-UiO-66 ^b	RSM	Oleic acid with methanol for biodiesel production	Time Molar ratio ^c Cat. Loading	Yield	137
POM-IL-MIL-100 ^d	RSM	Oleic acid with methanol for biodiesel production	Temp Time Molar ratio Cat. Loading	Conversion	134
Pt@UiO-67	RSM	Hydrodeoxygenation of anisole	Temp Pressure Molar ratio ^e	Conversion	147
Cu-MOF Ca-MOF	RSM	Waste cooking oil with methanol for biodiesel production	Temp Molar ratio ^f Cat. loading	Yield	138
Zn ₃ (BTC) ₂	RSM	Low-grade vegetable oil with methanol for biodiesel production	Temp Time Molar ratio ^f	Yield	139
IL@NH ₂ MIL-88B(Fe) ^b	RSM	Biodiesel synthesis from oleic acid and ethanol	Time Molar ratio Cat. loading	Conversion	140
CNTs/MOF-808 ^g	RSM	Photocatalytic degradation of carbamazepine (CBZ) and diazinon	pH Flow rate [CBZ] [Diazinon]	Degradation	142
(NH ₂)MIL-101(Fe)	RSM	Photocatalytic degradation of imidacloprid (IMC)	pH [IMC] [H ₂ O ₂] Time	Degradation	144
Ag-MOF	RSM	Photocatalytic degradation of herbicides	pH [Herbicide] Cat. Loading Time	Degradation	146

^a Silicotungstic acid incorporated into UiO-66. ^b Ionic liquid-metal-organic framework composite material. ^c Methanol:oleic acid ratio. ^d Polyoxometalate, ionic liquid and MOF composite material. ^e H₂:anisole. ^f Alcohol:oil ratio. ^g Methanol:oil. ^g Carbon nanotubes/MOF-808 was painted on glass plates.

1.2.2.3 Kinetic modelling of MOF catalysts

Section 1.1.3.2 outlined the advantages of kinetic modelling in the development of fine chemicals manufacturing and gave examples of how kinetic modelling has

been used to greater understand heterogeneously catalysed reactions. Examples pertaining to the use of kinetic modelling to study MOF-based catalytic systems via computational approaches are lacking.¹⁴⁸⁻¹⁵¹ This finding is in line with the observation by Gates and Yang in their 2019 review that there is currently a lack of fundamental understanding of the kinetics of MOF-catalysed reactions.¹⁰²

Modelling MOF catalysts is inherently more complex than many other homogeneous and heterogeneous catalyst platforms, not only because the reaction occurs over at least two phases (e.g. liquid and solid) but also because of the porous nature of the MOF-catalyst. The porosity means that mass transfer occurs within the pores as well as to and from the solid surfaces. To date, there are a number of studies that have considered diffusion within the pores of MOF-based catalysts^{148, 152-155} but it is widely acknowledged that this is a complex issue for which widespread quantitative representations currently do not exist in the field.^{102, 156, 157}

Simpler approaches to kinetically modelling chemical reactions, for example by using a software like DynoChem that is used by scientists during fine chemical development (see section 1.1.3.2), could provide a platform to more easily study the kinetics of MOF-based catalyst systems. However, such an approach has also not been exploited to date. Additionally, a combined design-of-experiments and kinetic modelling approach could serve as a way to both optimise MOF-based catalysed reactions and gain greater insight into the physicochemical processes occurring during the reaction.

1.2.3 MOF-based heterogeneous catalysis in continuous flow

In their 2020 review summarising the state of the field, Garcia and colleagues¹⁵⁸ showcased some of the key results pertaining to the use of MOFs as heterogeneous catalysts in continuous flow. Whilst the vast majority of examples regarding the use of MOF-based heterogeneous catalysts still involves their usage in a batch mode of operation, there are a diverse number of interesting studies involving the use of MOF-based materials in continuous flow. These studies on MOF-based materials in flow highlights the interest in and versatility of these materials for heterogeneous catalysis in continuous flow.

Examples include metal NP supported catalysts,¹⁵⁹⁻¹⁶⁴ enzymes,¹⁶⁵⁻¹⁶⁷ metal complexes^{168, 169} and pristine MOFs (including in composite materials), the latter

serving as Lewis acid catalysts (see section 1.2.3.1 below). A majority of these materials were tested in packed-bed reactors which are widely employed for continuous applications.

1.2.3.1 MOFs for Lewis acid catalysis in continuous flow

MOFs have previously been used as Lewis acid catalysts in liquid phase continuous flow for Friedländer,¹⁷⁰ acetalisation,¹⁷¹⁻¹⁷³ isomerisation,^{174, 175} Friedel-Crafts,^{176, 177} epoxide carbonylation¹²⁵ Diels-Alder,¹⁷⁷ epoxide ring opening¹⁷⁷ and aromatisation¹⁷⁸ reactions.

MIL-100(Fe) in powdered form was packed inside of a packed-bed reactor and used as a catalyst for the acetalisation of benzaldehyde.¹⁷³ During the process optimisation stage, which was more than 96 hours time-on-stream, no significant decrease in catalytic efficiency was observed with MIL-100(Fe) maintaining crystallinity (as evidenced by PXRD analysis of the material after the reaction) and > 90% conversion over this period of time.

Sanford *et al.*¹²⁵ studied a number of powdered MOFs species in continuous flow MIL-100(Sc), MIL-88D(Sc), MIL-66(Sc), and MIL-101(M) (M = Cr, Fe, Sc) (Figure 25) as catalyst for the carbonation of propylene oxide with CO₂ (Figure 25a). During initial testing over 5 hours time-on-stream, MIL-100(Sc) was found to possess the highest steady-state catalytic activity of all of the species (Figure 25b-c). As such, MIL-100(Sc) was selected for a 24 hour stability study (Figure 25d) with minimal loss in activity over this time period. In other studies, MIL-100(Sc) was also found to be more catalytically active than a range of other MOFs upon studying the catalytic activity in batch (see section 1.2.1.1).

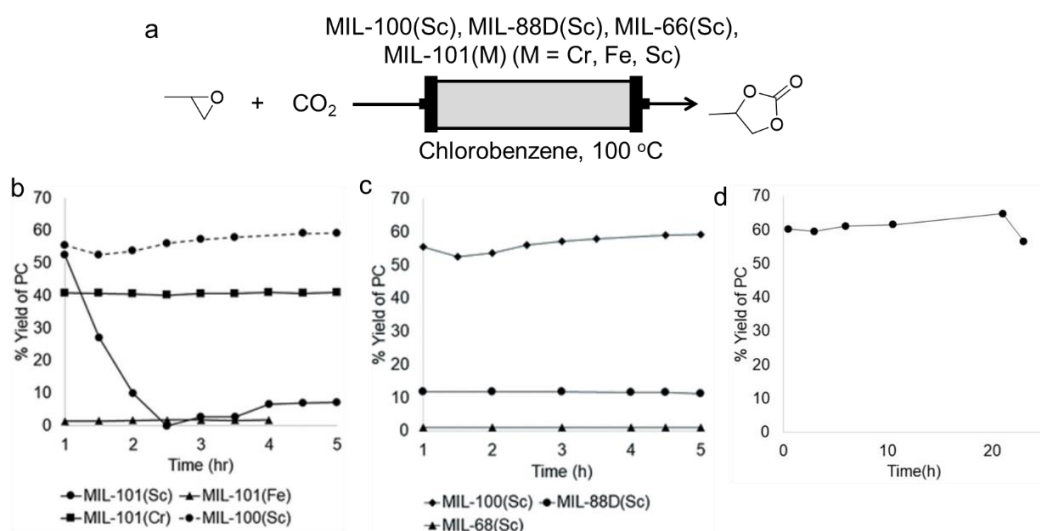


Figure 25: a) Epoxide carbonylation in continuous flow carried out by Sanford and colleagues using a range of different MOF species. b-c) Initial testing of catalysts over 5 hours time-on-stream. d) 24 hour stability study carried out with MIL-100(Sc). Figures b-d reproduced with permission.¹²⁵

Lin *et al.*¹⁷⁷ reported a strongly Lewis acidic MOF, ZrOTf-BTC, (made through two transformations of MOF-808) with the resultant catalytic activity outperforming homogeneous species $\text{Sc}(\text{OTf})_3$ in Diels–Alder, epoxide ring-openings and Friedel–Crafts acylations. The MOF was then supported onto SiO_2 , giving ZrOTf-BTC@SiO_2 , and studied in continuous flow in a packed-bed reactor (Figure 26a-c respectively).

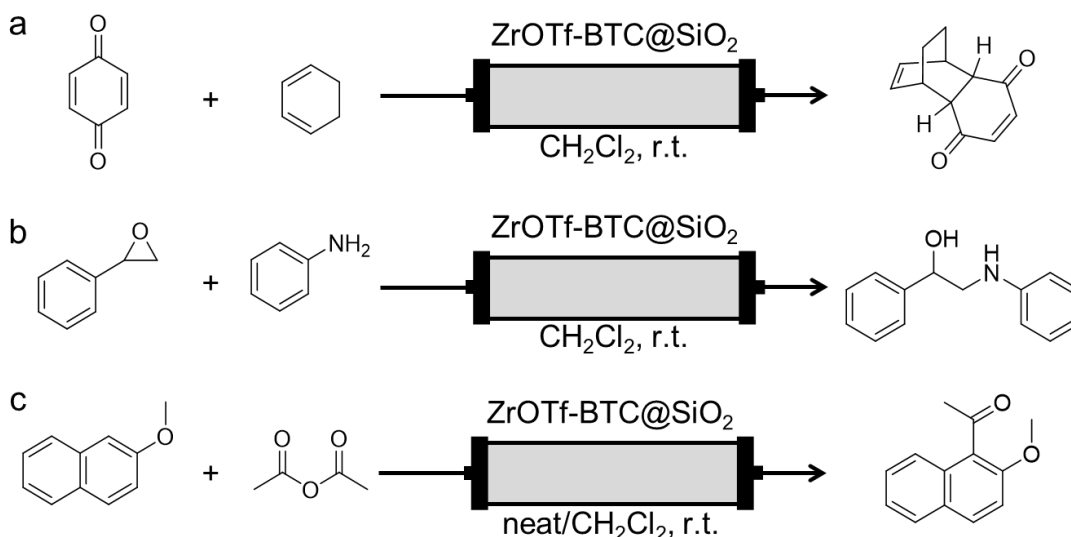


Figure 26: a) Diels-alder reaction between 1,4-benzoquinone and cyclohexa-1,3,-diene. b) Epoxide ring-opening reaction between styrene oxide and aniline. c) Friedel-crafts reaction between 2-methoxynaphthalene and acetic anhydride.

For the reaction between 1,4-benzoquinone and cyclohexa-1,3-diene (1:1.6 molar ratio respectively) (Figure 26a), the cyclisation product was obtained in quantitative yields when flowed through the column at 10 mL hr⁻¹ for 17 hours. These experiments correspond to a turnover frequency of 100 hr⁻¹ and turnover number of 1700. For the epoxide ring-opening reaction (Figure 26b), styrene oxide and aniline were flowed through the column at 60 mL hr⁻¹ with high yields (83 - 93%) obtained over 30 hours giving a turnover number of 2700. For the Friedel-Crafts reaction between 2-methoxynaphthalene in acetic anhydride/CH₂Cl₂ a flow rate of 30 mL hr⁻¹ was used (Figure 26c), forming 1-acetyl-2-methoxynaphthalene in high yields for the first 30 minutes which then, however, dropped to 65%. This drop in yield could be restored by simply washing with solvent (CH₃CN/CH₂Cl₂ (1:9, v/v)), with the performance in flow significantly outperforming that in batch. These results show that studying certain reactions in continuous flow may result in catalyst fouling which can be recovered by washing in solvent.

Some of the examples pertaining to the use of MOFs in continuous flow have accounted for the form of the material, which is an important consideration when designing new catalysts due to the high pressure drops typically encountered when using powdered catalysts. Galarneau *et al.*¹⁷⁰ prepared a composite of HKUST-1 (Cu₃(BTC)₂) in macro-/mesoporous silica monoliths, and used them for a liquid phase continuous flow Friedländer reaction between 2-aminobenzophenone and acetylacetone. Over the course of the 24 hours time-on-stream, stable conversions (85 - 90%) were obtained with 826 g of the reaction product produced per g of MOF per day. In a separate study using the same MOF, Martyanov *et al.*¹⁷⁴ prepared for the first time a HKUST-1@silica aerogel composite material with pellets ranging between 100 - 500 µm in size. These were then used as catalysts for the isomerisation of styrene oxide to phenyl acetaldehyde in a packed-bed reactor. Whilst the selectivity towards phenyl acetaldehyde remained high throughout the course of the flow reaction (> 90%), the conversion was found to decrease (from 87% to ≈ 40%) over 140 minutes time-on-stream which was attributed to fouling via the deposition of carbonaceous substrates on the surface of the catalyst.

1.2.3.2 Future application in continuous flow

In current publications using MOFs as heterogeneous catalysts for liquid phase continuous flow reactions, there does not appear to be a substantial effort to understand the effects of the form of these materials. Accounting for the effects of different forms is essential for future industrial application in continuous flow systems.

In their pure form, MOFs typically exist as fine powders meaning their usage in flow reactors (e.g. packed-bed reactors as in the majority of examples to date) could lead to high pressure drops across the reactor or reactor blockages - both of these phenomena hinder process efficiency. There are, however, some examples in the literature that have employed larger catalyst sizes such as monoliths,¹⁷⁰ pellets^{174, 175} and tablets¹⁶². In some cases, membranes were prepared, immobilised onto the end of a syringe or clamped in place with filtration equipment and the reagents pumped through.^{164, 165, 172}

For industrial applications, catalysts are commonly immobilised onto supports of various shapes such as monoliths, extrudates and porous beads.^{18, 56} In addition to maintaining regular enough packing to prevent a significant pressure drop across the reactor, it is also beneficial to employ catalyst supports exhibiting resistance to both crushing and abrasion inside of the reactor to minimise breakdown and plug formation. It is also advantageous to maximise the surface area of the active component of the catalyst and immobilise the species to the support in a way that ensures stability for long-term industrial operation thereby preventing leaching or physical detachment over time. Consideration must therefore be given to immobilisation approaches as physisorption or the formation of a single covalent bond between the active catalyst and support may not be robust enough for continuous flow operations.³⁰

One promising support material which provides a good balance between macro- and nano-scale properties is polymer-based spherical activated carbon (PBSAC).¹⁷⁹ These mechanically strong, commercially available spherical activated carbon pellets have a regular, tuneable size (50 – 700 μm), possess a high, graphitic carbon surface area ($> 1000 \text{ m}^2 \text{ g}^{-1}$) for catalyst deposition and have an established track record for successful operation in flow reactors (see section 1.3.2).

1.3 Polymer-based spherical activated carbon (PBSAC)

1.3.1 Activated carbon

Activated carbon is a microcrystalline carbon-based material that is highly porous and possesses a large surface area (up to 500 - 1500 m²/g) (Figure 27). Their production, from carbonaceous materials, typically involves a two-step process of carbonisation and then activation of organic material. During the carbonisation step, the organic material is pyrolysed between 300 – 800 °C under an inert atmosphere which removes most of the noncarbon elements (e.g. oxygen, hydrogen, nitrogen) and the residual carbon atoms arrange themselves into stacks of randomly arranged, flat, aromatic sheets. At this stage a basic pore structure is generated. However, the pores are blocked by tar deposits and other decomposition products that form during the carbonisation step. To remove these pore-blocking species, an activation step, typically carried out in an atmosphere of air, carbon dioxide or steam between 800 – 900 °C, is required to eliminate them and generate the final pore structure.¹⁸⁰⁻¹⁸³



Figure 27: Schematic representation of activated carbon. Figure reproduced with permission.¹⁸⁴

Preparing conventional activated carbons from natural sources (e.g. coconut shells, coal) may lead to activated carbons with wildly different pore structures, pore size distribution and purities. However, when using organic polymers as the precursor, clean activated carbon materials with consistent properties (e.g. particle size, surface area, carbon content) may be produced. If the polymer precursor is prepared in a spherical shape then the resultant activated carbon material can also preserve this spherical shape, giving polymer-based spherical

activated carbon (PBSAC) (Figure 28). The favourable properties of PBSACs were discussed in section 1.2.3.2.^{179, 185}



Figure 28: Optical image of PBSAC spheres.

1.3.2 PBSACs as catalyst supports in continuous flow

Previous research into the use of PBSAC spheres as catalyst supports has primarily involved active species such as metal nanoparticles,^{32, 186-192} metal oxides¹⁹³⁻¹⁹⁵ and ionic liquids^{196, 197} in both batch and flow.

Examples of the use of PBSAC-based systems for liquid phase continuous flow catalysis has heavily involved the use of palladium nanoparticles supported on PBSAC spheres, Pd@PBSAC, systems.^{32, 186-188, 190} Casas *et al.*¹⁹⁰ used a Pd@PBSAC catalyst for the hydrodechlorination of 4-chlorophenol. The catalyst demonstrated high stability with no significant loss in activity observed over 100 hours time-on-stream and with phenol observed as the main product. Cyclohexanone and cyclohexanol were formed in lower concentrations. The catalyst showed high mechanical strength and abrasion resistance with the shape and size catalyst particles remaining unchanged after the reaction (Figure 29).

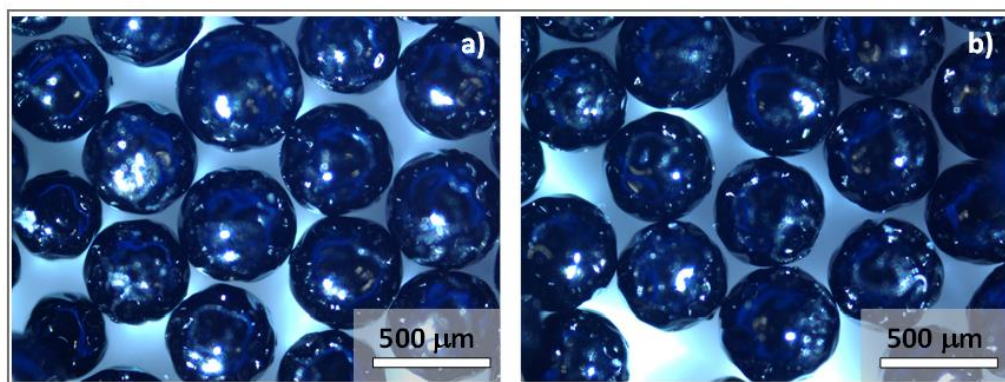


Figure 29: Light microscope image of Pd/PBSAC before (left) and after (right) use in 100 hour hydrodechlorination reaction. Figure reproduced with permission.¹⁹⁰

In 2020, researchers at GlaxoSmithKline (GSK) published a study using palladium nanoparticles supported on PBSAC spheres, Pd@PBSAC, for continuous hydrogenation reactions in pharmaceutical-scale trickle-bed reactors.³² The researchers conducted physical (i.e. mechanical strength, particle size distribution, pressure drop) and chemical (i.e. catalytic activity) property testing, both of which are important when designing industrial catalysts. The catalysts' physical properties were evaluated against a defined acceptance criteria: a narrow particle size distribution (PSD) within the target size range (between 50 - 400 μm , giving a tube-to-particle (D_t/D_p) ratio of ≥ 15 required to minimise flow maldistribution across the reactor at laboratory-scale), acceptable structural integrity, high mechanical strength (>100 MPa) and low pressure drop (maximum allowed pressure drop limit of 5 bar at 10 mL/min). A 5% palladium loading on 200 μm PBSAC spheres demonstrated a narrow PSD, high mechanical strength and the lowest pressure drop with minimal formation of fine particles upon testing. Accordingly the catalytic activity of 5% palladium loading on 200 μm PBSAC spheres was subsequently studied in the trickle bed reactor (Figure 30).

The reduction of 1-methoxy-4-nitrobenzene was tested in continuous flow with minimal decreases in conversion over 6 hours time-on-stream using GSK's current pilot plant equipment (Figure 30a-b). The deprotection of N-benzyl-4-methoxyaniline was also studied, with minimal loss in activity observed over 10 hours at the optimised conditions (10 bar, 75°C, 1.85 eq. H_2 , 0.16 M, and 1 mL/min).

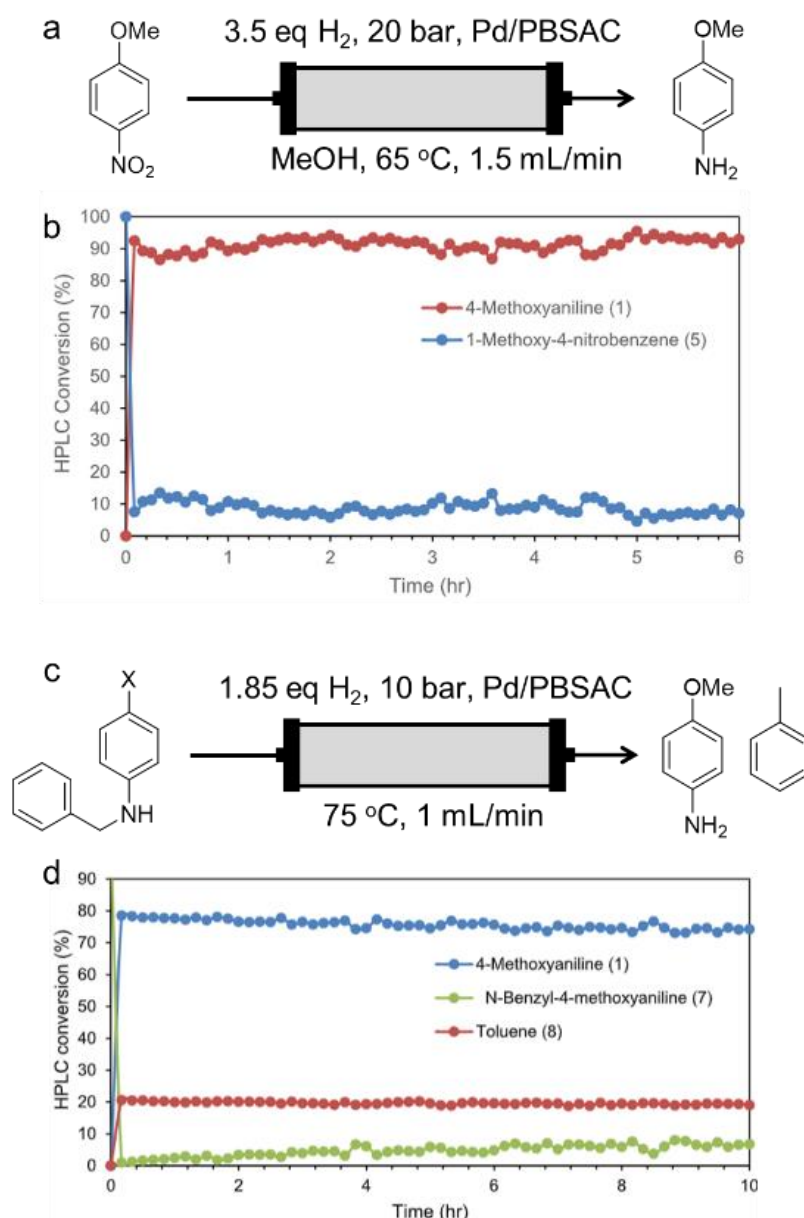


Figure 30: a-b) Reduction of 1-methoxy-4-nitrobenzene tested in continuous flow using Pd@PBSAC catalyst in GSK's pilot plant equipment, a stable catalytic activity was observed over 6 hours. c-d) Deprotection of N-benzyl-4-methoxyaniline tested in continuous flow, over 10 hours minimal loss in conversion was observed. Figures b and d reproduced with permission.³²

Metals other than palladium have been supported on PBSAC spheres and successfully employed in continuous flow. Murzin *et al.*¹⁸⁹ used platinum supported PBSAC catalysts, Pt@PBSAC, for aqueous phase reforming of a range of alcohols (1-propanol, propane-1,2-diol and glycerol) to alkanes. The continuous flow reaction was operated for a total time of \approx 300 hours (two cycles of 150 hours). Vlachos *et al.*¹⁹² used copper nanoparticles supported on PBSAC spheres, Cu@PBSAC, for the hydrodeoxygenation of 5-hydroxymethylfurfural to

2,5-dimethylfuran with 2-propanol used as a hydrogen donor. The conversion of 5-hydroxymethylfurfural was 100% with > 90% selectivity towards 2,5-dimethylfuran for 50 minutes before beginning to steadily decrease which was attributed to copper oxidation and nanoparticle agglomeration.

To date, the results obtained in continuous flow with PBSAC catalytic systems demonstrate positive results in which the catalyst can be operated in continuous systems over extended periods of time. The development of composite materials incorporating more complex catalytic nanomaterials, for example MOFs, is significantly less developed, however, and offers an opportunity to exploit the high versatility of MOF-based catalysts in continuous systems and improve their practicality due to the easier handling of these materials.

1.3.3 PBSACs as supports for MOFs

The incorporation of MOFs on activated carbon (AC)-based supports is not a novel concept and a number of examples exist regarding the fabrication of such materials, typically for adsorption-related applications. Observation of this data, however, suggests that the favourable properties of PBSAC spheres have not yet been exploited fully. Typically, powdered activated carbon has been used to support MOFs which is not desirable from a flow chemistry perspective due to the large pressure drop across the reactor and potential reactor blockage. To the best of my knowledge, only two examples to date^{198, 199} have involved the fabrication of a MOF@PBSAC composite. Neither of these two examples were used for continuous flow applications, although one of the materials was used as a catalyst in the degradation of chemical warfare agents.¹⁹⁹

In the nanoMOF project 'Nanoporous Metal-Organic Frameworks for production' (2009 – 2013) coordinated by Grählert,¹⁹⁸ HKUST-1 was immobilised onto PBSAC spheres by heating the components with hot melt adhesive in a rotary kiln. The resultant material was used for the adsorption of gases (cyclohexane, H₂S, NH₃) with an end use as a gas mask filter.

In one of the only existing examples of the immobilisation of UiO-66 onto PBSAC spheres to date, Navarro *et al.*¹⁹⁹ immobilised UiO-66 and UiO-66-NH₂ onto PBSAC spheres using layer-by-layer and solvothermal synthetic approaches with the resultant material used for the detoxification of nerve agents. The highlight of this research was the surface functionalisation of the PBSAC spheres (via H₂O₂

treatment) and subsequent controlled generation of a thin film of the MOF on the surface via the layer-by-layer synthetic approach. Caution should be exercised, however, when modifying the surface structure of PBSAC spheres due to the potential to lower the mechanical strength, an undesirable property for flow operations.

1.4 Research aim

The unsuitable (i.e. powdered) form of many promising industrial Lewis acidic heterogeneous catalyst candidates, in particular Lewis acidic MOFs, currently limits their application in continuous flow. The overall aim of this research is therefore to develop an approach that enables exploitation of these favourable catalytic properties in continuous flow by combining them with the scalable, industrially implementable properties of polymer-based spherical activated carbon supports. Success of this approach paves the way for further development into the exploitation of complex nanomaterials for continuous flow heterogeneous catalysis.

The transition from batch to continuous manufacturing has gained significant traction within the fine chemical industry over the past two decades due to the benefits of this mode of operation over the still widely-used batch processes. Similarly, the move away from the use of stoichiometric reagents and towards the use of heterogeneous catalysts offers a more efficient route to their production - in particular, the generation of heterogeneous Lewis acid catalysts as replacements for species that are required in stoichiometric amounts. Thus, the design of novel heterogeneous Lewis acidic catalysts that are suitable for use in continuous flow offers huge opportunity towards more efficient fine chemical manufacture.

MOFs are versatile, highly tuneable materials for which there is significant scope to exploit their catalytic properties. MOF catalysts have been identified as candidate catalysts for fine chemical synthesis. In their pristine form, some MOFs exhibit Lewis acidic catalytic properties, and positive results have been obtained when studying these materials as heterogeneous catalysts in both batch and continuous flow. To date, particularly positive results have been obtained with MIL-100(Sc), a member of the MIL-100 series of MOFs, and further understanding of the catalytic properties of these materials will be gained by using

tools such as design-of-experiments and kinetic modelling which are frequently used in fine chemical development. A substantial problem encountered when using MIL-100 and other MOFs in a continuous mode of operation, however, is that they typically exist as powders and so their direct application in flow reactors (e.g. packed-bed reactors) is not suitable due to the high pressure drop across the reactor and potential reactor blockages.

PBSAC spheres display a range of favourable properties that make them suitable for use in continuous flow as illustrated in preceding literature particularly using M@PBSAC (M = Pt, Pd), but the immobilisation of MOFs onto these materials has scarcely been explored to date. Thus, the development of a platform that enables the exploitation of MOF-based catalysis in continuous flow via the immobilisation of species like MIL-100(Sc) onto these support materials provides a new avenue for improvements in fine chemical manufacture. Additionally, this approach could serve as a general platform to exploit the high versatility of Lewis acidic MOF-based catalysts in continuous systems.

Before fabricating the novel MIL-100(Sc)@PBSAC composite material, powdered MIL-100(Sc) was prepared first. Chapter 2 details the materials characterisation and catalytic activity studies in batch establishing a firm understanding of the material as a Lewis acid catalyst for an industrially relevant transformation, namely the intramolecular cyclisation of citronellal. The catalytic properties of this material were further investigated using a DoE and kinetic modelling approach – two powerful tools which are widely employed during the development of fine chemicals.

Building on this crucial groundwork on the catalytic properties of MIL-100(Sc), Chapter 3 describes the synthesis of a novel catalytic material consisting of Lewis acidic MOF MIL-100(Sc) immobilised onto polymer-based spherical activated carbon supports, MIL-100(Sc)@PBSAC. This material was made reproducibly over many batches and deeply characterised using a range of analytical techniques: focused ion beam-scanning electron microscopy-energy dispersive X-ray analysis (FIB-SEM-EDX), powder X-ray diffraction (PXRD), N₂ adsorption, thermogravimetric analysis (TGA), atomic absorption spectroscopy (AAS), X-ray photoelectron spectroscopy (XPS), light scattering and crush testing.

Following preparation of the novel material, MIL-100(Sc)@PBSAC, Chapter 4 presents studies of the catalytic activity in both batch and continuous flow. Following the testing of key catalytic metrics in batch (i.e. reusability and effect of stirring rate) using the intramolecular cyclisation of citronellal as a model reaction (same as in Chapter 2), the novel material was then studied in a packed-bed reactor in continuous flow for the same reaction via stability testing at a range of different flow rates. After use in continuous flow, the catalytic material was then characterised using TGA, SEM and AAS to observe if any changes in the material had occurred. The catalytic activity towards a different set of reactions relevant to synthetic cannabidiol (CBD) synthesis was also conducted.

Finally, looking toward future developments for evaluating the generalisation of the MOF@PBSAC spheres platform, Chapter 5 presents preliminary results on a more complex composite catalytic system based on the immobilisation and postsynthetic functionalisation of UiO- MOFs on PBSAC spheres which was pursued with the aim of using this in a three-phase (gas-liquid-solid) reaction.

Chapter 2 Exploring the catalytic activity of MIL-100(Sc) by in-depth characterisation, design-of-experiments and kinetic modelling

2.1 Introduction

The industrial implementation of MOF-based heterogeneous catalysts for fine chemical manufacture has not yet been accomplished. Open questions remain about the current feasibility of these materials for this application compared to other bulk and supported heterogeneous catalysts which have been used for decades.^{102, 130}

During pharmaceutical development researchers make use of a range of tools, such as Design-of-Experiments (DoE)⁵⁸⁻⁶¹ and kinetic modelling^{60, 70, 71, 200}, that speed up development and enhance process understanding and control. Unfortunately, despite their potential value, widespread use of such tools has not been applied to MOF-based heterogeneous catalytic systems. As discussed in 1.2.2.2, most examples pertaining to the study of MOF-based catalysis via DoE/RSM explore biodiesel production^{134, 136-140} or photodegradation¹⁴¹⁻¹⁴⁶, with examples related to the catalysis of synthetic organic transformations (such as those employed in the fine chemical industry) lacking. This gap could be because MOFs may not currently be viewed as viable catalysts for fine chemical production. The lack of examples regarding the kinetic modelling of MOF-catalysed reactions could be due to the complexities in developing quantitative representations of reaction kinetics that account for the porous nature of the MOF, which is a widely acknowledged issue within the field.^{102, 156, 157}

In the same vein, deep understanding of the properties of catalyst systems and how this might relate to the resultant catalytic performance (i.e. structure-property relationships) is another factor that should also be considered when designing catalytic systems for industrial applications.⁵⁶ Despite the large and ever expanding literature, there too remains more open questions about general approaches to determining certain properties of MOFs that may be influential in determining the resultant catalytic properties, e.g. the actual stoichiometry of the MOF compared to the reported formula and the ratio of external to internal catalytic sites at given particle sizes. Many of these properties are still not reported consistently which in turn causes problems when trying to bridge the

gap between how the structures of these materials lead to their resultant catalytic properties.¹⁰² A generalised approach to describe the stoichiometry of UiO-66 was devised by Lillerud *et al.*,²⁰¹ but through analysis of their approach involving multi-technique characterisation (thermogravimetric analysis and ¹H NMR) it is clear that the development of such representations is challenging. This is likely to be the case when developing generalised representations for the properties of other MOFs too and may be why they are not reported.

This chapter aims to improve the potential application of MOF-based heterogeneous catalysts in an industrial setting (e.g. the pharmaceutical industry) by firstly synthesising and then studying the properties of a catalytically active MOF, MIL-100(Sc), with special pertinence to the resultant Lewis acidic catalytic properties (Part A) - for example the ratio of interior to exterior catalytic sites on a particle of a given size. The in-depth characterisation data was also used for the DoE and kinetic modelling approaches that will be used to greater understand the variables that give rise to favourable reaction outcomes (e.g. fast, catalytically efficient reactions) and the underlying mechanism of the chemistry that is occurring (Part B).

In Part A, a Lewis acidic catalytically active metal-organic framework MIL-100(Sc) was prepared in one step using conventional synthetic approaches and then thoroughly characterised using powder X-ray diffraction (PXRD), thermogravimetric analysis (TGA), infrared (IR) spectroscopy, N₂ adsorption, scanning electron microscopy-energy dispersive X-ray analysis (SEM-EDX), dynamic light scattering (DLS), and X-ray photoelectron spectroscopy (XPS).

Certain properties with special relevance to the catalytic performance of MIL-100(Sc), for example the MIL-100(Sc) stoichiometry and particle size, were studied in particular detail. TGA was used to propose a more representative stoichiometry of the MIL-100(Sc) that was synthesised in this work that takes into account the presence of defects throughout the framework and provides a more accurate description of the catalyst (i.e scandium) loading during a reaction. Doing so leads to the generation of more representative catalytic efficiency metrics such as the turnover frequency (TOF) for use in the DoE in Part B. Further research is still required, however, in order to provide a more accurate and generalised approach to describing the stoichiometry of this material for future

catalytic applications. Consideration of these are necessary if these materials are to be used in a pharmaceutical setting.

Particle size (distribution) and the impact of this property on the relative amount of sites located externally for a particle of a given size is essential for determining the catalytic activity (under certain assumptions, for example: there is not a relatively low reactant concentration, rates of reactant/product adsorption/desorption are slow enough, the reaction temperature is sufficiently high) and thus this was studied in greater detail. Whilst the particle size and distribution was studied by SEM-EDX and DLS, a novel approach for estimating the ratio of exterior to interior sites on a MIL-100(Sc) of a given size using the characterisation data that was obtained in this work (i.e. PXRD, TGA, N₂ adsorption, SEM-EDX data) was also suggested. In principle, this approach may be applied to other cubic MOFs, potentially providing an avenue to a generalised approach to enhanced structure-property understanding.

Part B involves studying the catalytic activity and kinetics of a MIL-100(Sc) Lewis acid catalysed reaction (the intramolecular cyclisation of citronellal) which builds upon the understanding of the properties of MIL-100(Sc) obtained in Part A. The catalytic activity was explored using a 2-level 3-factor full-factorial design-of-experiments (DoE) where a range of pertinent metrics (i.e. initial reaction rate, TOF, selectivity) not previously explored in DoE/RSM studies into MOF-based catalysts were compared and contrasted as a function of reaction temperature, catalyst loading and citronellal concentration. This approach to experimentation enabled more rapid and efficient exploration of the experimental space, when compared to classic one-variable-at-a-time (OVAT) approaches, and also led to the identification of interactions between variables. As well as identifying optimal conditions when studying the initial rate of reaction and TOF individually, a set of optimal conditions (i.e. a Pareto front, a set of solutions that are non-dominated to one another but are better than the rest of the solutions in the experimental space)²⁰² for these responses was proposed due to the trade-off that was identified. The firm understanding gained of MIL-100(Sc) as Lewis acid catalyst laid the groundwork for understanding the catalytic properties of novel MIL-100(Sc)@PBSAC composites fabricated in later work (detailed in Chapter 4).

Using the data that was obtained during the DoE, the kinetics of the reaction was also explored using user-friendly modelling software Dynochem®, which is commonly employed in a pharmaceutical setting.⁷² This was done to explore the underlying reaction mechanism of the reaction. To date, the kinetics of a MOF-catalysed reaction have not been explored using this software and generally examples pertaining to the use of kinetic modelling to study MOF-based catalytic systems via computational approaches are limited.¹⁴⁸⁻¹⁵¹ The ability of Dynochem® to obtain reliable kinetic data was first tested using a simpler system with homogeneous catalyst scandium triflate ($\text{Sc}(\text{OTf})_3$) which is considered a benchmark Lewis acid catalyst,¹⁷⁷ especially towards the intramolecular cyclisation of citronellal.²⁰³ It was found that a first-order mechanism, in line with previous reports, produced the best fit and that the activation energy values were similar to those reported previously. These results instilled confidence in the ability of Dynochem® to obtain accurate and reliable kinetic data. Next, kinetic models were generated using the data obtained in the DoE for the MIL-100(Sc) catalysed intramolecular cyclisation of citronella. The observed reaction kinetics showed better agreement with Langmuir-Hinshelwood (LH) kinetics, a common approach to modelling heterogeneous systems, compared to first order kinetics approaches. By using the experimental data obtained in this work to generate kinetic models, it is hoped that such practices can be more widely used as a relatively simple and easy tool for enhancing the understanding of MOF-catalysed reactions in the future.

Part A

2.2 Synthesis and characterisation of MIL-100(Sc)

2.2.1 Synthesis of MIL-100(Sc)

Before use as a Lewis acid catalyst, MIL-100(Sc) had to be prepared in a reproducible manner. Identification of the crystalline phases characteristic of MIL-100(Sc) across different batches was conducted through PXRD, serving as a rough indication of the reproducibility of the preparation.^{105, 106} A reproducible preparation is also necessary, in turn, for scaling up the synthesis of MIL-100(Sc) for future industrial application where consistent material quality is a critical parameter that needs controlling.²⁰⁴ These materials should also be distinguished from amorphous M-BTC MOFs, made from the same linker and metals as

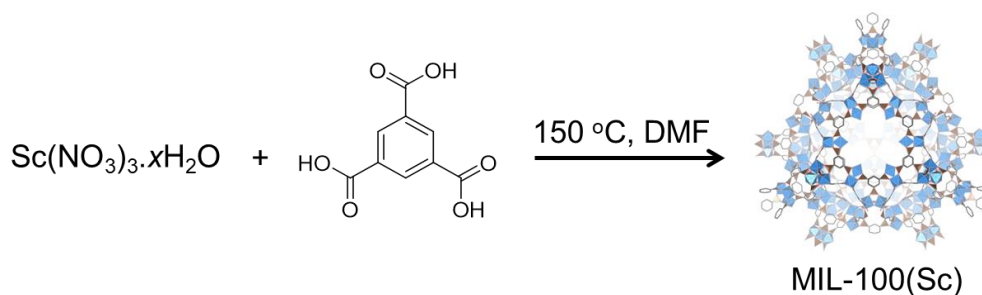
MIL-100(M) MOFs, but possessing a broad and ill-defined powder pattern.²⁰⁵ Besides PXRD, further characterisation was also conducted to identify some of the other vital properties of the synthesised materials that cannot be identified by this technique alone (e.g. BET surface area, particle size/shape, thermal stability). The synthesis of MIL-100(M) MOFs, described as a ‘star’ MOF by Hai-Long *et al.*¹⁰⁸, has previously been scaled-up with certain analogous (MIL-100(M), M = Fe, Cr, Al) now available to purchase from a range of suppliers highlighting the high potential of these MOFs as adsorbents,¹⁰⁹ drug carriers¹¹⁰ and catalysts.¹⁰⁷

One way that greater reproducibility of synthesis may be obtained is by limiting the synthesis to a single step thus making MIL-100(Sc), which may be prepared in one step directly from commercially available materials using conventional synthetic approaches, a suitable candidate.¹¹⁹ Much of the development work conducted into MIL-100(Sc) to date was spearheaded by Wright and colleagues and thus this work frequently makes reference to the work conducted by this research group.^{119, 120, 206} Previously, Wright *et al.* prepared MIL-100(Sc) solvothermally from scandium nitrate hydrate and benzene-1,3,5-tricarboxylic acid (trimesic acid) in N,N-dimethylformamide (DMF) at 150 °C for 48 hours (Table 4).¹¹⁹ Other similar approaches have been taken for the solvothermal preparation of MIL-100(Sc) too,^{123, 207, 208} and more broadly speaking MIL-100(M) MOFs in general.^{105, 106, 209-211} In this work, MIL-100(Sc) was prepared solvothermally in DMF according to the procedure carried out by Wright and colleagues (Table 4, Scheme 2).

Table 4: Conditions employed for synthesis of MIL-100(Sc) powder in this work, based on the conditions used by Wright *et al.*¹¹⁹

Method	Time (hours)	Solvent	Temperature (°C)	M:L molar ratio
Solvothermal	48	DMF	150	2:1

^a For the synthesis of MIL-100(Sc), scandium nitrate hydrate ($\text{Sc}(\text{NO}_3)_3 \cdot x\text{H}_2\text{O}$) (assumed that $x = 3$) and trimesic acid were used.



Scheme 2: Synthesis of MIL-100(Sc) carried out in this work, adopted from Wright *et al.* where precursors were added to a PTFE liner and heated solvothermally in a stainless steel autoclave at 150 °C for 48 hours.¹¹⁹

Figure 31 shows the typical PXRD pattern obtained of activated MIL-100(Sc) following solvothermal synthesis and a simulated pattern of isostructural MIL-100(Cr) (thus possessing a PXRD pattern with identical peaks) overlaid for comparison. Through observation of the two powder patterns it could be seen that a crystalline material with peaks characteristic of MIL-100(M) MOFs had been formed in one step. Also of note in the PXRD pattern of MIL-100(Sc) obtained in this work were three peaks between $2\theta = 7.5 - 9.5$ which were not present in the simulated MIL-100(Cr) powder pattern.¹⁰⁶ These peaks have been observed in the powder pattern of MIL-100(Sc) MOFs^{125, 207, 212, 213} and MIL-100(Fe) previously,^{214, 215} but were not directly commented upon by the authors. Previously, additional peaks have been observed in the PXRD pattern of other MOFs (i.e. UiO-66) due to the presence of correlated disorder in the framework as a result of a defective structure,^{216, 217} but it is not clear whether this type of disorder has been encountered in MIL-100 MOFs previously. These peaks could also be attributed to minority phases or incompletely removed solvent molecules from the framework resulting in the formation of new phases.

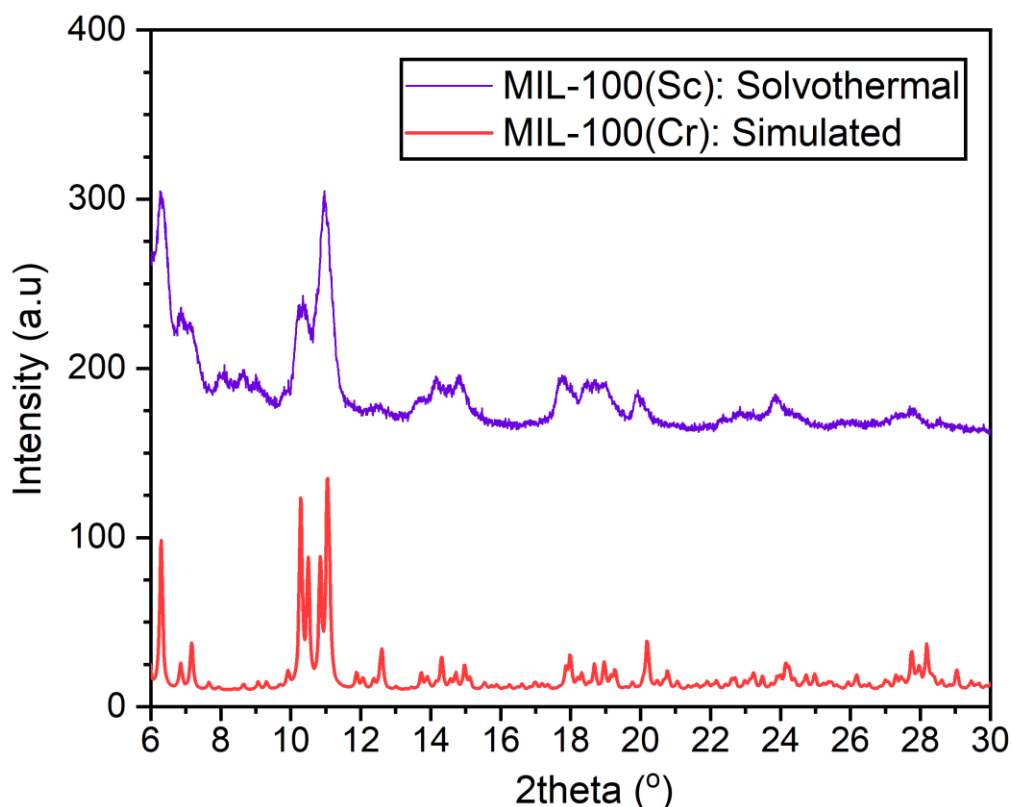


Figure 31: Typical PXRD pattern of the product obtained following solvothermal synthesis (purple) and the simulated powder pattern of isostructural MIL-100(Cr) (red) for comparison.¹⁰⁶

2.2.2 Activation of MIL-100(Sc)

Following synthesis, Wright and colleagues¹¹⁹ washed the MIL-100(Sc) with ethanol and water to remove any unreacted precursors. They also detailed activation steps prior to use as a catalyst which involved soaking the catalyst in methanol for 24 hours (to replace residual solvent molecules such as DMF present in the pores) before drying. The authors also noted that MIL-100(Sc), advantageously, may also be activated between catalytic reactions by simply soaking in methanol.¹¹⁹

In a more detailed study into material activation published by the same group two years later, MIL-100(Sc) was subjected to a range of different drying conditions and the resultant properties studied.¹²⁰ Following ‘prolonged washing’ with methanol and drying under vacuum at either 150 °C or 250 °C the authors found that some DMF remained in the pores suggesting this remains strongly bound to the Sc³⁺ sites in the framework. In catalytic studies, activation at 250 °C actually lowered selectivity as a result of the generation of unwanted by-products and reduced the pore volume. These findings suggested that the high temperatures

may have caused the MOF structure to partially degrade. The authors then concluded that washing with methanol followed by activation at 150 °C was chosen as the standard activation procedure.

Based on this work by Wright *et al.*,¹²⁰ the uncharacterised white powder that was formed following solvothermal treatment was washed with water and ethanol then soaked in methanol for 24 hours to activate the material. TGA was then used as a tool for finding optimal drying conditions for MIL-100(Sc).

In my initial work, a colour change from white to orange was previously observed upon drying under vacuum overnight at 150 °C (Figure 32). These drying conditions were first tested in line with the conditions employed by Wright *et al.*,¹²⁰ and more broadly the use of a vacuum to dry MIL-100(M) MOFs is common.^{113, 114, 122, 125, 210, 214}

When compared to the PXRD pattern of a different MIL-100(Sc) sample that was dried under conditions that did not induce a colour change (i.e. at 150 °C for 90 mins), drying at 150 °C under vacuum overnight did not appear to result in a crystallographic phase transition of the material (Figure 33).



Before vacuum overnight at 150 °C

After vacuum overnight at 150 °C

Figure 32: MIL-100(Sc) powder before (a) or after (b) drying under vacuum overnight at 150 °C. A colour change from white to orange was observed.

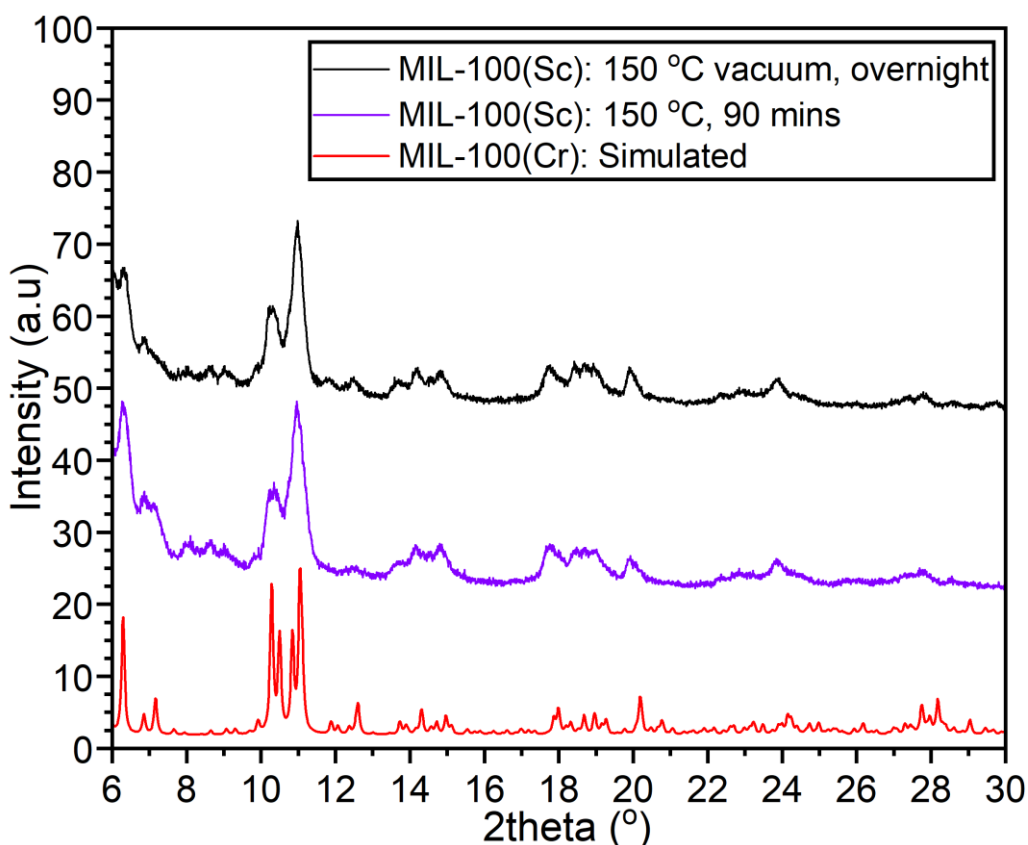


Figure 33: PXRD pattern of MIL-100(Sc) after being subjected to different drying temperatures: 150 °C under vacuum overnight (black), 150 °C for 90 mins (purple) and simulated pattern of MIL-100(Cr) (red).

Although in their study Wright *et al.*¹²⁰ did not report seeing a colour change upon drying the MOF at elevated temperatures where they also postulated that framework degradation was possibly occurring, we were still cautious about what implications a colour change may have upon the resultant properties of MIL-100(Sc) in this work. More broadly, a colour change has previously been shown to be related to particle degradation of MIL-100(Fe) particles²¹⁸ where, despite being half-degraded, the material maintained a powder pattern indicative of a crystalline MIL-100(M) MOF. The colour change to yellow may also have been due to the formation of N-Nitrosodimethylamine, which is yellow in colour,²¹⁹ as a result of the reaction between dimethylamine (formed via DMF thermal decomposition which occurs upon heating during the reaction) and nitrous acid (formed via reduction of nitrate ions (from scandium precursor) with protons formed by trimesic acid deprotonation).²²⁰

As we were unsure how the crystallinity of MIL-100(Sc) particles may have been impacted, we therefore selected the observation of a minimal colour change as one metric to determine the most suitable drying conditions.

Alongside minimising the extent of the colour change of the framework, drying conditions which were able to remove as much residual material from the pores of the framework were also selected as this is one indication into how activated the framework was for catalysis. The removal of residual solvent in the pores was determined by TGA. Figure 34 shows a typical TGA profile of MIL-100(Sc) obtained in this work as well as the corresponding 1st derivative weight obtained following analysis in air.

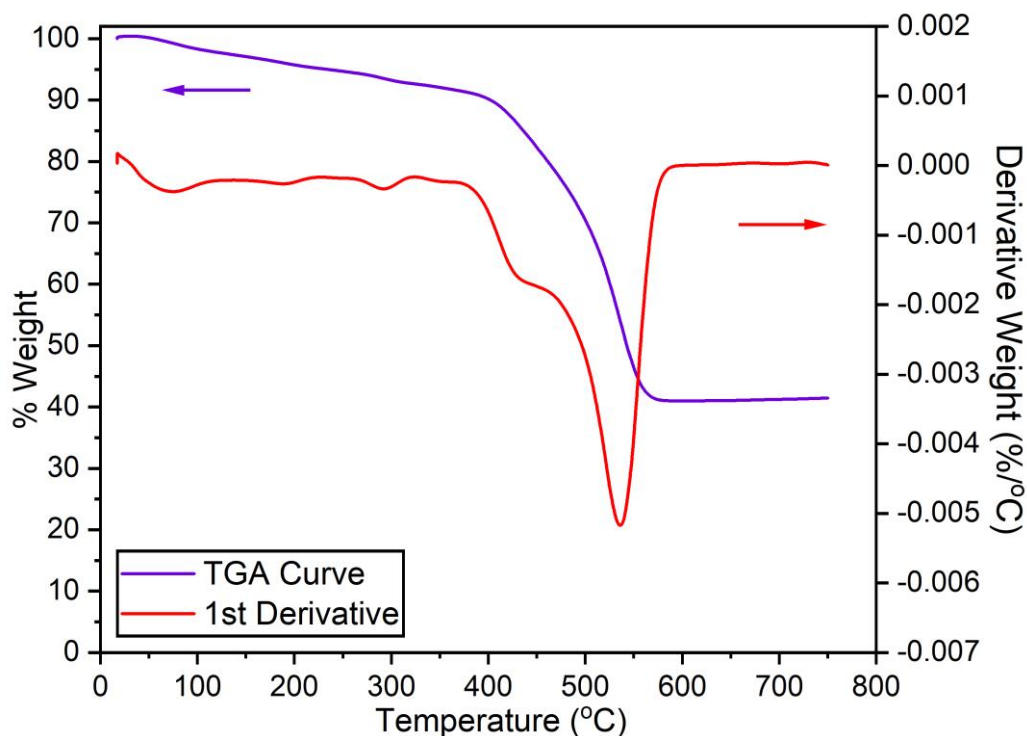


Figure 34: Typical TGA plot obtained for MIL-100(Sc) showing % weight change (purple) and first derivative weight change (red) with increasing temperature for MIL-100(Sc) dried at 150 °C for 90 mins. Samples were heated from room temperature at 10 °C min⁻¹ in flowing air. Arrows illustrate relevant Y-axis for data.

For MIL-100(M) MOFs, there are three significant mass losses in a typical TGA profile: 0 - 100 °C removal of free solvent present in the pores of the framework, 100 - 350 °C shows loss of more tightly bound solvent to the metal centres throughout the framework (e.g. DMF) and finally at > 350 °C the breakdown of the MOF framework.^{105, 111} The extent of the first two mass losses observed for these MOFs can depend on the activation conditions of the material prior to analysis (e.g. stirring in a solvent to replace residual solvent molecules present in the pores and the subsequent extent of drying) and so was used as the measure of how 'activated' the framework had become post drying in this work.

In the typical TGA profile of activated MIL-100(Sc) in this work, there was approximately a steady 10% loss in mass until the framework collapsed at ≈ 380 °C. The TGA profile of activated MIL-100(Sc) matches well with the profiles previously observed for other MIL-100(M) MOFs in the literature.^{105, 111}

2.2.2.1 Optimising drying temperature for framework activation

The two metrics that were tested when optimising drying conditions were whether, following drying, there was a colour change from white to orange (identified through visual inspection of the powder with no colour change preferable) and the amount of solvent material that was subsequently removed from the framework before thermal decomposition occurred at 380 °C (i.e. the ‘dryness’ of the sample). The drying conditions that did not induce a colour change whilst also making the sample as dry as possible (i.e. conditions resulting in the least amount of material removal before framework decomposition at 380 °C) were selected to be used when preparing MIL-100(Sc) for catalysis. Table 5 summarises the drying conditions that were chosen in the study following stirring of MIL-100(Sc) in methanol for 24 hours along with the resultant extent of colour change and mass loss (%) between the initial mass and the mass at 380 °C (assumed to be framework decomposition temperature), interpreted to be the residual mass of solvent in the pores. The resultant physical appearance and TGA profile of the related material shown in Figure 35 and Figure 36 respectively.

Table 5: Effect of drying conditions on colour and final mass of activated MIL-100(Sc).

Entry	Drying conditions	Colour change? a	Mass loss at 380 °C (%) ^b
1	Before drying	-	13.6
2	150 °C, 1.5 hours	N	8.6
3	60 °C, vacuum, 3 hours	N	10.6
4	100 °C, vacuum, overnight	Y ^c	9.4
5	200 °C vacuum, overnight	Y	7.7

^a from white to orange. ^b the % mass loss at 380 °C (before framework decomposition but after solvent removal) relative to the initial mass used in the experiment, interpreted to be the extent of removal of species from the pores.

^c Colour change was subtle.

As drying under vacuum is common for the activation of MIL-100(Sc) MOFs,^{113, 114, 122, 125, 210, 214} this was studied in greater detail at different temperatures (60 °C, 100 °C and 200 °C) and also compared with drying conditions at ambient pressure, like those employed by Wright *et al.*,¹²⁰ where the MOF was heated at 150 °C for a length of time (1.5 hours in this work).

No colour change was observed when the sample was heated under vacuum at 60 °C for 3 hours or upon heating the sample at 150 °C for 1.5 hours in an oven, with the latter process removing more solvent from the pores of the framework (residual material (e.g. DMF) contributed to 8.6% of the mass of the material after drying under vacuum at 60 °C for 3 hours whilst it contributed 10.6% when drying at 150 °C at ambient pressure for 1.5 hours). With more extreme drying conditions (Table 5, entry 4 and 5) a colour change was observed, despite this change being only subtle upon heating the sample at 100 °C under vacuum overnight. Given this, the amount of residual material in the pores of this sample (9.4%) was actually greater (but still similar) than when vacuum drying was not employed (Table 5, entry 2).

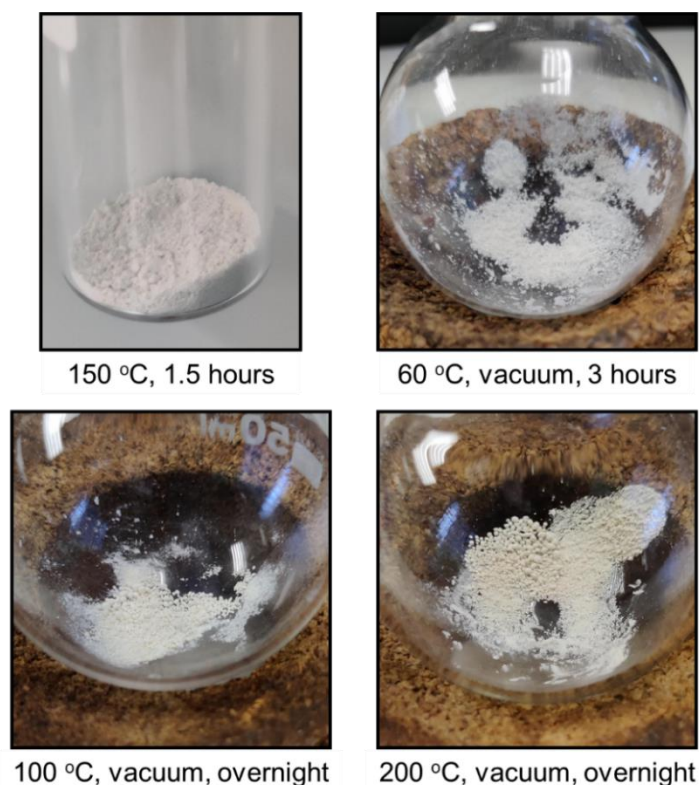


Figure 35: Images of samples that were submitted to different drying conditions and the colour change that was observed.

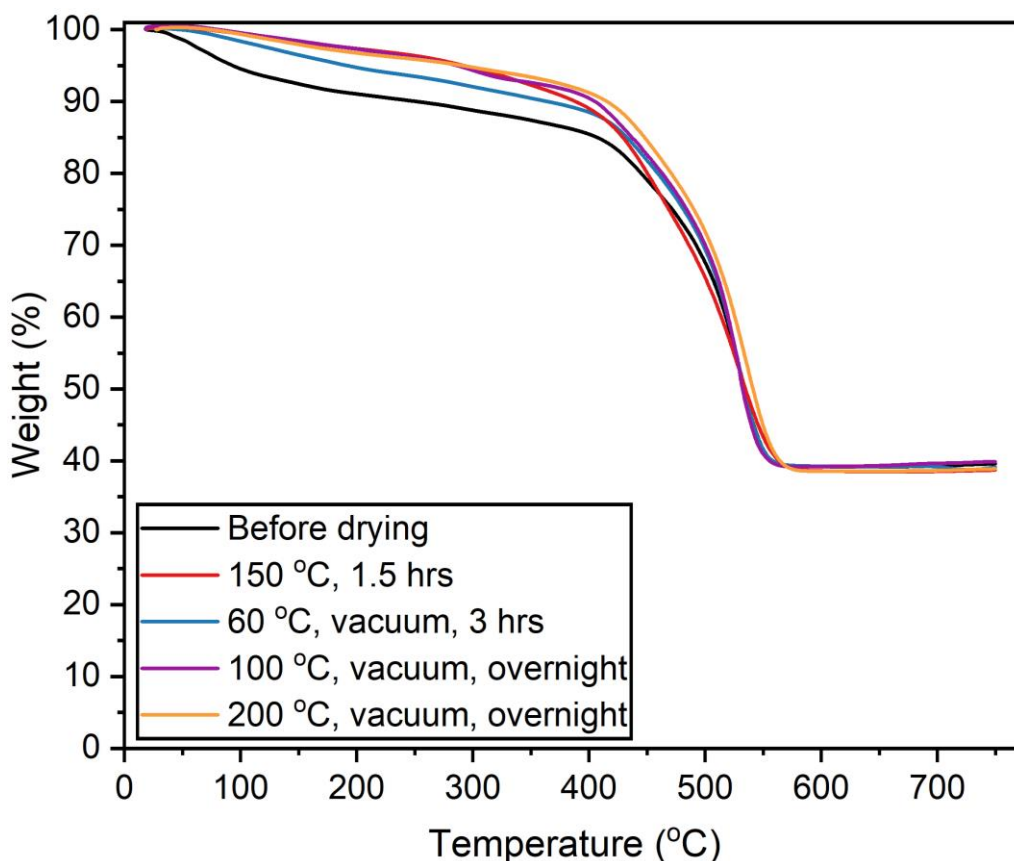


Figure 36: TGA profiles of different drying conditions employed for MIL-100(Sc) powder.

Comparison of the non-vacuum and vacuum-based drying conditions in the study found that the use of vacuum conditions for drying of the MOF seemingly did not increase the amount of material that was removed from the pores apart from when the highest temperatures (200 °C) were employed (Table 5, entry 5) which also led to the most amount of material being removed from the pores (7.7%). The most pronounced colour change was also observed at this temperature, however.

Due to the lack of change in colour and the removal of solvent from the pores, the drying conditions that were selected to activate MIL-100(Sc) for catalysis was heating at 150 °C for 1.5 hours. These results suggest that the use of a vacuum and extended heating times are not necessary to best activate MIL-100(Sc) although if they are used then relatively non-harsh drying conditions may be used (60 °C for 3 hours). An additional avenue of exploration for this work would come from varying the washing step carried out (i.e. stirring in methanol) before the material was dried to assess how much adsorbed material was removed.

2.2.3 Stoichiometry of MIL-100(Sc)

In their initial synthesis of MIL-100(Sc), Wright *et al.* used a 2:1 molar ratio of M:L (M = metal, L = linker) which is different from the 2:1.5 molar ratio present in the reported stoichiometry of MIL-100(Sc) of $[\text{Sc}_3\text{O}(\text{BTC})_2\text{X}]$ (where X = singly charged anion required to balance the charge of the framework) thus making trimesic acid the limiting reagent.¹¹⁹

By making the trimesic acid the limiting reagent in the synthesis, this procedure may lower the amount of extra-framework trimesic acid (i.e. trimesic acid that is not incorporated into the MIL-100(Sc) framework but is encapsulated within the pores) which, if present, may negatively impact the catalytic activity by strongly coordinating to the catalytically active scandium sites and by blocking/occupying the pores.^{221, 222} In their work, Taulelle *et al.*²²¹ confirmed the presence of extra-framework trimesic acid by IR spectroscopy where there are peaks at approximately 1720 cm^{-1} (C=O) and $1349/1273\text{ cm}^{-1}$ (C-O) in the spectrum of MIL-100(M) MOFs. MIL-100(Sc) following activation (i.e. washed with water and ethanol, stirred in methanol for 24 hours then dried at $150\text{ }^\circ\text{C}$ for 90 minutes) was probed by IR spectroscopy to confirm whether any extra-framework trimesic acid was present in the framework (Figure 37). The lack of peaks at these specific wavenumbers in the spectrum indicated the absence of extra-framework trimesic acid in the MIL-100(Sc) framework.

The lack of peaks corresponding to extra-framework trimesic acid in the IR spectrum suggests that the washing, activating and drying steps were effective at removing this species or that all of the linker used for the synthesis was incorporated into the framework which would prove useful when using TGA to calculate the molecular formula of MIL-100(Sc) (section 2.2.3.1).

More broadly for MIL-100(M) MOFs, the two bands between 1384 and 1451 cm^{-1} and 1574 and 1629 cm^{-1} correspond to symmetric and asymmetric stretches of the carboxylate groups within trimesic acid molecules incorporated into the MOF framework respectively.²⁰⁵ The two peaks at 707 cm^{-1} and 764 cm^{-1} correspond to C-H stretching vibrations in the benzene group in trimesic acid molecules that are also incorporated into the framework.²²³

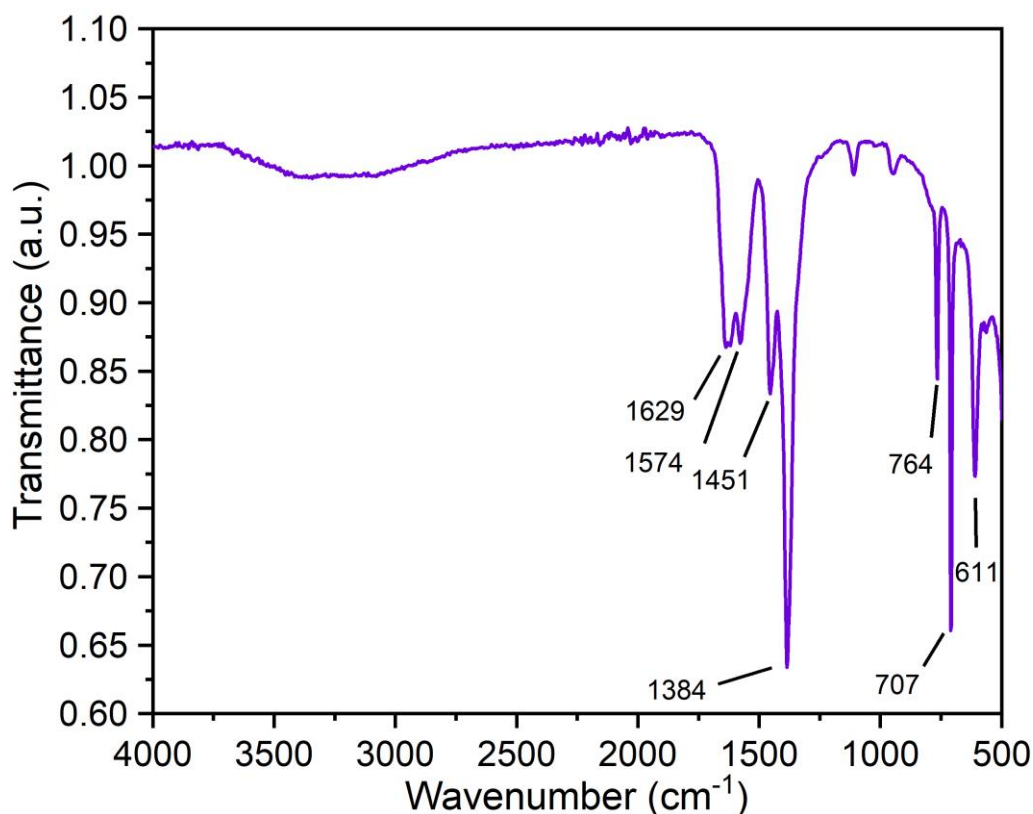


Figure 37: FT-IR spectrum of activated MIL-100(Sc) in this work (washed with water and ethanol, stirred in methanol for 24 hours and dried at 150 °C for 1.5 hours) between 500 - 4000 cm^{-1} .

Wright *et al.*¹²⁰ studied the IR spectrum of methanol-activated MIL-100(Sc) and found that a peak at 3672 cm^{-1} corresponding to methanol bound to metal sites disappeared upon heating at elevated temperatures. They also found that other peaks corresponding to methanol disappeared upon heating. In the IR spectrum of activated MIL-100(Sc) in this work, none of the peaks corresponding to methanol are present thus it was assumed that the drying step was effective at removing all of the methanol from the pores of the MOF. The identity of the broad weak peak between 3000 - 3500 cm^{-1} is frequently attributed to the O-H stretch in residual molecules, thus for MIL-100(Sc) in this work it was assumed that there was a small amount of residual water left within the framework.²²⁴

2.2.3.1 Accounting for defects

It was also postulated that adopting a 2:1 M:L ratio for the synthesis of MIL-100(Sc) as opposed to that dictated by the reported stoichiometry (2:1.5) may alter the composition of the framework that was formed. The resultant material properties derived from the synthesis conditions could also have implications for the catalytic performance of this framework, such as by making

the catalytic sites more available for reagents due to the creation of defects, and so this was explored further. The implications of structure defects on reagent accessibility to the catalytically active sites in MIL-100(Sc) was studied in section 2.4.1.1.

Much work has been carried out to date regarding the generation of defects for MOFs, which can typically be categorised as either missing linkers or clusters, primarily for UiO-based MOFs. Use of acid modulators in the synthesis such as acetic acid,²²⁵ benzoic acid,²²⁶ hydrochloric acid,^{227, 228} trifluoroacetic acid²⁰¹ and formic acid^{201, 216} can be used to generate defects throughout the framework, with the latter also generated in-situ during a MOF synthesis by the thermal decomposition of the reaction solvent (DMF) which may in turn be incorporated into the framework as formate anions.

In their pioneering defect engineering work with UiO-66, Lillerud *et al.*²⁰¹ devised an approach to determine the stoichiometric formula of UiO-66 following synthesis with various acid modulators. The approach cleverly exploited composition information derivable from ¹H NMR and TGA data. To date, defects have not been studied in such great depth for MIL-100(M) MOFs^{111, 115, 222, 229-231} which is surprising given the popularity of these MOFs and the possible implications for the resultant catalytic properties.

There does not yet exist a generalised approach to quickly approximate the stoichiometry of MIL-100(M) MOFs, with the formula of prepared materials often reported in the literature as something synonymous to that of a defect-free material ($[M_3O(BTC)_2X]$, where X = singly charged anion); such general assumptions may not be an accurate description of the structure of the framework in actuality. To enhance the application and understanding of these materials for catalysis, the role of defects situated throughout MIL-100(M) framework should be considered and one approach to this is by providing a more accurate description of the molecular formula. We therefore used TGA to re-estimate the formula of MIL-100(Sc) in this work whilst taking into account basic charge balancing requirements that must be applied to all MIL-100(M) MOFs.

The stoichiometry of MIL-100(M) in this work was therefore solely estimated using the reported components of the MOF: trimesic acid, the scandium trimer node (Sc_3O) and a simple anion (OH^-) required to balance the charge of the framework.

When analysed in air the residual mass in the TGA profile of MIL-100(Sc) corresponds to the mass of Sc_2O_3 that was formed following framework decomposition (assuming complete, stoichiometric oxidation). By comparing the mass of residual scandium present after framework decomposition to the mass of MIL-100(Sc) present after solvent removal but before framework decomposition (i.e. at $\approx 380^\circ\text{C}$), the stoichiometry of MIL-100(Sc) was inferred. Figure 38 shows a TGA plot of MIL-100(Sc) following activation by soaking in methanol for 24 hours and then drying at 150°C for 90 minutes.

At the end of the analysis, 2.15 mg of Sc_2O_3 was present or 1.40 mg of scandium. The mass of scandium constituted 27.0% of the original mass used for the analysis and 29.2% of the 'dry' mass present when framework decomposition starts (380°C). The stoichiometry of the 'dry' MIL-100(Sc) was assumed to be $[\text{Sc}_3\text{O}(\text{BTC})_a(\text{OH})_b]$. Taulelle and colleagues²²¹ studied the activation of MIL-100(Al) and found that at 350°C hydroxide anions were still bound to the Al^{3+} sites thus it was assumed that these ions were still bound to the Sc^{3+} sites in MIL-100(Sc) upon decomposition at $\approx 380^\circ\text{C}$ in this work.

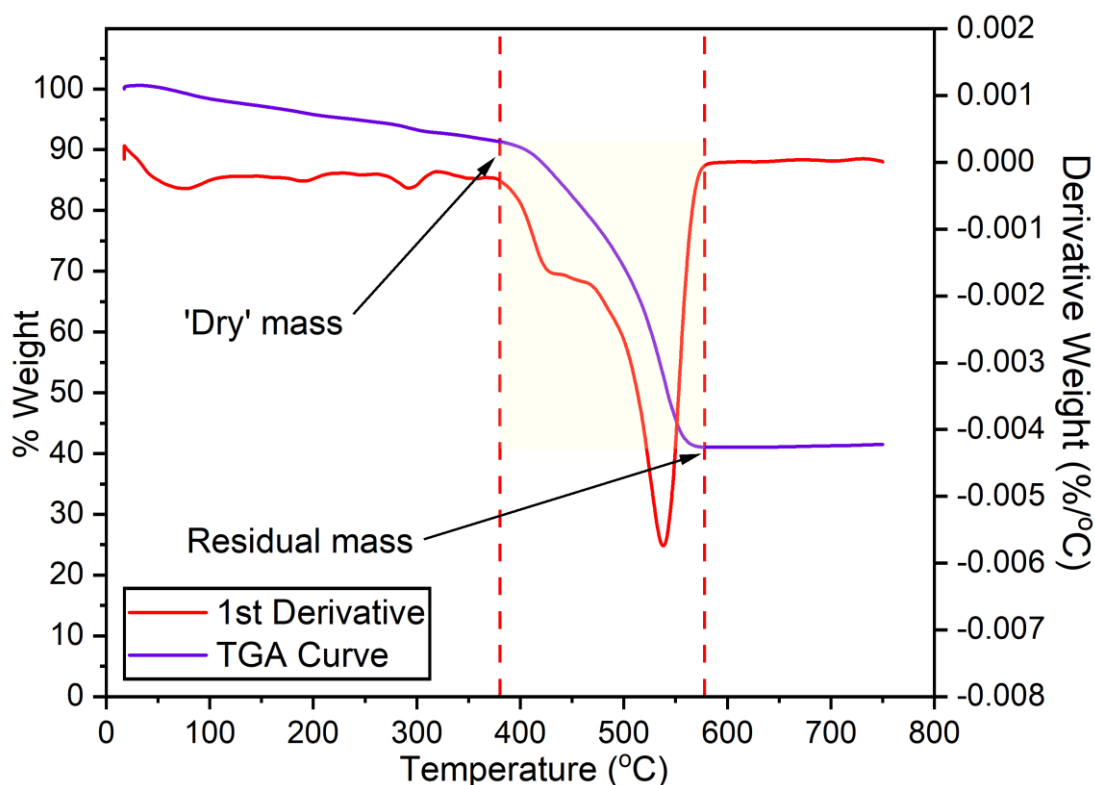


Figure 38: TGA plot showing how stoichiometry of MIL-100(Sc) was determined using the 'dry' mass of MIL-100(Sc) at 380°C and the residual mass following framework decomposition at approximately 580°C .

Table 6: Shows starting mass, mass just before framework decomposition (at 380 °C) and the mass present following framework decomposition (at 600 °C) of an activated MIL-100(Sc) sample in this work. These are also presented as weight percentages.

Temperature (°C)	Mass (mg)	Mass (%)	Mass (%)
18 (Start of analysis)	5.23	100	-
≈ 380 (Decomposition starts) 'Dry mass'	4.78	91.5	100
≈ 600 (Decomposition complete) mass of Sc ₂ O ₃	2.15	41.1	45.0
Residual mass of scandium	1.40	27.0	29.2

MIL-100(Sc) possesses the reported formula [Sc₃O(BTC)₂OH] consistent with a scandium weight % of about 23.2%. The higher scandium composition of ≈ 29.2% weight of the 'dry mass' of MIL-100(Sc) in this work suggests that this material may be more consistent with a different stoichiometry. For this reason, different potential stoichiometric formulas, closer to a 29.2% weight scandium loading, were proposed.

Table 7 presents the reported¹¹⁹ and proposed formula of MIL-100(Sc). The charge disparity in the material was compensated for by the coordination of more hydroxide anions to Sc³⁺ sites. The actual formula of MIL-100(Sc) produced in this work, assuming that all of the scandium present in the material was bound in crystalline MIL-100(Sc) and ignoring surface termination effects, may be closer to [Sc₃O(BTC)_{1.23}OH_{3.31}] which was obtained simply by obtaining a TGA profile of the material. The lower than stoichiometric amount of trimesic acid molecules throughout the framework points to the presence of missing linker defects, approximately 0.77 per node. Due to these defects, this may make the window sizes of the framework larger and thus make reagent molecules better able to access the scandium sites. the ability of reagents to enter the pores of MIL-100(Sc) are discussed in section 2.4.1.1.

Table 7: Proposed formula of MIL-100(Sc) in this work following TGA analysis compared with the literature reported formula.¹¹⁹

Formula	Scandium wt. %
[Sc ₃ O(BTC) ₂ (OH)] (reported formula)	23.2
[Sc ₃ O(BTC) _{1.23} (OH) _{3.31}] (this work)	29.2

The limitations of this approach to determining MIL-100(Sc) should also be appreciated. Using data obtained from TGA analysis alone, the presence of missing clusters are not accounted for. Additionally, previous work by Lillerud²⁰¹ on UiO-66 and Gates²²² on MIL-100(Al) found that formic acid, which is also formed during the synthesis when DMF decomposes, may be incorporated into the framework and was not accounted for by this approach. Despite these limitations, this method for MIL-100(Sc) stoichiometry determination is a more realistic depiction than what is commonly reported and paves the way for further development of this approach.

For determining the scandium (catalyst) loading of reactions in the design-of-experiments (section 2.4.2), it was assumed that scandium constituted 27.0% mass of the MIL-100(Sc) used in this work as the same activation process was carried out for each batch (Table 6). This also allowed for more accurate calculation of reaction metrics such as turnover frequency (TOF) which in turn enabled us to greater understand and optimise the reaction conditions.

2.2.4 Textural properties of MIL-100(Sc)

Following activation (150 °C for 1.5 hours), the textural properties of activated MIL-100(Sc) were assessed by carrying out N₂ adsorption/desorption at -196 °C. Analysis of the N₂ adsorption isotherm shows that MIL-100(Sc) exhibited an isotherm characteristically intermediate to type I and type IV isotherms including a secondary uptake at $P/P_0 = 0.12$, in line with previous reports for MIL-100(M, M = Fe, Cr) (Figure 39).^{105, 106} Type I isotherms, indicative of a microporous material, are characterised by a steep uptake in adsorption at low P/P_0 due to the filling of micropores. Type IV isotherms, indicative of mesoporous materials, firstly show steady increase in the amount adsorbed at low to mid-range P/P_0 values due to monolayer-multilayer adsorption in the mesopores followed by a hysteresis loop as a result of capillary condensation.²³ These observations therefore indicate the presence of both micro- and mesopores in MIL-100(Sc). MIL-100(Sc) was found to have a BET surface area of 1524 m²/g (calculated using the BETSI method²³²), a pore volume of 0.90 cm³/g (at $P/P_0 = 0.99$) and a micropore volume of 0.09 cm³/g (calculated from t-plot) – similar to previous observations.^{119, 213}

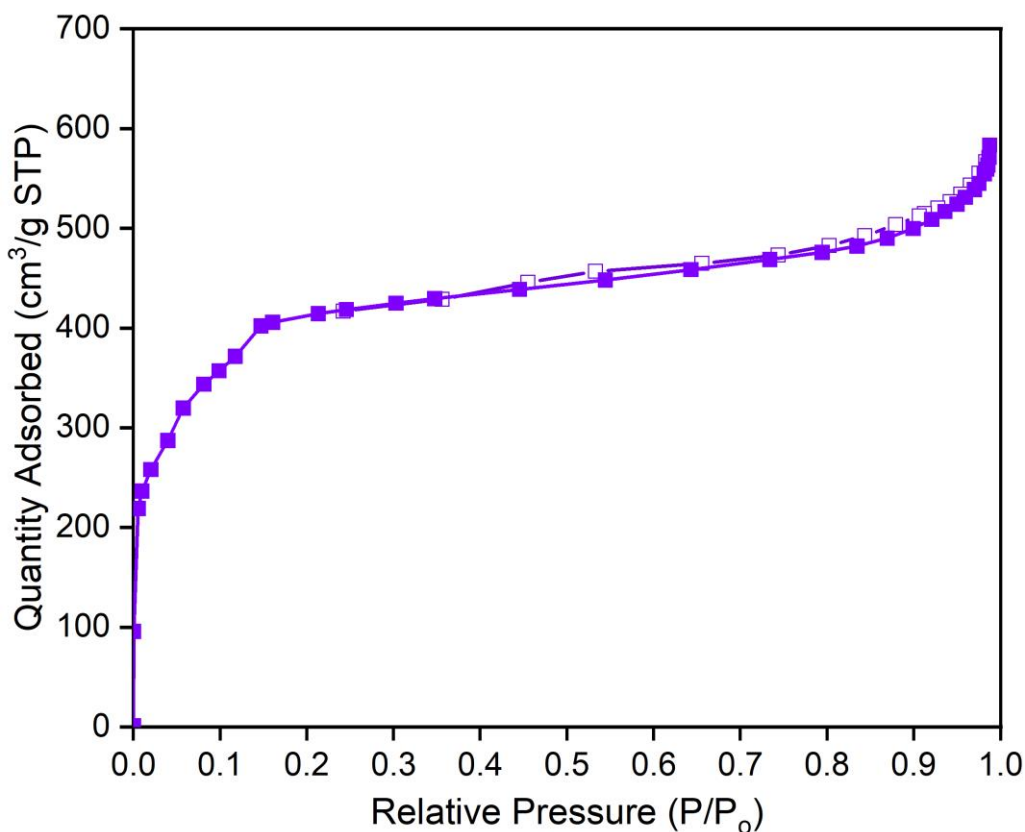


Figure 39: N₂ adsorption and desorption isotherm of MIL-100(Sc) obtained at -196 °C.

2.2.5 MIL-100(Sc) particle size distribution, morphology and composition

2.2.5.1 Scanning electron microscopy-energy dispersive X-ray analysis

Understanding of the morphology, particle size and elemental composition of MIL-100(Sc) was acquired by carrying out SEM-EDX. The SEM images of MIL-100(Sc) in Figure 40a-c show aggregated MIL-100(Sc) particles, with individual particles possessing a roughly spherical morphology, similar to previous observations.²⁰⁷ The particle diameter (calculated by manually measuring the diameter of 75 particles, enough for the cumulative average particle diameter to converge to a stable value (Figure 40d)) was also measured - e.g. between particles 70 and 75 there was a 0.3 nm change in the cumulative average diameter. The shape of the size distribution was approximately symmetric with an average particle diameter of 203.5 nm (see section 6.1.5.1 for particles that were sized) (Figure 40e). The width of the distribution was characterised by a standard deviation of 48.2 nm (%RSD = 23.7%). The

presence of the constituent elements of MIL-100(Sc) (i.e. scandium, carbon, oxygen) was confirmed using EDX mapping (Figure 41).

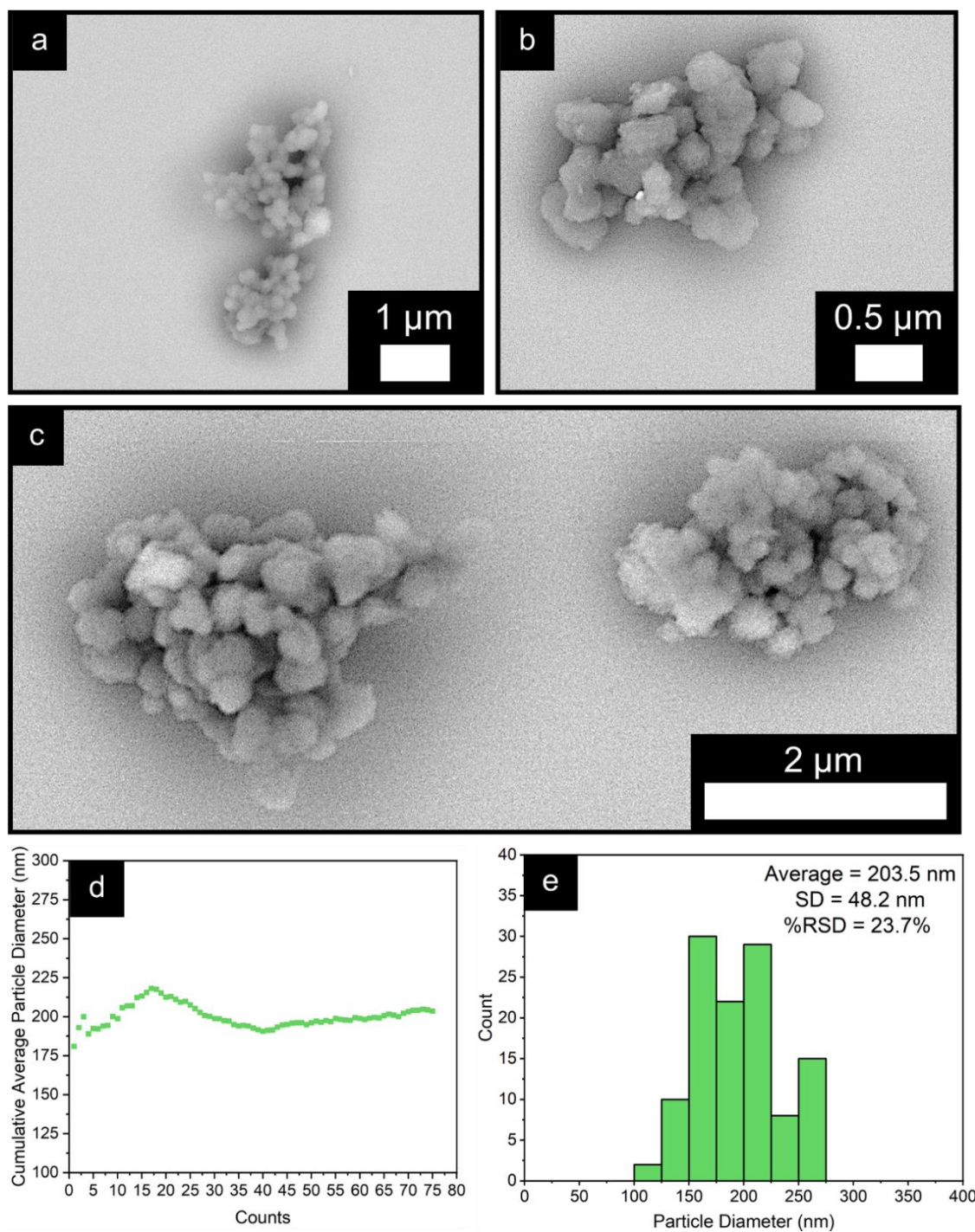


Figure 40: a-c) SEM image of MIL-100(Sc) particles. d) Histogram of average particle diameter (nm) for 75 particles. e) Cumulative average particle diameter (nm) of the 75 particles sized.

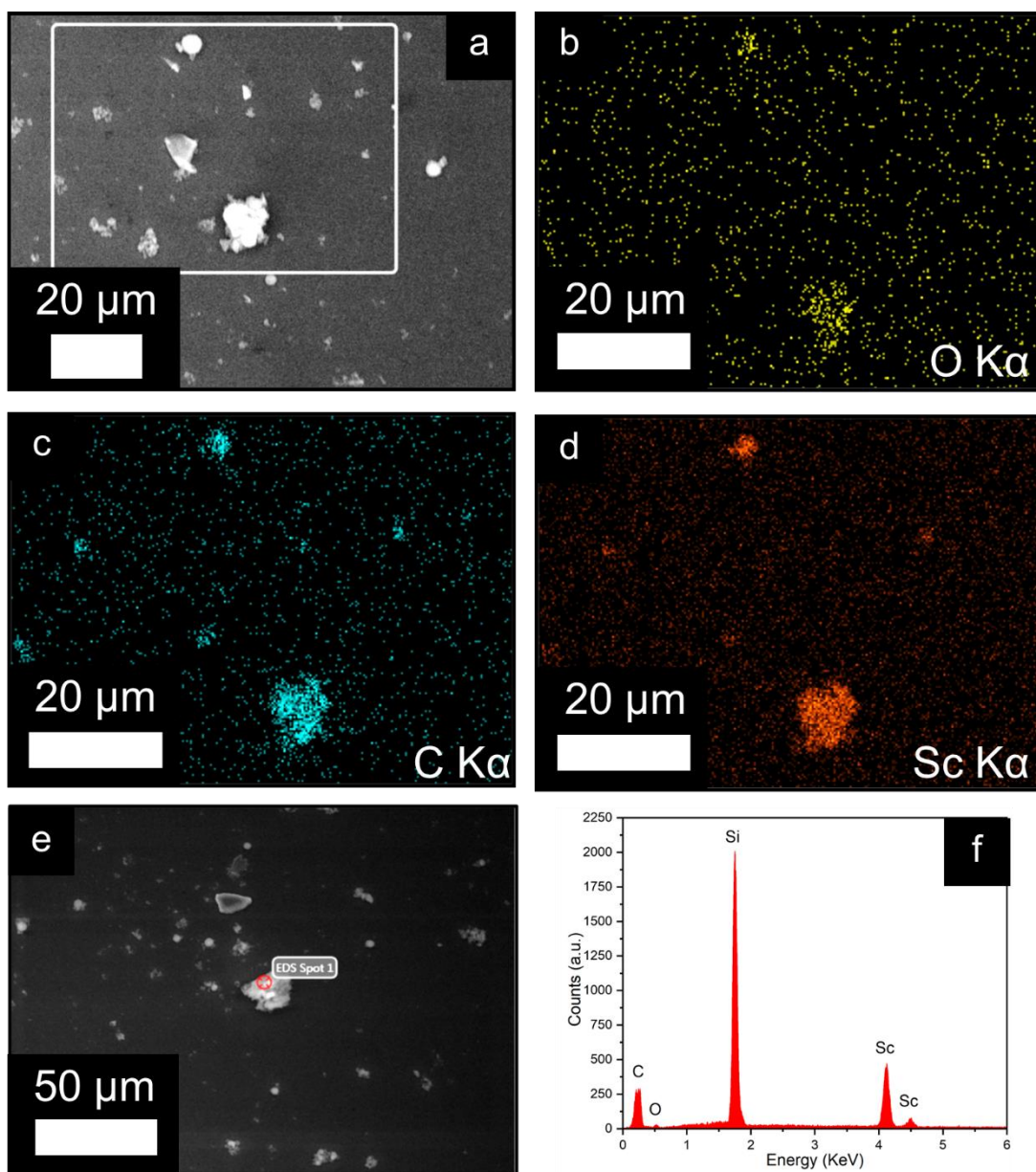


Figure 41: a) SEM image where EDX map was obtained. b-d) O K α , C K α and Sc K α EDX map, respectively. e) Spot where EDX spectrum was obtained and f) resultant EDX spectrum. Note that large Si K α peak arises from the silicon wafer the sample was dispersed on.

2.2.5.2 Particle size distribution

The particle size distribution of MIL-100(Sc) powder that may be present during a reaction was investigated using dynamic light scattering. A Mastersizer 3000 unit equipped with a Hydro MV automated wet dispersion unit provided live measurement of particle size distribution along with stirring and sonication of MIL-100(Sc) particles to disperse them in water (Figure 42). This analysis technique may better represent the size distribution of MIL-100(Sc) particles present during a chemical reaction, where particle aggregation is likely to occur,

when compared to sizing of individual particles in SEM images. Additionally, the number of particles analysed per unit time is much greater for this technique compared to sizing by SEM, meaning that the latter may not account for any sample heterogeneity that could be present.



Figure 42: Mastersizer 3000 unit (middle) equipped with a Hydro MV automated wet dispersion unit (right).

Table 8 shows D10, D50, D90 and D[3,2] values of solvothermally prepared MIL-100(Sc). D10, D50 and D90 values correspond to the hydrodynamic diameter below which 10%, 50% and 90% of the particles were smaller in size than respectively. For example, 10% of the particles had a smaller diameter than 200 ± 7 nm in this analysis. The D[3,2], or sauter mean diameter, may be used to quote the average particle size of a sample and is the diameter of a sphere that has the same volume:surface area ratio as the particle of interest.

Table 8: D10, D50, D90, span and D[3,2] values obtained for MIL-100(Sc) during light scattering analysis.

D10 (nm)	D50 (nm)	D90 (nm)	D[3,2] (nm)
200 ± 7	727 ± 20	3183 ± 180	466 ± 16

Whilst the D10 was similar in value (200 ± 7 nm) to the average particle diameter calculated manually by SEM (203.5 ± 48.2 nm), it is clear through observation of the D50 and D90 values that the majority of particles analysed (90%) were

greater in size with D90 values reaching a greater than 10-fold increase in size indicative of particle aggregation. This large variation in size values observed in this analysis may be representative of those present during a reaction where MIL-100(Sc) particle aggregation is also likely to be occurring due to opportunity for particles to minimise surface energy.

Whilst a greater understanding of particle size distribution can be obtained by this technique, it is also important to recognise the limitations to obtain reliable particle size values. In this analysis, size values are quoted as hydrodynamic diameter which may give an inaccurate description of particle size as it assumes that particles are spherical (which may be true for individual particles of MIL-100(Sc) but not aggregates) and may also change depending on the ionic strength of the solvent and surface structure of the material being sized. This analytical technique also favours larger particles due to the intensity of scattered light being proportional to the sixth power of particle diameter.²³³

$$d_H = \frac{kT}{3\pi\eta D} \quad \text{Eqn. 2}$$

Where d_H = hydrodynamic diameter

k = Boltzmann constant

T = temperature

η = solvent viscosity

D = diffusion coefficient

2.2.6 Estimating interior vs. exterior catalyst site ratio

With a range of characterisation data now obtained, we next sought to use this to calculate other important properties of this material with special relevance to catalysis. Although fundamentally different in nature, one important feature of both MOF and nanoparticle-based catalysis is the number of catalyst sites that are partaking in catalysis relative to the total number present – as high a number as possible is desirable for catalysis applications from an efficiency standpoint.

With increasing MOF particle size, the number of sites available for catalysis on the exterior relative to the interior decreases exponentially over a given size range. This relationship may have important implications, both positive and negative depending on the desired outcome, when designing MOF-based

catalysts for specific catalytic applications. Chemical species are able to more easily access sites located on the outside of particles relative to the those located internally due to internal diffusion limitations. Thus in smaller particles where more sites are located externally the catalytic activity may be higher. In contrast, the steric restrictions imposed by the interior of a MOF relative to the exterior where such restrictions are not present may also be exploited to dictate the selectivity of a given reaction thus making the use of larger particles preferable. In both cases, the ability to estimate the ratio of exterior to interior metal sites in a MOF catalyst can therefore be of great value when designing a catalytic system for a specific purpose.

In this work, the number of catalytically active scandium sites located on the exterior vs. interior of MIL-100(Sc) particles was estimated using experimental SEM, PXRD, TGA and N₂ adsorption data (summarised by Table 9). These analytical techniques are standard and widespread enabling approaches, similar to that carried out in this research, to be applied to other MOFs.

Table 9: Analytical technique and the corresponding information that may be derived when estimating the number of catalytically active scandium sites located on the exterior of the framework vs the interior.

Analytical Technique	Information derived
PXRD	Unit cell parameter(s)
TGA	Composition/stoichiometry
N ₂ adsorption	BET surface area
SEM	Particle size

2.2.6.1 At single particle size

For the first estimation of exterior vs. interior sites at a given particle size it was assumed that the particles were cubic and perfectly monodisperse cubes 204 nm in diameter - this was the average diameter value obtained by SEM sizing analysis.

MIL-100 MOFs are cubic meaning that unit cell parameter values are all equal ($a = b = c$) and all internal angles are 90°. MIL-100(Sc) has a unit cell parameter (a) of 74.52 Å,²⁰⁷ thus it was calculated that the volume of one unit cell is equal to 41379 Å³ or 413.79 nm³.

$$\text{Volume of one MIL – 100(Sc) unit cell} = abc \quad \text{Eqn. 3}$$

$$= (74.52 \text{ \AA})^3$$

$$= 41379 \text{ \AA}^3$$

$$= 413.79 \text{ nm}^3$$

As it was assumed that the particles were cubic rather than spherical, the diameter of a cubic particle was determined to be the length of one side (Figure 43).

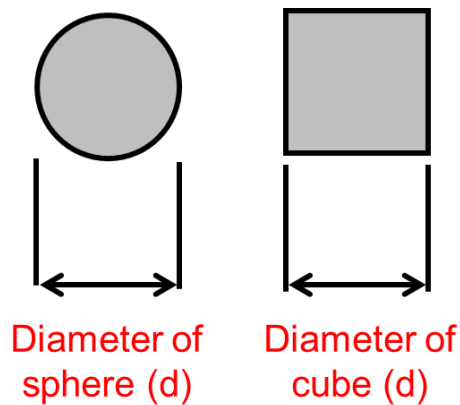


Figure 43: Diameter of a spherical particle (left) and diameter of a cubic particle (right).

Thus, in a perfectly cubic particle with a diameter (d) of 204 nm (as determined by SEM particle sizing) the volume is 8,489,664 nm³ and thus in a single MIL-100(Sc) particle of that size there are 20517 unit cells (as one unit cell is 413.79 nm³ in volume) (Figure 44).

$$\text{Vol. of one 204 nm diameter particle} = d^3 \quad \text{Eqn. 4}$$

$$= (204 \text{ nm})^3$$

$$= 8,489,664 \text{ nm}^3$$

$$\text{No. of unit cells in one 204 nm particle} = \frac{\text{Vol. of 204 nm particle}}{\text{Vol. of one unit cell}} \quad \text{Eqn. 5}$$

$$= \frac{8,489,664 \text{ nm}^3}{413.79 \text{ nm}^3} = 20517 \text{ unit cells}$$

In the crystal structure data of MIL-100(Fe)¹⁰⁵ it is reported that the unit cell of contains 816 metal units, thus in one unit cell of MIL-100(Sc) it was also assumed that there were 816 units of scandium. Given this, it was calculated that in 20517 unit cells (the number of unit cells in one 204 nm particle) there were 16,741,605 scandium atoms, or 2.78×10^{-17} moles of scandium.

Sc atoms per particle

$$= \text{Unit cells per particle} \times \text{Sc atoms per unit cell} \quad \text{Eqn. 6}$$

$$= 20517 \times 816$$

$$= 16,741,605 \text{ atoms}$$

$$= 2.78 \times 10^{-17} \text{ moles}$$

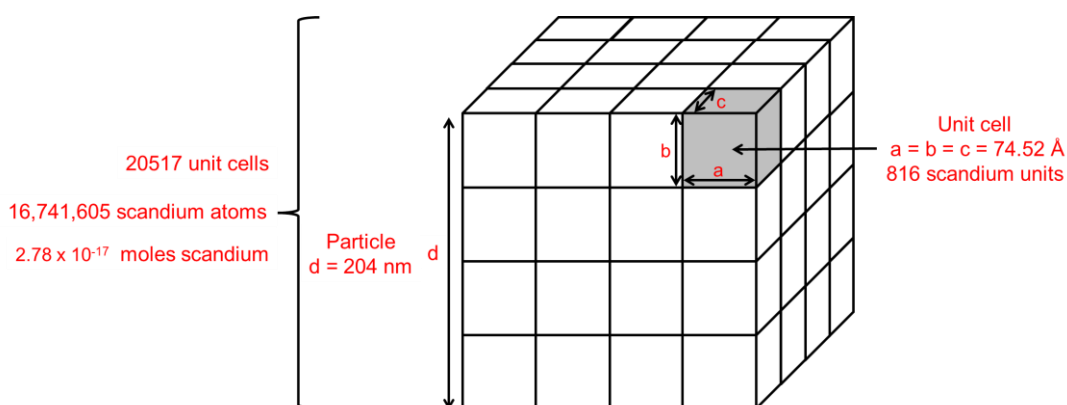


Figure 44: A hypothetical MIL-100(Sc) particle 204 nm in diameter consisting of cubic unit cells with 816 scandium units with a unit cell parameter of 74.52 Å. Such a particle was calculated to contain 20517 unit cells. Note: relative lengths in the illustration are not to scale.

For a hypothetical experiment, 100 mg of perfectly dry activated MIL-100(Sc) was used possessing a stoichiometry of $[\text{Sc}_3\text{O}(\text{BTC})_{1.23}(\text{OH})_{3.31}]$ (as determined by TGA in section 2.2.3 in this work). It was also determined from TGA analysis that the MIL-100(Sc) prepared in this work was 29.2% scandium by weight, thus 29.2 mg scandium was present in the hypothetical reaction (involving 100 mg as stated), or 6.50×10^{-4} moles. As 6.50×10^{-4} moles of scandium was used in the reaction and one particle (204 nm in diameter) contains 2.78×10^{-17} moles of scandium then 2.34×10^{13} particles were used in the reaction (Figure 45).

$$\text{No. of particles in reaction} = \frac{\text{Total moles of scandium}}{\text{moles of scandium per particle}} \quad \text{Eqn. 7}$$

$$2.34 \times 10^{13} = \frac{6.50 \times 10^{-4}}{2.78 \times 10^{-17}}$$

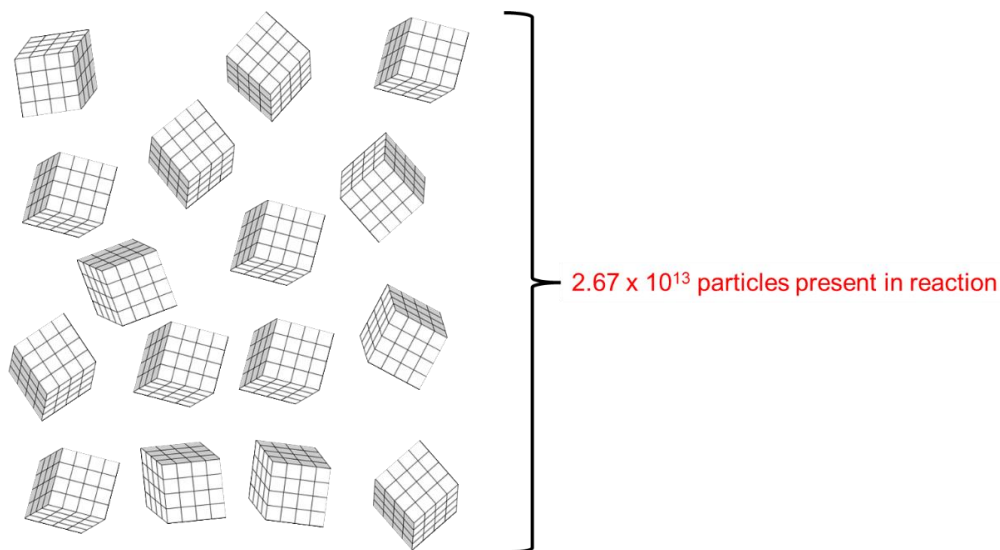


Figure 45: In a hypothetical reaction involving 100 mg of completely dry MIL-100(Sc) which was completely monodisperse, comprising 204 nm particles, it was calculated that 2.67×10^{13} particles were present.

The BET surface area accounts for the interior and exterior surface area of MIL-100(Sc) particles and was calculated to be 1524 m²/g. Thus in the reaction involving the use of 100 mg MIL-100(Sc) the total surface area of the reaction was 152.4 m². The number of particles in this reaction was calculated to be 2.67×10^{13} so the surface area per particle was 6.51×10^{-12} m².

$$\text{BET surface area per particle} = \frac{\text{Total surface area of reaction}}{\text{Number of particles}} \quad \text{Eqn. 8}$$

$$6.51 \times 10^{-12} \frac{\text{m}^2}{\text{particle}} = \frac{152.4 \text{ m}^2}{2.34 \times 10^{13} \text{ particles}}$$

To take into account just the exterior surface area of MIL-100(Sc) particles the surface area of a cube that was 204 nm in diameter was calculated – this was determined to be 2.50×10^{-13} m²

$$\begin{aligned} \text{Surface area of a cube} &= 6a^2 && \text{Eqn. 9} \\ &= 6(2.04 \times 10^{-7} \text{ m})^2 \\ &= 2.50 \times 10^{-13} \text{ m}^2 \end{aligned}$$

The fraction of surface area on the exterior of the MOF relative to the total surface area was calculated by working out the percentage of the exterior surface area per particle to the BET surface area per particle - this was calculated to be 4.37 %. It was also assumed that this was also equal to the amount of scandium atoms present on the exterior of the particle too.

$$\% SA \text{ exterior of MOF} = \frac{\text{Exterior SA per particle (m}^2\text{)}}{\text{BET SA per particle (m}^2\text{)}} \times 100 \quad \text{Eqn. 10}$$

$$\frac{2.50 \times 10^{-13} \text{ m}^2}{6.51 \times 10^{-12} \text{ m}^2} \times 100 = 4.37\%$$

By this approach, the amount of sites located on the outside of the framework relative to the inside depends on the particle size and shape (SEM), unit cell parameters (PXRD), metal composition percentage (TGA), number of sites per unit cell and the BET surface area (N₂ adsorption) - all of these variables inputted into the approach can be varied depending upon the MOF in question thus making this approach potentially applicable to other MOFs.

2.2.6.2 Particle size and % sites located on the exterior of the framework

Figure 46 shows the derived relationship between particle size and number of sites located on the exterior of the framework which was determined by applying this methodology at a range of different particle sizes (black squares). Below approximately 100 nm in diameter there is an increase in the % of sites located externally proportional to the cube of particle length, whilst above this size there is a steady decrease. Below a particle size of 9.222 nm the % of sites located on the exterior becomes greater than 100% and thus calculation breaks down as the surface area of the cube becomes larger than the BET surface area per particle. For particles greater than 100 nm, there is a small amount and steady decrease of particles on the exterior of the particle of about 5%.

The estimations generated by this approach only work for cubic particles of a specific diameter. In reality, as indicated by the light scattering data, the particle size shows that a wide distribution of sizes and also potential aggregation to produce particles which are not cubic and greater than 1 μm in size, where the % of sites located on the exterior is < 1%.

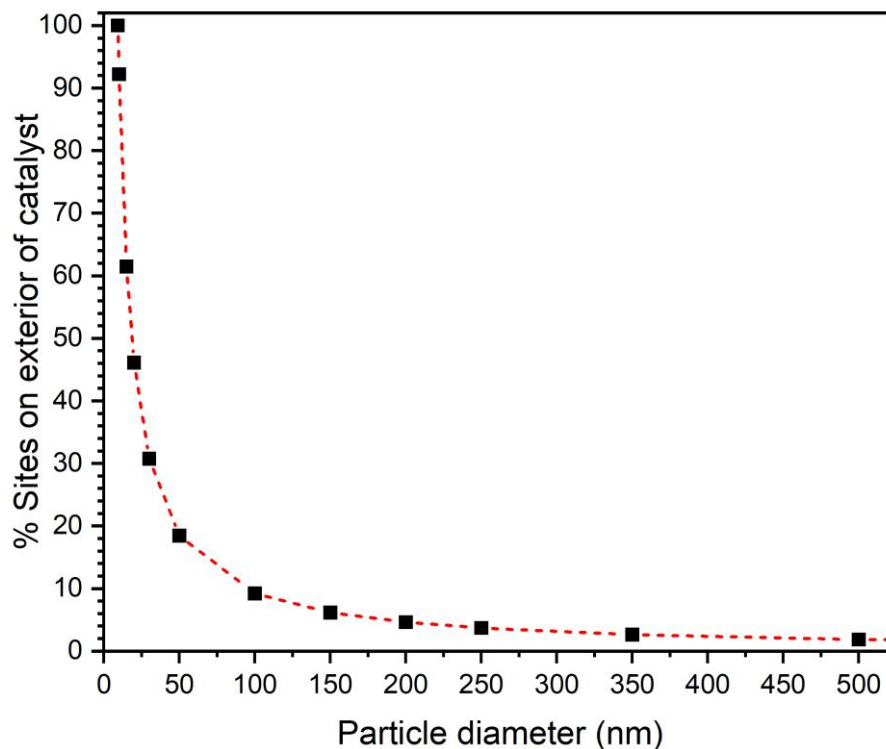


Figure 46: Relationship between % of sites located on the exterior of MIL-100(Sc) vs. particle diameter.

This approach, although not entirely translatable to a real catalytic system, provides a logical basis for estimating the number of sites on the exterior of the MOF using data obtainable from conventional analytical techniques - this paves the way for further development of this approach. In a broader literature context the concept of gauging the number of catalytic sites located on the exterior of catalytic materials is more widespread, particularly for metal nanoparticles, where large efforts have been conducted into determining the fraction of surface/bulk atoms of different shapes including cubes,^{234, 235} spheres,²³⁶ regular tetrahedron,²³⁵ regular octahedron, disk-shaped,²³⁵ cuboctahedron²³⁷ and truncated octahedron²³⁸. Although metal nanoparticles are fundamentally different catalytic materials to MOFs by nature, the approaches carried out to date offered additional complexity to this work as they consider different particle shapes such as spheres. This research could therefore be developed further by considering particle shapes other than cubes.

2.2.7 Probing surface structure by XPS

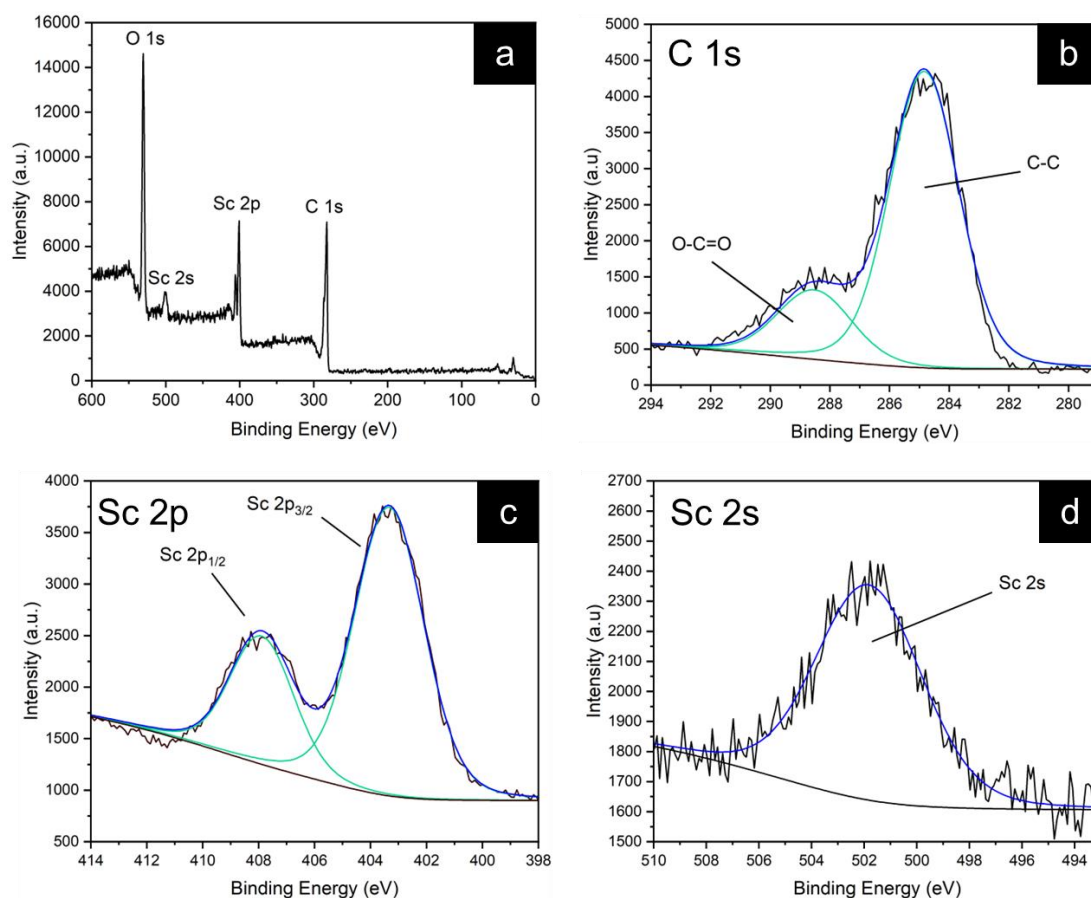


Figure 47: a) XPS spectra of MIL-100(Sc) showing O 1s, Sc 2s, Sc 2p and C 1s peaks respectively. b) C1s region of the spectrum which was deconvoluted to give three peaks at peaking at 284.8, 287.2 and 289.9 eV - these correspond to the C-C, C-O and C=O bonds respectively. c) Sc 2p region of the spectrum. d) Sc 2s region of the spectrum.

X-ray photoelectron spectroscopy (XPS) was carried out on MIL-100(Sc) to analyse the chemical composition and the oxidation state of scandium at the surface. Figure 47a shows a survey of the XPS spectrum with O 1s, Sc 2s, Sc 2p and C 1s peaks observed, corresponding to the constituent elements in MIL-100(Sc). Figure 47b-d shows the C 1s, Sc 2p and Sc 2s regions respectively. The C 1s region of the spectrum the range of 282 - 293 eV was deconvoluted into two peaks at 284.8 and 288.5 eV - these correspond to the C-C and O-C=O bonds present in the trimesic acid linker molecule, respectively.¹¹⁴ The Sc 2p region, in the range of approximately 398 - 412 eV was also deconvoluted into two peaks corresponding to the 2p_{3/2} and 2p_{1/2} at 403.4 and 407.9 eV respectively. The position of these two bands indicate that scandium was present

in a 3+ oxidation state, the reported oxidation state of scandium in MIL-100(Sc).¹¹⁹ The Sc 2s peak was present at 501.9 eV.²³⁹

2.3 Conclusion: Part A

In Part A of this chapter MIL-100(Sc), a Lewis acidic catalytically active metal-organic framework, was synthesised in one step according to literature-based procedures and thoroughly characterised using a range of analytical techniques (PXRD, TGA, N₂ adsorption, SEM-EDX, light scattering, IR spectroscopy and XPS). The characterisation of this material had a specific focus on properties that are relevant to catalysis (i.e. the actual stoichiometry of the MOF compared to the reported formula, the ratio of external to internal catalytic sites at given particle sizes) and this enhanced system understanding as a whole. Once ideal drying conditions for catalysis were identified, a more realistic approach to calculating the stoichiometry using TGA data was determined which will prove useful when trying to quantify the catalytic properties of the MOF (e.g. reagent accessibility) due to the enhanced understanding of the defects that are generated in the synthesis. Determining the scandium composition of the framework will also be used for the calculation of pertinent reaction metrics such as turnover frequency.

Also in Part A of this chapter, a logical approach that enables estimation of the number of exterior sites relative to interior sites in MIL-100(Sc) was proposed which is an important property for catalysis applications. This approach makes use of characterisation data obtainable from widely applied analytical techniques: PXRD, TGA, SEM and N₂ adsorption and may be applicable to other MOFs.

Part B

2.4 Catalytic activity studies into MIL-100(Sc)

The commercial viability which has been demonstrated for 'star MOF'¹⁰⁸ MIL-100(M) demonstrates the utilisation of this type of material as catalysts for organic transformations pertinent to fine chemical production. The basic mode of catalysis of MIL-100(M) MOFs is as a Lewis acid via the coordinatively unsaturated metal sites on the trimer nodes (M₃O) situated throughout the framework.¹¹² As discussed in more detail in section 1.2.1.1, the use of

MIL-100(M) MOFs for Lewis acid catalysed reactions has been reported for a number of organic transformations.^{105, 113-125}

The decision to pursue MIL-100(Sc) in this work as opposed to other MOFs was in large part due to the groundwork laid by Wright *et al.*^{119, 120} and Čejka *et al.*¹²³, the results of which were discussed in section 1.2.1.1. Their findings showed MIL-100(Sc) to be more catalytically active than both isostructural MOFs (i.e. MIL-100(M), M = Fe, Cr, Al, In), other highly-cited MOFs (i.e., MIL-101(Sc), MIL-101(Cr), HKUST-1(Cu), CPO-27(Ni), STA-12(Ni)) and catalytically active heterogeneous zeolite species (i.e. Sc³⁺-exchanged zeolite Beta) towards a range of Lewis acid catalysed reactions (i.e. intermolecular carbonyl-ene reactions of nucleophilic alkenes and aldehydes; Friedel–Crafts type Michael addition reactions between electron-rich heterocycles and electron-deficient alkenes; ketimine and aldimine formation; Prins condensation reaction).

Whilst the studies to date regarding the catalytic activity of MIL-100(Sc) as Lewis acid catalysts have demonstrated impressive results for a number of different reactions, studies into MIL-100(M) MOFs via the use of reaction optimisation tools such as design-of-experiments (DoE) or response surface methodology (RSM) (which are widely used in pharmaceutical development,⁵⁸⁻⁶¹ see section 1.1.3) are scarce.¹³⁴ This finding also appears to be mirrored in the wider MOF-catalysis literature where widespread use of these tools is not reported with most examples pertaining to the studies exploring biodiesel production^{134, 136-140} or photodegradation¹⁴¹⁻¹⁴⁶ – see section 1.2.2.2 for more discussion on the use of DoE/RSM to study MOF-catalysed reactions. Examples regarding the catalysis of organic transformations that are routinely exploited in the fine chemical industry are lacking. Studying MOF-catalysed reactions using these approaches offers a range of advantages (e.g. more efficient mapping of experimental space, identification of optimised reaction conditions, identification of interactions that exist between variables) which could offer essential cost savings with MOFs currently limited by their relatively expensive production on large scales.¹⁰⁹

It was also previously discussed (section 1.2.2.2) that for each DoE/RSM study conducted into MOF-based catalysts, similar variables were explored: temperature, time, catalyst loading and reagent molar ratio/concentration with no studies exploring responses other than conversion or yield (or degradation). In a chemical system, a range of other metrics can be explored such as the initial

reaction rate and TOF to provide insight into the nature of a reaction, guide conditions selection and enhance system understanding. Such metrics have not been explored in a DoE/RSM study for a MOF-catalyst to date. Developing a deeper understanding of these reaction metrics and how they may be related to each other could help guide reaction conditions to give both time and catalytically efficient (and thus more cost effective) reactions. Previous studies did not investigate more than one response at a time thus the opportunity to study the relationship between responses, including potential trade-offs, was missed. Beyond optimising processes, the data generated in a DoE can be used to obtain mechanistic information through the generation of kinetic models via model-based design-of-experiments (see section 1.1.3.2). In this research, identifying the optimum conditions for the MIL-100(Sc)-catalysed intramolecular cyclisation of citronellal lays the groundwork for obtaining a firm understanding of MIL-100(Sc) as a catalyst prior to the fabrication of novel MIL-100(Sc)@PBSAC composites in later chapters (see Chapter 4).

Through analysis of the current state of the art, shortcomings of this portion of the MOF-catalysis literature are evident and thus this research sought to fill this research gap. In this research, the catalytic activity of MIL-100(Sc) for a model reaction, the intramolecular cyclisation of citronellal, was studied using a DoE. For each experiment in the DoE, kinetic data were collected along with a range of pertinent reaction metrics that have not previously been studied for MOF-based catalyst systems: initial reaction rate, TOF and selectivity.

2.4.1 The intramolecular cyclisation of citronellal

One reaction that MIL-100(Sc) has not previously been used to catalyse is the intramolecular cyclisation of citronellal. This reaction, when carried out using enantiomerically pure citronellal, constitutes an important step in the Takasago process for the synthetic production of (-)-menthol, one of the most consumed flavour compounds worldwide with an estimated 30,000 metric tonnes of menthol consumed annually.^{77, 240, 241} Due to the industrial significance of this reaction, it is frequently used to quantify and compare the Lewis acidic catalytic activity of novel catalysts, both homogeneous and heterogeneous,²⁴² with the use of the more economical racemic equivalent, (±)-citronellal, often preferred.

In this reaction, (\pm)-citronellal undergoes an intramolecular carbonyl-ene reaction resulting in the formation of one of four isomers of isopulegol (Figure 48); industrially the formation of (-)-isopulegol is the most desirable as this species is further hydrogenated to produce the (-)-menthol isomer responsible for the characteristic mint flavour.²⁴¹ For the cyclisation step, Takasago reports the use of a homogeneous tris(2,6-diarylphenoxy)aluminum (ATPH) catalyst offering a benchmark diastereoselectivity of > 99%.^{243, 244} When studying this reaction using a novel Lewis acid catalyst important metrics include the rate of the reaction as well as the selectivity towards the formation of (\pm)-isopulegols and diastereoselectivity towards (\pm)-isopulegol formation.

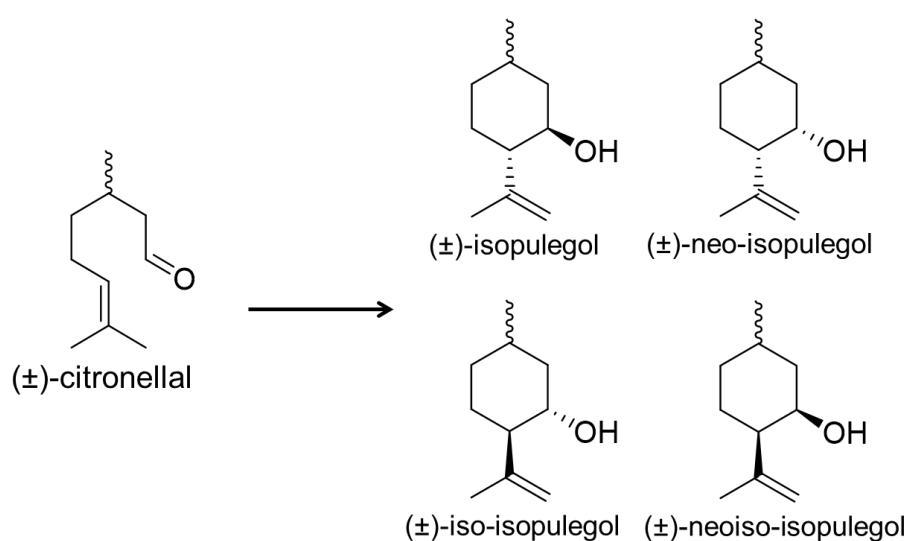


Figure 48: Intramolecular cyclisation of citronellal catalysed by Lewis acids forms four isopulegol isomers.

More specifically to MOFs, the activity of $\text{Cu}_3(\text{BTC})_2$,^{245, 246} UiO-66 ,²⁴⁷⁻²⁵² MOF-808 ²⁵³ and $\text{MIL-100}(\text{Fe})$,¹¹⁸ $\text{MIL-101}(\text{Cr})$,²⁵⁴ bimetallic $\text{Zr}(\text{Ti})\text{-NDC}$ ²⁵⁵, Ni-BDC ²⁵⁶ and PdBF_4 ,²⁵⁷ and have previously been studied. Table 10 shows a comparison of these different MOFs including $\text{MIL-100}(\text{Sc})$ studied in this work as well as some other popular examples involving heterogeneous and benchmark homogeneous catalysts.

Table 10: Comparison of catalytic activity of MIL-100(Sc) in this work towards intramolecular cyclisation of citronellal compared to other MOFs and other popular examples of heterogeneous and homogeneous (where stated) catalysts taken from the literature.

Catalyst	Cat. activity (mmol g _{cat} ⁻¹ hr ⁻¹) ^a	Reaction time (hours)	Selectivity to isopulegols (%)	Selectivity to isopulegol (%)	Ref
MIL-100(Sc) (this work) ^b	66.0	0.3	>97	48 - 58	-
Cu ₃ (BTC) ₂	0.6	≈ 80	100	65 - 69	245
Cu ₃ (BTC) ₂	-	-	-	66 - 73	246
UiO-66 ^c	4.9	6 - 24	-	70 - 82	247
UiO-66 ^d	2.1	10	-	75 - 77	248
UiO-66 ^e	0.4 - 1.3	20	-	75 - 86	249
UiO-66	8.8 - 9.6	6	-	70 - 75	251
UiO-66	-	20	-	-	252
MOF-808 ^f	83.1	1.5 - 8	-	55 - 85	253
MIL-100(Fe) ^g	0.2	24	-	62 - 73	118
Pd@MIL-101(Cr)	0.9	12	99	73	254
MIL-101(Cr)	0.6	18	99	74	254
Zr(Ti)-NDC ^h	0.6	24	98 - 99	60 - 76	255
Ni-BDC ⁱ	-	1 - 2	-	-	256
PdBF ₄ ^j	12.2	3	96	67	257
Sn-Beta	341.2	1	> 99	85	258
H-Beta	-	8	> 99	75	259
Zr-TUD-1 ^k	-	0.5 - 1	99.6	62 - 69	260
ZrO ₂	-	1	0 - 99	68 - 72	261
SiO ₂ ^l	-	1 - 48	24 - 83	61 - 80	262
Al ₂ O ₃ ^l	-	0.1 - 16	45 - 95	61 - 68	262
Sc(OTf) ₃ (homogeneous)	-	1	> 95	94	203
ATPH ^m (homogeneous)	-	1 - 4	96	> 99	244

^a Catalytic activity. mmol of citronellal converted per gram of catalyst per hour. Data in this column of the table was taken from Wade *et al.*²⁵⁷ ^b Best results obtained in this work in the DoE. See Table 13 for summary of these results. ^c Using functionalised terephthalic acid (BDC) linkers: BDC-X; X=H, NH₂, CH₃, OCH₃, F, Cl, Br, NO₂. ^d Synthesis modulated using differing equivalents of trifluoroacetic acid and hydrochloric acid. ^e Comparison of catalytic activity for hydrated and dehydrated UiO-66. ^f A range of species were made by treatment

with sulfuric acid. ^g Study into post-synthetic acid treatment of MIL-100(Fe) on catalytic performance. ^h NDC = 2,6-naphthalendicarboxylate. Monometallic (just Zr) and bimetallic (Zr and Ti) were prepared and the catalytic activity compared. ⁱ Bulk and nanosheets of Ni-BDC were prepared and the catalytic activity compared. ^j Pd pincer complex incorporated into benzotriazolate. ^k Zirconium incorporated into a 3-D mesoporous silicate. ^l Various acids (i.e. H₃PO₄, CH₃SO₃H, HCl and (COCl)₂) were adsorbed onto silica and alumina and the catalytic activity studied. ^m Homogeneous tris(2,6-diarylphenoxy)aluminum catalyst.

In this research, it was found that under appropriate conditions MIL-100(Sc) was able to catalyse this reaction to completion after 0.3 hours with a high selectivity towards isopulegols (> 97%) (see Table 13 for full results). The high selectivity towards isopulegols formation was common amongst many the other MOF catalysts (> 96%) (where reported) too.

Across the studies employing a MOF to catalyse the intramolecular cyclisation of citronellal, the conversions and length scales of reactions varied enormously from less than 1 hour (such as in this work) to greater than 80 hours highlighting the breadth of activity of these species and the conditions employed to catalyse this reaction. The observed variation in reaction times is further understood by comparison of the catalytic activity in terms of the amount of citronellal converted per gram of catalyst per hour of reaction (Table 10, column 2), the data of which was adapted from Wade *et al.*²⁵⁷ Based on this metric, the data from the DoE in this work shows that MIL-100(Sc) is the second most active MOF to catalyse this reaction to date. Consideration should be given to the range of different reaction solvents (i.e. toluene, acetone, cyclohexane) and temperatures (i.e. 50 °C - 110 °C) employed, however, which could have drastically influenced the catalytic activity. These differences complicate direct comparison of the catalysts.

The selectivity towards isopulegol formation varied from 48 - 58% in this research which was on the lower side of the reported selectivity values found for MOFs within the literature (55 - 86%). Despite this, for a number of the studies reported, modification was carried out on the MOF, i.e. via the use of isorecticular synthesis²⁴⁷ and acid treatment^{118, 248, 253}, which in turn altered the properties of the framework and improved the selectivity. In this research, further modification of MIL-100(Sc) was not carried out, thus one approach to improve the selectivity further in future may be to modify the MOF. More pertinent to MIL-100(M) MOFs,

De Vos *et al.*²⁴⁸ improved the diastereoselectivity of MIL-100(Fe) from $\approx 62\%$ to $\approx 73\%$ using a post-synthetic treatment with acids (trifluoroacetic acid or perchloric acid) which created Brønsted acid sites. De Vos *et al.*²⁴⁸ suggested that the observed increase in selectivity was potentially due to a dual-site mechanism involving both Brønsted acid and Lewis acid sites. The ability to potentially tune the selectivity of MOF-based reactions by modifying the framework with simple treatments poses one exciting area for further development in the literature.

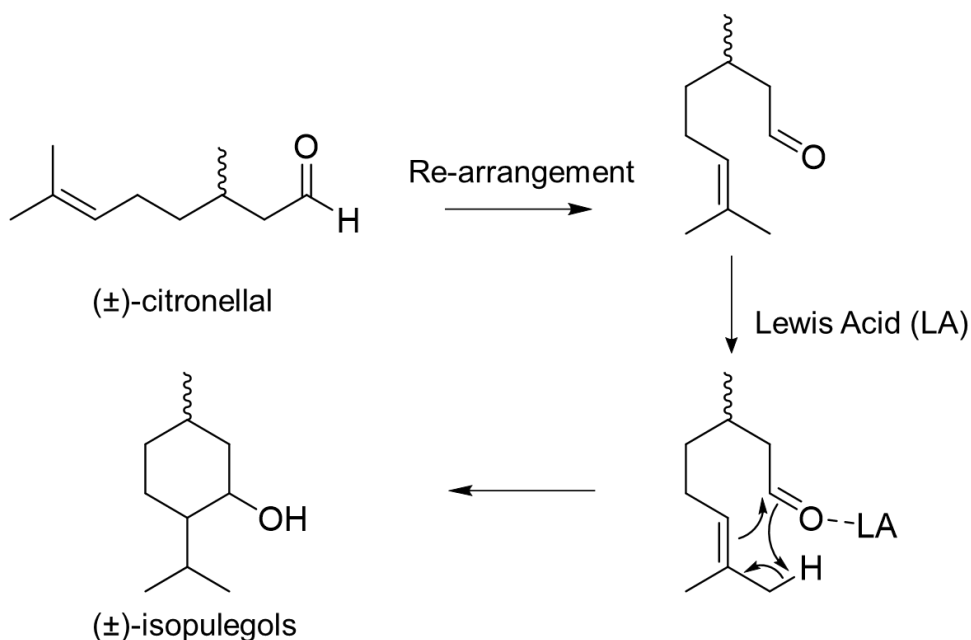
Further, useful insight into why the diastereoselectivity differs between species for this reaction is given by the study conducted by Speybroeck *et al.*²⁴⁶ who theoretically and experimentally studied activity and selectivity of different species (homogeneous catalysts ZnBr_2 and ATPH and MOF Cu_3BTC_2) and found that the diastereoselectivity is dependent upon the free-energy differences between the diastereomeric transition states found in the different catalytic species, thus also suggesting that this result is linked to the intrinsic properties of the catalyst. Overall, homogeneous species $\text{Sc}(\text{OTf})_3$ and ATPH offer the highest selectivity values towards isopulegol at 94% and $> 99\%$ respectively, greater than any MOF previously used to catalyse this reaction and other popular heterogeneous catalysts.

2.4.1.1 Molecular modelling

An important aspect of MOF-based catalysis is whether reactants and products present are able to access and leave the pores of the MOF where, based on work conducted in sections 2.2.5 and section 2.2.6 in relation to MIL-100(Sc) particle size and distribution, a majority of the catalytically active sites are located during a reaction. Due to this, the sizes of citronellal and isopulegols were calculated and compared with the size of the windows and cages in MIL-100(M) MOFs to greater understand whether these molecules are able to leave or enter the pores over the course of a reaction (Figure 49). This is an important consideration for obtaining high catalytic activities as it has already been discussed that larger substrates resulted in lower activities due to an inability to access the pores (see section 1.2.1.1).

The proposed mechanism of the reaction involves coordination of linear citronellal which then adjusts its shape to enable nucleophilic attack of the alkene

bond to the carbonyl group with a hydrogen atom also transferred from the methyl group to generate the alcohol group (Scheme 3).²⁴⁶



Scheme 3: Proposed mechanism of citronellal cyclisation involving re-arrangement, Lewis acid catalyst coordination and cyclisation of citronellal in a concerted fashion to produce isopulegol.

A perfectly stoichiometric MIL-100(M) MOFs (i.e. with a formula of $[M_3O(BTC)_2X]$), possess two cages: a smaller cage, 25 Å in diameter, built from rings of five supertetrahedra with windows approximately 6 Å in diameter and a large cage, 29 Å in diameter, built from rings of five and six supertetrahedra, the latter resulting in larger-sized windows approximately 9 Å in diameter (Figure 49).

Upon assessment of the size of citronellal and isopulegol molecules (carried out by measuring the distance between the atoms at the longest and widest parts of citronellal and isopulegol molecules plus the van der Waals radius of the atoms, see section 6.2.4) and the window sizes of stoichiometric MIL-100(M) (i.e. a stoichiometry of $[M_3O(BTC)_2X]$), both citronellal, in its linear conformation with a critical diameter of 6.4 Å due to the two methyl groups present, and isopulegol molecules may be unable to enter the smaller windows, ≈ 6 Å in diameter, present in both the small and large cages but should be able to enter and leave the larger windows, ≈ 8.6 Å in diameter. Thus, when considering the feasibility of this reaction inside the pores of MIL-100(Sc), there should be enough space for a citronellal molecule in a linear conformation to enter and then to adjust its shape for isopulegol formation before exiting the pores.

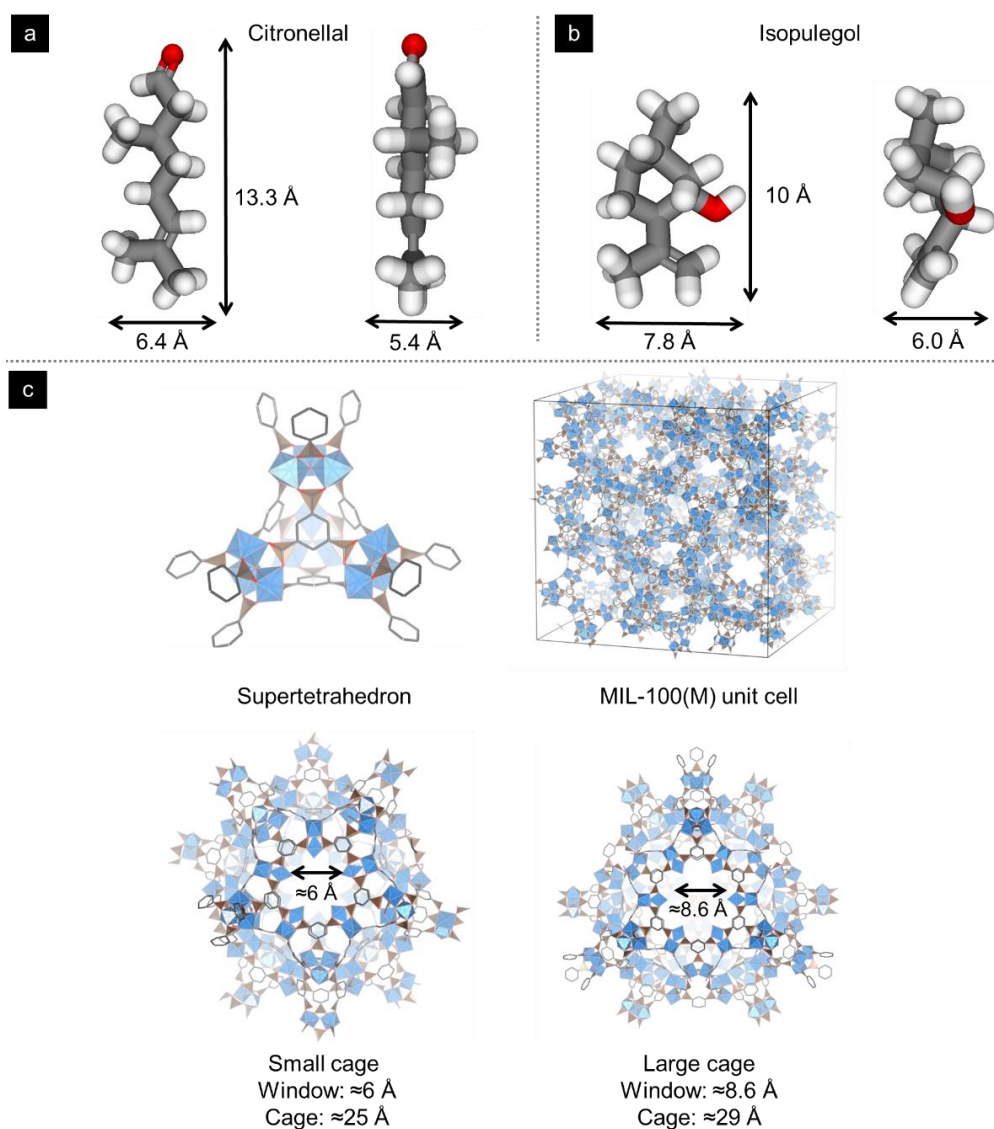


Figure 49: a) Citronellal molecule and related dimensions. b) Isopulegol molecule and related dimensions. c) Anticlockwise: Supertetrahedron unit of MIL-100(M), small cage, large cage and unit cell of MIL-100(M). Structures of MIL-100(M) are based on a defect-free structure with a stoichiometry of $[M_3O(BTC)_2X]$.

One important consideration that should be given to assessment of whether species are able to enter/leave the pores of MIL-100(M) is the presence of defects. Figure 49c shows a unit cell of MIL-100(M) of perfect stoichiometry, $[Sc_3O(BTC)_2X]$ (where X = singly charged anion), but TGA analysis of the MIL-100(Sc) prepared in this work (section 2.2.3) which possessed a formula of $[Sc_3O(BTC)_{1.23}(OH)_{3.4}]$ was more indicative of a defective structure with 0.77 missing linkers per node. The presence of defects throughout the structure of MIL-100(Sc) structure may enable greater reagent accessibility. It is also possible that missing clusters are situated throughout the framework which may also

enable greater reagent access. Based on this analysis it is plausible to assume that both citronellal and isopulegol can access the catalytic sites located on the interior of the MIL-100(Sc) framework.

2.4.2 Design-of-experiments (DoE)

The experimental space of the MIL-100(Sc) catalysed intramolecular cyclisation of (\pm)-citronellal was explored by carrying out a design-of-experiments (DoE). A 2-level 3-factor full factorial design (FFD) consisting of 11 experiments (8 corner point experiments and 3 centre point replicates) was chosen (see section 1.1.3.1 for more discussion of these designs) (Figure 50).

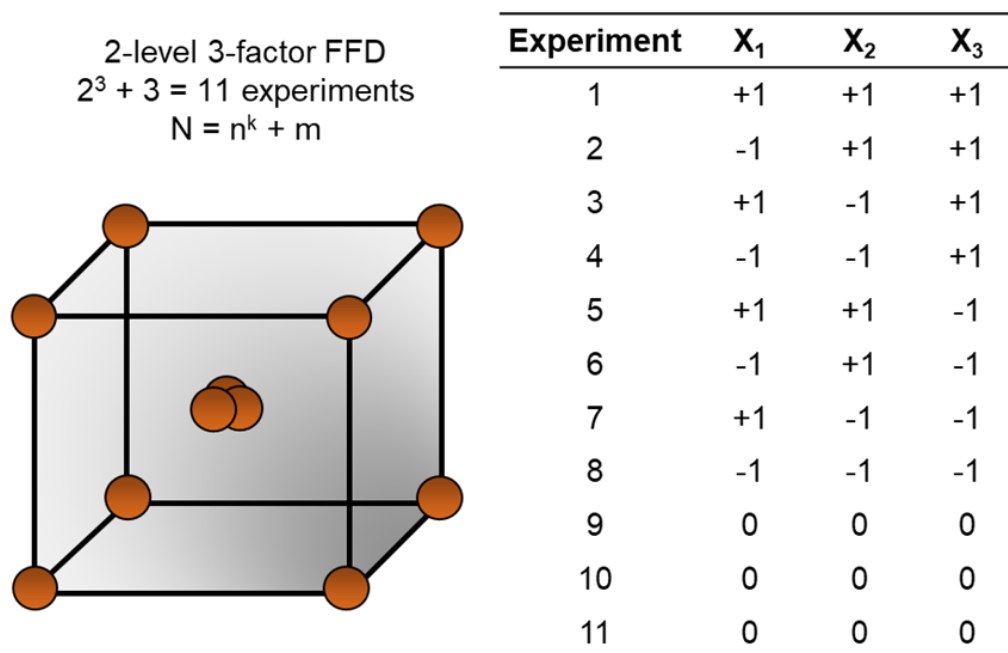


Figure 50: 2-level 3-factor FFD DoE carried out in this work consisting of 11 experiments: 8 corner-point experiments and 3 replicate experiments in the centre. Repeat of Figure 7.

The three variables and respective levels that were studied in the 2-level 3-factor FFD DoE for the MIL-100(Sc) catalysed intramolecular cyclisation of citronellal were reaction temperature (70 - 110 °C), citronellal concentration (0.1 - 0.74 M) and the citronellal:scandium molar ratio (2.4 - 14.0) (i.e. catalyst loading, see appendix 2.8.1.1 for precise catalyst loading masses). Consideration of variables such as these are all important in pharmaceutical development and were also similar to those employed for DoEs involving the use of a MOF previously (Table 10). The variable ranges studied offered practical

experimentation at the scale employed and responses studied (i.e initial rate/TOF) were assumed to vary significantly with them.

All of the reactions in the DoE were carried out in toluene owing to the popularity of this solvent when studying the catalytic activity of MOFs for this reaction previously.^{245, 247, 248, 253, 255, 257} It has also previously been observed that coordinating solvents (i.e. acetonitrile and methanol) competed effectively with reactant molecules for coordination to the Sc³⁺ sites of MIL-100(Sc) thus resulting in lower catalytic activity when compared to less polar solvents (i.e. dichloromethane and toluene), thus we elected to employ toluene as the reaction solvent.¹¹⁹ Table 12 shows the list of 11 experiments that were carried out for the DoE in the 2-level 3-factor FFD design.

Table 11: Set of variables and conditions studied in the DoE in toluene.

Reaction Temperature (°C)	Citronellal Concentration (M)	Citronellal:scandium molar ratio
70 - 110	0.1 - 0.74	2.4 – 14.0

Table 12: The list of 11 experiments conducted in the 2-level 3-factor FFD DoE in this work. Note: despite being systematically tabulated, the experiments were carried out in a random order outputted by the DoE software.

Experiment	Reaction Temperature (°C)	Citronellal Concentration (M)	Citronellal:Sc molar ratio
1	110	0.67	12.5
2	110	0.10	2.4
3	110	0.11	13.4
4	110	0.74	2.8
5	90	0.44	8.3
6	90	0.44	8.3
7	90	0.45	8.4
8	70	0.74	14.0
9	70	0.11	2.5
10	70	0.11	13.5
11	70	0.74	2.8

Due to the shortage of data in the literature involving the study of a MOF-based catalyst via a DoE, the main aim of the DoE was to more comprehensively study the behavior of the system by studying the effect of variables on a range of different reaction outputs, including intrinsic metrics that provide greater understanding into the nature of the system such as TOF and initial rate, rather

than just one metric such as conversion/yield which are dependent upon when the sampling was conducted. If required then conversion/yield values could be acquired for each sampling timepoint conducted. With the data inputted into the DoE, optimal conditions could be identified for each individual response studied (e.g. initial rate, TOF) and trade-offs that existed between these responses could be identified with sets of optimal conditions (i.e. a Pareto front).

With the timepoints that were taken over the course of each reaction, concentration profiles of citronellal consumption and the four isopulegol isomers that were formed were obtained. This, in turn, enabled the calculation of a range of important reaction metrics: conversion (Eqn. 11), selectivity towards (±)-isopulegols (Eqn. 12), selectivity towards (±)-isopulegol over other (±)-isopulegol isomers (diastereoselectivity) (Eqn. 14), initial rate (Eqn. 15) and turnover frequency (TOF) (Eqn. 15) and how these metrics changed over the course of a reaction.

$$\text{Conversion}(\%) = \frac{[(\pm) - \text{Citronellal}]_0 - [(\pm) - \text{Citronellal}]_t}{[(\pm) - \text{Citronellal}]_0} \times 100 \quad \text{Eqn. 11}$$

$$[(\pm) - \text{Citronellal}]_0 = (\pm) - \text{Citronellal concentration at } t = 0 \text{ (M)}$$

$$[(\pm) - \text{Citronellal}]_t = (\pm) - \text{Citronellal concentration at given time } t \text{ (M)}$$

$$\begin{aligned} \text{Selectivity to } (\pm) - \text{isopulegols } (\%) & \quad \text{Eqn. 12} \\ & = \frac{[(\pm) - \text{Isopulegols}]_t}{[(\pm) - \text{Citronellal}]_0 - [(\pm) - \text{Citronellal}]_t} \times 100 \end{aligned}$$

$$[(\pm) - \text{Isopulegols}]_t = (\pm) - \text{Isopulegols concentration at a given time } t \text{ (M)}$$

$$[(\pm) - \text{Citronellal}]_0 = (\pm) - \text{Citronellal concentration at } t = 0 \text{ (M)}$$

$$[(\pm) - \text{Citronellal}]_t = (\pm) - \text{Citronellal concentration at given time } t \text{ (M)}$$

$$\text{Selectivity to isopulegol } (\%) = \frac{[(\pm) - \text{Isopulegol}]_t}{[(\pm) - \text{Isopulegols}]_t} \times 100 \quad \text{Eqn. 13}$$

$[(\pm) - \text{Isopulegol}]_t = (\pm) - \text{Isopulegol concentration at a given time } t \text{ (M)}$

$[(\pm) - \text{Isopulegol}]_t = (\pm) - \text{Isopulegols concentration at a given time } t \text{ (M)}$

$$\text{Initial rate (M min}^{-1}\text{)} = \frac{\Delta [(\pm) - \text{Citronellal}]_t \text{ (M)}}{\Delta \text{ time (mins)}} \quad \text{Eqn. 14}$$

$\Delta [(\pm) - \text{Citronellal}]_t$

$= (\pm) - \text{Citronellal conc change between given time } t \text{ (M)}$

$\Delta \text{ time} = \text{Time difference between two values (mins)}$

$$\text{TOF (min}^{-1}\text{)} = \frac{\text{moles of } (\pm) - \text{Citronellal consumed}}{\text{moles of catalyst} \times \text{time (hrs)}} \quad \text{Eqn. 15}$$

For calculations of TOF, the moles of catalyst was approximated to be equivalent to the moles of scandium present, i.e, it was assumed that all of the scandium present participated in the catalysis. This was determined from TGA data of the activated MIL-100(Sc) (150 °C for 90 mins), where scandium constituted 27% of the weight (section 2.2.3). This is a crude estimation as the reported stoichiometry of MIL-100(Sc) dictates that per node only two of the three scandium sites are coordinatively unsaturated whereas other studies have found that activated isostructural MOF MIL-100(Al) only possessed one coordinatively unsaturated site per node.²²¹ We chose to ignore the presence of coordinatively saturated (and thus unavailable for catalysis) scandium sites for TOF calculations in favour of considering the system as a whole. This approach was adopted because we were unable to distinguish between the fraction of sites that were active within the framework. The TOF values calculated were therefore conservative estimates meaning that MIL-100(Sc) may be more active than the values calculated. Determination of intrinsic TOF values considering only the fraction of sites that were active are therefore one potential avenue for further exploration in this research. The TOF values quoted in this work were still useful benchmarks for which to quantify the performance of MIL-100(Sc) as all of the scandium was designed to be catalytically active.

Figure 51 shows the concentration profiles of (\pm)-citronellal and (\pm)-isopulegols (left) and conversion and selectivities (right) over the course of a typical reaction in the DoE. The selectivity towards (\pm)-isopulegols and (\pm)-isopulegol tended to remain constant over the course of the reaction, suggesting that no further reaction was occurring to any individual isomer preferentially. Experimental data for the rest of the experiments in the DoE can be found in the appendices (2.8.1.2).

Experiment 2: 110 °C, [Citronellal] = 0.10 M, Citronellal:Sc ratio: 2.4

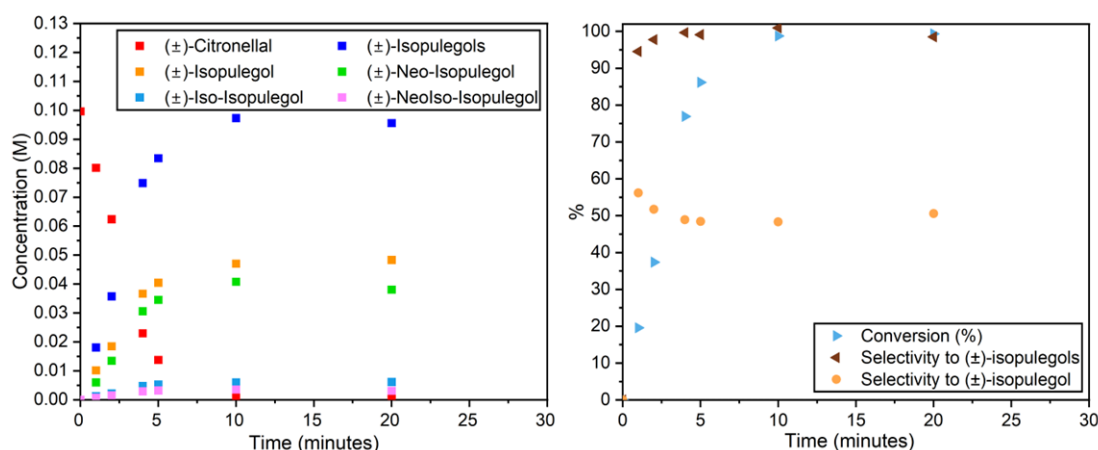


Figure 51: Concentration profiles of (\pm)-citronellal and (\pm)-isopulegol isomers (left), conversion, selectivity to (\pm)-isopulegols and (\pm)-isopulegol (right).

Through inspection of the concentration profiles for each experiment in the DoE (and thus also the initial rate values), it was clear that the experimental conditions studied covered a wide range of experimental space from the perspective of reaction length. The fastest experiment (2) was complete after approximately 20 minutes versus the slowest (10) which was still incomplete after 17 days. The importance of catalyst loading when selecting conditions that complete the reaction within a reasonable timeframe should also be highlighted. Experiment 2, which was identical to experiment 3 apart from the 5-fold difference in catalyst loading, was complete after just 20 minutes versus 7 days.

For each experiment in the DoE, the reaction metrics that were calculated are summarised by Table 13. The initial reaction rate and TOF values are quoted after five minutes of reaction (or ten minutes for reaction 10, the slowest reaction, which was the length of time required for reliable detection of products) whilst the selectivity towards (\pm)-isopulegols and (\pm)-isopulegol are reported as an average value for each reaction once a stable formation was observed.

Table 13: Initial rate of reaction, selectivity towards (±)-isopulegols and the selectivity towards the formation of (±)-isopulegol for each experiment in the DoE.

Exp. No.	Initial rate (M min ⁻¹) ^a	TOF (hr ⁻¹) ^a	Selectivity towards (±)-isopulegols (%) ^c	Selectivity towards (±)-isopulegol (diastereoselectivity) (%) ^c
1	0.0357	41.9	96	48
2	0.0172	25.0	97	51
3	0.00203	14.8	68	54
4	0.0592	13.4	84	53
5	0.00751	8.5	94	47
6	0.00460	5.2	97	50
7	0.00374	4.2	89	52
8	0.00570	6.5	91	52
9	0.00109	1.6	92	53
10	0.000174	1.3	84	58
11	0.0144	3.3	47	59

^a Initial rate and TOF are quoted as the maximum values that were obtained for each reaction. ^c Selectivity values are quoted as average values once a stable value was reached for each experiment.

2.4.2.1 DoE model analysis and fitting

Values for the initial rate, TOF, selectivity towards (±)-isopulegols and diastereoselectivity that were derived from the experimental data for each of the 11 experiments was inputted into the DoE software (Umetrics MODDE version 13). Thereafter, the model was fitted leading to the generation of saturated models which includes all model terms.

The two main metrics used to assess the quality of fit of DoE models are R² and Q² values. The R² value is a percentage measure (between 0 and 1) of how well the model fits the data with a value of ≤ 0.5 representative of a model with low significance. The Q² value is an estimation of future prediction precision. The value of Q² should be > 0.1 for a significant model and > 0.5 for a good model. Again, the closer the value is to 1 the better the model. For a good model, the difference in R² and Q² values should be < 0.3.⁶⁶

When the model for a given response is first fitted leading to the generation of a saturated model, the Q² value that is observed may be low due to the presence of non-significant terms, thus these terms can be removed from the model to improve this value which also improves the future prediction precision of the model.^{63, 66}

When values are inputted into the DoE software the model can be fit leading to an assessment of model quality using the R^2 and Q^2 metrics. Subsequent model refinement leading to improved R^2 and Q^2 values is then carried out by improving the shape of response distributions and removing non-significant terms.^{63, 66}

Upon fitting a model in MODDE, two other metrics are present which are model validity and reproducibility. When the value of model validity is < 0.25 then this indicates statistically significant model problems (e.g. outliers, incorrect model, transformation problem). The reproducibility metric gives insight into the variation of the centre-point experiments all of which were carried out at identical conditions. Again, for these metrics the closer their value to unity the better the model.^{63, 66}

2.4.2.2 Initial rate: model analysis and validation

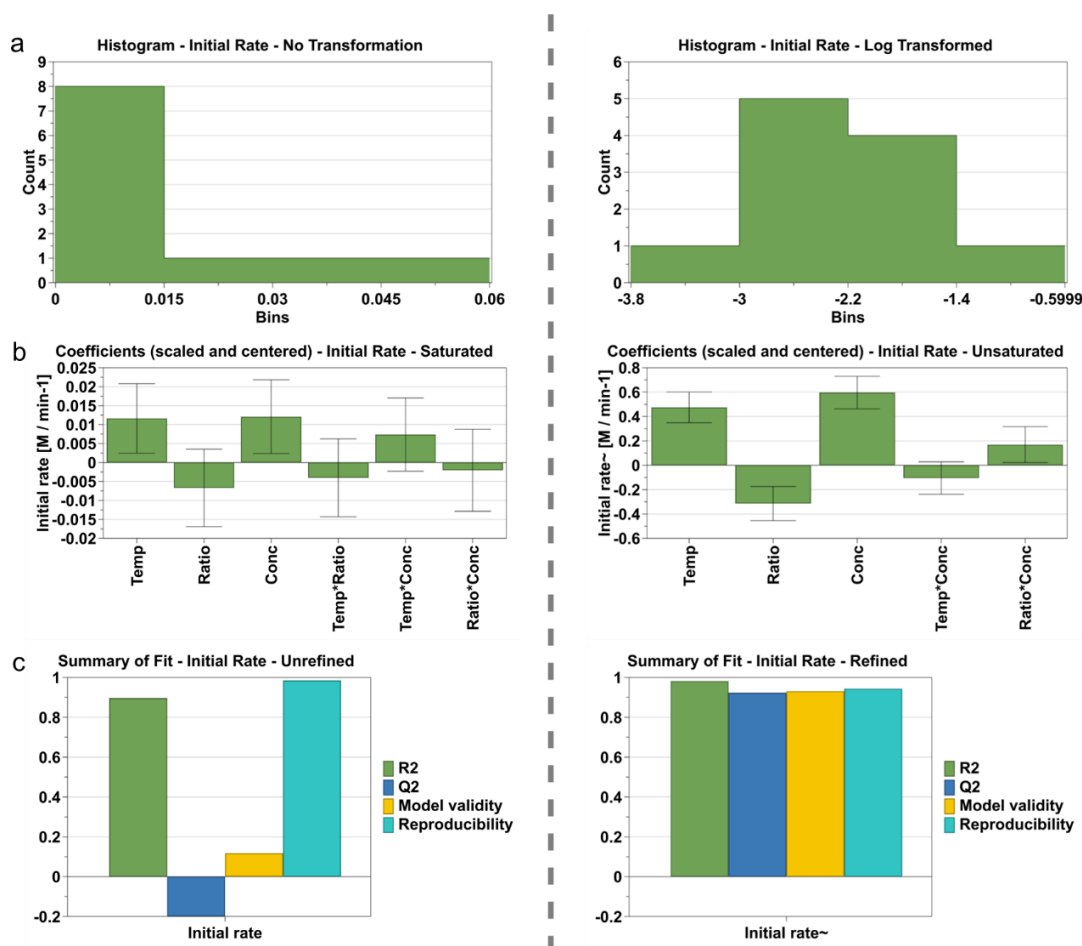


Figure 52: a) Left: Untransformed histogram in saturated model, right: log transformed histogram. b) Left: Saturated coefficient plot of untransformed model with all terms shown. Right: Unsaturated coefficient plot of log transformed model with terms removed to give best validation metrics. c) Left: Validation metrics of the saturated, unrefined model. Right: Highest validation metrics of final unsaturated and log transformed model.

The saturated model for initial rate is shown in Figure 52c (left graph) possessing an R^2 of 0.90, a negative Q^2 value, a model validity value of 0.12 and a reproducibility value of 0.98. A negative Q^2 value implies that there is no acceptable level of predictability in the model and thus the model was refined.

The model was first changed by transforming the data in order to change the distribution of the responses (Figure 52a). The unrefined model showed a positively skewed set of data, however, a 'bell-shaped' distribution is most desirable as this gives better model estimates and statistics. A logarithmic transformation was applied to the data to achieve a more normal distribution. These operations were carried out using in-built functions on MODDE software. This operation alone increased the R^2 to 0.98, the Q^2 to 0.78, model validity to 0.86 but slightly lowered the reproducibility to 0.95 (see appendix 0 for summary of fit).

A plot of the coefficients is shown (Figure 52b) with each term 'scaled and centred' which means that the relative effect of different factors which have different units have on the output can be compared. Each term has an uncertainty associated with it, i.e. a 95% confidence interval. Where the confidence interval overlaps with $y = 0$, the term was deemed to be non-significant because the effect is statistically indistinguishable from zero (Figure 53). The positive or negative value of the coefficient also gives an indication into how this variable impacts the output (e.g. a positive value for the temperature means that higher temperature values increase the initial rate).^{63, 66}

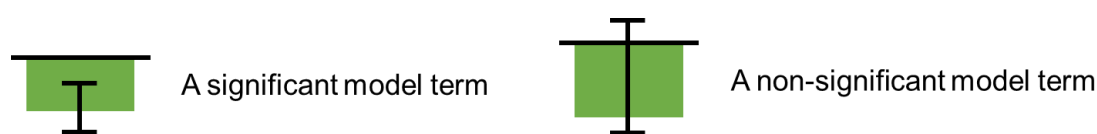


Figure 53: Significant and non-significant model terms in the coefficient plot.

In the unrefined model, only the reaction temperature and concentration were found to be significant terms and thus the Q^2 value was poor. The coefficient plot also shows interaction terms (i.e. Temp*Ratio, Temp*Conc and Ratio*Conc), all of which were deemed to be non-significant in the unrefined model. Once the model was log transformed, the citronella:scandium ratio also became a significant term and the error bars of all terms including the interaction terms

decreased in size (despite the latter still remaining non-significant). Such improvements were accompanied by an increase in the Q^2 to 0.78 (appendix 0). Next, different coefficients were removed in a stepwise fashion from the log transformed but saturated model to find which combination gave the best model validation metrics (i.e. the highest Q^2 value). It was found that removal of the Temp*Ratio interaction term, which was the most non-significant term, gave the best overall validation metrics and led to Ratio*Conc becoming a significant term in the model. In this model, the Temp*Conc term remained non-significant but its removal lowered the Q^2 value and so this was kept in the model.

The highest validation metrics that were obtained were an R^2 of 0.98, Q^2 of 0.92, model validity of 0.93 and reproducibility of 0.94. These very high validation metric values are suggestive of a well-fitted model with a high degree of predictive ability.

In the final coefficient plot, the Ratio*Conc interaction term was found to be significant and thus this was explored further using interaction plots (Figure 54a-b). The interaction plot shows that at both a low and high citronellal concentration increasing the citronellal:scandium ratio lowered the initial rate observed (Figure 54a), with a more pronounced effect at lower citronellal concentrations (due to the steeper curve) (Figure 54a, green trend). Conversely, at both a low and high citronellal:scandium ratio increasing the citronellal concentration increased the rate (Figure 54b), with a larger increase observed at higher citronellal:scandium ratios. With OVAT experimentation, valuable insight into the interactions between variables and their non-linearities in behaviour such as this cannot be obtained.

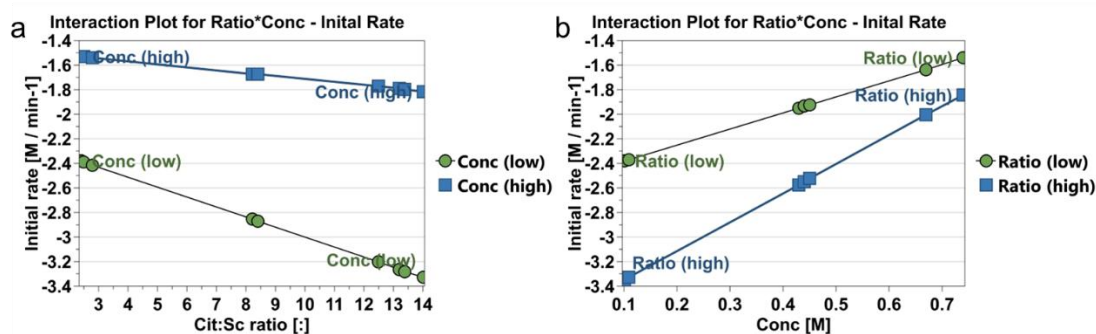


Figure 54: a-b) Interaction plot from the final initial rate DoE model for Ratio*Conc interaction term.

With a model generated that possessed a high degree of predictive ability, a contour plot was generated which shows all of the parameter space and the resultant predicted initial rate values at a given set of conditions (Figure 55). Insight into the chemistry over a wide range of conditions like this cannot be achieved using OVAT and so the ability to do this serves as one of the big advantage of using a DoE.

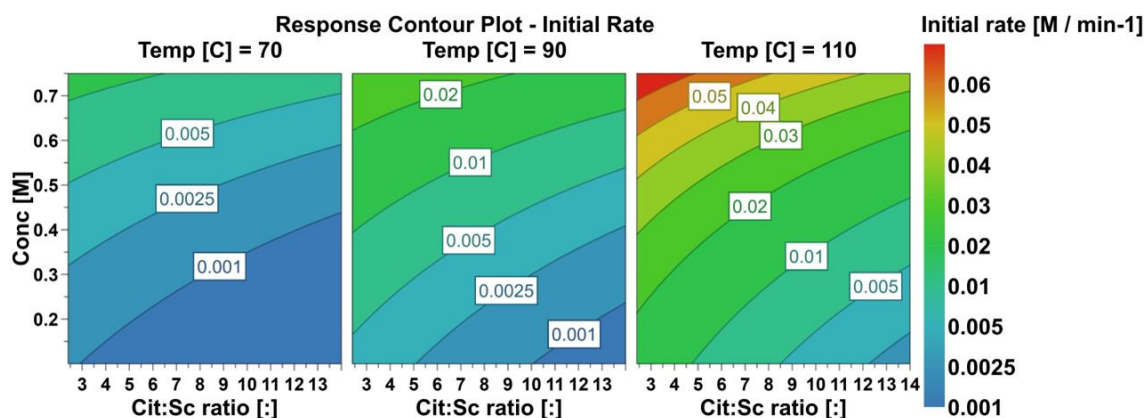


Figure 55: Contour plot generated which shows the initial rate as a function of the variables studied.

The initial rate of reaction was strongly dependent upon the reaction temperature employed which is highlighted by the rate values at different temperatures. Such a trend was expected given the exponential relationship between reaction rate and temperature as dictated by the Arrhenius equation (Eqn. 16).

$$k = Ae^{-\frac{Ea}{RT}} \quad \text{Eqn. 16}$$

Apart from at the highest the temperatures, the highest initial rate values at each temperature were obtained at a low citronellal:scandium molar ratio (i.e. higher catalyst loading) and higher values of citronellal concentration. The difference in rates at 110 °C can be visualised more clearly through inspection of Figure 56 which shows a surface plot of the rate with approximately a 40-fold difference between the fastest and slowest initial rates.

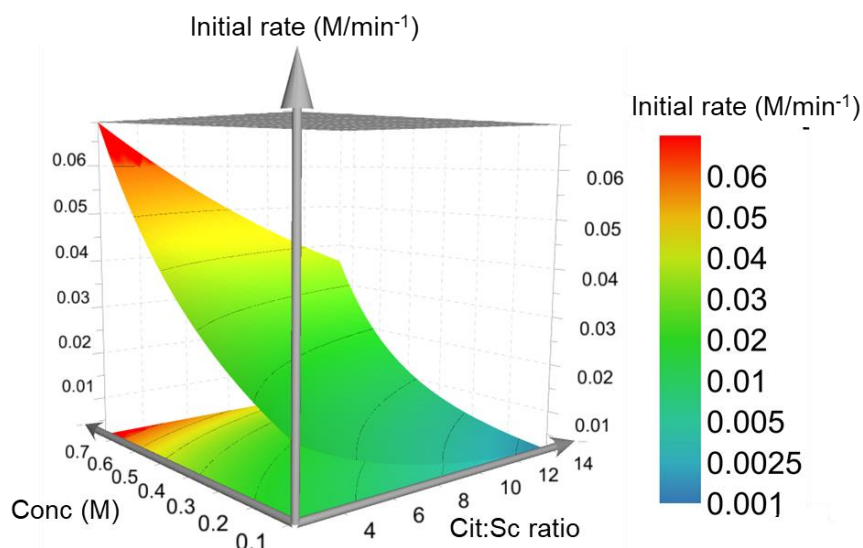


Figure 56: Surface plot of initial rate at 110 °C highlighting the difference in initial rate values observed for the experiments in the DoE.

2.4.2.3 Turnover frequency: model analysis and validation

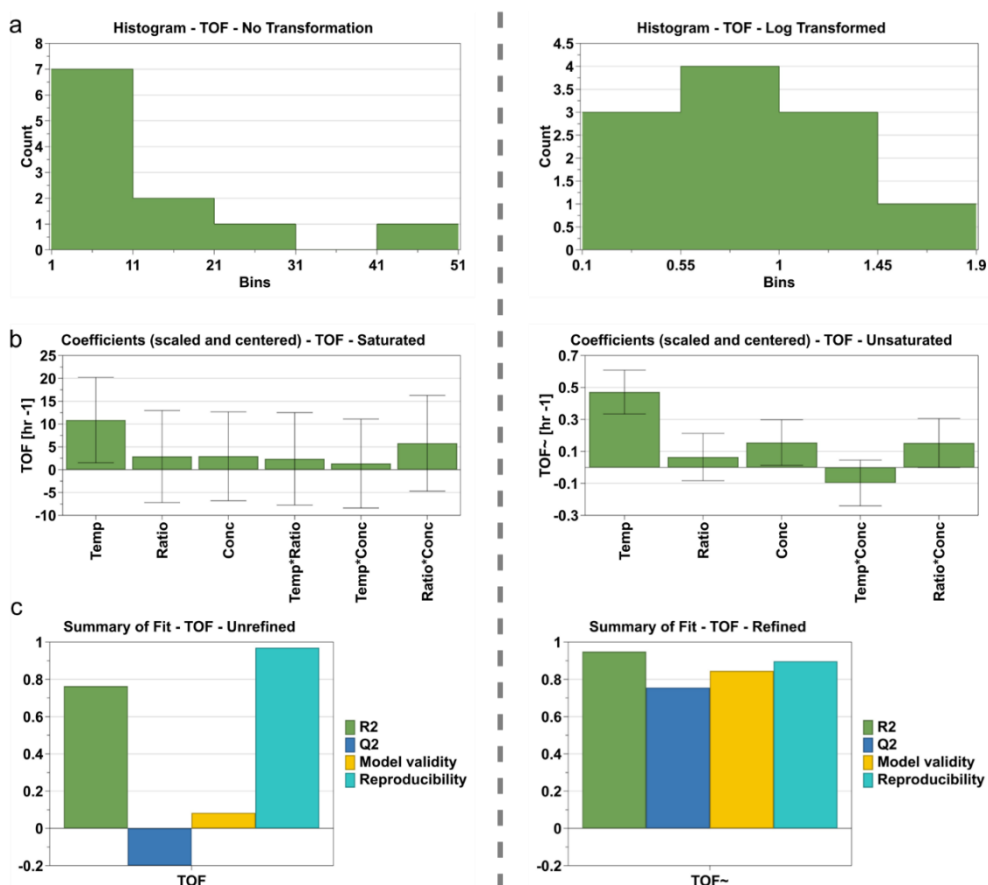


Figure 57: For TOF a) Left: Untransformed histogram in saturated model, right: log transformed histogram. b) Left: Saturated coefficient plot of untransformed model with all terms shown. Right: Unsaturated coefficient plot of log transformed model with terms removed to give best validation metrics. c) Left: Validation metrics of the saturated, unrefined model. Right: Validation metrics of final unsaturated and log transformed model.

The saturated, unmodified validation metrics for TOF is shown in Figure 57c (left graph) and produced a poor model with a negative Q^2 value as a result of many very non-significant model terms. This model also possessed an R^2 of 0.76, a model validity value of 0.082 and a reproducibility value of 0.97. An analogous model refinement process that was carried out for the initial rate model was carried out for the TOF values.

The untransformed TOF values, like the initial rate values, showed a positive skew which was corrected with a log transformation and produced a normally distributed set of values (Figure 57a). All of the terms in the raw coefficient plot of the unrefined model, apart from temperature, were very non-significant as highlighted by the large error bars (and negative Q^2 value). By log transforming the response values, it was observed that the size of these error bars decreased despite the terms still remaining non-significant. As a result of this the Q^2 increased to 0.31 (appendix 0).

Like with the initial rate model, it was found that the best validation metrics were obtained simply with the removal of the Temp*Ratio term in the coefficient plot, i.e. the difference in TOF at a low/high temperature was not dictated by the citronellal:scandium ratio (and vice versa). In the final model, the temperature and concentration terms were found to be significant, however, the citronellal:scandium ratio term remained non-significant suggesting that there was no clear relationship between these values and the resultant TOF values. Despite being non-significant, this is not a negative result; rather it just means that the ratio did not have a strong effect on the outcome of the response.

The best validation metrics that were obtained were an R^2 of 0.95, a Q^2 of 0.76, a model validity of 0.85 and a reproducibility of 0.90. These metrics are still suggestive of a good model with a high predictive ability (although not as high as the initial rate model).

A contour plot was generated for the model (Figure 58). The TOF values at 110 °C were an order of magnitude greater than at 70 °C highlighting the influence of reaction temperature once again.

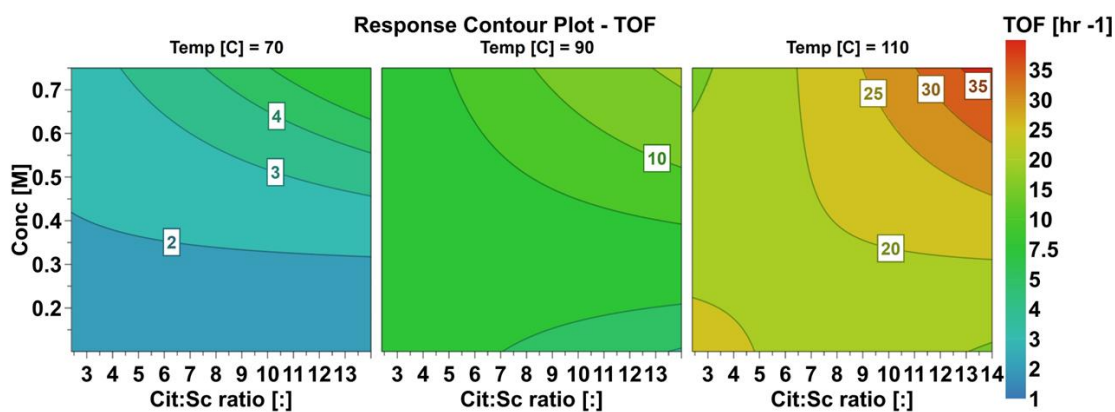


Figure 58: Contour plot generated which shows the TOF as a function of the variables studied.

At 70 °C and 110 °C, the greatest TOF values were obtained at the highest citronellal concentration and the highest citronellal:scandium molar ratio. In such experiments, 49 mg of MIL-100(Sc) was used compared to 245 mg (experiment 4 and 11) or 7 mg (experiment 3 and 7). The combination of a relatively high citronellal concentration but intermediary catalyst loading led to the greatest turnover number, as in experiment 2 where the next highest TOF was reported a similar catalyst loading was used (35 mg) but the concentration of (\pm)-citronellal used was much lower (0.1 M).

Despite the \approx 40-fold difference in the initial rates of reaction between experiments 3 and 4 it was interesting to observe similar TOF values for these reactions (14.8 hr^{-1} and 13.4 hr^{-1} respectively) suggesting similar catalytic efficiencies despite drastically different reaction length scales. It is clear that higher temperatures are desirable for obtaining the highest TOF values. The reaction surface at 110 °C was more effectively visualised using a surface plot (Figure 59).

There was a difference in trend for the TOF model compared to the initial rate model suggesting a trade-off existed for the maximum of each metric. Due to this trade-off, the optimiser function was used to find the conditions which produced the maximal values of each output across the range of experimental conditions. The optimiser tool in MODDE allows the user to specify target response values and the range of experimental conditions that will be explored. For the optimisation of TOF and initial rate, the objective was to maximise both values across the whole range of conditions used in the DoE. Upon running the optimiser, a range of conditions that gave rise to a number of predicted initial rate

and TOF values were outputted. These values were subsequently plotted and a Pareto front was identified in the data (Figure 60) highlighting the trade-off that exists between these two variables.

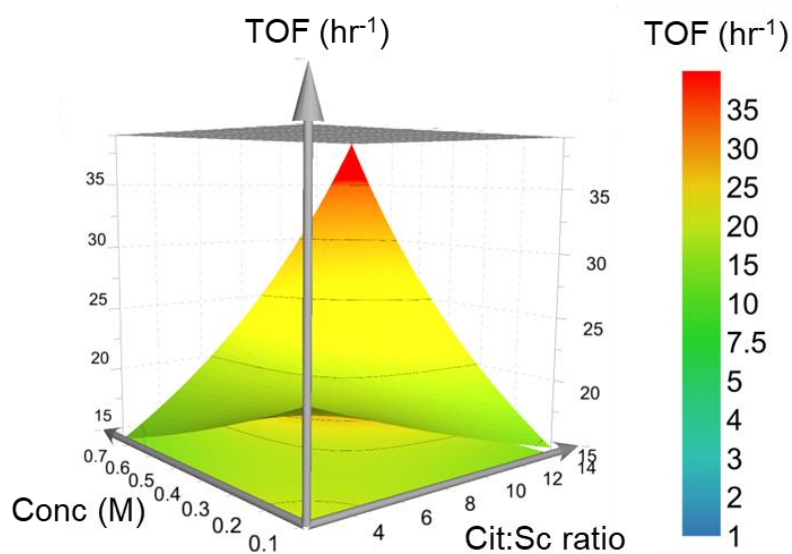


Figure 59: Surface plot of TOF at 110 °C showing the variation in values that were predicted by the model.

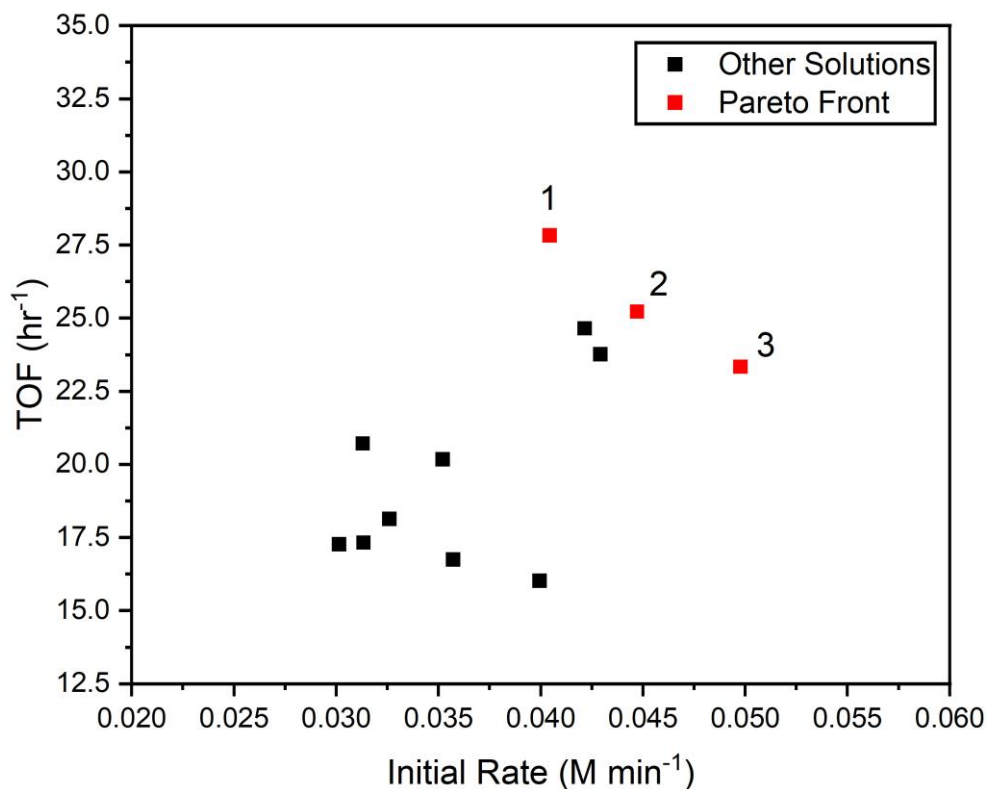


Figure 60: Plot of optimised data points outputted by MODDE software. A Pareto front (red points) was identified illustrating the trade-off upon attempting to maximise these conditions.

The conditions that gave rise to the optimal solutions were tabulated (Table 14), with the best rates and TOFs obtained at high temperatures and concentrations but with a trade-off existing between the citronellal:scandium ratio – the higher this value the greater the TOF but the lower the rate. This is a logical trend as a higher citronellal:scandium ratio is indicative of a lower catalyst loading and thus the efficiency was greater.

Table 14: The three sets of conditions outputted by MODDE that gave rise to the best combined initial rate and TOF values and thus gave rise to the Pareto front.

Solution	Temperature (°C)	Concentration (M)	Cit:Sc ratio	Initial Rate (M min ⁻¹)	TOF (hr ⁻¹)
1	108.6	0.75	10.8	0.0404	27.8
2	109.3	0.75	9.5	0.0447	25.2
3	110	0.75	8.2	0.0498	23.3

Contour plots for initial rate and TOF with an optimised set of conditions are shown in Figure 61, where the optimal set of conditions (110 °C, 0.75 M citronellal, citronellal:scandium molar ratio: 8.2) is indicated by the star in each plot.

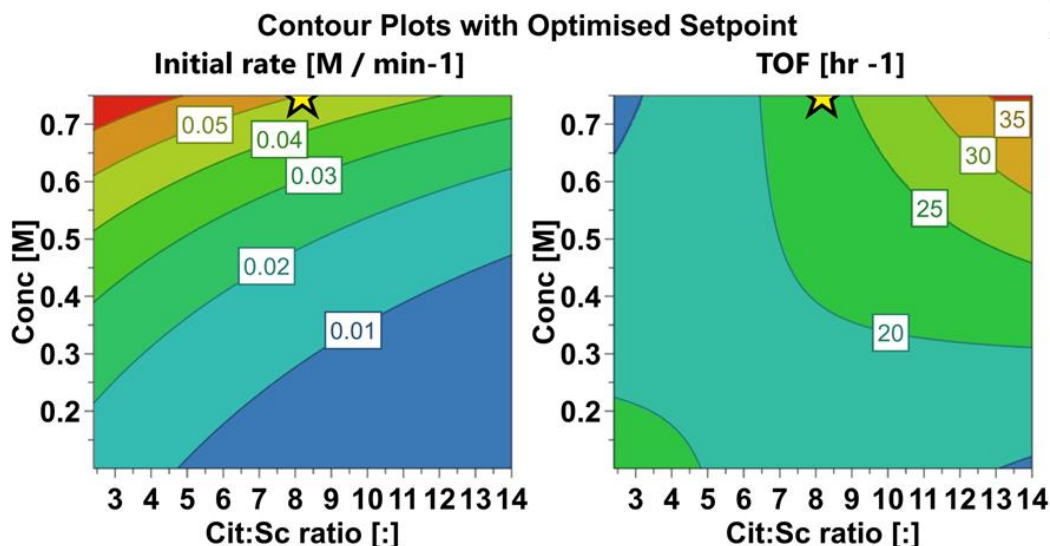


Figure 61: Contour plot of initial rate and TOF with optimised conditions outputted by MODDE shown by target icon (temperature: ≈ 110 °C, citronellal concentration: 0.75 M, citronellal:scandium molar ratio: 8.2).

2.4.2.4 Selectivity towards isopulegols: model analysis and validation

The selectivity of the reactions towards isopulegols formation varied from 47% - 97%. The saturated model produced a model with a relatively large R²

value (0.86) but a negative Q^2 value suggesting the model gives no degree of predictability. Alongside this, all terms were non-significant apart from the Ratio*Conc interaction term. Due to the poor validation metrics of the saturated model, refinement was attempted, firstly with a negative log transformation to produce a normally distributed histogram. This in turn resulted in a model where all of the terms were saturated with the Q^2 value still negative.

The fact that the Q^2 value did not improve when model refinement was attempted means that there were no factors identified showing a strong effect on the selectivity of the reaction towards (\pm)-isopulegols.

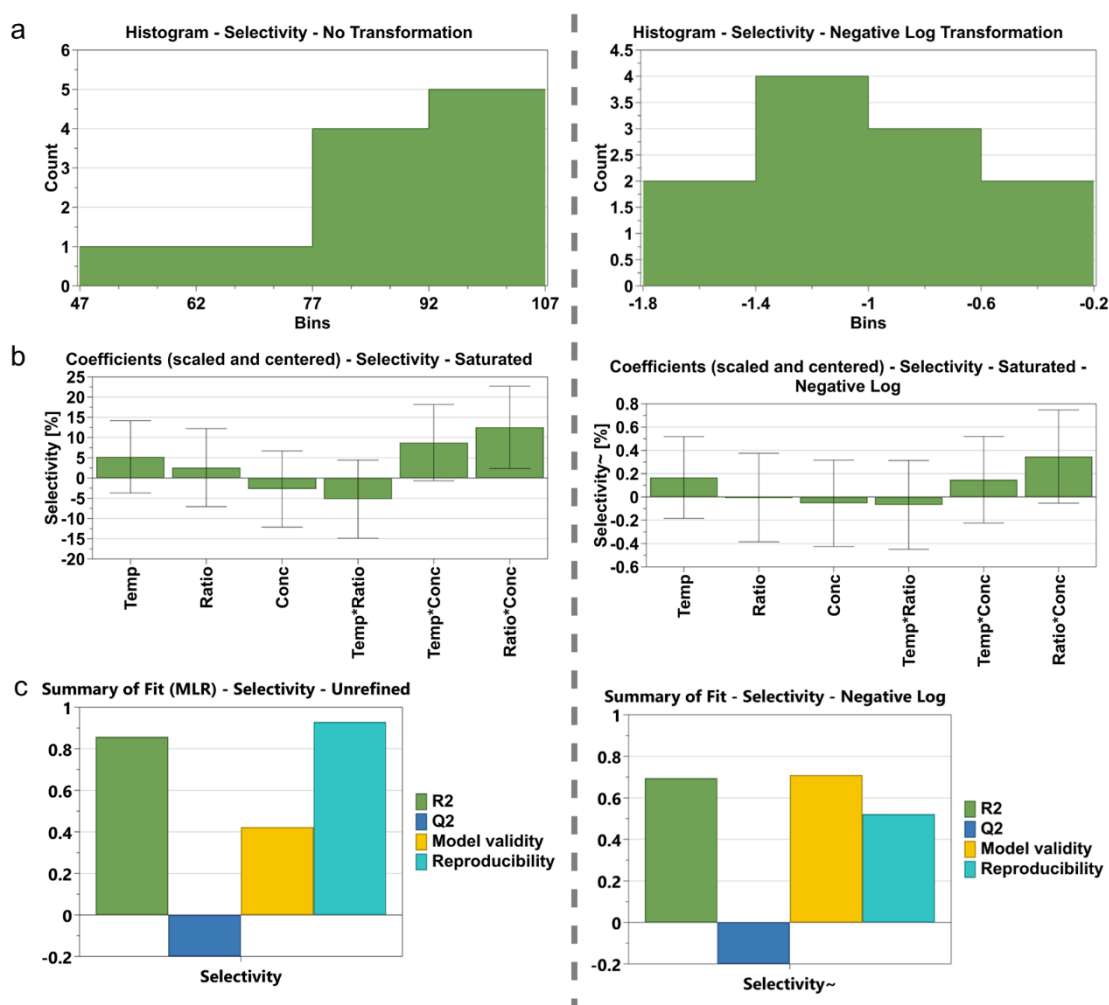


Figure 62: For selectivity towards (\pm)-isopulegols a) Left: Untransformed histogram in saturated model, right: negative log transformed histogram. b) Left: Saturated coefficient plot of untransformed model with all terms shown. Right: Saturated coefficient plot of negative log transformed model with terms removed to give best validation metrics. c) Left: Validation metrics of the saturated, unrefined model. Right: Validation metrics of the negative log transformed and saturated model.

The two reactions that produced the highest initial rate and TOF values (4 and 1 respectively), and thus would be two favourable sets of experimental conditions to use, gave selectivities to isopulegols of 84 and 96%, the latter amongst the best results in the DoE. Such an observation was deduced via simple analysis of the reaction data.

For the experiments that employed the largest catalyst loading (i.e. at the lowest Cit:Sc ratio and highest citronellal concentration at 70 and 110 °C, 245 mg MIL-100(Sc), experiments 4 and 11), the largest initial rate values were observed. Some of the lowest selectivity values towards (\pm)-isopulegols (84% and 47% respectively) were also observed in these experiments, however. The lower selectivity was not a result of further isopulegol reaction (as no decrease in concentration was observed over time). As the catalyst loading was relatively high in these reactions, there may have been a greater number of surface-catalysed reactions which may in turn have resulted in different product formation, relative to pore-catalysed reactions where size restrictions exist and larger products, if formed at all, may be too large to leave the pores. Additionally, the combination of the high citronellal concentration and high MIL-100(Sc) loading could have caused greater amounts of citronellal self-reaction²⁶³ or reactions between citronellal and isopulegol²⁰³ which would lower the selectivity of the reaction towards isopulegols.

The slowest reactions (i.e. at the lowest Cit:Sc ratio and highest citronellal concentration at 70 and 110 °C, 245 mg MIL-100(Sc)) in the DoE were still incomplete after a week of reaction. Similar to the reactions where the catalyst loading was the highest (4 and 11), for these slower reactions a lower selectivity towards (\pm)-isopulegols was also observed (68% and 84% respectively) which might be due to the extensively long reaction times resulting in undesired side product formation. As there was insufficient amounts of catalyst present for the reaction to proceed at a reasonable rate, it is possible that the unreacted citronellal, which was present in the reaction vessel at elevated temperatures, may have decomposed. Even at ambient storage conditions citronellal decomposes over time and thus the elevated temperatures in the reaction vessel may have sped this process up. Again, for these reactions no decrease in the concentration of isopulegols was measured suggesting no product self-reaction.

2.4.2.5 Selectivity towards isopulegol: model analysis and validation

The selectivity towards the formation of (\pm)-isopulegol remained largely unchanged in each of the experiments (47 – 58%) which is reflected in the low validation metrics where R^2 was 0.68 and Q^2 was negative (Figure 63c). The terms in the coefficient plot were also all non-significant. A number of transformations were carried out on the data to see what effect this would have on the spread of data but none produced a more normal distribution of response values than the untransformed data. The terms in the coefficient plot were also systematically adjusted with the best model possessing a Q^2 of 0.01.

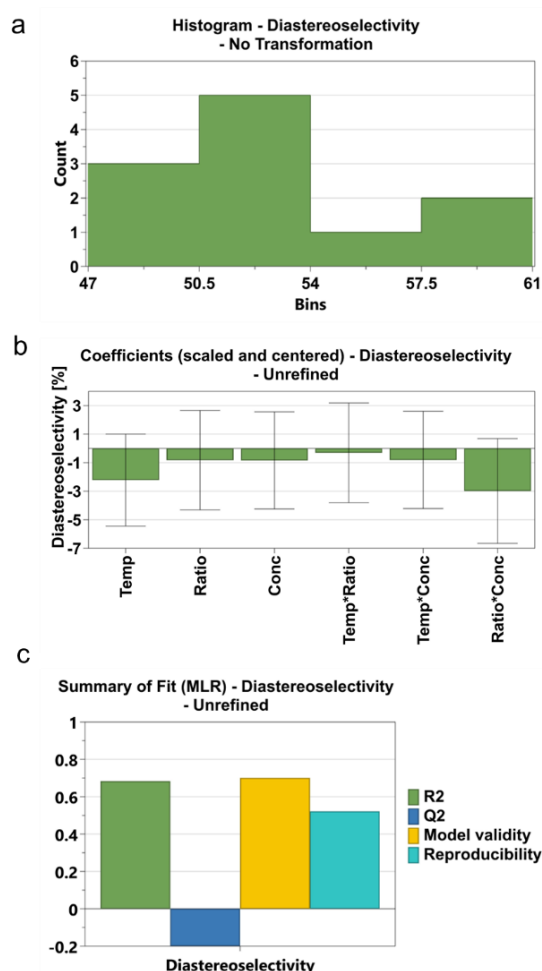


Figure 63: For diastereoselectivity a) Untransformed histogram in saturated model. b) Left: Saturated coefficient plot of untransformed model with all terms shown. c) Left: Validation metrics of the saturated, unrefined model.

These results are unsurprising as mentioned in section 2.4.1, the diastereoselectivity of this reaction may depend to a larger extent on the intrinsic properties of the catalyst (where the properties of the catalyst were not tailored to improve the diastereoselectivity) (i.e. the free-energy differences of isopulegol

transition states which is a function of the catalyst material used²⁴⁶) as opposed to the experimental conditions employed.

2.4.2.6 Summary of the DoE

A 2-level 3-factor FFD DoE was carried out for the intramolecular cyclisation of citronellal catalysed by MIL-100(Sc) with the reaction temperature (70 – 110 °C), (±)-citronellal concentration (0.1 – 0.74 M) and citronellal:scandium molar ratio (2.4 – 14.0) all varied. For the experiments, timepoints were taken throughout the course of the reaction and analysed via GC to monitor the consumption of (±)citronellal and production of (±)-isopulegols and a range of reaction metrics (initial rate, conversion, TOF, selectivity towards (±)-isopulegols, diastereoselectivity) were determined. DoE models with good fits were developed for initial rate and TOF metrics highlighting the range of experimental conditions employed. It was found that a trade-off existed between obtaining the highest initial rate and TOF values with optimal sets of conditions proposed. Poor fitting models were produced for the selectivity towards (±)-isopulegols and the diastereoselectivity suggesting that the variable range studied did not have a strong effect on these responses.

Importantly, a DoE which involved metrics such as initial rate and TOF has not been carried out previously for MOF-catalyst systems. These results pose an exciting avenue for further exploration of these systems which would seek to additionally study not only metrics such as the initial rate and TOF but also a system that shows variation in the outcome with the conditions studied.

2.5 Kinetic model development

Equipped with the experimental data from the 2-level 3-factor DoE that was conducted for the intramolecular cyclisation of citronellal catalysed by MIL-100(Sc), the underlying mechanism of this reaction was explored via kinetic modelling with the aim for this type of reaction analysis to become commonplace for MOF-catalysed reactions.

As discussed in more detail in section 1.1.3.2, kinetic models can be used to gain important mechanistic insights (e.g. reaction pathways, activation energies, possible sources of side products) into a chemical reaction which can be used to predict how a reaction will occur. This in turn, can make them easier to control which in turn can speed up process development and lower costs.^{60, 70, 71}

Dynochem[®] is a user-friendly kinetic modelling software that is employed in the pharmaceutical industry during drug development.⁷⁹⁻⁸⁹ Papageorgiou *et al.*⁷⁹ used Dynochem[®] to identify safe reaction conditions for the scale-up of a highly exothermic hydrogenation reaction. The study shows how a model which employed Langmuir-Hinshelwood (LH) kinetics to model a Pt/C catalyst and also the maximum expected exotherm as a function of the agitation speed in the reaction vessel. Wells *et al.*⁸⁷ carried out a joint DoE and kinetic model study using an automated reaction screening platform on a late phase developmental candidate. The data obtained for the DoE was also used to study the mechanism of the reaction with a good fit obtained to the data with a model containing 8 terms. Due to the good fit between the model and the experimental data knowledge and confidence in controlling the formation of the impurity was gained. As discussed in section 1.2.2.3, examples pertaining to the use of kinetic modelling to study MOF-based catalytic systems via computational approaches are lacking^{148, 149} and there is currently a lack of fundamental understanding of the kinetics of MOF-catalysed reactions.¹⁰² To date, Dynochem[®] has not been employed to model the kinetics of a MOF-catalysed reaction or to model the kinetics of the intramolecular cyclisation of citronellal. If an intuitive software like Dynochem[®] could successfully be applied to a MOF-based catalytic system, like those studied in this work, this software could be used as a platform going forwards to more easily study the kinetics of these systems. Due to the lack of studies regarding this, the ability of this software to obtain reliable kinetic data for this reaction was first tested using a simpler system with homogeneous catalyst scandium triflate which is considered a benchmark Lewis acid catalyst,¹⁷⁷ with some of the highest reported isopulegol selectivity values to date (Table 10).²⁰³

2.5.1 Homogeneous catalyst: scandium triflate

In 1998 Newman *et al.*²⁰³ reported (and patented²⁶⁴) the use of homogeneous Lewis acid catalyst scandium triflate as an efficient catalyst for the intramolecular cyclisation of enantiomerically pure citronellal, offering high selectivities towards both isopulegols and isopulegol formation in dichloromethane (DCM) (Table 10, Table 15).

The authors stated that at higher reaction temperatures (>78 – 25 °C) the selectivity of the reaction towards isopulegols formation was lower due to the

formation of oligomeric material (the reaction of citronellal with isopulegol). The formation of this oligomeric material was inhibited by lowering the reaction temperature (Table 15), resulting in increased selectivities towards isopulegols and isopulegol of > 95% and 94% respectively, the latter amongst the highest reported to date. We used this work as a basis to model the kinetics of the scandium triflate catalysed cyclisation of (±)-citronellal in this work, where both room temperature (25 °C) reactions and reactions at -78 °C were carried out but also at other temperatures too (-20 °C, -30 °C and -40 °C) (Table 16).

The experimental data obtained in this research contrasts with the experimental results obtained by Newman *et al.*²⁰³ where yield and selectivity values increased upon lowering the reaction temperature due to an inhibition in the formation of 'oligomeric material'. In this work, an inhibition in the formation of oligomeric material upon lowering the reaction temperature was not observed and it was found that at -78 °C the reaction did not proceed at all after 6 hours.

Table 15: Results obtained by Newman *et al.*^{203, 264} when using scandium triflate for the intramolecular cyclisation of citronellal with DCM.

Mol % Sc(OTf) ₃	Temp (°C)	Selectivity towards (±)-ISPs (%)	Selectivity towards (±)-ISP (%)
5	25	58	80:20
10	-40	86	88:12
5	-78	> 95	94:6

ISPs = isopulegols, ISP = isopulegol.

Table 16: Time and temperature dependent yields and selectivity for scandium triflate catalysed racemic citronellal cyclisation in DCM in this work. Conditions for this work: 5 mol% Sc(OTf)₃. 0.1 M citronellal.

Temp (°C)	Yield of (±)-ISPs (%)	Isomer ratio ((±)-ISP:others) (%)	Ref
25	58	80:20	203
25	77	74:26	This work
-20	71	80:20	This work
-30	68	81:19	This work
-40	66	83:17	This work
-78	NR	NR	This work
-78	> 95	94:6	203

ISPs = isopulegols, ISP = isopulegol, NR means no reaction after 6 hours.

In all of the other reactions, the formation of (±)-isopulegol was the most frequently observed isomer followed by (±)-neo-isopulegol and then

(±)-iso-isopulegol whilst the formation of (±)-neoiso-isopulegol was not observed in any experiments.

As the temperature was increased from -40 °C to 25 °C, the selectivity towards (±)-isopulegols increased from 66% to 77% whilst the selectivity towards (±)-isopulegol decreased from 83% to 74%. Both of these trends are attributed to the formation of proportionately smaller amounts of (±)-neo-isopulegol at lower reaction temperatures (Table 17).

Table 17: Isomer-specific yields and selectivity ratios obtained in this work for the cyclisation of (±)-citronellal using scandium triflate.

Temp (°C)	Yield (±)-ISP (%)	Yield (±)-neo-ISP (%)	Yield (±)-iso-ISP (%)	Yield (±)-ISPs (%)	Isomer ratio (%) ^a
25	57	17	3	77	74:26
-20	57	12	2	71	80:20
-30	55	11	2	68	81:19
-40	55	9	2	66	83:17

ISPs = isopulegols, ISP = isopulegol. ^a (±)-ISP:others.

Kinetic experiments were carried out at -20 °C, -30 °C and -40 °C where timepoints were collected throughout the course of the reaction to monitor the disappearance/appearance of reactants/products. The reaction temperatures studied offered suitable reaction times for kinetic analysis ranging from approximately 10 - 140 minutes.

The aim of the kinetic model that was developed for this system was to greater understand the underlying mechanism of this reaction when catalysed by scandium triflate (by observing the quality of fit) and to calculate other useful metrics such as the activation energy (E_a) using the kinetic data obtained at different temperatures. Comparison of activation energy values with literature reported values for this reaction provides a point of comparison and justification of the use of Dynochem[®] to generate kinetic models.

2.5.1.1 Building the kinetic model

The assumptions of the kinetic model that was built into Dynochem[®] were as follows:

- The intramolecular cyclisation of citronellal proceeds by a concerted mechanism following activation of the carbonyl group by the catalyst. Because the concentration of catalyst was not changing over the course of a reaction

the term was removed from the rate equation thus making the reaction first order overall with respect to citronellal.

- The formation of neoiso-isopulegol was not observed in any reactions and thus was excluded from the model.
- Product formation that is a result of (±)-citronellal consumption that does not produce (±)-isopulegols is termed the 'defunctionalisation of citronellal'. These side-products are defined as defunctionalisation products (DFPs) and are a mass balancing term in the model. Defunctionalisation was assumed to follow first-order kinetics.^{76, 263}
- No reverse reactions are assumed to have occurred.⁷⁶
- No further hydrogenation of isopulegols to produce menthols occurred and so the formation of these has been excluded from the kinetic model.
- The temperature dependence of the reaction is assumed to follow the Arrhenius equation (Eqn. 17).⁷⁶

$$k_r = k_{ref} \exp \left(-\frac{E_a}{R} \left[\frac{1}{T} - \frac{1}{T_{ref}} \right] \right) \quad \text{Eqn. 17}$$

k = Rate constant of reaction (units depend on reaction order)

k_{ref} = Reference rate constant at a particular temperature

A = Pre – exponential factor of reaction (units depend on reaction order)

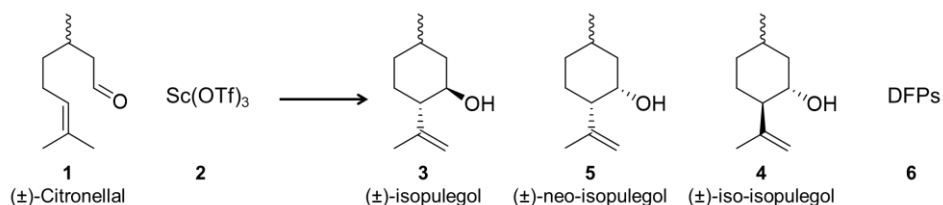
E_a = Activation energy of reaction (J mol⁻¹)

R = Ideal gas constant (J K⁻¹ mol⁻¹)

T = Temperature of reaction (K)

T_{ref} = reference temperature for the reference rate constant (K)

The final kinetic model is summarised by Scheme 4 with the resultant reaction pathways inputted into the model shown by Eqn. 18, Eqn. 19, Eqn. 20 and Eqn. 21.



Scheme 4: Scheme of (±)-citronellal cyclisation catalysed by scandium triflate.



The model was built using the assumptions stated and the data obtained from the experimentation (at -20 °C, -30 °C and -40 °C) was inputted into the kinetic model and then run. Once the fitting was started it proceeded to completion in a matter of seconds with rate constant values and activation energy values. Figure 64 shows the kinetic plots at each temperature, showing experimentally obtained data points and the subsequent model fit. Through visual observation there is excellent agreement between the experimentally obtained data and simulated data produced by the model at each temperature suggesting that the first order reaction kinetics was accurately describing the chemical behaviour of this system.

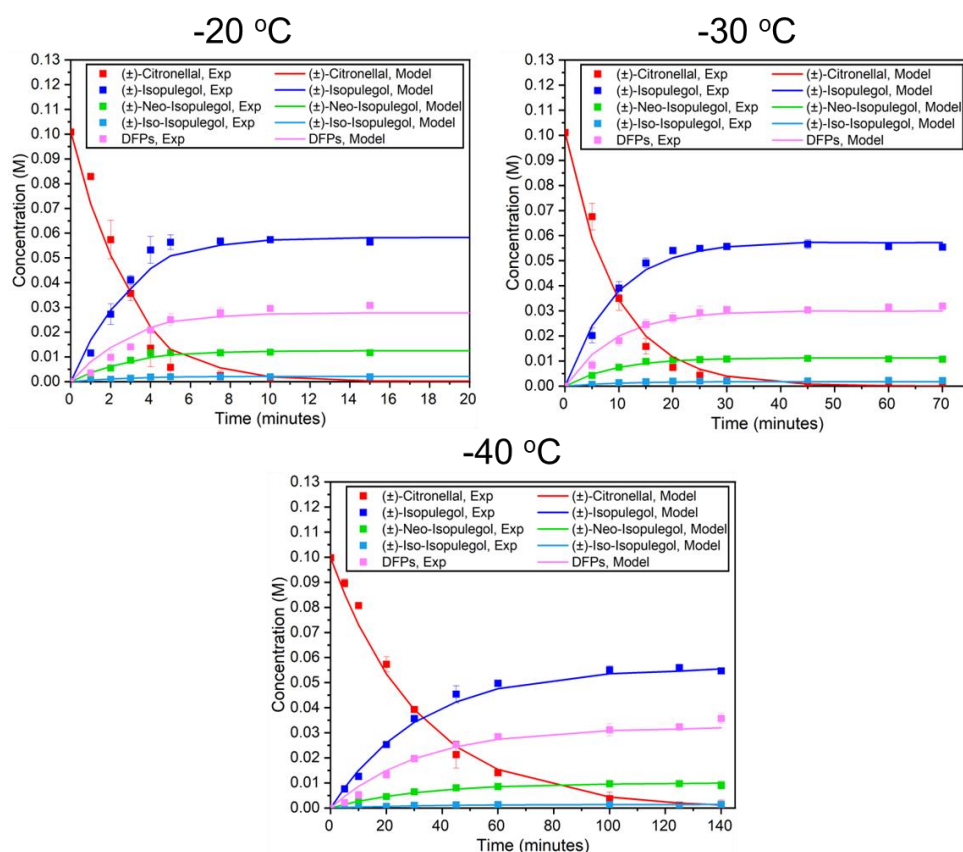


Figure 64: The kinetic experiments carried out in the model (5 mol % Sc(OTf)₃, 0.1 M (±)-citronellal, DCM) at -20 °C, -30 °C and -40 °C and model fit. For each species, the model fits the experimental data well.

The data at the three different temperatures was used to obtain activation energies for each reaction (Table 18).

Table 18: The reaction and subsequent activation energy determined by the kinetic model.

Reaction	E _a (kJ mol ⁻¹) (CI (%))
1 + 2 → 3 + 2	59.4 (± 4.6%)
1 + 2 → 4 + 2	63.9 (± 4.0%)
1 + 2 → 5 + 2	68.0 (± 3.5%)
1 + 2 → 6 + 2	54.8 (± 5.1%)

These values are similar in value to what has previously been reported in the literature. Nair *et al.*²⁶⁵ reported an activation energy value of 49.8 kJ mol⁻¹ (specific isopulegol isomers not specified) following kinetic studies using a sulfated zirconia-carbon molecular sieve composite catalyst. An-Nan Ko *et al.*²⁶⁶ reported an activation energy value of 64.9 kJ mol⁻¹ (specific isopulegol isomers also not specified) when using mesoporous molecular sieves Al-MCM-41.

The fact that a first order mechanism, for which this reaction has previously been reported to be, produced the best fit and that the activation energy values were similar to those reported previously, instilled confidence in the ability of Dynochem® to obtain accurate and reliable kinetic data. Due to this, we next modelled the data obtained in the DoE with MIL-100(Sc)

2.5.2 Heterogeneous Catalyst: MIL-100(Sc)

Due to the success with homogeneous catalyst scandium triflate, the experimental data obtained in the DoE with MIL-100(Sc) (section 2.4.2) was used to build a kinetic model for this system using Dynochem®.

Modelling this type of system is inherently more complex not only because the reaction occurs in two phases (liquid and solid) but also because of the porous nature of the MOF-catalyst meaning that mass transfer within the pores occurs.

With this research, however, we sought to identify whether the kinetics of MOF-catalysed reactions could be modelled more simply with a software like Dynochem® that an R&D chemist within the pharmaceutical industry could use to study the kinetics of MOF-catalysed reactions.

When used in combination with the data obtained from a DoE, such as the one carried out in this work, a large amount of system understanding could be gained. By inputting different reaction mechanisms into Dynochem® and observing the quality of the resultant fit of the model to the experimental data greater insight into the mechanism could be gained.

2.5.2.1 Studying reaction mechanisms

Many of the basic assumptions that were made for the homogeneous system involving scandium triflate were also true for this system:

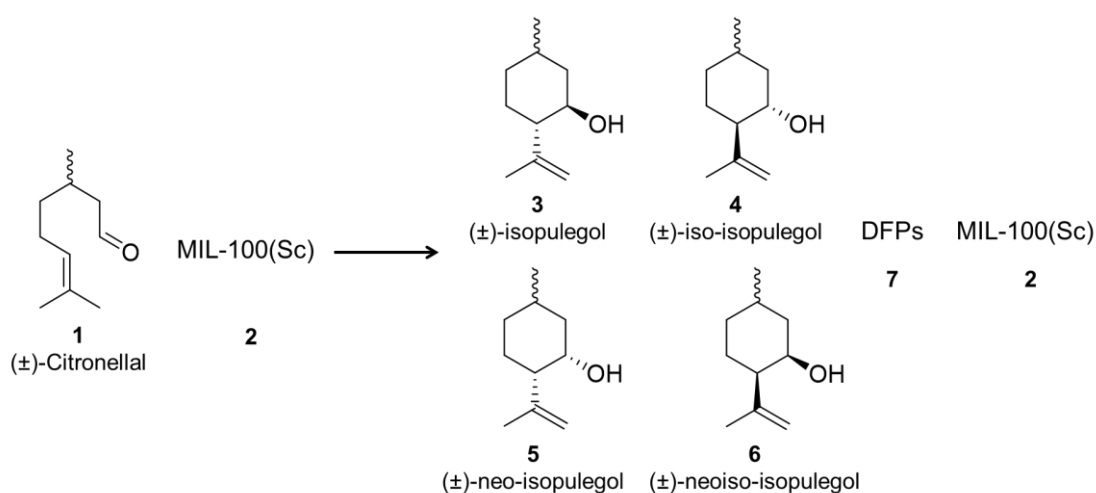
- The intramolecular cyclisation of citronellal proceeds by a concerted mechanism following activation of the carbonyl group by the catalyst. Because the concentration of catalyst was not changing over the course of a reaction the term was removed from the rate equation thus making this reaction first order overall with respect to citronellal.
- Product formation that is a result of (±)-citronellal consumption that does not produce (±)-isopulegols is termed the 'defunctionalisation of citronellal'. These side-products are defined as defunctionalisation products (DFPs) and are a

mass balancing term in the model. Defunctionalisation was assumed to follow first-order kinetics.^{76, 263}

- No reverse reactions are assumed have occurred.⁷⁶
- No further hydrogenation of isopulegols to produce menthols occurred and so the formation of these has been excluded from the kinetic model.
- The temperature dependence of the reaction is assumed to follow the Arrhenius equation.⁷⁶

Before attempting to fit the model, an assessment was first made into the length scales of the reactions carried out in the DoE; due to the excessively long reaction times in experiments 3 and 10 (> 5 days) these were omitted from model fitting. For initial testing of this kinetic model, the quality of fit for experiments at a single temperature (110 °C) were tested and the model with the best fit would be used to fit the model at other temperatures, therefore experiments 1, 2 and 4 from the DoE were fitted first.

The first mechanism that was tested (Scheme 5) was synonymous with the mechanism that produced the excellent fit that was observed for the homogeneous system involving scandium triflate. These individual steps are summarised by Eqn. 22, Eqn. 23, Eqn. 24, Eqn. 25 and Eqn. 26.



Scheme 5: Scheme of first model that was fitted for the (±)-citronellal cyclisation catalysed by MIL-100(Sc) using experimental data from the DoE.

$$1 + 2 \rightarrow 3 + 2 \quad \text{Eqn. 22}$$

$$1 + 2 \rightarrow 4 + 2 \quad \text{Eqn. 23}$$

$$1 + 2 \rightarrow 5 + 2 \quad \text{Eqn. 24}$$

$$1 + 2 \rightarrow 6 + 2 \quad \text{Eqn. 25}$$

$$1 + 2 \rightarrow 7 + 2 \quad \text{Eqn. 26}$$

The model fit model can be seen in Figure 65 and the associated rate constants can be found in Table 19. The model generally produced a poor fit to the data in experiment 1 and 4 with the model predicting more rapid changes in the consumption of citronellal and formation of isopulegols than was observed experimentally. For this model a total sum of squares (SSQ) of 16.86 between model and experimental values was outputted and subsequent rate constant values had large confidence intervals (> 35%). These results suggest that this mechanism was not appropriate to describe the behaviour of this system.

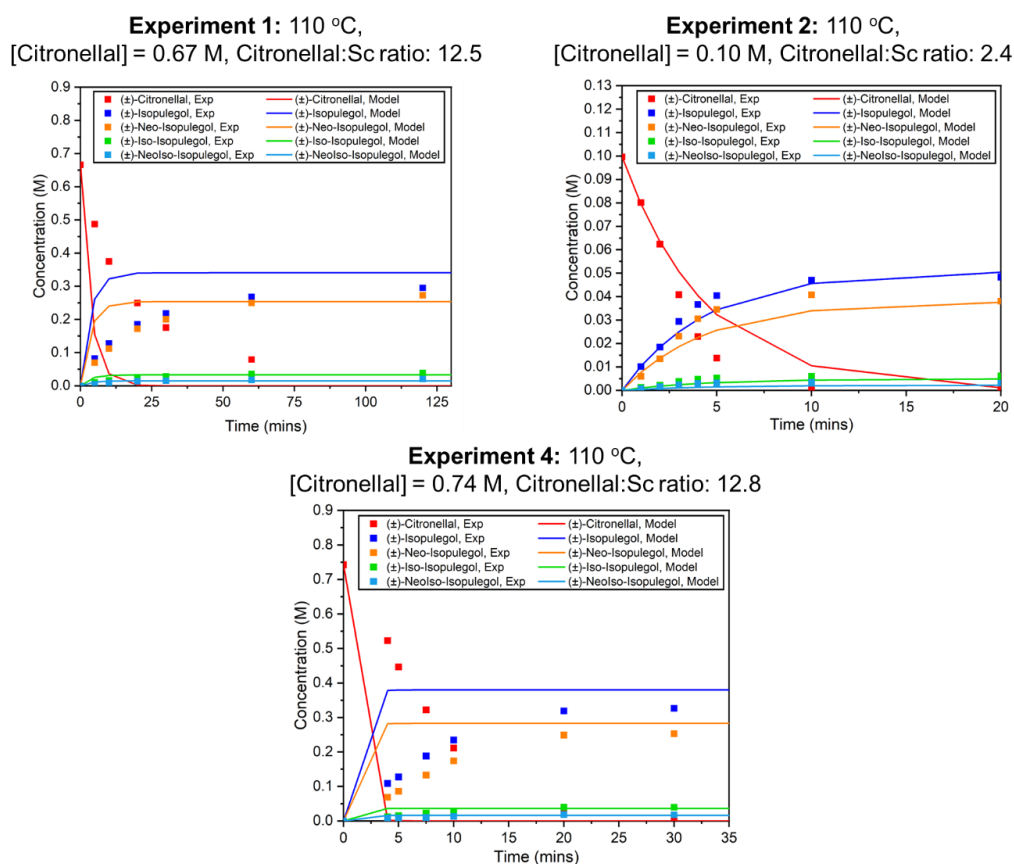


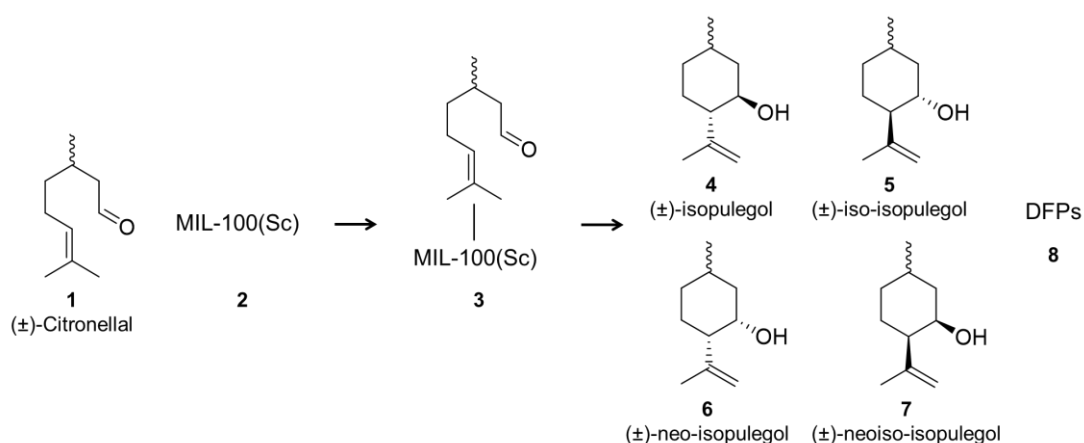
Figure 65: The DoE experiments (1, 2 and 4) that were used to test the fit of the model fit.

Table 19: The rate constant value outputted by Dynochem® and associated confidence interval.

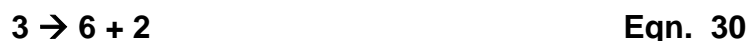
Reaction	Rate constant (k) (L mol ⁻¹ min ⁻¹) (CI (%))
1 + 2 → 3 + 2	2.80 (± 35.4%)
1 + 2 → 4 + 2	2.08 (± 36.1%)
1 + 2 → 5 + 2	0.27 (± 36.5%)
1 + 2 → 6 + 2	0.12 (± 37.9%)
1 + 2 → 7 + 2	0.20 (± 35.5%)

The second mechanism that was tested (Scheme 6) was based on the Langmuir-Hinshelwood (LH) model which is commonly accepted approach for heterogeneously catalysed reactions^{18, 78} and has also been used previously to model the kinetics of the intramolecular cyclisation of citronellal with an Ru/H-BEA catalyst.⁷⁶ This mechanism involves an adsorption step between the reactant(s) and the catalyst followed by the reaction and then product desorption and catalyst regeneration.

In the model, an adsorption step between a citronellal molecule and a scandium site in MIL-100(Sc) was added (Eqn. 27). In LH kinetics it can be assumed that the surface reaction is the rate determining step and that the product is weakly bound meaning it rapidly desorbs after formation.⁷⁸ To avoid adding too many parameters to the model and potentially risk overfitting the data, the reaction step was accompanied by catalyst regeneration in a concerted fashion, thus skipping the desorption step (Eqn. 28, Eqn. 29, Eqn. 30, Eqn. 31, Eqn. 32).



Scheme 6: Scheme of model based on LH kinetics that was fitted for the (±)-citronellal cyclisation catalysed by MIL-100(Sc) using experimental data from the DoE. Species 3 is an adsorption complex between a (±)-citronellal molecule and MIL-100(Sc).



Before the model was run, it was assumed that the rate of the adsorption step (like the desorption step) was much faster than the rate of the chemical reaction and so this value was fixed at an arbitrarily high value (1×10^9) during the modelling. Similar approaches to modelling heterogeneous systems on Dynochem[®] has also been done previously.⁷⁹ The equilibrium constant term was modelled but it was found that this term had a low statistical significance as data regarding this term was not supplied to the model (Table 20).

Table 20: The equilibrium constant value outputted by Dynochem[®] and associated confidence interval for the model based on LH kinetics.

Reaction	Equilibrium constant (K) (L mol ⁻¹) (CI (%))
1 + 2 → 3	537231 (low sensitivity)

The model fit of the kinetic model based on LH kinetics can be seen in Figure 66a and the associated rate constants can be found in Table 21. This model produced a better fit (SSQ = 9.79) to the experimental data compared to the first order model (SSQ = 16.86) suggesting that this mechanism is more appropriate to describe the behaviour of this system, which is unsurprising given the heterogeneous nature of MIL-100(Sc). Comparison of the modelled and experimental data across the three experiments also showed closer matches for this model, particularly for experiments 1 and 4. Additionally, the confidence intervals associated with the rate constant values were some 20% smaller ($\approx 15\%$) than for the model based on kinetics used for homogeneous systems.

Although the implementation of LH kinetics into the model improved the fit when compared to the first order mechanism, the overall fit to the experimental data

was still poor (SSQ = 9.79). One factor for this could be due to the fact that internal diffusion within the MOF framework was not accounted for. Future model development would seek to improve the model fit further by accounting for these phenomena. Quantifying mass transfer through pores is an ongoing challenge.

To further explore the poor fit between experimental data and model fit, the same data was independently fitted to a first-order exponential decay curve (Figure 66b) where a much improved fit was obtained. This further highlights the unsuitability of using DynoChem[®] to model this system.

Table 21: The rate constant value outputted by Dynochem[®] and associated confidence interval for the model based on LH kinetics.

Reaction	Rate constant (k) (min ⁻¹) (CI (%))
3 → 4 + 2	0.16 (± 15.1%)
3 → 5 + 2	0.12 (± 15.4%)
3 → 6 + 2	0.019 (± 15.8%)
3 → 7 + 2	0.0081 (± 16.3%)
3 → 8 + 2	0.014 (± 18.0%)

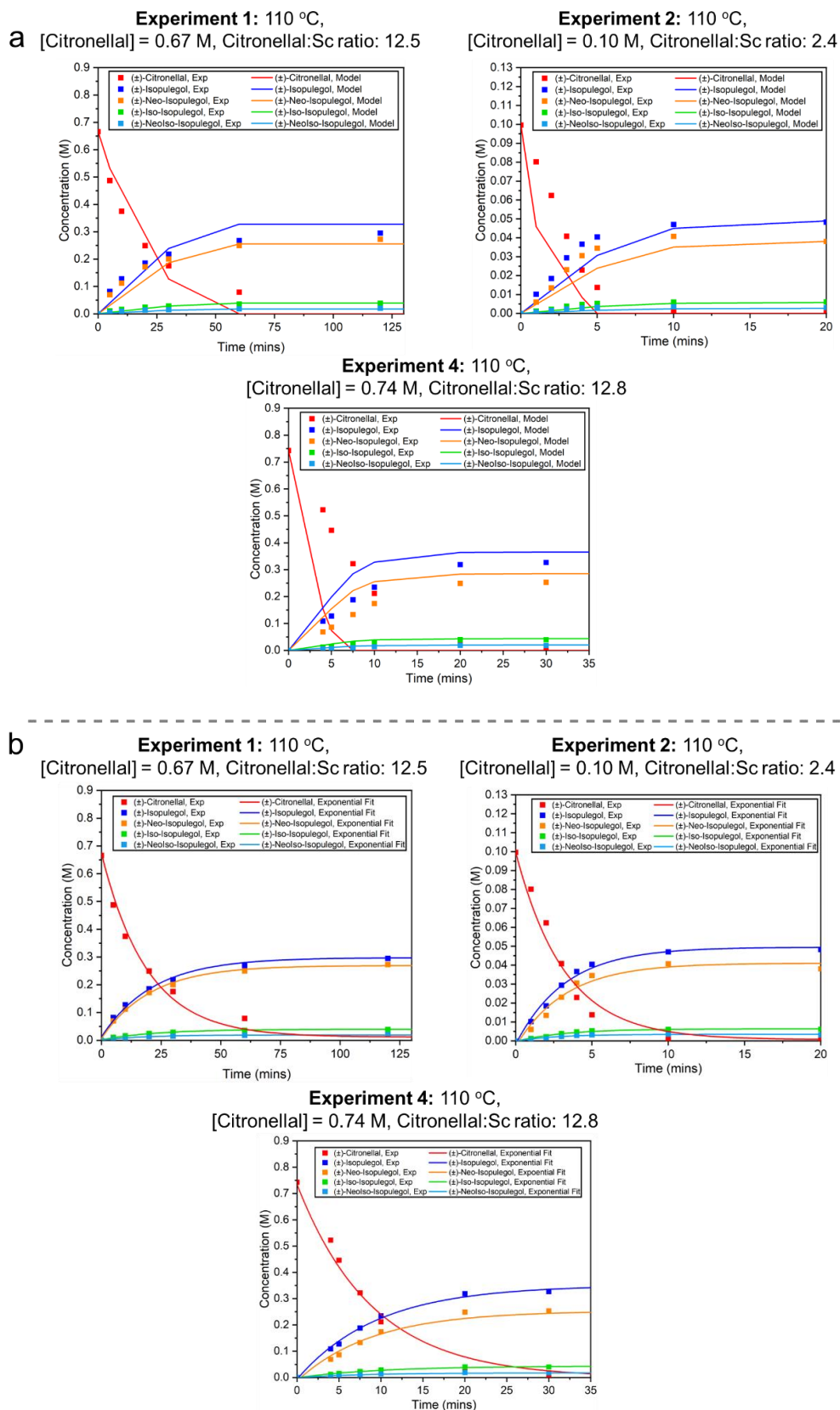


Figure 66: a): The DoE experiments (1, 2 and 4) that were used to test the model fit and the subsequent model fit of the kinetic model based on LH kinetics. **b)** A first-order exponential decay curve was fitted to the same DoE experiments (1, 2 and 4) showing an improved fit.

2.5.2.2 Obtaining an activation energy (E_a)

Table 22: The reaction and subsequent activation energy determined by the kinetic model for the MIL-100(Sc) catalysed citronellal cyclisation based on LH kinetics.

Reaction	E_a (kJ mol ⁻¹) (CI (%))
$3 \rightarrow 4 + 2$	81.2 (\pm 7.6%)
$3 \rightarrow 5 + 2$	84.7 (\pm 7.7%)
$3 \rightarrow 6 + 2$	87.9 (\pm 7.7%)
$3 \rightarrow 7 + 2$	94.9 (\pm 7.5%)
$3 \rightarrow 8 + 2$	51.9 (\pm 12.9%)

Due to the better model fit with the experimental data fitted for the LH kinetics-based model, the data at 70 °C from the DoE, alongside the data at 110 °C was used to model the activation energy of the system. The activation energy for this reaction was found to be greater than with the homogeneous system involving scandium triflate by approximately 30 kJ mol⁻¹ (Table 22). This suggests that the rate of reactions catalysed by MIL-100(Sc) are more sensitive to changes in the reaction temperature compared to scandium triflate.

2.6 Conclusion: Part B

The lack of exploitation of using DoEs to explore heterogeneously catalysed MOF-based reactions was addressed in Part B of this chapter. Statistically significant DoE models were generated upon studying the initial rate and TOF as a function of the reaction temperature, concentration and catalyst loading (i.e. citronellal:scandium) for the MIL-100(Sc) catalysed intramolecular cyclisation of citronellal. The generation of these models to identify favourable reaction conditions suggests that these tools can (and should) be used more widely to study MOF-based catalytic systems for there is much more detailed system understanding to be gained when compared to OVAT experimentation. Additionally, by using the data obtained in a DoE to generate kinetic models further mechanistic insight can be gained. In their review of the literature Gates and Yang¹⁰² identified that there is a lack of fundamental reaction kinetics of MOF-catalysed reactions; although relatively simple mechanistic deductions were made using Dynochem® in this work it is hoped that this proof-of-concept can be used as a springboard for further development into more detailed descriptions of MOF-catalysed systems in the future.

2.7 Conclusions of the chapter

The work in this chapter was carried out with a strong focus on exploiting practices carried out during pharmaceutical development. If MOFs are to be used as catalysts in industrial settings like these in the future then firstly a firm grasp should be had on their properties (i.e. stoichiometry, particle size (distribution)) and the resultant catalytic performance. Given the amount and depth of characterisation that was carried out on MIL-100(Sc) in Part A of this chapter, this was achieved in this work and the catalytic activity was explored with a good degree of confidence in the properties of the material that was synthesised. To our advantage MIL-100(M) MOFs are amongst the most well-studied MOFs thus making the characterisation carried out in this work easier but similar levels of detail should also be given to other, less well-studied MOF-catalyst systems going forward. In a wider context, there still remains open questions about the use of MOFs as industrial catalysts that need to be addressed such as attaining repeatable syntheses.¹⁰² Such improvements in the field may happen naturally assuming continued growth. Ultimately, if MOF-based catalysts can live up to their potential and deliver properties that cannot be achieved otherwise (i.e. in fine chemical reactions affording high chemo-, stereo- and regioselectivity)¹³⁰ then the industry will make room to accommodate them. To be able to make an assessment of this in the first place, however, it would be beneficial for these materials to be viewed through a 'pharmaceutical industry lens' like as was attempted in this work.

By assessing the current state of the MOF-catalysis field with a 'pharmaceutical industry lens' it is also clear just how drastically underutilised tools like DoEs and kinetic modelling, that are so widely practised in this industry, are. By studying the catalytic activity of MIL-100(Sc) via a combined DoE and kinetic modelling approach in Part B of this chapter, we demonstrated the feasibility and power of these tools to enhance system understanding. This work laid the groundwork for obtaining a firm understanding of MIL-100(Sc) powder as a catalyst prior to the fabrication of novel MIL-100(Sc)@PBSAC composites in Chapter 3. Going forward, it would be good to see more research groups take advantage of these tools to not only enlarge the stock of knowledge surrounding these materials but to also provide the basis for guidelines on how to exploit their usage in a pharmaceutical setting using these approaches.

2.8 Appendices

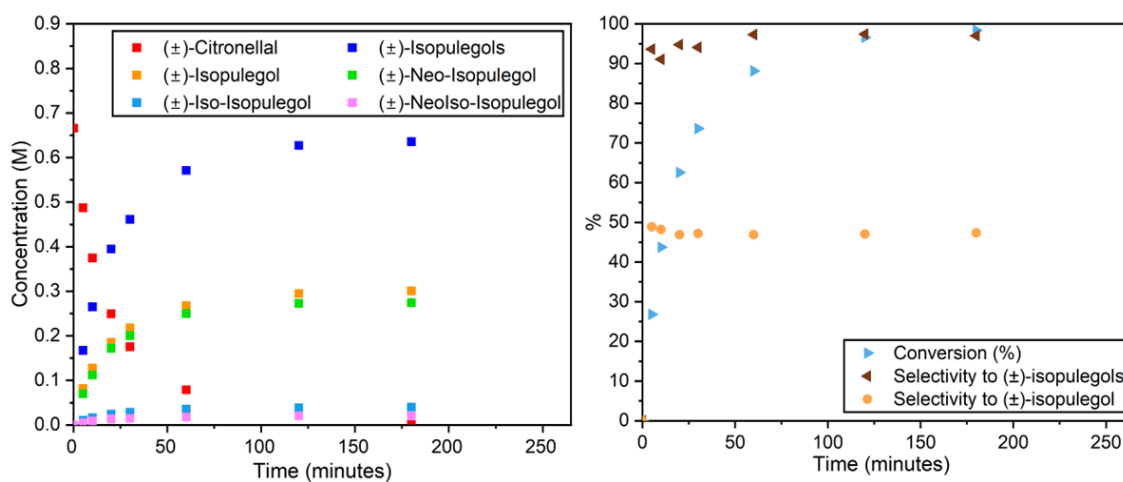
2.8.1.1 DoE experiment masses (see section 2.4.2)

Table 23: Mass of MIL-100(Sc) used for each experiment.

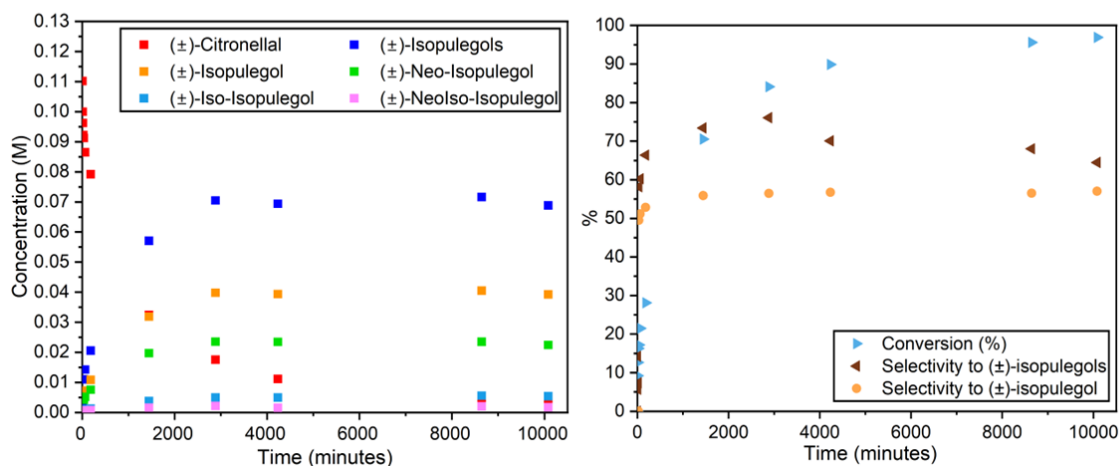
Experiment	MIL-100(Sc) mass used (mg)
1	49
2	35
3	7
4	245
5	47
6	47
7	47
8	49
9	35
10	7
11	245

2.8.1.2 DoE experiment results (see section 2.4.2)

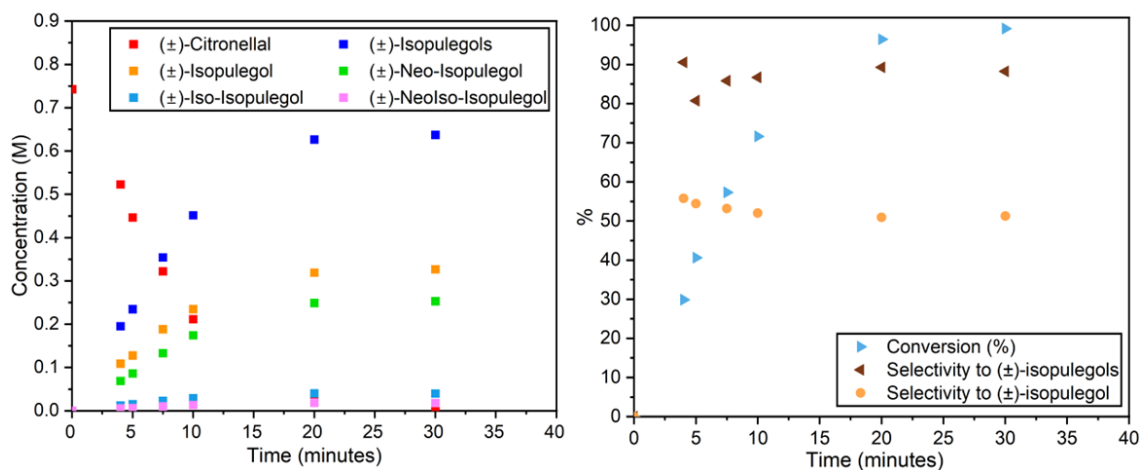
Experiment 1: 110 °C, [Citronellal] = 0.67 M, Citronellal:Sc ratio: 12.5



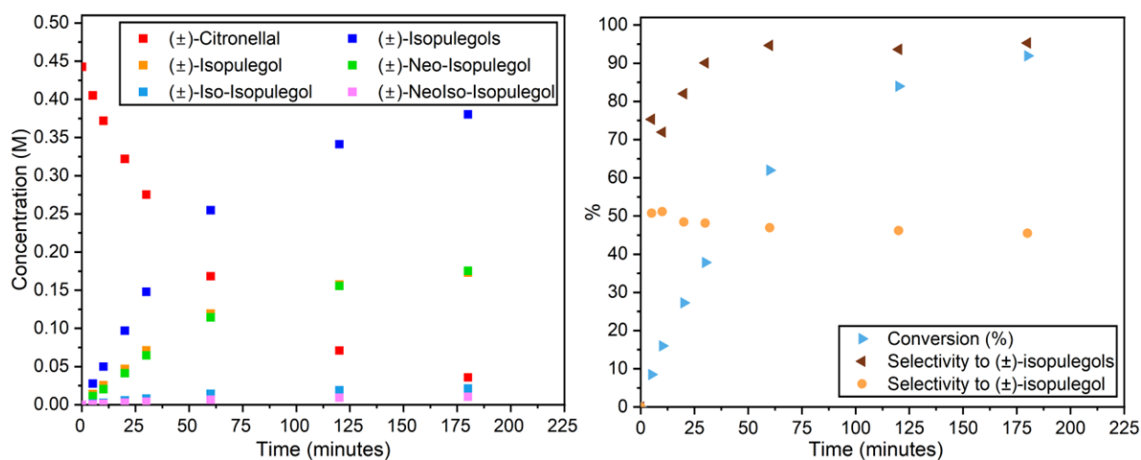
Experiment 3: 110 °C, [Citronellal] = 0.11 M, Citronellal:Sc ratio: 13.4



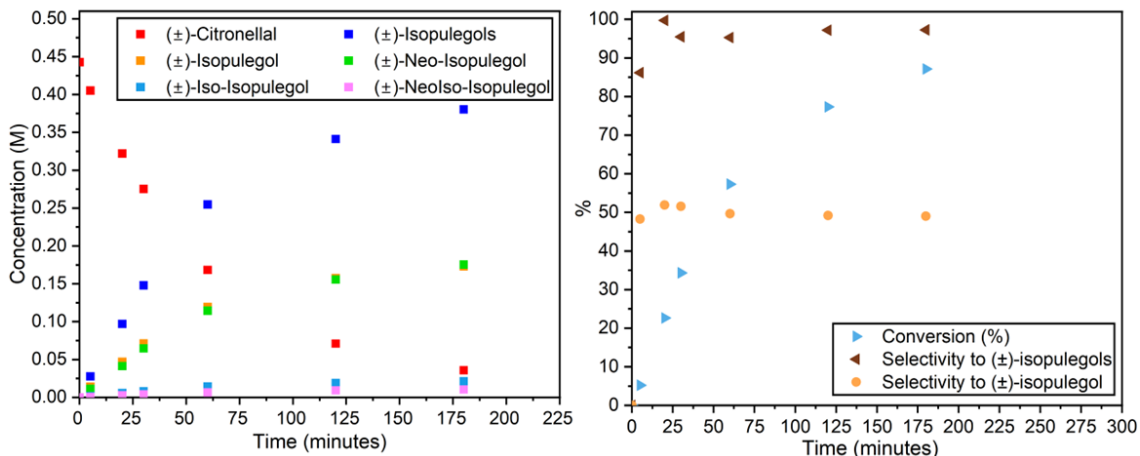
Experiment 4: 110 °C, [Citronellal] = 0.74 M, Citronellal:Sc ratio: 2.8



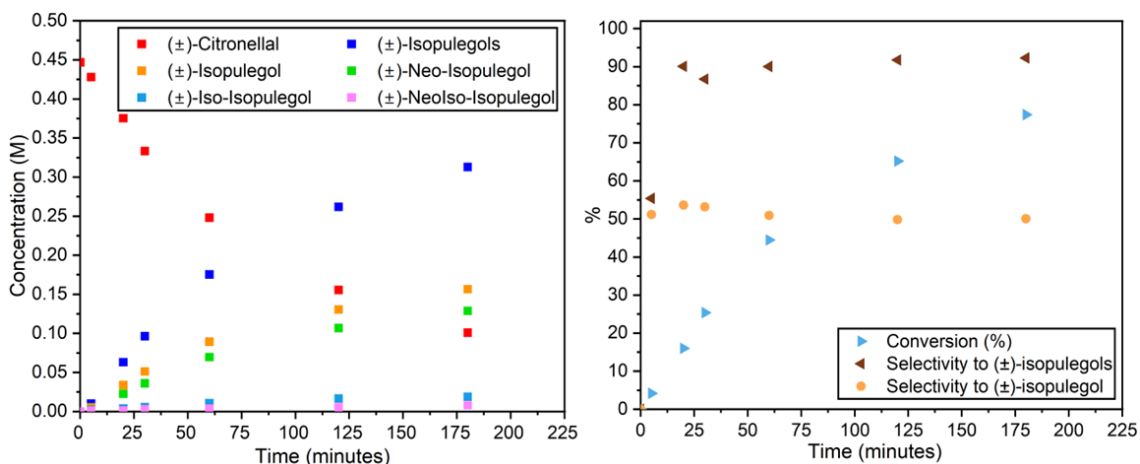
Experiment 5: 90 °C, [Citronellal] = 0.44 M, Citronellal:Sc ratio: 8.3



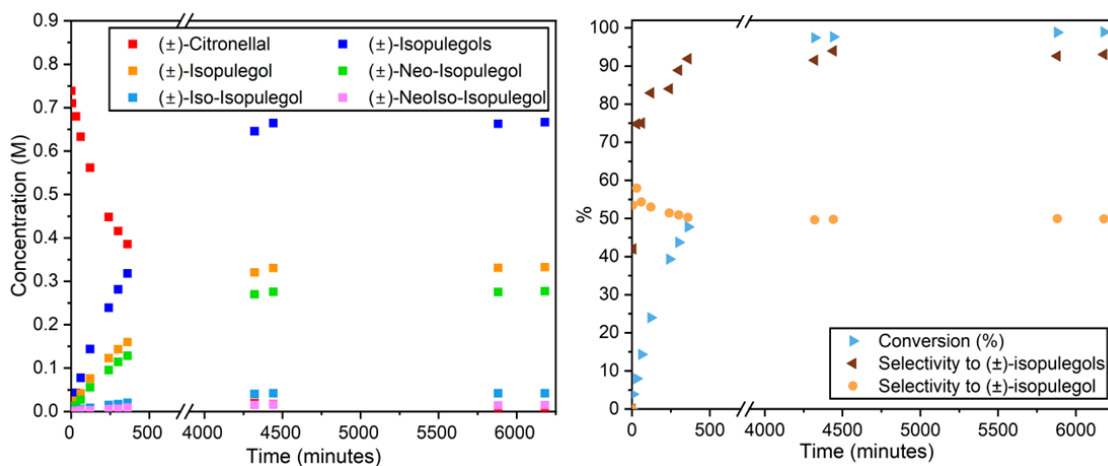
Experiment 6: 90 °C, [Citronellal] = 0.44 M, Citronellal:Sc ratio: 8.3



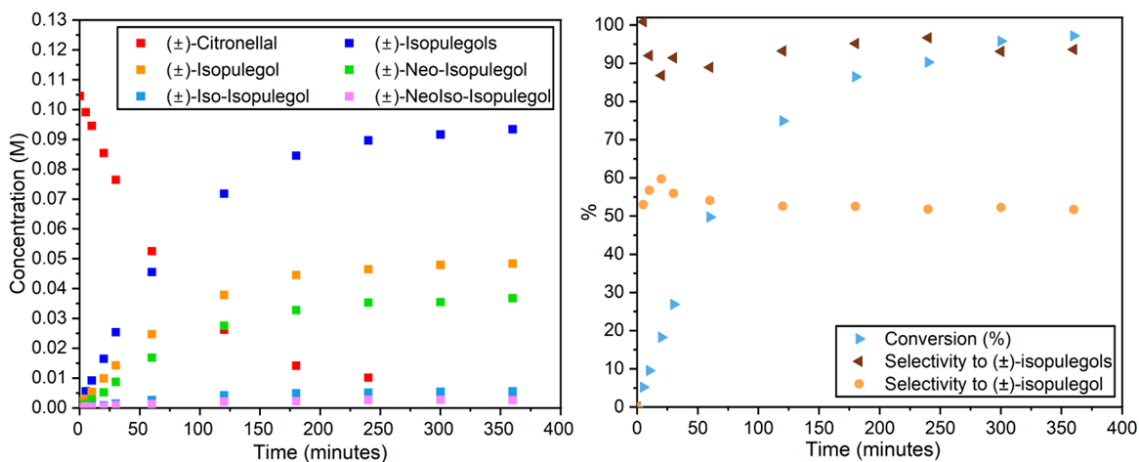
Experiment 7: 90 °C, [Citronellal] = 0.45 M, Citronellal:Sc ratio: 8.4



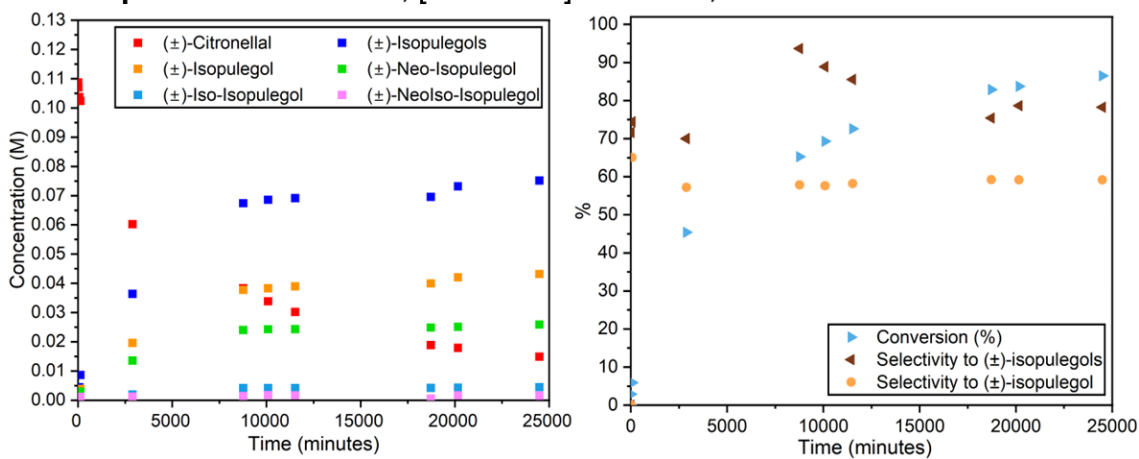
Experiment 8: 70 °C, [Citronellal] = 0.74 M, Citronellal:Sc ratio: 14.0



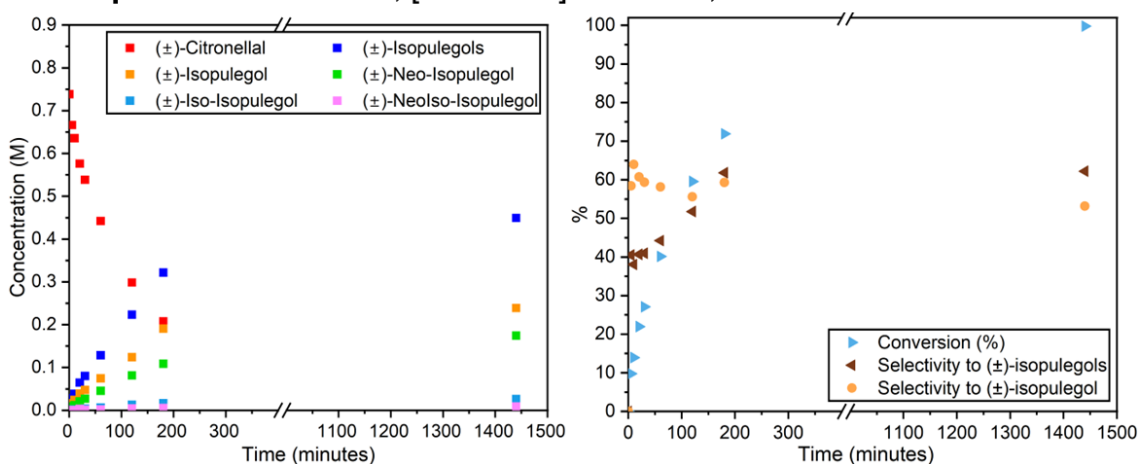
Experiment 9: 70 °C, [Citronellal] = 0.11 M, Citronellal:Sc ratio: 2.5



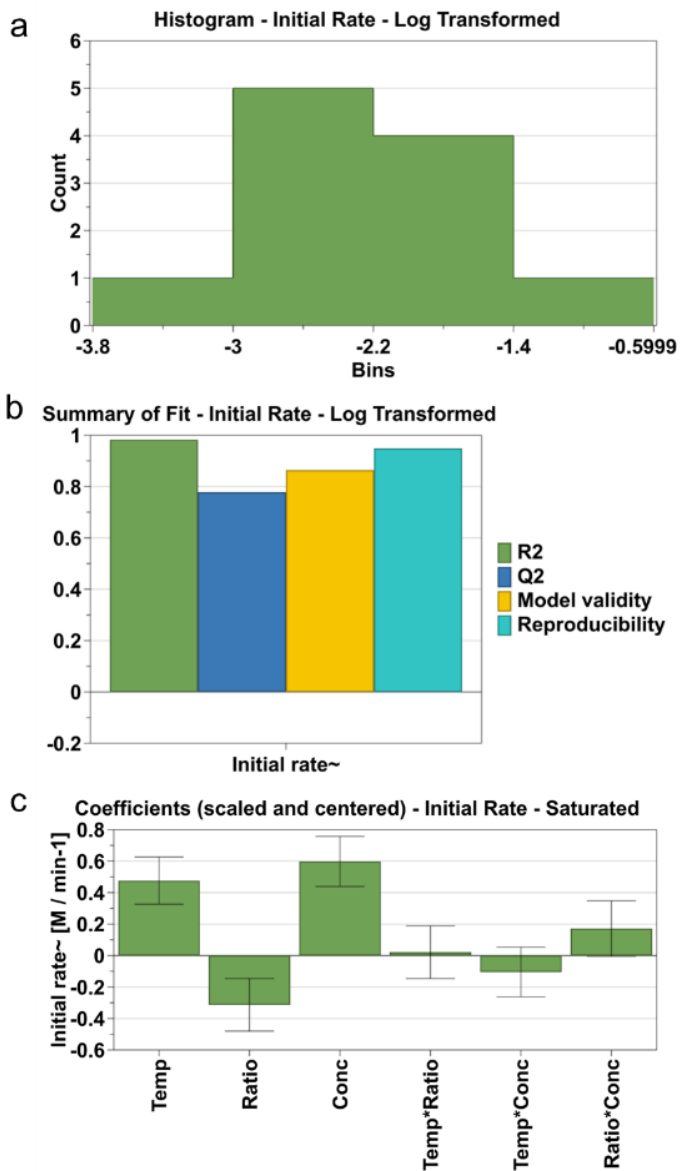
Experiment 10: 70 °C, [Citronellal] = 0.11 M, Citronellal:Sc ratio: 13.5



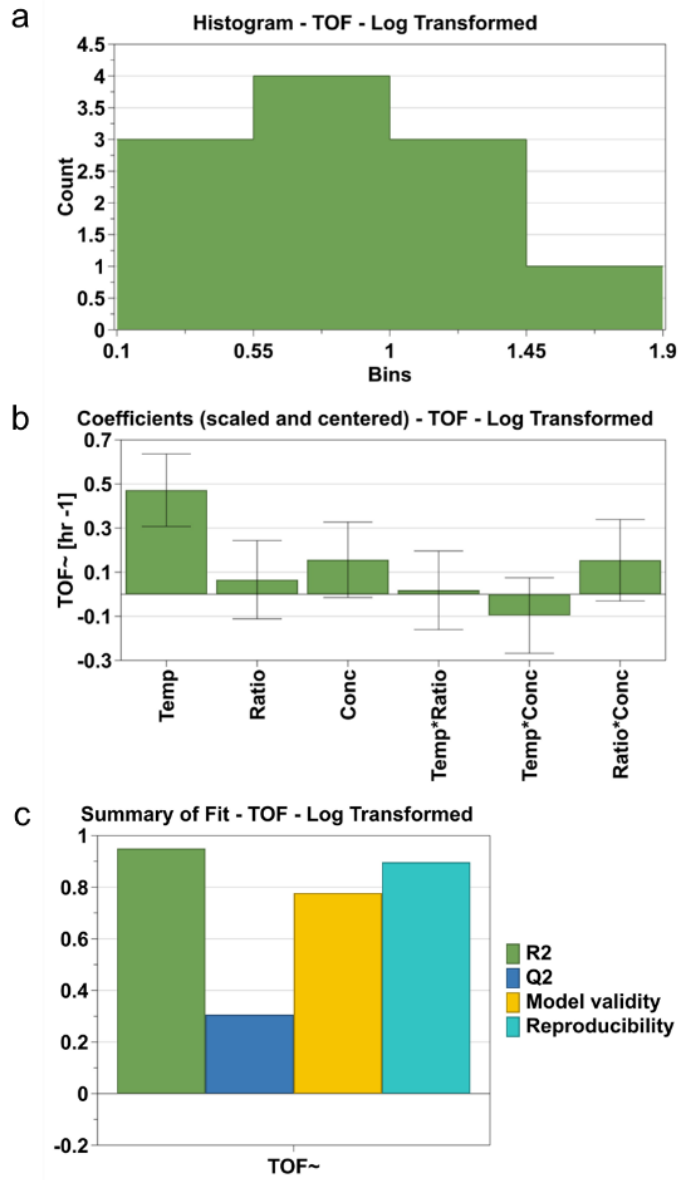
Experiment 11: 70 °C, [Citronellal] = 0.74 M, Citronellal:Sc ratio: 2.8



2.8.1.3 Initial Rate, log transformed, saturated model (see section 2.4.2.2)



2.8.1.4 TOF, log transformed, saturated model (see section 2.4.2.3)



Chapter 3 Development of a novel metal-organic framework catalyst suitable for continuous flow operations

3.1 Introduction

In most cases, reported MOF-based heterogeneous catalysts have been used in a batch mode of operation.¹⁰² Despite this, there have been some successful examples employing these materials in a continuous mode of operation which were summarised by Garcia and colleagues.¹⁵⁸

Like many other catalytically active heterogeneous species, MOFs typically exist as fine powders in their pure form so their direct application in flow reactors (e.g. packed-bed reactors) may lead to large pressure drops across the reactor or blockages. One approach to negate such effects is to shape the powdered MOFs into larger structures by in-situ growth on a substrate, i.e. the active species is anchored onto larger-sized shaped support materials.²⁶⁷ Analogous to this concept, for industrial applications catalysts are commonly immobilised onto supports of various shapes such as monoliths, extrudates and porous beads. Common support materials include alumina, silica, polymers and carbon.^{18, 56}

As well as packing regularly enough to prevent a large pressure drop across the reactor, catalyst supports that are resistant to both crushing and abrasion when inside of the reactor are desirable to avoid breakdown and plug formation. These mechanical considerations are balanced with the requirement for maximising the surface area of the active component of the catalysts and immobilising this species to the support in a manner that ensures sufficient stability for long-term industrial operation (e.g. to prevent leaching or physical detachment over time). Additional consideration must be given to immobilisation approaches as physisorption or the formation of a single covalent bond between the active catalyst and support may not be robust enough for continuous flow operations.³⁰

Activated carbon (AC)-based supports, which come in a range of different forms, are widely used because of their favourable catalyst support properties, including high surface areas up to 500 - 1500 m² g⁻¹, functionalisable surfaces, and high chemical and thermal stability (see section 1.3 for more discussion).^{268, 269} One promising AC-based support material which provides a good balance between macro- and nano-scale properties, thus making them suitable for continuous flow operations, is polymer-based spherical activated carbon (PBSAC).¹⁷⁹ These

supports are mechanically strong, with commercially available spherical activated carbon pellets exhibiting a regular, tunable size and possessing a high, graphitic carbon surface area for catalyst deposition. Moreover, their successful operation in flow reactors has been established (see section 1.3.2). Previous research into the use of PBSAC spheres as catalyst supports has primarily involved active species such as metal nanoparticles,^{32, 186-191} metal oxides,¹⁹³⁻¹⁹⁵ and ionic liquids.^{196, 197, 270, 271} However, composite materials incorporating more complex catalytic nanomaterials, for example MOFs, is significantly less developed.^{199, 272}

In section 1.2.1, we discussed the MIL-100(M) (M = metal centre) series of MOFs which are an isostructural series of large-pore MOFs known to exhibit Lewis acid catalytic activity via metal-containing M₃O trimers situated throughout the framework. MOFs of this type have a general stoichiometry of [M₃O(BTC)₂X], where M is a metal, BTC is benzene-1,3,5-tricarboxylic acid (trimesic acid) and X is a singly charged anion required to balance the positive charge of the framework.¹⁰⁵⁻¹⁰⁷ MIL-100(Sc) exists as a powder, however, and so would not be appropriate to directly study in continuous flow reactors. We therefore decided to immobilise this species onto PBSAC spheres and study the catalytic activity in continuous flow. Whilst the formation of composite materials consisting of MIL-100(Fe) and activated carbon has previously been reported elsewhere,^{273, 274} the physical form of these materials have been limited to powders. The formation of MIL-100 MOFs immobilised on macroscopic support materials such as PBSAC spheres is therefore a priority for incorporation into continuous flow reactors.

In this chapter we report the synthesis and characterisation of a novel Lewis acidic heterogeneous catalyst for operation in continuous flow consisting of catalytically active MOF MIL-100(Sc) supported onto PBSAC spheres, termed MIL-100(Sc)@PBSAC.

3.2 Synthesis of MIL-100(Sc)@PBSAC composites

The shaping of MOFs into larger structures is regarded as essential for their industrial application. Recent reviews highlight the efforts being made regarding the shaping of these materials.^{267, 275, 276} These review articles also highlight recent efforts in preparing shaped materials via in-situ crystallisation of MOFs

onto a substrate, indicating such an approach is considered as a feasible route to shaped MOF materials.

Section 1.3.2 discussed the merits of using PBSAC spheres as a support material in continuous flow, and studies regarding this directly in a pharmaceutical setting have already been carried out.³² The in-situ growth of MOFs on this support could serve as an ideal way to design new catalysts for continuous flow systems.

The incorporation of MOFs onto AC-based supports is not a novel concept, and a number of examples exist regarding the fabrication of such materials, typically for adsorption-related applications – see list of MOF@AC materials for adsorption applications in Table 24.

Table 24 shows some of the most popular examples of such materials. The most common approach taken to prepare these materials has been the use of in-situ hydrothermal or solvothermal synthesis; these syntheses are typically carried out as an extension of conventional MOF synthesis in which the activated carbon is simply added to the reaction vessel that was used to prepare the MOF.

The favourable properties of PBSAC spheres, however, have not yet fully been exploited with only two examples to date^{198, 199} that involve the fabrication of a MOF@PBSAC composite; neither demonstrated catalysis in continuous flow applications, although one of the materials was used as a catalyst in the degradation of chemical warfare agents.¹⁹⁹ Typically, powdered activated carbon has been used to support the MOF which is not desirable from a flow chemistry perspective due to the large pressure drop across the reactor and potential reactor blockage.

Previous work^{273, 274} has shown that the incorporation of MIL-100(M) MOFs onto AC powders is possible. Hernández-Maldonado *et al.*²⁷³ immobilised MIL-100(Fe) onto AC powder for the removal of contaminants from water. The composite system was found to be reusable after three cycles with no loss in adsorption ability and retained a high degree of crystallinity proving that these materials can be successfully immobilised onto activated carbon.¹⁹⁹

Table 24: Summary of key papers showcasing the preparation of metal-organic framework-activated carbon composite materials.

Year	Material	Synthesis	Application	Ref
2011	MOF-5 on powdered platinum doped AC	Solvothermal	Hydrogen storage	277
2013	[Ln ₂ (C ₄ H ₄ O ₄) ₃ (H ₂ O) ₂].H ₂ O on AC ^a	Hydrothermal	Adsorption (toxic compounds)	278
2013	MIL-101(Cr) on pelletised AC	Hydrothermal	Gas storage (hydrogen)	279
2009 - 2013	HKUST-1 on PBSAC	Co-agglomeration in rotary kiln	Adsorption	198
2015	HKUST-1 on powdered AC	Hydrothermal ^b	Adsorption (methane)	280
2016	HKUST-1 on powdered AC	Solvothermal	Adsorption (dye removal)	281
2016	HKUST-1 on powdered AC ^c	Heating ^d	Electrode	274
2016	MIL-100(Fe) on powdered AC	Reflux	Electrode	274
2017	MOF-199 on powdered AC	Hydrothermal	Adsorption (sulphur compound)	282
2018	MIL-101(Cr) on powdered AC	Hydrothermal	Gas storage and capture (methane storage, CO ₂ capture)	283
2018	M-BTC (M = Mn, Fe, Cu, Co) on powdered AC	Solvothermal, ^e Hydrothermal, ^e Heating	Oxygen reduction catalyst	284
2019	MIL-88B on powdered AC	Solvothermal	Photocatalytic dye degradation (from wastewater)	285
2019	STAM-17-OEt on granular AC	Reflux	Adsorption (ammonia removal)	286
2019	MIL-101(Cr) on powdered AC	Hydrothermal	Adsorption (dye removal)	287
2020	MIL-100(Fe) on powdered AC	Solvothermal	Adsorption (water contaminants)	273
2020	UiO-66 on powdered AC	Solvothermal	Adsorption (of cationic and anionic metals)	288
2021	ZIF-67 on powdered AC	Solvothermal	Oxygen reduction catalyst	289
2021	UiO-66(Zr) on PBSAC and fabric AC	Layer-by-layer and solvothermal	Detoxification of warfare agents	199
2022	MIL-53(Fe) on powdered AC	Solvothermal	Adsorption (dye removal)	290
2022	MIL-101(Cr) on powdered AC	Hydrothermal	Gas storage (hydrogen)	291
2023	Pellets of USTA-16 and AC	Pre-made MOF and AC pelletised	Gas capture (CO ₂)	292

^a Form of AC not stated. ^b Stirring maintained throughout whole synthesis. ^c Pellets were also made of the powdered samples by adding 5% PVDF binder. ^d Heating below reflux. ^e Carried out in glass pressure tube.

Based on the precedent set by the existing literature, a logical first step was to test whether MIL-100(Sc)@PBSAC composites could feasibly be prepared by in-situ solvothermal approaches (like for a majority of the existing examples of related materials). This initial approach served as a proof of concept that such a material could be formed, which if it could, would open the door for the exploration of other, more versatile synthetic approaches (e.g. reflux).

3.2.1 Solvothermal synthesis

In an initial synthesis, PBSAC spheres were added to the autoclave reaction vessel and a synthesis analogous to that carried out in section 2.2.1 for powdered MIL-100(Sc) was carried out (Table 25). The quantity of PBSAC spheres was taken as 52% w/w MIL-100(Sc) loading, assuming 100% yield of MIL-100(Sc) formation in immobilised form with a stoichiometry of $[\text{Sc}_3\text{O}(\text{BTC})_{1.32}(\text{OH})_{3.31}]$, as determined when prepared solvothermally – see section 2.2.3 for a calculation.

At this scale, the amount of PBSAC spheres added to the reaction vessel was \approx 150 mg which, without scaling-up the synthesis (which, in turn, could alter the properties of the resultant material), would demand many repeat syntheses upon use in continuous flow. For example, one flow reaction typically used \approx 1 g of MIL-100(Sc)@PBSAC (see section 4.3). Thus, with an eye of future application in flow reactors these initial conditions were deemed impractical. Nevertheless, this approach would serve as an initial demonstration of the fabrication of this novel material.

Table 25: Conditions employed for synthesis of powdered MIL-100(Sc) in this work, based on the conditions used by Wright *et al.*²⁸⁶

Time (hours)	Solvent	Temperature (°C)	M:L molar ratio ^a	MIL-100(Sc) loading (% w/w) ^b
48	DMF	150	2:1	52%

^a ratio of $(\text{Sc}(\text{NO}_3)_3 \cdot x\text{H}_2\text{O})$ and trimesic acid. In the formula of scandium nitrate hydrate, it was assumed that $x = 3$. ^b Assuming 100% MIL-100(Sc) yield and immobilisation on PBSAC spheres.

The resultant material is shown in Figure 67a illustrating that a white material had coated the outside of many of the PBSAC spheres. It should also be noted that significant amounts of loose MIL-100(Sc) had also formed independently of the spheres. PXRD analysis of the sample was carried out where upon comparison with the simulated pattern of isostructural MIL-100(Cr) suggests that this white

coating was MIL-100(Sc) due to the observation of the characteristic MIL-100(Sc) peak at $2\theta = 9.5 - 11$ (Figure 67b) (note that the broad peak between $2\theta = 12.5 - 25$ at was due to the amorphous nature of the AC-based support^{286, 293}). This result suggests that an in-situ approach was successful at generating the targeted composite material.

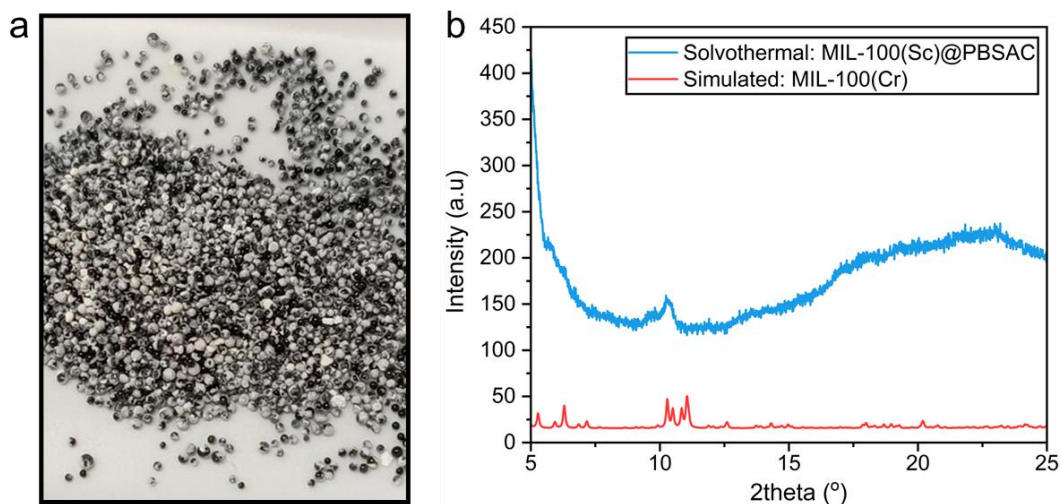


Figure 67: a) Image of material formed following in-situ solvothermal approach. b) Powder X-ray diffraction patterns of simulated MIL-100(Cr) (red) and MIL-100(Sc)@PBSAC material prepared by in-situ solvothermal synthesis (blue).

Following the initial synthesis via an in-situ solvothermal approach, we decided to explore alternative synthetic approaches due to some of the inherent disadvantages associated that might make it unfavourable to use, including the relatively small-scale of catalyst production (i.e. ≈ 150 mg at the scale explored).

One of the main reasons for avoiding the use of solvothermal synthetic approaches is due to the intrinsic safety implications surrounding the use of a closed vessel at elevated temperatures (and pressures).^{294, 295} Such dangers would be exaggerated even more at larger scales if larger-scale catalyst production were implemented. In 2021, the unsafe use of a hydrothermal autoclave reactor led to an unfortunate death at a research institute in China.^{295, 296} Reflux synthetic approaches offers a safer avenue to material production and also possess a number of additional advantages over solvothermal synthesis (Table 26). Most, if not all, synthetic chemistry labs will have access to reflux equipment (which is relatively cheaper) and know how to carry out reactions under solvent reflux. As such, reflux presents a more versatile approach to catalyst production.

Table 26: Comparison of solvothermal and reflux synthetic approaches.

Solvothermal	Reflux
Less safe	Safer
More expensive, less conventional equipment	Cheaper, conventional equipment
Less common technique ^a	Very common, widespread technique
No stirring ^b	Stirring

^a In context of general synthetic chemistry. ^b In autoclave reactor configuration used in this work stirring could not be carried out.

The autoclave reactor configuration used for this work also did not allow for stirring during the synthesis to improve the contact between reagents. Silvestre-Albero *et al.*²⁸⁰ highlighted the importance of stirring during MOF-AC synthesis to minimise the reactants' diffusional limitations so that the MOF (HKUST-1) could preferentially crystallise in the pores of the AC support. The researchers wanted the MOF to crystallise in the pores to protect it from mechanical compression. Such considerations are also important when designing catalysts for flow processes where high pressures are employed. Limiting MIL-100(Sc) formation to the pores of PBSAC spheres may offer greater protection for the MOF, potentially reducing the rate of leaching over the course of a flow reaction. MIL-100(Sc) appeared to crystallise on the exterior of the PBSAC spheres during the solvothermal synthesis, providing further justification for attempting a reflux-based synthetic approach.

The decision to pursue a reflux approach to MIL-100(Sc)@PBSAC fabrication was also bolstered by how easily transferrable the synthesis of MIL-100(Sc) was to reflux. Mitchell *et al.*²¹³ prepared MIL-100(Sc) using reflux synthesis with the resultant material possessing improved crystallinity and BET surface area in less time (8 hours versus 48 hours for the solvothermal synthesis) than for MIL-100(Sc) prepared solvothermally. In this research, crystalline MIL-100(Sc) was made by reflux under identical conditions (see Figure 72, green for PXRD). This resultant material prepared in this research was calculated to possess the formula: $[\text{Sc}_3\text{O}(\text{BTC})_{1.45}\text{OH}_{2.65}]$ using the approach with TGA that has previously been used to calculate MIL-100(Sc) stoichiometry (see section 2.2.3 and 3.3.3.1 for calculation). As the composition of MOF precursors used for the powdered synthesis was identical to that used for the composite synthesis in this work, it was assumed that any MIL-100(Sc) immobilised onto PBSAC spheres in this work would possess this formula.

3.2.2 Reflux synthesis of MIL-100(Sc)

For the synthesis of MIL-100(Sc)@PBSAC composites via reflux we adapted a procedure from Morris *et al.*¹² who successfully synthesised a composite of MOF STAM-17-OEt on granular AC by reflux. Figure 68 details this process. Not only did their reflux step incorporate stirring, but there were also two steps prior to this that involved stirring the MOF precursors with the AC to greater disperse them on the support. Other, similar mixing steps have also been applied to the synthesis of a number of other MOF@AC composites^{273, 274, 280-286, 288, 290} which was part of the rationale for choosing these synthetic conditions.

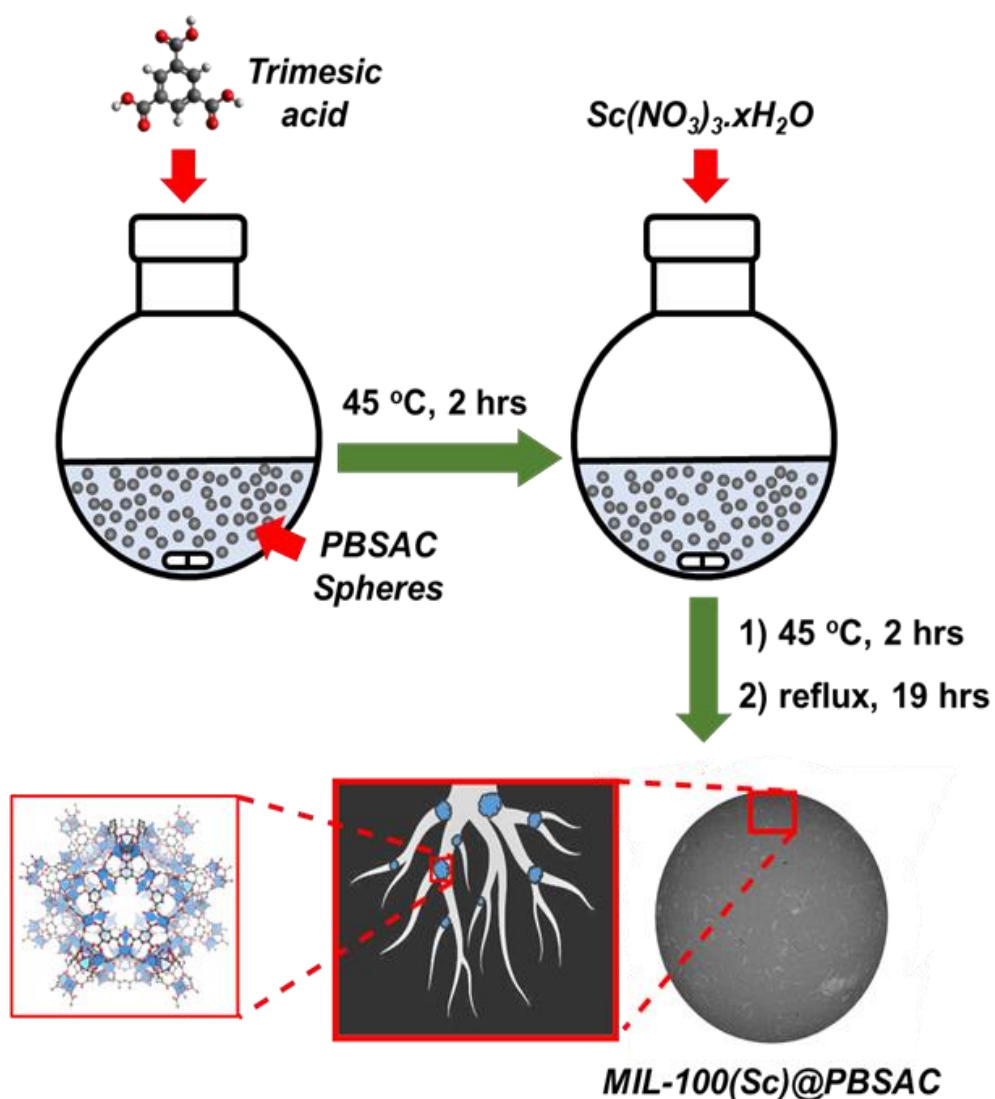


Figure 68: Synthetic procedure of MIL-100(Sc)@PBSAC composites carried out in this work.

In the procedure, unfunctionalised PBSAC spheres were stirred in a solution of trimesic acid in DMF for 2 hours at 45 °C. Then, following addition of scandium

nitrate, the solution was stirred for another 2 hours at 45 °C. The solution was then refluxed for 19 hours. Upon minutes of the solution reaching reflux (i.e. the identification of vapour condensation back into the reaction vessel) the solution turned white. After the synthesis of MIL-100(Sc)@PBSAC spheres, the material was activated by stirring in methanol for 72 hours at 40 °C to replace residual solvent material present inside of the pores of the framework. Finally, the material was dried at 60 °C under vacuum.

Similar to previous observations²⁸⁶ with other MOF@AC composite materials, the visual appearance of MIL-100(Sc)@PBSAC spheres after reflux was unchanged from the as-received PBSAC spheres. This consistent appearance suggested that MIL-100(Sc) formation was not occurring on the exterior of the PBSAC spheres (Figure 69). This may have been caused by the stirring and such a feature might be considered beneficial from a flow process perspective due to the enhanced catalyst stability associated with protecting the MOF in the pores of the support.²⁸⁰ Typically, a small amount of material was also lost from the PBSAC in the form of black powder owing to impact with the stirrer bar inside of the reaction vessel over time.



Figure 69: Visual appearance of MIL-100(Sc)@PBSAC (image) was unchanged from as received PBSAC spheres.

Due to the formation of excess loose MIL-100(Sc) in the in-situ solvothermal production of MIL-100(Sc)@PBSAC (section 3.2.1), we attempted a synthesis under both identical conditions (i.e. a maximum theoretical MIL-100(Sc) loading of 52% w/w) and at a range of other maximum theoretical loadings (6%, 12% and 29% w/w) (i.e. the amount of MOF immobilised onto the PBSAC spheres as a

percentage of the maximum that could have formed, assuming 100% yield of MIL-100(Sc) immobilisation on PBSAC spheres) in an attempt to reduce the amount of waste generated (in the form of loose, MIL-100(Sc) powder) in the synthesis. Scandium is also an expensive metal which provided further motivation for doing so.²⁹⁷

Adjustments to the loading were attempted by keeping the amounts of metal, linker and solvent added to the reaction vessel the same but adjusting the amount of PBSAC spheres added. Despite these adjustments, the formation of loose powdered MIL-100(Sc) was still observed in all syntheses. Identification of this powder as MIL-100(Sc) was confirmed by PXRD analysis (see appendix 3.5.1.1). The calculated immobilisation efficiencies of the synthesis (Table 27, all < 100%) means that this observation was unsurprising.

Table 27: Conditions employed for the reflux synthesis of MIL-100(Sc)@PBSAC in this work.

Maximum scandium / MIL-100(Sc) loading (% w/w)	Measured scandium / MIL-100(Sc) loading (% w/w) ^a	Immobilisation efficiency (%) ^b
14.30 / 52.57	0.77 ± 0.57 / 2.82 ± 2.11	5.4
7.82 / 28.76	0.88 ± 0.42 / 3.25 ± 1.53	11.3
3.23 / 11.87	1.75 ± 0.52 / 6.42 ± 1.93	54.2
1.63 / 5.98	1.47 ± 0.37 / 5.40 ± 1.35	90.3

^a Calculated by TGA. See section 3.3.3.1 for generalised calculation of the approach. The formula of MIL-100(Sc) was assumed to be $[\text{Sc}_3\text{O}(\text{BTC})_{1.45}(\text{OH})_{2.65}]$. ^b This is the amount of MOF immobilised onto the PBSAC spheres as a percentage of the maximum that could have formed, assuming 100% yield of MIL-100(Sc) immobilisation on PBSAC spheres.

Table 27 shows the maximum theoretical loading, measured loading (see section 3.3.3.1 for calculation) and subsequent efficiency of immobilisation of MIL-100(Sc). Inspection of the data shows that improvements in the MIL-100(Sc) loading onto PBSAC spheres were not observed in the higher loading syntheses, with the resultant calculated loadings all within experimental error of each other for each batch. This finding seems to suggest that the amount of MIL-100(Sc) formation onto the PBSAC spheres may have reached a maximum for this synthetic approach. Much higher loadings have been obtained previously with different forms of AC, indicating the maximum loading behaviour seen here may be due to the particular shape of the PBSAC spheres. When using granular AC, McHugh *et al.*^{286, 298} obtained large loadings of up to 77% w/w. They attributed

this high loading to the presence of large voids ($\approx 50 \mu\text{m}$) of the granular AC and found that for other forms of AC, which possessed a larger degree of microporosity and general lack of larger porosity, the immobilisation was not as effective as there was not enough space for MOF crystals to grow. Their finding that the MOFs may preferentially grow in larger voids is also corroborated by SEM-EDX analysis of MIL-100(Sc)@PBSAC composites in this research (section 3.3.4), indicating MIL-100(Sc) preferentially grows in cracks on the surface of the PBSAC spheres that are $\approx 3 \mu\text{m}$ in width.

Further investigation into the relationships between the properties of the support material and resultant MOF loadings are one avenue that could be explored further, and doing so could pave the way for optimising the loadings; such considerations are especially necessary when systems involve the use of expensive metals like scandium. If indeed the MOF prefers to grow in larger voids, then two ways of generating more cracks on the surface on the spheres could be to alter the degree of activation during preparation of the PBSAC spheres.²⁹⁹ This was not further pursued in this work as for the optimisation of the loading to be worthwhile, the catalytic properties need to be tested first which was the focus of this research.

Because similar loading values were measured for each attempted synthesis, thus making the 52.57% w/w and 28.76% w/w (maximum possible loading) syntheses very wasteful (immobilisation efficiencies of 5.4% and 11.3% respectively) for which excess loose powdered MIL-100(Sc) was observed to form, we chose to take forward the 11.87% w/w and 5.98% w/w maximum possible loading syntheses for further study. The synthesis of these materials produced the least amount of waste (i.e. loose powdered MIL-100(Sc)). Additionally, the production scales of these materials ($\approx 1 - 3 \text{ g}$) was more similar to the masses required for the flow reactions in this research ($\approx 1 \text{ g}$) (section 4.3), making these syntheses more suitable. The most catalytically active of these materials was then characterised using FIB-SEM-EDX, XPS, N_2 adsorption, and crush testing and evaluated in continuous flow.

The catalytic activity of the 11.87% w/w and 5.98% w/w loading samples was compared in batch using the intramolecular cyclisation of (\pm)-citronellal as the model reaction. This reaction was studied in Chapter 2. Table 28 shows the

experimental results of a reaction involving the two different samples and unfunctionalised PBSAC spheres as a control.

Table 28: Experimental data obtained when comparing the catalytic activity of the two batches of different loadings (11.87% w/w and 5.98% w/w maximum possible loading syntheses) in the attempted synthesis of MIL-100(Sc)@PBSAC and a control sample involving as received PBSAC spheres. Conditions: 0.1 M (\pm)-citronellal, 110 °C, toluene, 150 mg catalyst.

Material	Conversion after 2 hours (%)	Yield after 2 hours (%) ^a
PBSAC spheres (control)	6.4	1.1
5.98% w/w	13.5	8.1
11.87% w/w	74.1	59.8

^aYield of (\pm)-isopulegols.

The data suggest that despite the batches possessing similar loadings, the 11.87% w/w sample was significantly more active than the 5.98% w/w sample (59.8% yield versus 8.1% yield respectively), with the latter not showing significant improvements above the control sample (1.1% yield).

Because of the favourable catalytic activity results obtained with the 11.87% w/w composite batch, the corresponding synthesis was repeated to increase the total quantity of material and used for flow experiments. From this point forward, all reference to MIL-100(Sc)@PSBAC in this chapter corresponds to that prepared under the conditions employed to prepare a batch with a maximum loading of 11.87% w/w, a calculated loading value of 6.42% w/w (see section 3.3.3.1 for calculation).

3.3 Characterisation of MIL-100(Sc)@PBSAC

3.3.1 Studying the synthesis of MIL-100(Sc)@PBSAC

3.3.1.1 Confirming trimesic acid adsorption

With the conditions that would be used to synthesise MIL-100(Sc)@PBSAC composites decided, the synthesis of this material was studied in greater detail. Firstly, the pre-synthesis mixing step was studied in greater detail for the fabrication of this material. This step involved stirring the PBSAC spheres in a solution of trimesic acid in DMF for 2 hours at 45 °C and then stirring for another 2 hours at 45 °C following the addition of scandium nitrate to the solution. A qualitative measurement of trimesic acid adsorption onto PBSAC spheres in the

initial mixing step was recorded by carrying out TGA on a control sample in which PBSAC spheres and trimesic acid, in the quantities used in the synthesis (90.5 mg trimesic acid, 1.10 g PBSAC spheres), were stirred for 2 hours at 45 °C in DMF, washed with excess water and ethanol and then stirred in methanol for 72 hours (see section 6.3.5). In the TGA profile of this PBSAC-trimesic acid control sample (Figure 70a) there is a small weight loss at approximately 300 °C corresponding to the thermal decomposition of adsorbed trimesic acid (Figure 70b), serving to confirm that trimesic acid adsorbs in the initial mixing step.

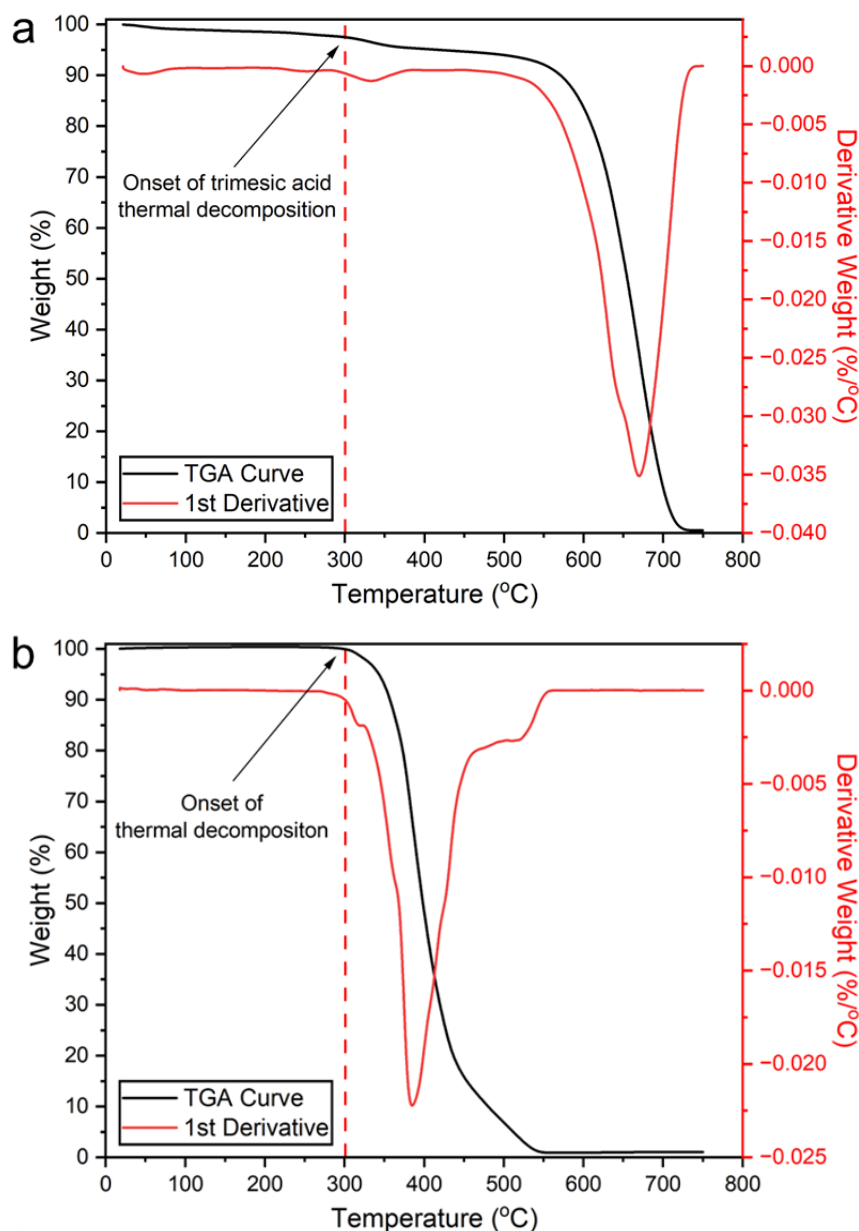


Figure 70: a) TGA profile of PBSAC-trimesic acid control sample. There is a small weight loss beginning at approximately 300 °C corresponding to the thermal decomposition of adsorbed trimesic acid. b) TGA profile of trimesic acid. Thermal decomposition begins to occur at approximately 300 °C. Figures reproduced with permission.³⁰⁰

3.3.1.2 Repeatability of synthesis

Batch-to-batch reproducibility in catalyst synthesis, i.e. the repeat production of a material with consistent properties, is highly desirable when designing catalysts suitable for industrial employment. To assess the reproducibility of synthesis of MIL-100(Sc)@PBSAC composites, the catalytic activity towards the intramolecular cyclisation of (\pm)-citronellal was compared for each batch (24 batches) as a gauge of the reproducibility, with the yield of (\pm)-isopulegols recorded after 2 hours of reaction.

Figure 71 shows the catalytic activity across the synthesis of 24 batches of MIL-100(Sc)@PBSAC, with an average yield of 25.5% \pm 4.6% (%RSD = 17.9%). The variation in these results is also unsurprising given the variation in scandium loading observed for this material (1.75% \pm 0.52%, %RSD = 29.7%) (see section 3.3.3.1 for loading determination) which had a larger %RSD value. The measurement of reaction yield was also carried out relatively early on in the timescale of the reaction where variation in the concentrations of species is the largest (later on in the reaction the opposite is true). As-received PBSAC spheres gave no yield in the same time period.

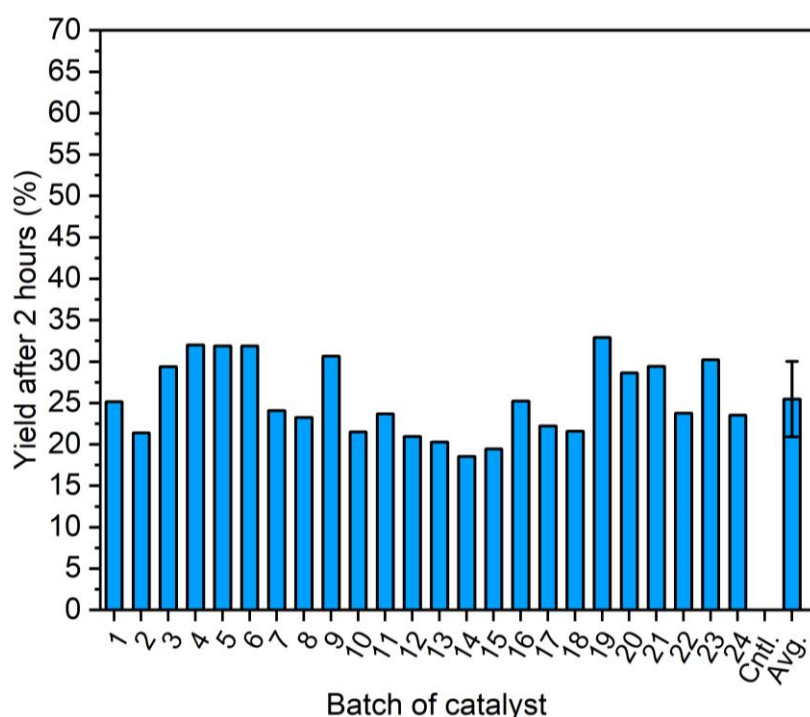


Figure 71: An assessment of the repeatability of synthesis of MIL-100(Sc)@PBSAC composites over 24 batches. The intramolecular cyclisation of (\pm)-citronellal was used as the model reaction, with the yield after 2 hours of reaction. Conditions: 0.1 M (\pm)-citronellal, toluene, 110 °C, 65 mg catalyst.

3.3.1.3 Confirming crystalline MIL-100(Sc) immobilisation

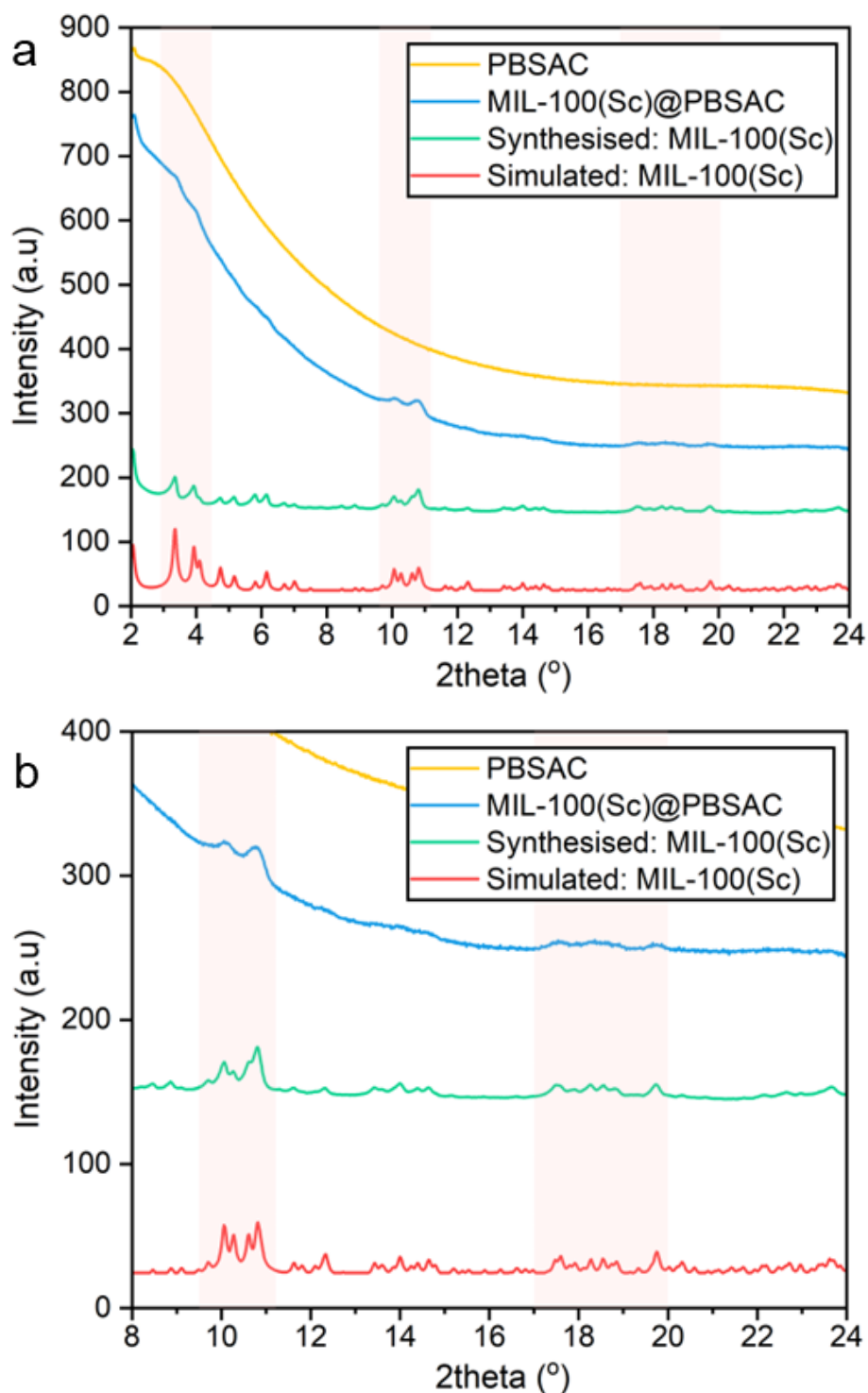


Figure 72: a-b) Powder X-ray diffraction patterns of MIL-100(Sc) simulated by adjusting the unit cell parameter of MIL-100(Cr) to 74.518 Å (red), MIL-100(Sc) synthesized by reflux (green), MIL-100(Sc)@PBSAC composites (blue) and PBSAC spheres (control) (yellow). N.B. The data presented in (b) is identical to (a) but displays narrower y-axis and x-axis ranges to enable clearer MIL-100(Sc) peak visualisation. Figures reproduced with permission.³⁰⁰

The immobilisation of crystalline MIL-100(Sc) onto PBSAC spheres was confirmed using powder X-ray diffraction (Figure 72). Despite significant diffuse background scattering in the powder pattern of MIL-100(Sc)@PBSAC as a result of the amorphous phases present in the activated carbon support,^{286, 293} there are visible peaks at $2\theta = 3 - 4.5, 9.5 - 11$ and $17 - 20^\circ$ corresponding to the presence of crystalline MIL-100(Sc). This assignment was made by comparison with the underlying simulated pattern of MIL-100(Sc) (calculated by adjusting the unit cell parameter (a) of MIL-100(Cr), as reported previously²⁰⁷) and by comparison with reflux prepared powdered MIL-100(Sc).^{105, 119} This pattern confirms that crystalline MIL-100(Sc) was incorporated onto the PBSAC spheres.

3.3.2 Studying porosity

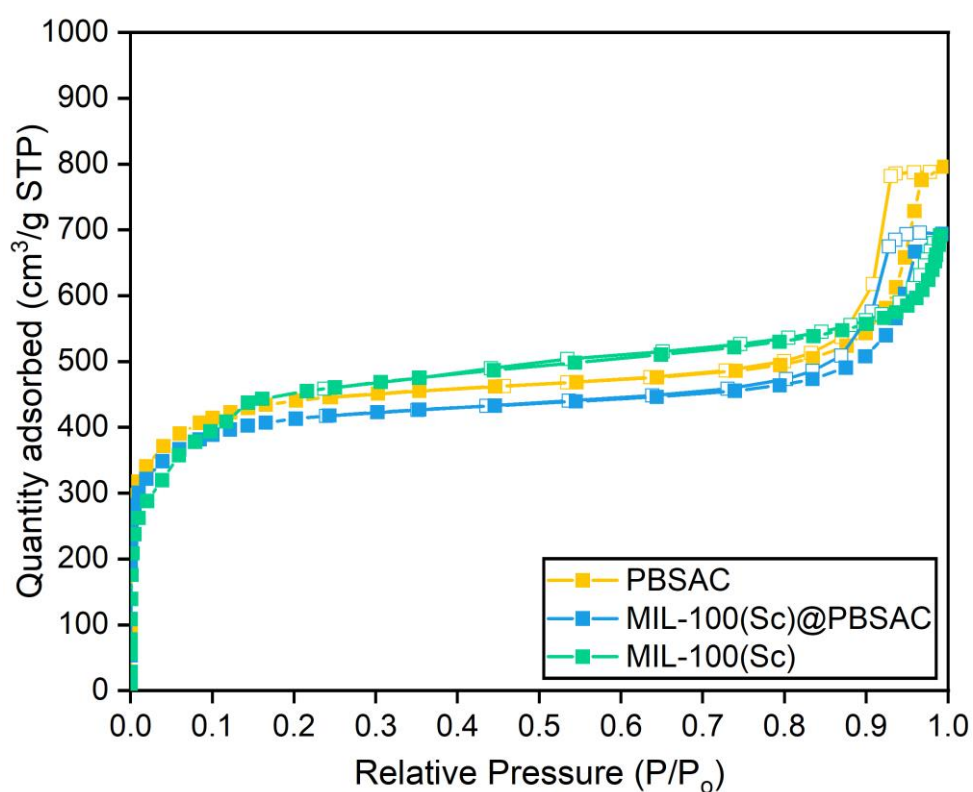


Figure 73: N₂ adsorption/desorption isotherms of PBSAC (yellow), MIL-100(Sc)@PBSAC (blue) and MIL-100(Sc) (green). The adsorption isotherm is represented by filled points whilst the desorption isotherm is represented by hollow points. Figure reproduced with permission.³⁰⁰

N₂ adsorption/desorption analysis was used to characterise the surface and pores in the materials. Unfunctionalised PBSAC spheres displayed a type IV isotherm characteristic of mesoporosity, with a notably steep rise in adsorption at low P/P₀ values also suggesting the presence of micropores in PBSAC (Figure 73). This material also possesses a large BET surface area of 1648 m²/g which

is beneficial for a high dispersion of catalyst particles (Table 29). As discussed in section 2.2.4, MIL-100(Sc) exhibits an N₂ isotherm characteristically intermediate to type I and type IV isotherms including a secondary uptake at P/P₀ = 0.12, in line with previous reports for MIL-100(M, M = Fe, Cr) materials.¹⁰⁵ The BET surface area of MIL-100(Sc), when prepared in an analogous manner to the composite but without the addition of the PBSAC spheres, was calculated to be 1628 m²/g. When the constituent materials were combined to form MIL-100(Sc)@PBSAC, a slight decrease in BET surface area to 1544 m²/g was recorded. We hypothesise that this is a result of some of the pores of the PBSAC spheres becoming blocked by the MOF upon composite formation. Decreases in the surface area of similar magnitudes have been reported for other MOF@AC composite materials relative to the surface area of the constituent materials previously.^{277, 288, 301}

Table 29: BET surface area, micropore volume and total pore volume of PBSAC, MIL 100(Sc) and MIL-100(Sc)@PBSAC.

Sample	BET Surface area (m ² /g) ^a	Pore volume ^b (cm ³ /g)	Micropore volume ^c (cm ³ /g)
PBSAC	1648	1.23	0.41
MIL-100(Sc)	1628	1.07	0.13
MIL-100(Sc)@PBSAC	1544	1.07	0.39

^a BET surface area calculated using the BETSI method. See reference ²³² for more information. ^b Calculated at P/P₀ = 0.99. ^c Calculated from t-plot.

Upon immobilisation of MIL-100(Sc) onto PBSAC spheres, a decrease in the total pore volume of PBSAC from 1.23 cm³/g to 1.07 cm³/g was observed, suggesting that MIL-100(Sc) is partially occupying the pores of PBSAC spheres (Table 29). There was no significant difference in the micropore volume of MIL 100(Sc)@PBSAC (0.39 cm³/g) compared to unfunctionalised PBSAC spheres (0.41 cm³/g). Figure 74 shows the BJH desorption differential pore volumes of PBSAC, MIL-100(Sc)@PBSAC and MIL-100(Sc) in the range of 0 - 50 nm. This visualisation illustrates that there is a decrease in the pore volume of MIL-100(Sc)@PBSAC composites compared to unfunctionalised PBSAC spheres.

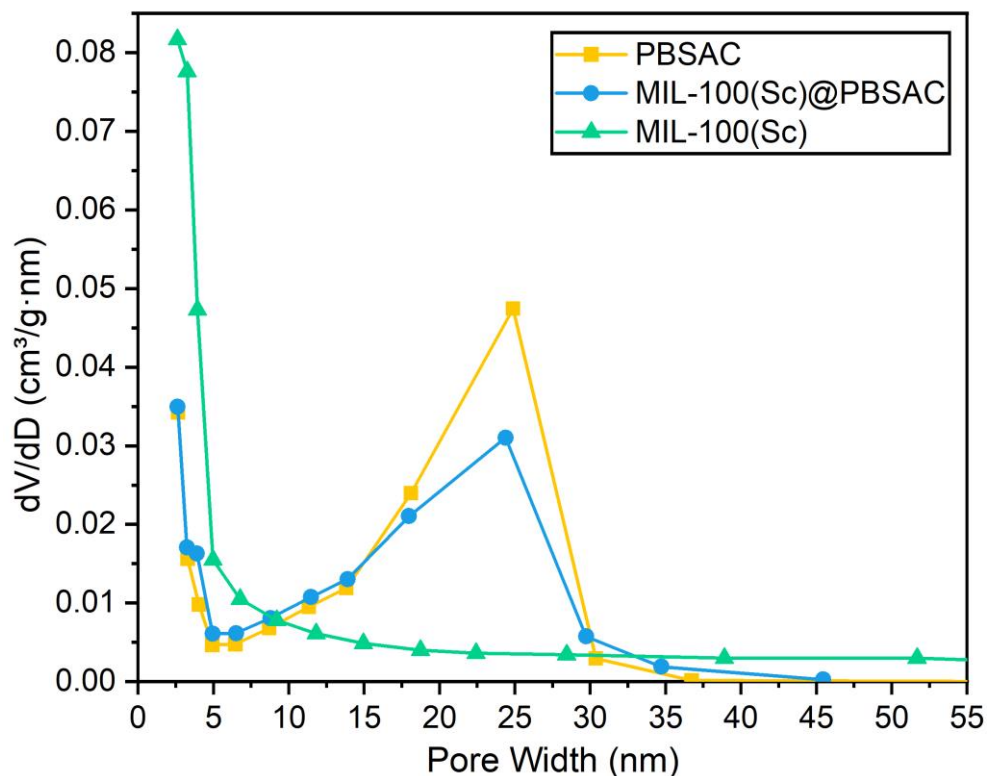
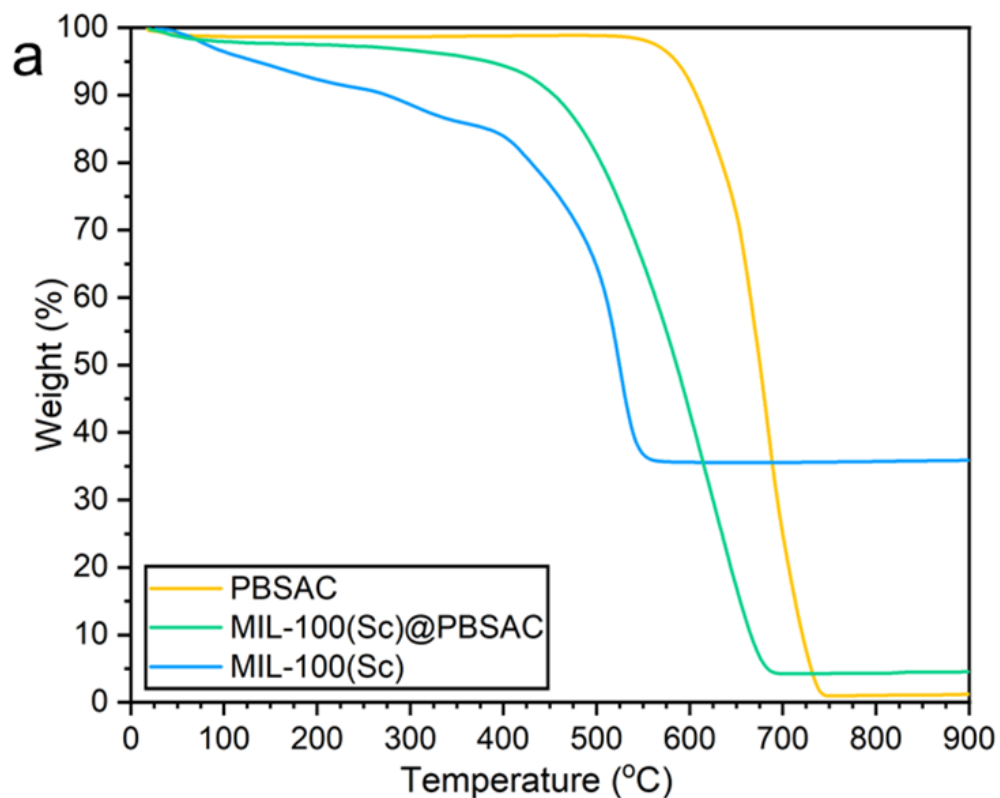


Figure 74: Plot of BJH desorption differential pore volume vs. pore width for PBSAC (yellow), MIL-100(Sc)@PBSAC (blue) and MIL-100(Sc) (green). Figure reproduced with permission.³⁰⁰

3.3.3 Studying thermal stability, composition and metal loading



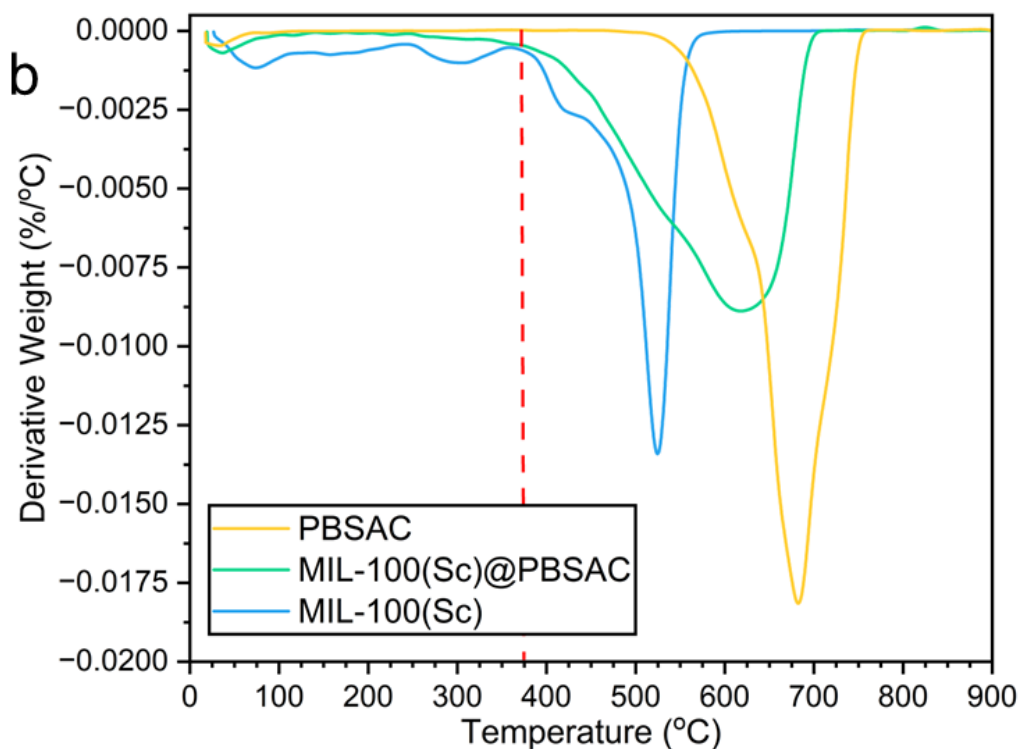


Figure 75: a) TGA profiles of PBSAC (yellow), MIL-100(Sc)@PBSAC (green) and MIL 100(Sc) (blue) in flowing air. b) TGA derivative weight loss plot for PBSAC (yellow), MIL-100(Sc)@PBSAC (green) and MIL-100(Sc) (blue). MIL-100(Sc) and MIL-100(Sc)@PBSAC decomposition begins at a similar temperature (≈ 380 °C). Figures reproduced with permission.³⁰⁰

Insight into the thermal stability of the materials and the loading of MIL-100(Sc) on PBSAC spheres was obtained using thermogravimetric analysis (TGA) (Figure 75a-b). As discussed in section 2.2.2, there are three characteristic mass changes in the TGA profiles of MIL-100 MOFs: at 0 - 100 °C is the removal of free solvent present in the pores of the framework, 100 - 350 °C shows loss of more tightly bound solvent to the metal centres throughout the framework and finally at ≈ 380 °C the breakdown of the MOF structure occurs.^{105, 111}

In the TGA profile of the MIL-100(Sc)@PBSAC composite (Figure 75a, green), the material exhibits a steady decrease in mass of approximately 5% (corresponding to the loss of material bound to the Sc^{3+} sites) before framework decomposition occurred at ≈ 380 °C. The composite MIL-100(Sc)@PBSAC was found to be less thermally stable than unfunctionalised PBSAC spheres where thermal decomposition occurred at ≈ 550 °C; with the thermal decomposition temperature being more similar in value to that of powdered MIL-100(Sc) where framework decomposition occurs at ≈ 380 °C (upon inspection of the 1st derivative weight Figure 75b). Incorporation into PBSAC spheres was therefore

shown not to improve the thermal stability of MIL-100(Sc), despite previous reports of enhanced MOF stability upon incorporation onto AC substrates.²⁷³

3.3.3.1 Calculating MIL-100(Sc) loading on PBSAC spheres by TGA

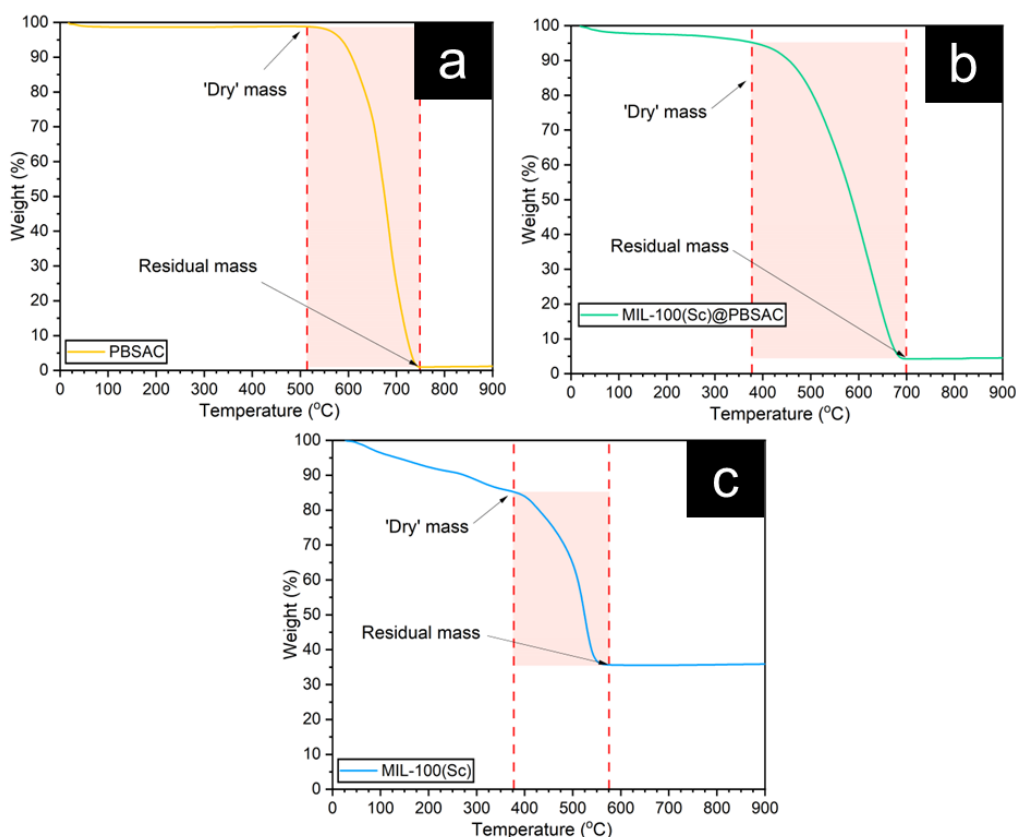


Figure 76: a) TGA profile of PBSAC spheres showing the dry mass (≈ 515 °C) and residual mass following framework decomposition at ≈ 740 °C. b) TGA profile of MIL-100(Sc)@PBSAC showing the dry mass (≈ 380 °C) and residual mass following framework decomposition at ≈ 700 °C. c) TGA profile of MIL-100(Sc) showing the dry mass (≈ 380 °C) and residual mass following framework decomposition at ≈ 580 °C. Figures reproduced with permission.³⁰⁰

An approach to the calculation of MIL-100(Sc) stoichiometry by TGA was discussed in section 2.2.3. An analogous approach was carried out to determine the stoichiometry of reflux-prepared, MIL-100(Sc) powder. When prepared by reflux, MIL-100(Sc) powder possesses a scandium wt.% of 27.2%, this scandium wt.% value may correspond to a 'dry' (i.e. following solvent removal) stoichiometry of $[\text{Sc}_3\text{O}(\text{BTC})_{1.45}(\text{OH})_{2.65}]$ where it is assumed that the anion used to balance the charge of the framework is OH^- . Under the assumption that this is also the formula of MIL-100(Sc) incorporated onto PBSAC spheres, full incorporation of the scandium used in the synthesis of MIL-100(Sc)@PBSAC

composites gives a 11.87% MIL-100(Sc) loading (a scandium loading of 3.23% w/w).

For MIL-100(Sc)@PBSAC composites (Figure 76b) and PBSAC spheres (Figure 76a), an average residual mass of 4.05 ± 0.80 % and 1.37 ± 0.40 % was determined, respectively, using Eqn. 33 and Eqn. 34.

The residual mass of PBSAC was subtracted from the residual mass of MIL-100(Sc)@PBSAC composites which gave the amount of Sc_2O_3 present in MIL-100(Sc)@PBSAC composite samples following framework decomposition. This value was then used to calculate the loading of scandium on PBSAC spheres (in MIL-100(Sc)@PBSAC) (Eqn. 34) (NB: Sc_2O_3 is 65.2% scandium by mass thus this was accounted for when determining the scandium loading).

$$\text{Resid. mass (\%)} = \frac{\text{mass after material decomposition (mg)}}{\text{'Dry' mass (mg)}} \times 100 \quad \text{Eqn. 33}$$

$$\begin{aligned} \text{Sc loading } \left(\% \frac{\text{w}}{\text{w}}\right) &= \frac{\text{Resid. mass composite (\%)} - \text{Resid. mass PBSAC (\%)}}{100} \times 65.2 \\ \text{Sc loading (\% w/w)} &= \frac{4.05 (\%) - 1.37 (\%)}{100} \times 65.2 \\ &= 1.75\% \text{ w/w} \pm 0.52\% \text{ w/w} \end{aligned} \quad \text{Eqn. 34}$$

The MIL-100(Sc) loading on PBSAC spheres was then calculated assuming that the framework had the stoichiometry $[\text{Sc}_3\text{O}(\text{BTC})_{1.45}(\text{OH})_{2.65}]$ with a 27.2% w/w scandium loading, as given in Eqn. 35. The MIL-100(Sc) loading on PBSAC spheres was calculated to be $6.42\% \pm 1.93\%$ w/w (a scandium loading of $1.75\% \pm 0.52\%$ w/w). The loading value obtained by carrying out these calculations was also similar in value to the value obtained with atomic absorption spectroscopy (AAS), $5.71\% \pm 0.93$ % w/w (a scandium loading of $1.55\% \pm 0.25$ % w/w). The loading values that were calculated were lower than the maximum value based on the mass of Sc used in the preparation (11.87 % w/w MIL 100(Sc) loading), which is in keeping with the observed formation of loose powdered MIL-100(Sc) in the reaction vessel alongside MIL-100(Sc)@PBSAC spheres.

$$\begin{aligned}
 \text{MIL} - 100(\text{Sc}) \text{ loading } \left(\% \frac{w}{w} \right) &= \frac{1.75}{\left(\frac{27.2}{100} \right)} \\
 &= 6.42 \% w/w \pm 1.93 \% w/w
 \end{aligned}
 \tag{Eqn. 35}$$

3.3.4 Studying the surface structure

The surface structure and location of MIL-100(Sc) on PBSAC spheres was studied using scanning electron microscopy and energy dispersive X-ray analysis (SEM-EDX). Although not visible to the naked eye, imperfections such as scratches and cracks ($\approx 3 \mu\text{m}$ in width) are situated throughout the outer surface of unfunctionalised PBSAC spheres (Figure 77). These cracks are a result of the activation procedure when PBSAC spheres are prepared.²⁹⁹ The EDX spectrum (Figure 77d) shows peaks assigned to characteristic X-ray emission from carbon, oxygen and small amounts of sulfur. The sulfur content was attributed to the polymer precursor used in PBSAC production. PBSAC production from polymers include sulfonic acid groups in the polymer, based on styrene and divinylbenzene, that serve as a crosslinking agent as their thermal decomposition leads to the formation of free radicals (and thus generation of cross-linkages).²⁹⁹

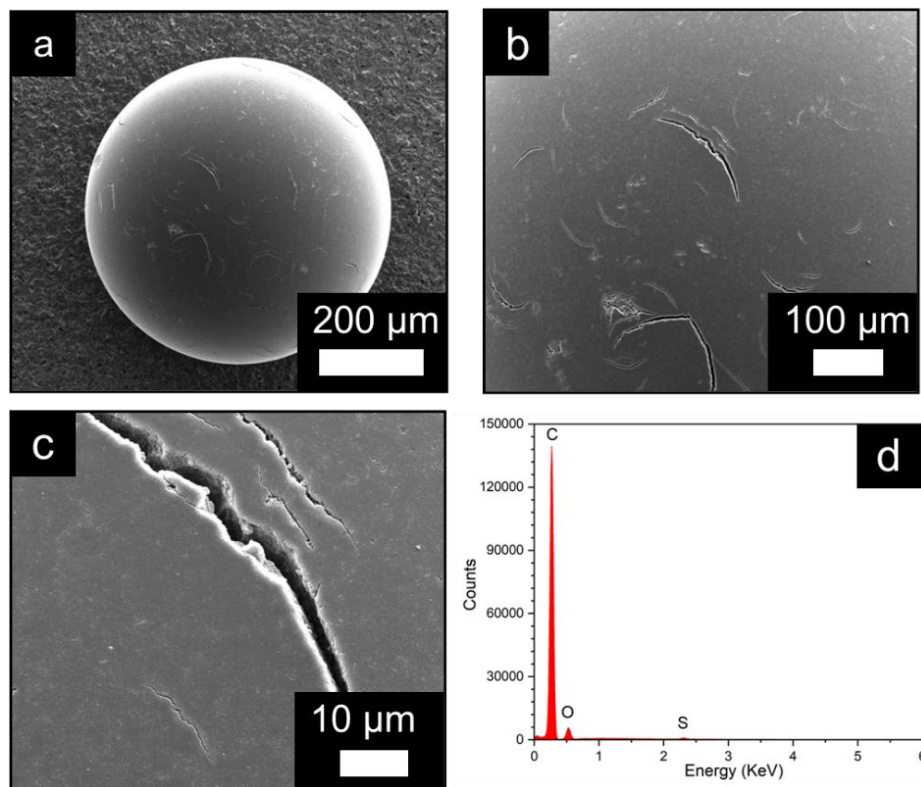


Figure 77: a-c) SEM images of a PBSAC bead showing; a) the whole bead and (b-c) a crack located on surface of a PBSAC bead. d) EDX spectrum of PBSAC sphere. Figures reproduced with permission.³⁰⁰

It appears that MIL-100(Sc) crystallises inside the cracks located on the exterior surface of the PBSAC spheres preferentially (Figure 78) and thus, as was mentioned in section 3.2.2, exploitation of this feature may be one approach to controlling the loading of MOFs on PBSAC spheres.

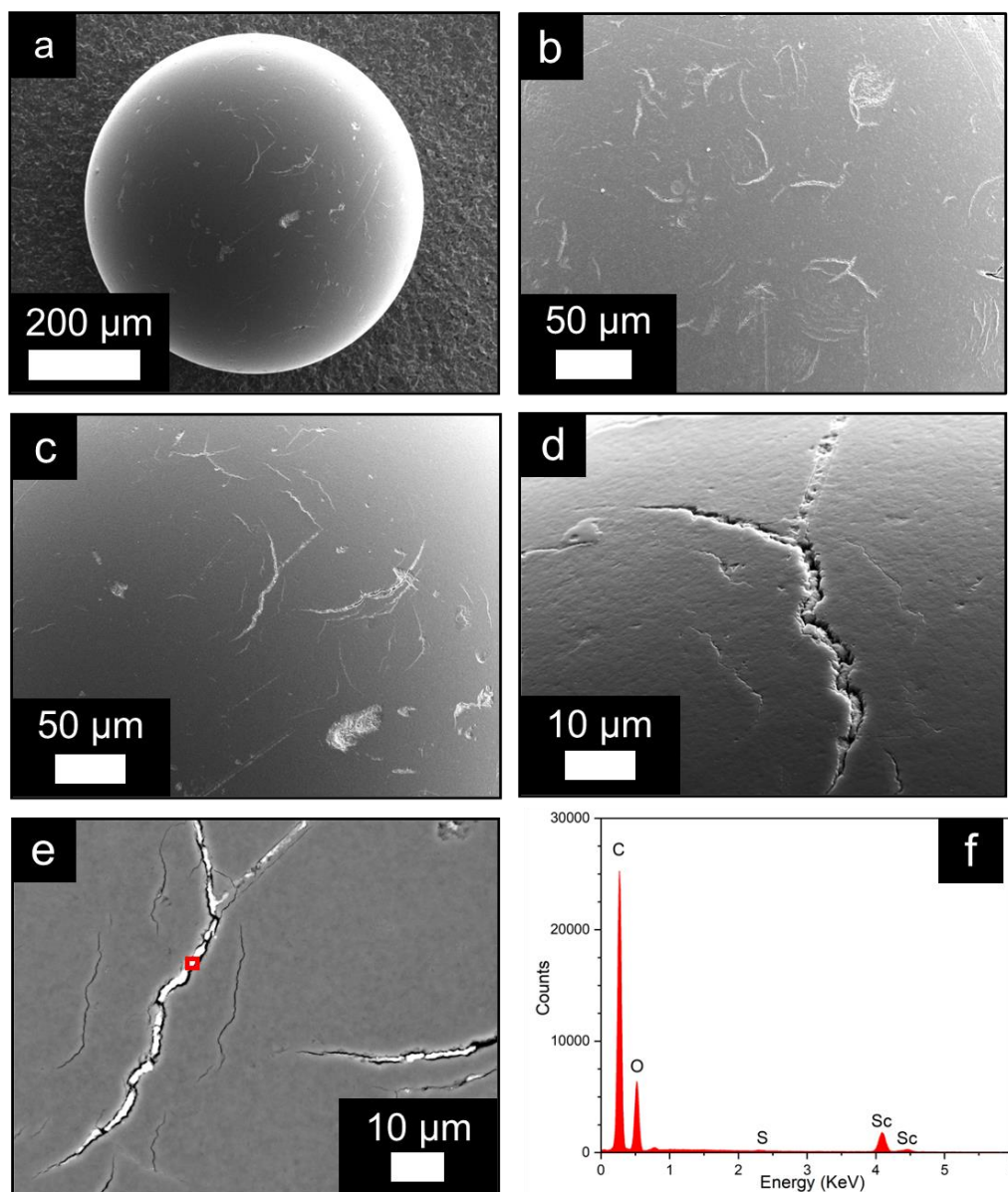


Figure 78: a) SEM image of MIL-100(Sc)@PBSAC composite sphere. b-d) Magnified SEM images of the surface of a MIL-100(Sc)@PBSAC sphere illustrating the cracks and scratches on the surface with MIL-100(Sc) present inside of these cracks. e) SEM image of a MIL-100(Sc)@PBSAC sphere with the region where EDX spectra was obtained is highlighted. f) Resultant EDX spectra of this region. Figures a, c and f reproduced with permission.³⁰⁰

EDX mapping of the surface of MIL-100(Sc)@PBSAC was also carried out to provide confirmation that MIL-100(Sc) was located in these cracks (Figure 79). A line scan was carried out to plot the scandium K α intensity across the surface and

a filled crack (Figure 79b). The increase in scandium $K\alpha$ counts when the line scan reached the crack relative to the rest of the surface suggests that this was indeed MIL-100(Sc) present in the crack (Figure 79c).

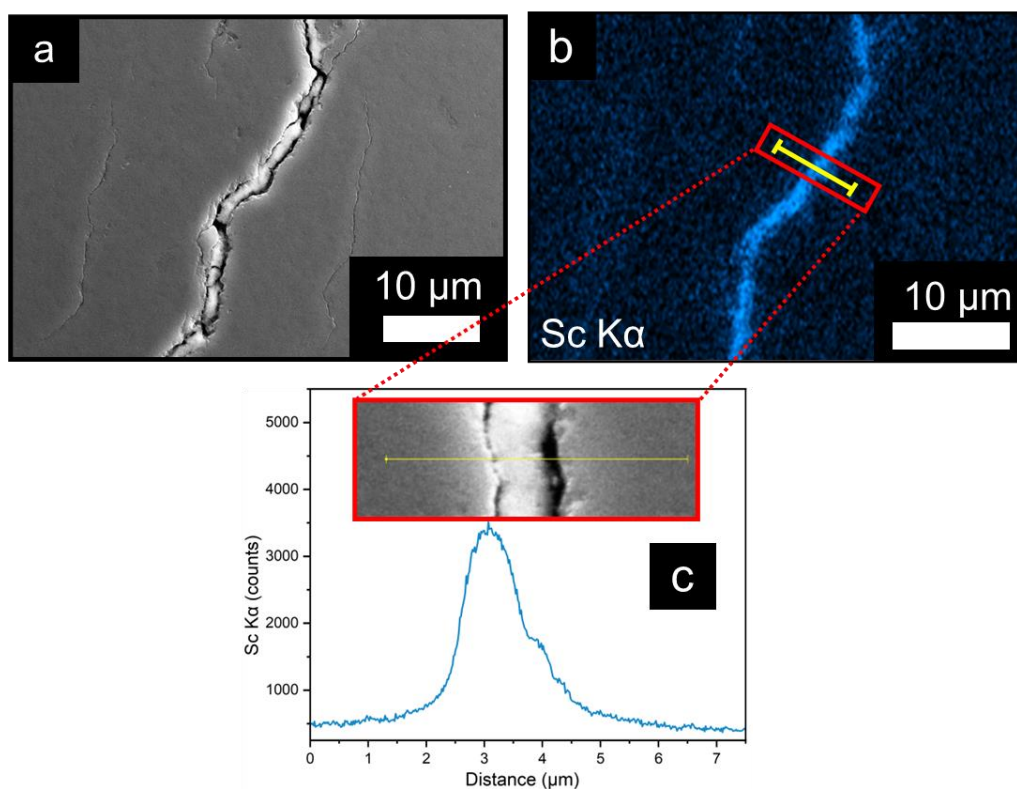


Figure 79: Magnified SEM image of the surface of a MIL-100(Sc)@PBSAC sphere illustrating the cracks and scratches on the surface with MIL-100(Sc) present inside of these cracks and position where EDX map was acquired. b) Sc $K\alpha$ EDX map of the surface of a MIL-100(Sc)@PBSAC sphere. c) EDX line scan location across a crack on the surface of a MIL-100(Sc)@PBSAC sphere indicated by the yellow line in the inset image and subsequent scandium $K\alpha$ counts across a crack on the surface of MIL-100(Sc)@PBSAC as a function of the distance. Figure a reproduced with permission.³⁰⁰

We also decided to probe both the depth of the crack and how deeply MIL-100(Sc) resided in the cracks. To do this, focused ion beam-scanning electron microscopy-energy dispersive X-ray analysis (FIB-SEM-EDX) was used. A section of the surface of a MIL-100(Sc)@PBSAC bead was etched away to a depth of 10 μm and analysed by EDX analysis (Figure 80a-d). This analysis revealed that the cracks penetrated further than 10 μm into the surface of the PBSAC spheres, but that a majority of the MIL-100(Sc) that is immobilised in these cracks resides near the surface (approximately 2.5 μm from the surface).

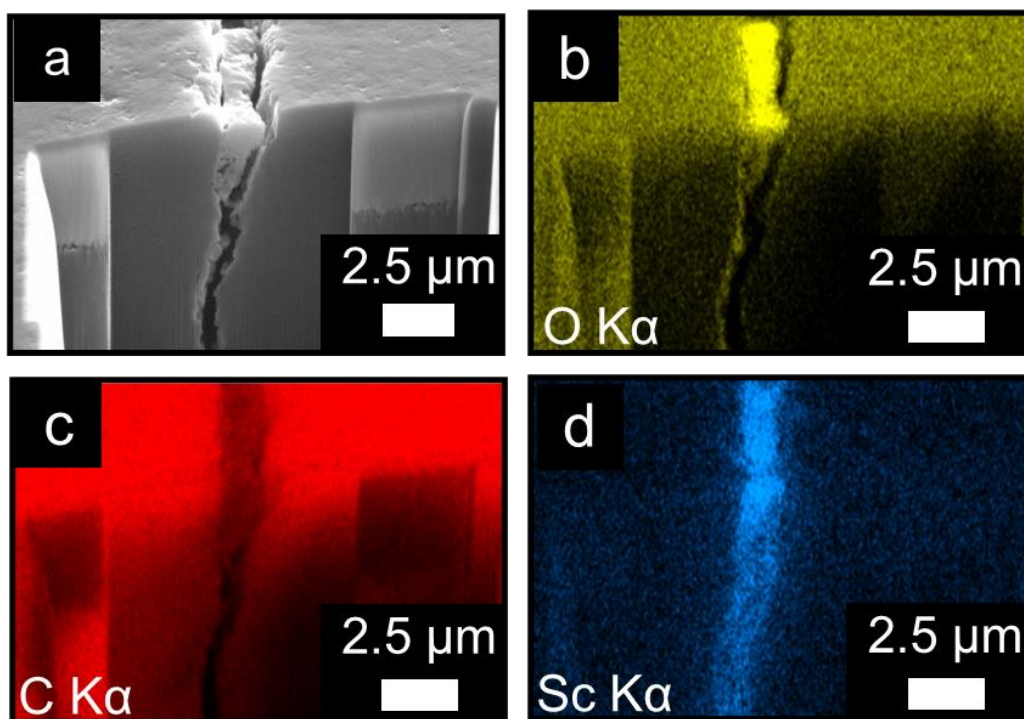


Figure 80: a) SEM image showing a 10 μm FIB cross-section to show the surface crack of a MIL 100(Sc)@PBSAC sphere. (b-d) O K α , C K α and Sc K α EDX map respectively of the etched sample. Figures reproduced with permission.³⁰⁰

XPS was also used to probe the surface structure of the PBSAC spheres and MIL-100(Sc)@PBSAC spheres. Figure 81a shows the survey of an as-received PBSAC sphere, containing a C 1s peak and a smaller O 1s peak. The presence of sulfur, although observed in the EDX spectrum during SEM analysis, was not observed in the XPS survey spectrum. Figure 81b shows the deconvoluted C 1s region on the spectrum, revealing the presence of C-C, C-O and C=O bonds at 284.8, 285.7 and 289.9 eV, respectively. Such analysis reveals insights into the type of carbon-oxygen bonding that is present on the surface of the PBSAC spheres. Navarro *et al.*¹⁹⁹ generated oxygen functionalities on the surface of PBSAC spheres via soaking in H₂O₂ to coordinate to zirconium clusters in their layer-by-layer approach to UiO-66@PBSAC fabrication. Oxygen functionalities on the surface of PBSAC spheres could feasibly coordinate to the scandium SBU of MIL-100(Sc), improving the anchoring of the MOF to the support. The oxidation of PBSAC spheres has previously also been carried out by treatment with sulfuric acid^{190, 191} and nitric acid¹⁹¹.

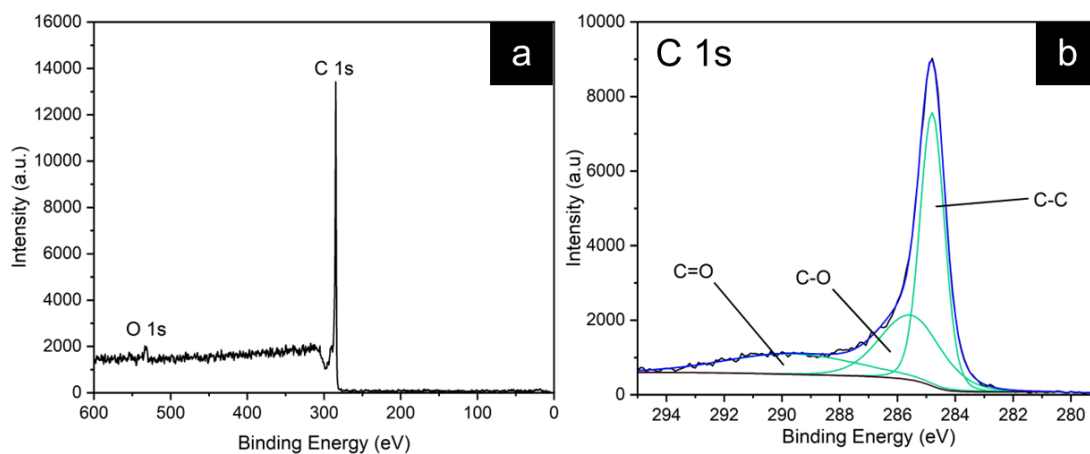


Figure 81: a) Survey of as received PBSAC showing O 1s and C 1s peaks respectively. b) C1s region of the spectrum which was deconvoluted to give three peaks reach maxima at 284.8, 285.7 and 289.9 eV - these correspond to the C-C, C-O and C=O bonds respectively.

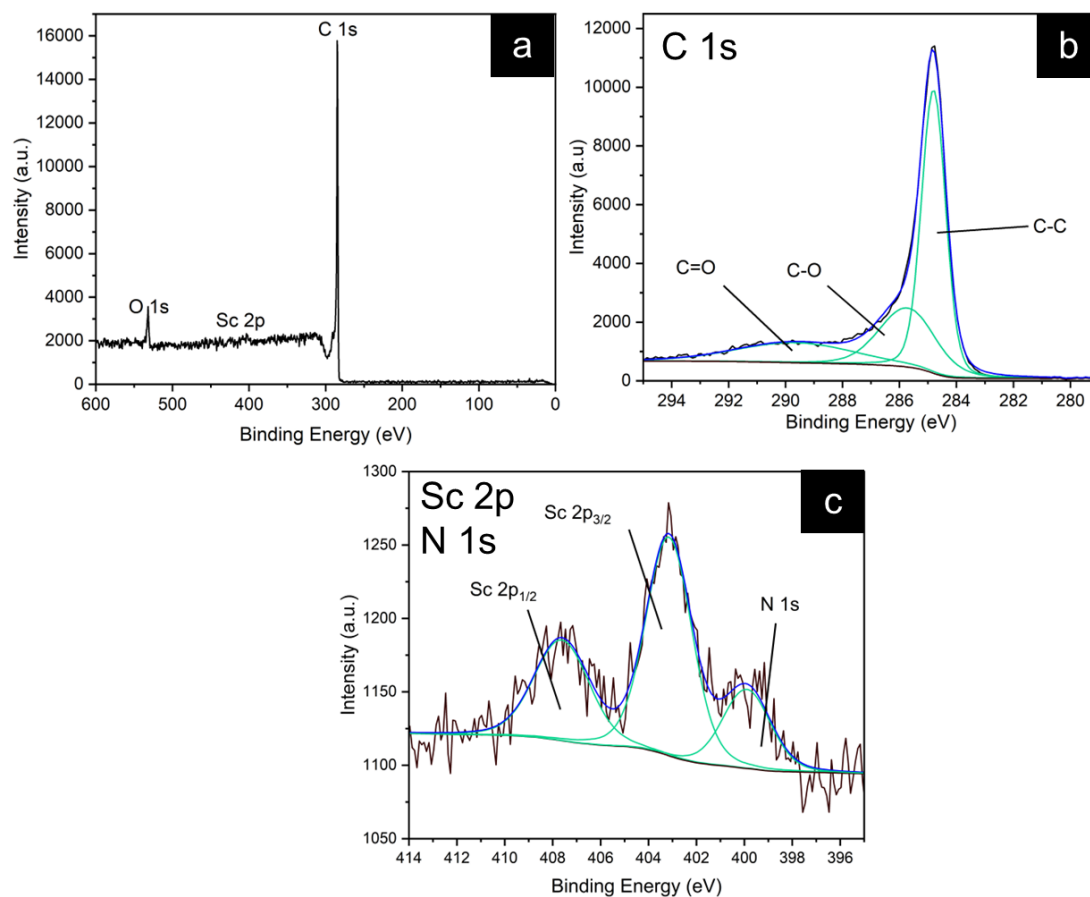


Figure 82: a) Survey of MIL-100(Sc)@PBSAC showing O 1s, Sc 2p/N 1s and C 1s peaks respectively. b) C1s region of the spectrum which was deconvoluted to give three peaks peaking at 284.9, 285.8 and 289.9 eV - these correspond to the C-C, C-O and C=O bonds respectively. c) Sc 2p region of spectrum with three peaks. The first correspond to the 2p_{3/2} and 2p_{1/2} at 403.1 and 407.6 eV respectively. The third peak, at 399.9 eV, was assigned to N 1s.

Figure 82a-c shows the XPS survey, C 1s region and Sc 2p region for MIL-100(Sc)@PBSAC, respectively. The survey contained a small Sc 2p peak at ≈ 399.9 eV and the O 1s peak was relatively larger in size when compared to the as-received PBSAC spheres, consistent with the additional oxygen incorporated by the presence of MIL-100(Sc). The small size of the Sc 2p peak however still suggests that a majority of the surface still consisted of the PBSAC spheres. Analysis of the C 1s region of the MIL-100(Sc)@PBSAC spheres compared to PBSAC spheres revealed a largely unchanged composition, with a maximum shift of 0.1 eV. The Sc 2p region, in the range of approximately 401 - 412 eV was deconvoluted into two peaks corresponding to the $2p_{3/2}$ and $2p_{1/2}$ at 403.1 and 407.6 eV respectively. A third peak was also present at 399.9 eV. We postulate that this was an N 1s peak as a result of the interaction of DMF (or thermal decomposition product dimethylamine) with the oxygen functionalities present on the graphitic carbon surface. Previously, treatment of graphene oxide with DMF resulted in nitrogen-containing groups being grafted onto the surface with an N 1s peak in the XPS spectrum at ≈ 400 eV subsequently observed.³⁰²⁻³⁰⁴

3.3.5 Mechanical and physical properties for flow chemistry

The high mechanical strength of PBSAC spheres in relation to other shaped forms of activated carbon is one of their properties that has led to their exploration as catalyst supports in continuous flow due to the high pressures and long reaction times employed in this mode of operation. Accordingly, the crush strength of PBSAC and MIL-100(Sc)@PBSAC was measured to assess the mechanical strength of the composite material. This was done for single particles by moving a stage towards the particle with increasing force until the particle crushed. Figure 83 shows the equipment that was used for this procedure.

Both the crush strength of MIL-100(Sc)@PBSAC and unfunctionalised PBSAC spheres were similar in value; the lack of change in mechanical strength that was observed following MIL-100(Sc)@PBSAC synthesis in conditions involving refluxing in DMF for 16 hours also demonstrates the chemical robustness of the PBSAC spheres (Table 30).



Figure 83: The apparatus used to test the crush strength of MIL-100(Sc)@PBSAC and PBSAC spheres. Particles were placed in a stage and a piston was moved towards the spheres at a constant force until the sphere was crushed.

Table 30: D10, D50 and D90 size range of PBSAC spheres and MIL-100(Sc)@PBSAC. The tube-to-diameter (D_t/D_p) range was calculated for each size range. The crush strength of MIL-100(Sc)@PBSAC was unchanged from PBSAC spheres.

Sample	D10 (μm)	D50 (μm)	D90 (μm)	D_t/D_p ratio ^a	Crush strength (N) ^b
PBSAC	359	465	602	16 - 26	0.69 ± 0.27
MIL-100(Sc)@PBSAC	-	-	-	-	0.44 ± 0.29

^a For 1/2" diameter tubing with an internal diameter of 0.94 cm. ^b Uncertainty values correspond to standard deviation.

As well as the crush strength, the particle size of PBSAC spheres was determined in order to calculate the reactor tube diameter (D_t) to particle diameter (D_p) ratio (D_t/D_p ratio) as this may have implications on the uniformity of liquid flow through the column. Generally speaking, a D_t/D_p ratio of ≥ 15 is desirable to minimise flow maldistribution across the reactor.³⁰⁵ With a D10, D50 and D90 (corresponding to the diameter below which 10%, 50% or 90% of particles are smaller, respectively) of 359 μm , 465 μm and 602 μm respectively (Figure 84), 1/2" tubing with an internal diameter of 0.94 cm was selected for the packed-bed reactor. This ensures uniform flow across the catalyst bed upon operation in continuous flow as the D_t/D_p ratio varied from approximately 16 - 27 (between the D90 to D10 value range) (Table 30).

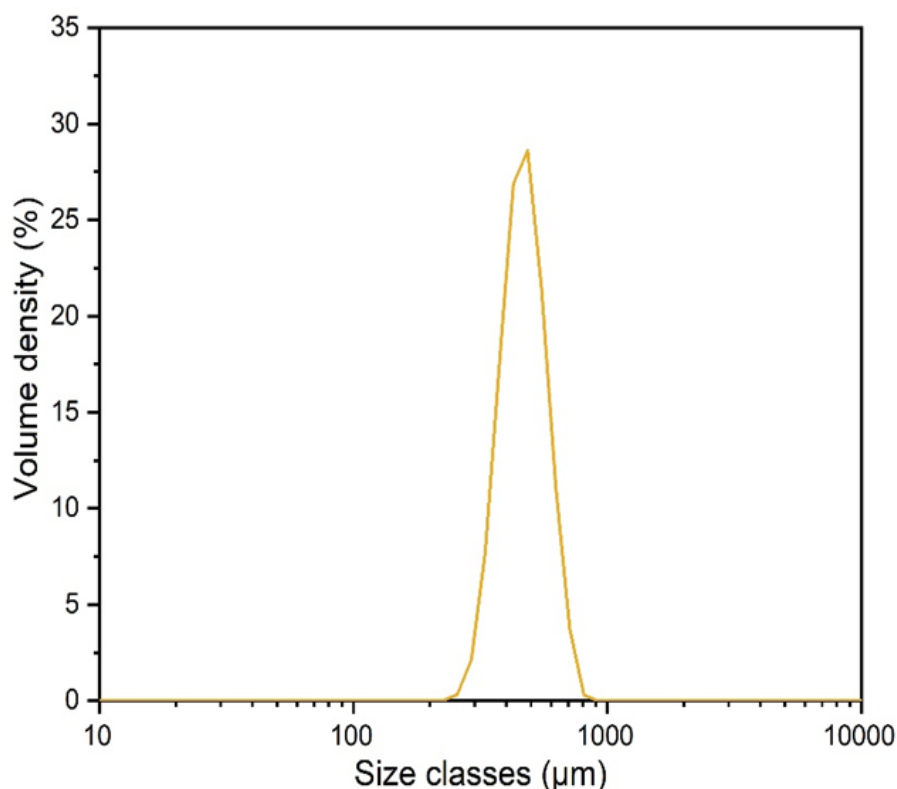


Figure 84: Volume distribution of PBSAC spheres obtained from Mastersizer 3000 laser diffraction analysis. Figure reproduced with permission.³⁰⁰

3.4 Conclusions of the chapter

Before the benefits of continuous flow can fully be realised for MOF-based heterogeneous systems, the powdered form of MOFs needs to be addressed as the translation of these flow processes to larger industrial scales will become limited by the powdered form of these catalysts. Toward that end, in this chapter we have designed a novel catalyst consisting of the Lewis acidic catalytically active MOF, MIL-100(Sc), immobilised onto activated carbon spheres ideally shaped for use in packed-bed, continuous flow reactors. We thoroughly characterised this material using a range of analytical techniques (PXRD, TGA, AAS, N₂ adsorption, FIB-SEM-EDX, XPS, light scattering, crush testing) to determine how much MIL-100(Sc) was immobilised and how the MIL-100 was distributed within and across the PBSAC spheres. The MIL-100(Sc) resides primarily in the pores and cracks situated throughout the surface of the carbon spheres. The production of the composite catalyst was found to be reproducible across many batches.

By immobilising MIL-100(Sc) on a versatile and cheap support material like PBSAC, we propose that this work may provide the basis for a general approach to exploit the high versatility of MOF-based catalysts in continuous systems and improve their practicality due to the easier handling of these composite materials. Much like the ‘plug-and-play’ nature of continuous flow systems, where different standardised modules (e.g. reactors, separators) can be quickly added or replaced to a given system, we envision a ‘plug-and-play’ catalyst where any selected MOF can be immobilised onto PBSAC spheres and studied in continuous flow. This possibility is also attractive when considering the almost infinitely tunable nature of MOFs. When envisioning this, consideration does need to be given to the additional complexity encountered when synthesising other MOF@PBSAC systems, however. For example, the preparation of some MOFs may require the use of a modulator (e.g. UiO- MOFs) or additional postsynthetic modification steps which adds another layer of complexity to the design of these materials.

3.5 Appendices

3.5.1.1 Formation of loose powdered MIL-100(Sc) during reflux synthesis of MIL-100(Sc)@PBSAC composites

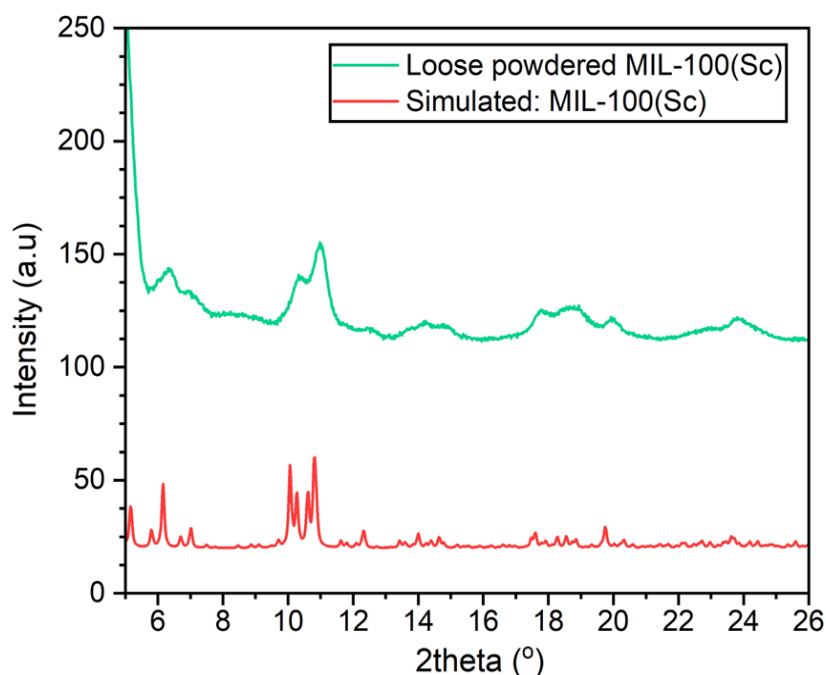


Figure 85: PXRD pattern of loose powdered MIL-100(Sc) (green) that was formed in the reaction vessel during MIL-100(Sc)@PBSAC synthesis compared with the simulated pattern of MIL-100(Sc). Figure reproduced with permission.³⁰⁰

Chapter 4 Studying the catalytic activity of MIL-100(Sc)@PBSAC composites in batch and continuous flow

4.1 Introduction

In their 2020 review, Garcia *et al.*¹⁵⁸ highlighted key literature pertaining to the use of MOFs as heterogeneous catalysts in continuous flow. Although examples regarding the use of MOF-based heterogeneous catalysts to date predominantly involves their usage in a batch mode of operation, a number of studies also explore their utility in continuous flow. Table 31 showcases the diversity of MOF-based materials that have been used previously to catalyse a range of reactions in continuous flow, their form, and the reactor that was used.

Table 31: Summary of literature examples employing a MOF-based heterogeneous catalysts for liquid phase continuous flow reactions.

Year	MOF, Form	Reactor	Reaction	Ref
2012	Cu ₃ (BTC) ₂ -MonoSil, Monolith	PBR ^a	Friedlander reaction	170
2014	Pd@MIL-101-NH ₂ , Powder	PBR	Suzuki-Miyaura cross-coupling	159
2015	CHS@Cu ₃ (BTC) ₂ ^b , Powder	PBR	Aldehyde acetalization	306
2015	Pd@MIL-88B-NH ₂ (Cr)@nano-SiO ₂ , Powder	PBR	Aerobic alcohol oxidation	160
2016	Cu ₃ (BTC) ₂ , Powder	PBR	Aldehyde acetalization	171
2016	Ru complex inside MIL-101(Al)-NH ₂ , Powder	PBR	Olefin Metathesis	168
2017	HKUST-1@SiO ₂ ^c , Pellet	PBR	Isomerization of styrene oxide	174
2017	Cu ₃ (BTC) ₂ /cellulose acetate, Mixed matrix membrane	Syringe ^d	Aldehyde acetalization	172
2017	[Me ₂ NH ₂][Mn ₂ (L)(H ₂ O) ₂] ^e , Powder	PBR	Friedel–Crafts	176
2018	Pd@UiO-66-NH ₂ , film on inner wall of capillary	Capillary	Reduction	161
2018	OPH@MIL-100(Fe) ^f , Membrane	Syringe ^d	Degradation of nerve agents	165
2018	Co(CO) ₄ ⁻ inside MIL-101(Cr), Powder	PBR	Carbonylation of β-lactones	169
2018	UiO-66(Zr), Powder	PBR	Transfer hydrogenation	307
2018	MIL-100(Sc), MIL-88D(Sc), MIL-66(Sc), MIL-101(M) (M = Cr, Fe, Sc), Powder	PBR	Propylene oxide carbonation	125
2019	ZrOTf-BTC@SiO ₂ , Powder	PBR	Diels-Alder, epoxide ring openings, Friedel-Crafts, alkene hydroxyalkylation	177
2019	ZIF-8, Pelletised	PBR	Glucose conversion	175
2021	MIL-100(Fe), Powder	PBR	Aldehyde acetalization	173
2021	MOF-microreactor ^g , Pickering emulsion	PBR	Kinetic resolutions	166

2021	PCN-160-Pd ^h , Tableted	PBR	Suzuki-Miyaura cross-coupling	162
2022	Esterase loaded onto NU-1000, Powder	PBR	Hydrolysis	167
2022	ZSM-5@IRMOF-1 ⁱ , Pelletised	PBR	IPA to aromatics	178
2023	Pd NPs on UiO-66(Hf), Powder	PBR	Semi-hydrogenation	163
2023	ZIF-8/Pd-TPU ^j , Membrane	Filter	Reduction	164

^a PBR = packed-bed reactor. The form of these reactors varied across the references - for example sometimes a glass column or steel tubing was used. We class a reactor as a PBR in these examples if the catalyst was packed into it and liquid was pumped through. ^b yolk/shell copper hydroxysulfates@MOF. ^c Silica aerogel. ^d Immobilised on the bottom of a syringe and reagents pumped through. ^e Porous chiral MOF: [Mn₂(L)(H₂O)₂] where L = different enantiopure phosphono-carboxylate ligands. ^f OPH = Organophosphorus hydrolase enzyme. Loaded onto commercial polymer membrane. ^g MOF layer grown around emulsifier stabilised droplet containing enzymes for size-selective reactions. ^h Homogeneous palladium incorporated into MOF PCN-160. ⁱ Zn-based metal-organic framework-zeolite composite. ^j Membrane of Pd NPs immobilised on ZIF-8 and thermoplastic polyurethane.

The examples listed in Table 31 may broadly be categorised into to metal NP supported catalysis,¹⁵⁹⁻¹⁶⁴ bio-catalysis,¹⁶⁵⁻¹⁶⁷ catalysis by metal complexes^{168, 169} and catalysis by pristine MOFs as Lewis acid catalysts. Lewis acidic MOF-catalysed reactions in continuous flow include Friedländer,¹⁷⁰ acetalisation,¹⁷¹⁻¹⁷³ isomerisation,^{174, 175} Fridel-crafts,^{176, 177} epoxide carbonylation¹²⁵ Diels-Alder,¹⁷⁷ epoxide ring opening¹⁷⁷ and aromatisation¹⁷⁸ reactions. The use of MOFs for Lewis acid catalysis in continuous flow was discussed in more detail in section 1.2.1.1.

Despite success on the academic level, when using MOFs as catalysts in continuous flow, the translation of these flow processes to larger industrial scales will become limited by the powdered form of the many of these catalysts (see Table 31, column 2 for the form of the materials). Upon use in a packed-bed reactor, the most commonly used reactor to study MOFs in continuous flow, employing powder-based catalysts will make these reactors liable to produce a high pressure drop and blockages. Such phenomena are common in powder systems^{18, 56} but these effects have not been explored significantly in MOF powder-based flow reactors. Some of the examples listed in Table 31 employed larger catalyst sizes such as monoliths,¹⁷⁰ pellets^{174, 175} and tablets¹⁶². In a few cases, membranes were prepared, immobilised and the reagents pumped

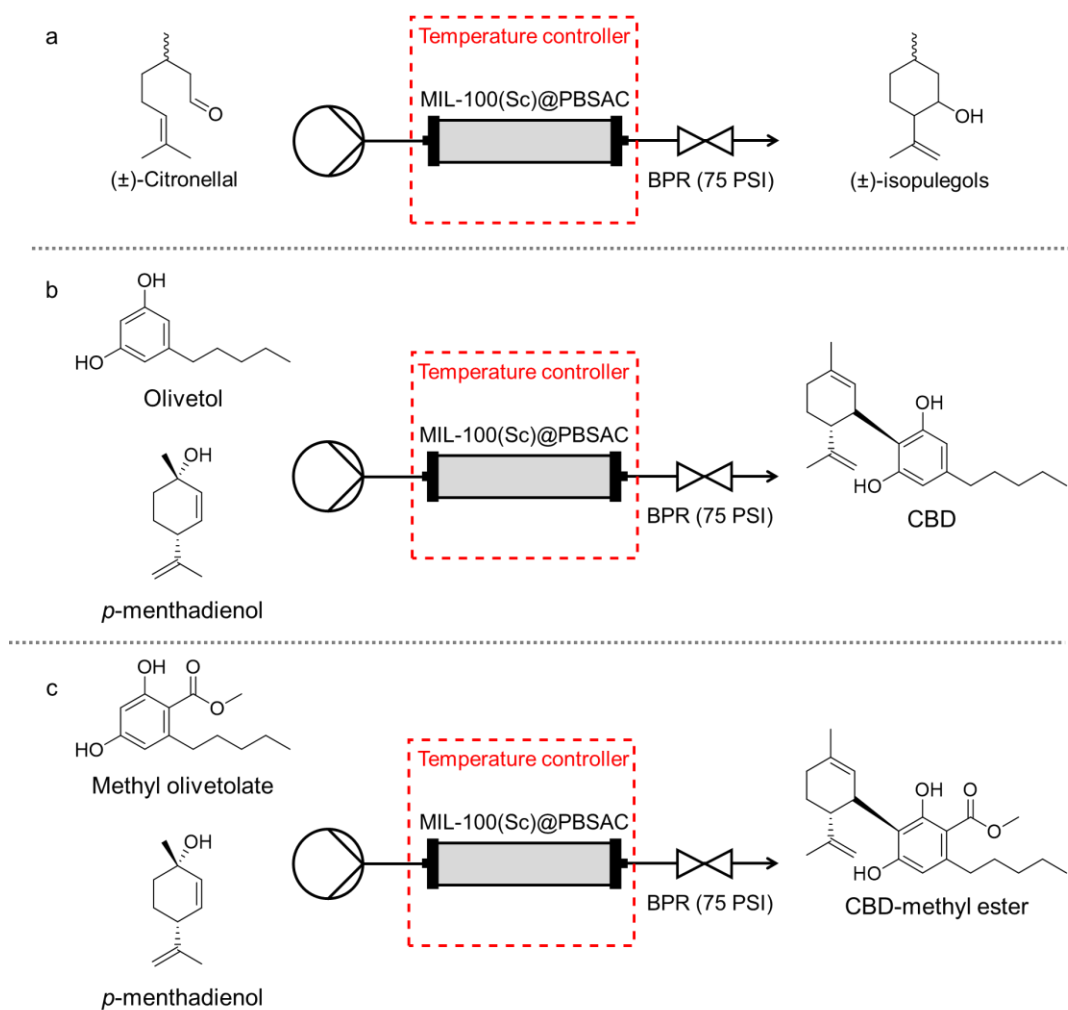
through.^{164, 165, 172} It is still evident, however, that the form of MOFs does not seem to be a major consideration.

The adaption of these powdered materials into larger forms is therefore desirable for continuous flow applications. One way of doing so, as discussed in section 1.1.2.4, is to anchor the catalyst onto a larger-sized support material. This was achieved in Chapter 3, where a novel material consisting of a Lewis acidic catalytically active MOF, MIL-100(Sc), was immobilised onto polymer-based spherical activated carbon (PBSAC) spheres ideally shaped for use in packed-bed, continuous flow reactors. This new catalyst, termed MIL-100(Sc)@PBSAC, could be reproducibly made across many batches and was characterised using a range of analytical techniques (PXRD, TGA, AAS, N₂ adsorption, FIB-SEM-EDX, XPS, crush testing, light scattering) to identify how much and where MIL-100(Sc) was located and other physical properties that are appropriate for continuous flow (e.g. the mechanical strength and particle size). Similar materials consisting of a MOF immobilised onto PBSAC spheres have been successfully prepared previously for warfare agent detoxification¹⁹⁹ and adsorption¹⁹⁸ applications, however, these systems were not designed for the explicit purpose of studying liquid phase chemical reactions pertinent to fine chemical production (as would ideally be observed in a pharmaceutical setting) in continuous flow. The catalytic activity of MIL-100(Sc)@PBSAC composites was also confirmed in section 3.3.1.2 where batch catalytic studies were conducted as a means of probing the reproducibility of the synthesis.

A generalised approach of transferring MOF catalysts, many of which exist as powders, into larger forms is a potential step forward towards widespread application and where we believe this research fits in to the current landscape of the field. The versatile properties of PBSAC spheres (e.g. narrow size distribution, high mechanical strength, functionalisable graphitic carbon surface) (see section 1.3 for discussion of this) serve as a good vehicle for a generalised approach to transfer these systems into more usable forms.

With a platform to prepare the novel MIL-100(Sc)@PBSAC composites that offered consistency over crucial parameters (e.g. reproducible synthesis, loadings and catalytic activity, high mechanical strength, narrow size distribution), we next sought to study the catalytic activity of this material further in both batch and continuous flow. This chapter firstly reports studies into the catalytic activity

of this novel material in batch and continuous flow using the intramolecular cyclisation of citronellal as a model reaction (Scheme 7a) (see section 2.4.1) for more information on this reaction) and then extends this approach to the examination of the catalytic activity towards a step in the production of cannabidiol (CBD) or cannabidiol-methyl ester (CBD-ME) in continuous flow. The two reactions that were studied involved the coupling of *p*-menthadienol with olivetol or methyl-olivetolate to produce CBD or CBD-methyl ester, respectively (Scheme 7b-c). See section 4.3.3 for more discussion into the chemistry of cannabinoids.



Scheme 7: Summary of reactions studied in continuous flow using MIL-100(Sc)@PBSAC composites in this work. a) The intramolecular cyclisation of citronellal, coupling of b) olivetol or c) methyl olivetolate with *p*-menthadienol in a Friedel-Crafts reaction to produce CBD or CBD-methyl ester respectively.

4.2 Catalytic activity of MIL-100(Sc)@PBSAC in batch

Upon fabrication of novel MIL-100(Sc)@PBSAC composites (Chapter 3), the Lewis acidic catalytic activity was confirmed via tests to probe how reproducible the synthesis of this material was (see section 3.3.1.2). Before studying this material in continuous flow, we therefore decided to firstly study some other catalytic properties in batch, i.e. how reusable the material is and the effect of stirring rate on the rate of reaction.

4.2.1 Reusability testing

Although studying catalysts in continuous flow systems enables an assessment of catalyst stability over time-on-stream, before studying MIL-100(Sc)@PBSAC composites in continuous flow we first made an initial assessment of the reusability of this material as a catalyst in batch. This provided initial cost-effective insight into the stability of the catalyst before more extended and resource-intensive studies were conducted in continuous flow. We used the intramolecular cyclisation of citronellal, the reaction used in Chapter 2 where the Lewis acidic catalytic activity of MIL-100(Sc) powder was explored, as a model reaction to do this.

The test involved studying the yield of isopulegols after 1 hour of reaction over a period of 5 runs, with the catalyst reactivated between runs by simply soaking in methanol for 24 hours. The catalyst was then dried under a nitrogen flow. Figure 86 shows the data. Over the course of the 5 runs there was no significant change in the yield values that were obtained, suggesting that the catalyst was reusable at these conditions. Also, due to the easier handling of these materials compared to powders no catalyst was lost between runs reducing the amount of (expensive, due to scandium) waste generated.

These initial results highlighted the reusability of MIL-100(Sc)@PBSAC composites, but it could also be plausible that the conditions employed in the study (i.e. 1 hour reaction time) were not stressful enough to induce catalyst degradation, for example by leaching of scandium from the support. This was intentional, as for this study we were more interested in determining if the catalytic activity could, for example, be maintained between runs after soaking in methanol for 24 hours and drying the catalyst using simple means (i.e. by blowing nitrogen over them) or whether more stringent handling conditions were required, such as

extended periods of methanol washing and complete drying of the MOF (at more extreme drying conditions). More insightful information into the nature of catalyst deactivation (e.g. leaching) would be acquired upon experimentation in a continuous mode of operation.

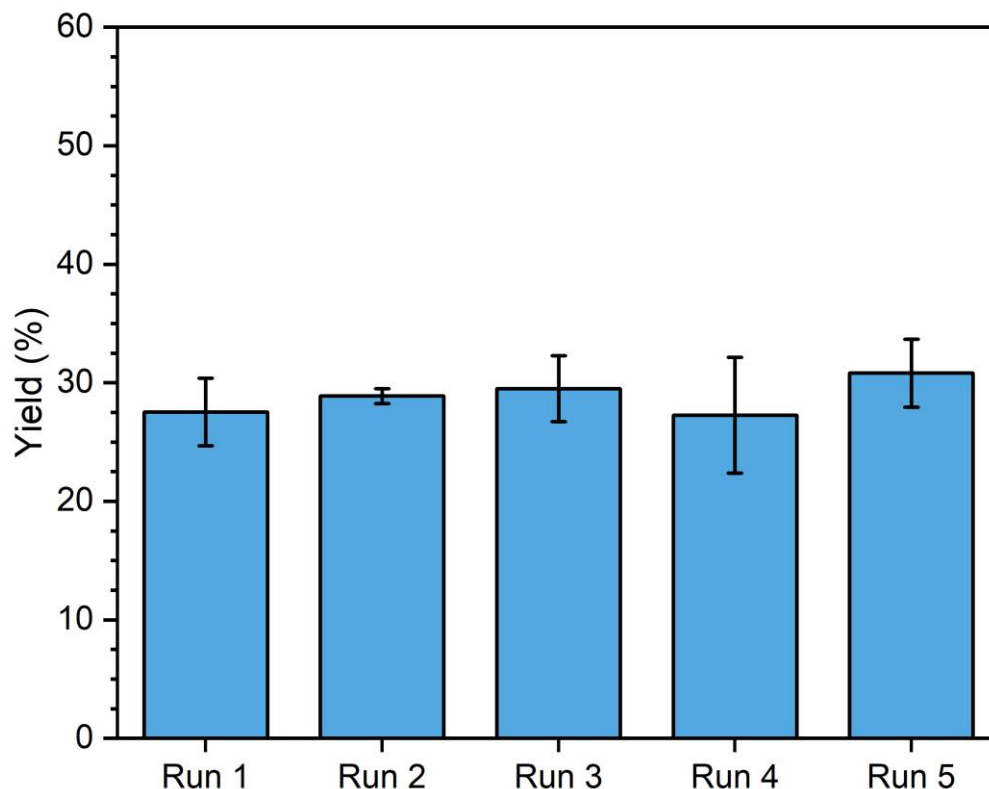


Figure 86: Reusability testing of MIL-100(Sc)@PBSAC composites in batch. Conditions: 0.09 M Citronellal, toluene, 110 °C, 1 hour, 150 mg catalyst. Catalyst reactivated by soaking in methanol for 24 hours and dried by blowing nitrogen over the catalyst.

It is clear that, based on this study, strict air and water-free conditions are not required to handle MIL-100(Sc)@PBSAC. This is an important consideration from an industrial application perspective as this will dictate the handling conditions.

4.2.2 Effect of stirring rate

For heterogeneous catalysis in batch, the stirring rate can significantly influence the observed catalytic activity as this can affect the external mass transfer, i.e. the diffusion of reactants to the external surface of the catalyst. Adequate stirring rates can help mitigate external mass transfer limitations and thus increase the observed reaction rate. Limitations in the reaction rate caused by inadequate external mass transfer may occur when the rate of mass transfer of reactants from the bulk solution to the catalyst surface is slower than the internal mass

transfer (i.e. the transfer of reactants through the MOF pores) or catalytic reaction (i.e. adsorption, reaction and desorption) itself.

With these considerations in mind, we decided to study if the stirring rate influenced the rate of reaction or whether the reaction rate was more dependent upon the internal mass transfer or intrinsic catalytic activity of MIL-100(Sc)@PBSAC. The change in (\pm)-citronellal concentration was measured over 6 hours at a range of different stirring rates (120, 250, 500, 750, 1000 and 1500 rpm) (Figure 87).

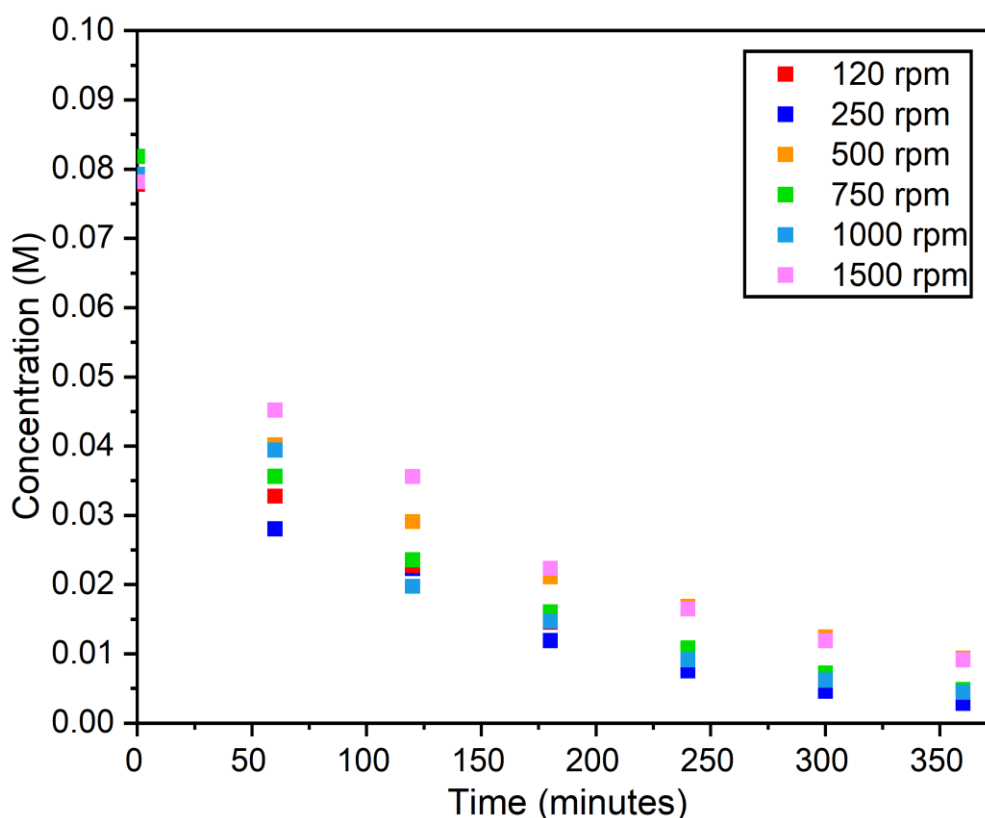


Figure 87: Effect of stirring rate and observed catalytic activity. Conditions: 0.08 M (\pm)-citronellal, 110 °C, toluene, 150 mg catalyst.

Over the large range studied (120 - 1500 rpm), the rate of consumption of citronellal showed no large dependence on the stirring rate. This observation suggests that across the stirring rate range studied the reaction rate is more dependent upon internal mass transfer (within both the pores of MIL-100(Sc) and PBSAC spheres of the composite material) and the intrinsic rate of reaction of MIL-100(Sc).

4.3 Catalytic activity of MIL-100(Sc)@PBSAC in continuous flow

Figure 88a-d shows the flow system used in this work to study the catalytic activity of MIL-100(Sc)@PBSAC composites for the intramolecular cyclisation of citronellal and the 'protected route' to CBD-methyl ester, i.e. the coupling of methyl olivetolate and *p*-menthadienol, in continuous flow (Scheme 8).

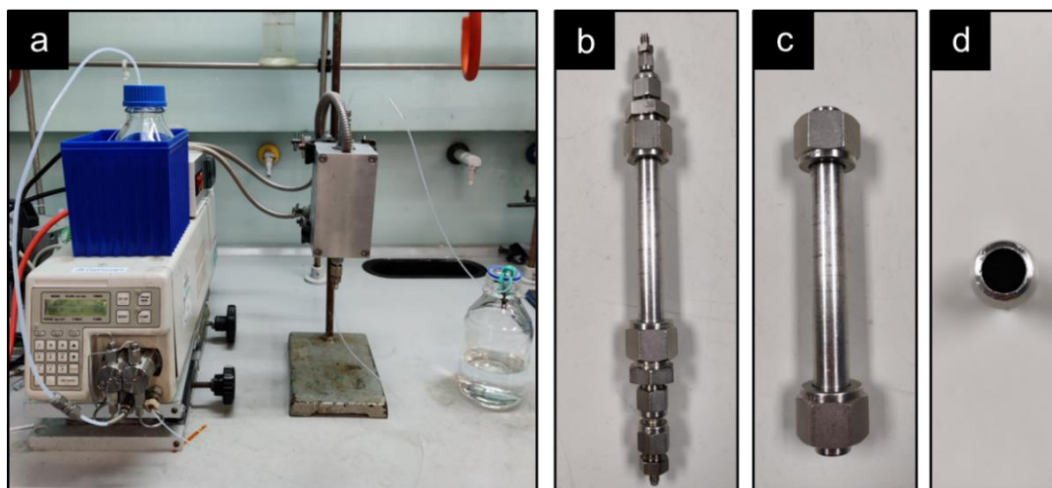
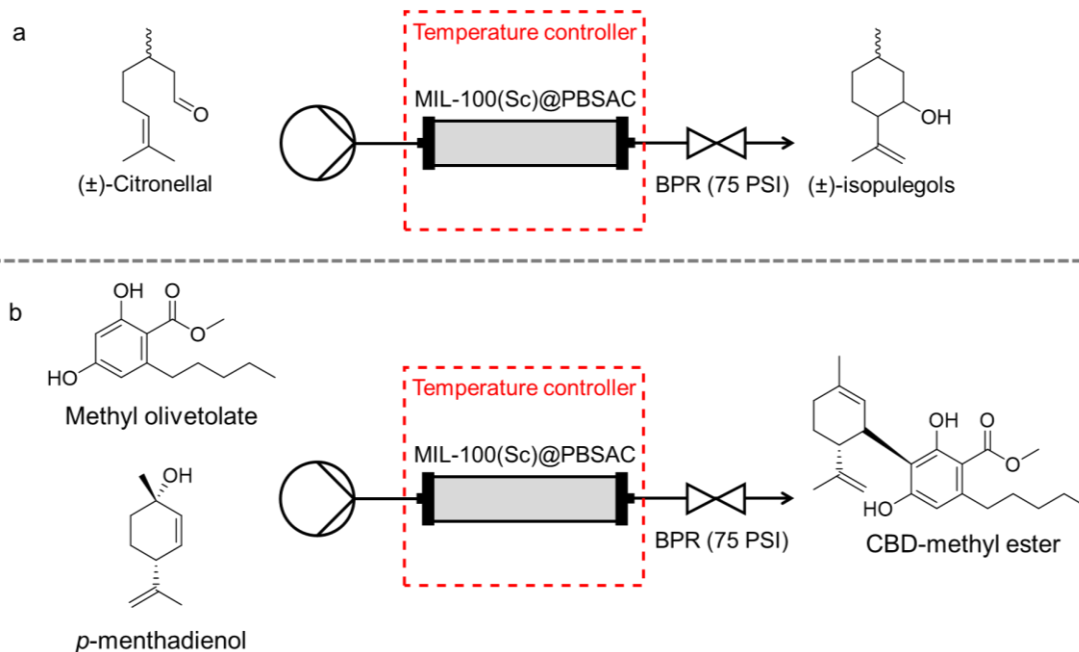


Figure 88: a) Flow setup used in this work. MIL-100(Sc)@PBSAC composites were packed inside a vertically placed stainless steel packed-bed reactor heated using an aluminium heating block, heating coils and a Eurotherm temperature controller. A HPLC pump was used to pump reagents to the reactor through PTFE tubing and system pressure was maintained using a back pressure regulator (BPR) (75 psi) (not shown). Samples were collected at the tubing outlet. b-d) Packed-bed reactor used for flow reactions b) with and c) without connectors attached and d) aerial view. Figures reproduced with permission.³⁰⁰



Scheme 8: a) The intramolecular cyclisation of citronellal and the b) 'protected route' to CBD-methyl ester (see section 4.3.3 for more detail) studied using the flow system described in Figure 88.

As described in section 6.4.4, this setup consisted of a vertically placed stainless steel packed-bed reactor (1/2" OD, 0.065" wall thickness, length: 12 cm) heated using an aluminium heating block which was connected to a Eurotherm temperature controller, PTFE tubing (1/16" OD, 1/32" ID), a cartridge back pressure regulator (BPR) (75 psi) and a Jasco HPLC pump. This reactor internal diameter was selected to give a reactor tube diameter (D_t) to particle diameter (D_p) of 16 – 26 for PBSAC spheres (D_{10} : 359 μm , D_{90} : 602 μm , see section 3.3.5), with ≥ 15 desirable to minimise flow maldistribution (see section 3.3.5 for more discussion).³⁰⁵ The aluminium heating block provided efficient contact with the packed-bed reactor for uniform heating across the bed and the use of a BPR enabled use of reaction solvents above their boiling point at atmospheric pressure.

For a typical reaction when studying the intramolecular cyclisation of (\pm)-citronellal in continuous flow, the packed-bed reactor was plugged at both ends with two 1 cm wide cotton wool balls and filled with a homogeneous mixture of MIL-100(Sc)@PBSAC spheres (1 g) and glass spheres (9 g) (500 μm) leading to an even distribution of the catalytically active material throughout the reactor. The heating block temperature controller was set to 110 °C. A solution of (\pm)-citronellal (≈ 0.4 M in toluene, n-decane internal standard) was pumped from bottom to top for an ideal distribution throughout the packed-bed.

4.3.1 Studying residence time distribution

Before carrying out flow reactions, we first studied the residence time distribution of molecules in this flow system. In the context of this research, the residence time distribution (RTD) is the distribution of time that molecules spend in the packed-bed reactor.³⁰⁸ Understanding the RTD of species in continuous flow processes is important for quantifying the amount of time molecules are able to react which, in turn, can have important implications from a product quality perspective (e.g. spending too long in the reactor can lead to side-reactions, forming off-target products and lowering product yield).

To study the RTD of the flow system used in this work we carried out a pulse test which is one common approach for quantifying the RTD.³⁰⁸ Another common approach to RTD determination is via the development of computational simulations (e.g. computational fluid dynamics) but such approaches require

large amounts of information to be recorded and the computational data needs to be experimentally verified.^{308, 309} The pulse test involves spiking a pulse of tracer material, for this study acetone was used, into a pre-filled flow stream of toluene and measuring the absorption over time. In this setup, an online UV-Vis spectrometer recorded measurements every second at 290 nm to monitor the absorption of acetone over time as it eluted from the system. The test was carried out at five different flow rates: 0.5, 1, 2, 4 and 6 mL/min. The RTD function, $E(\Theta)$ is a probability distribution function that is used to describe the amount of time molecules spend in the reactor. This was calculated at each flow rate by dividing the absorbance at each timepoint by the total area under the curve. The $E(\Theta)$ was then plotted against time to ascertain the length of time acetone spent within the flow system. A plot of the residence time distribution function ($E(\Theta)$) vs. residence time is shown in Figure 89.

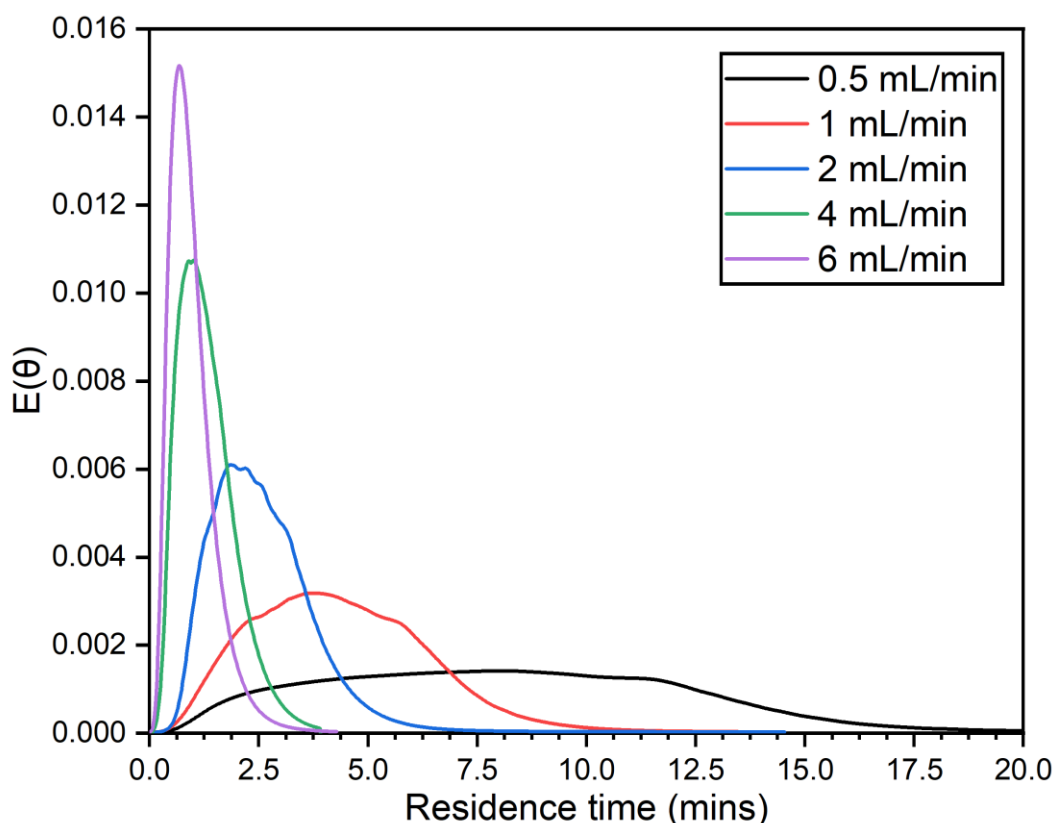


Figure 89: Plot of normalised residence time distribution ($E(\Theta)$) vs. residence time at each flow rate studied.

As flow rates were lowered, the range of time that molecules spent in the reactor increased. The reasons for this could be due to increased amounts of back-mixing, an increased amount of time for the acetone molecules to both interact with the catalyst in the packed-bed (similar to a chromatographic effect)

and to travel down different flow paths. Consideration should also be given to the differences in the interaction strength of the catalyst with the tracer molecule used (acetone) or reactants used for a chemical reaction (e.g. citronellal). As the catalyst support comprised graphitic carbon, a stronger interaction with citronellal molecules might be anticipated due to greater dispersion forces. Such differences in interactions could in turn result in a broader RTD than what was observed with the tracer molecule.

With this data, the average residence time of the system was also calculated. This was calculated by determining the area under the curve in a plot of $tE(\Theta)$ against time (Table 32, column 2). As the flow rate is decreased, the increasing skew of the RTD means the average value is biased to the long-time tail relative to the modal peak in the RTD. The residence time was also calculated by dividing the volume of the reactor, calculated to be 8.5 mL, by the flow rate. The reactor volume itself was determined by measuring the increase in mass of the reactor before and after filling with 2-propanol and relating this to the volume (by dividing the mass increase by the density of 2-propanol ($0.786 \text{ cm}^3/\text{g}$ at $25 \text{ }^\circ\text{C}$) (Table 32, column 3). Both approaches gave similar residence time values across all flow rates, instilling confidence in either approach.^{308, 310} The volumes calculated via the pulse method were typically 0.5 to 0.9 mL larger than those calculated using the mass increase method (apart from at $0.5 \text{ mL}/\text{min}$). This difference is indicative of the dead volume (i.e. tubing, pumps) of the system as the mass increase method only took into account the volume of the reactor.

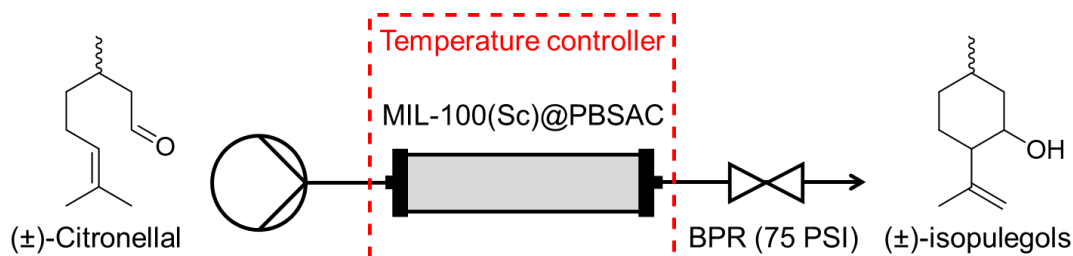
Table 32: Residence time of reactants within the filled packed-bed reactor at a given flow rate as determined by the pulse method or the volume gained upon filling with 2-propanol.

Flow Rate (mL/min)	Pulse method avg. residence Time (mins) ^a	Mass change residence time (mins) ^b
0.5	16.9	17.0
1	9.2	8.5
2	5.2	4.3
4	2.6	2.1
6	1.9	1.4

^a Calculated by determining the area under the curve in a plot of $tE(t)$ against time. ^b Calculated by measuring the increase in mass of the reactor before and after filling with 2-propanol and relating this to the volume (by dividing the mass increase by the density of 2-propanol ($0.786 \text{ cm}^3/\text{g}$ at $25 \text{ }^\circ\text{C}$)).

4.3.2 The intramolecular cyclisation of (±)-citronellal

To date, there are several examples regarding the study of the intramolecular cyclisation of citronellal within a continuous flow system that involves the use a heterogeneous catalyst (Table 33), but none (to the best of the author's knowledge) that employ a MOF-based catalyst in this mode of operation.



Scheme 9: The flow system used in this work in which (±)-citronellal (≈ 0.4 M in toluene) was pumped through a packed-bed reactor containing 1 g of MIL-100(Sc)@PBSAC and maintained at 110 °C.

Table 33: Summary of research conducted regarding the continuous flow intramolecular cyclisation citronellal with heterogeneous catalysts.

Year	Catalyst, Form	Reactor	Performance	Ref
2004	Sn- β , Zeolite, form not stated	PBR	> 99% conversion for 48 hours, 118 g converted, 11,500 TON	258
2015	H-ZSM-5, Zeolite, Pelletised	TBR ^a	$\approx 100\%$ citronellal conversion for 2 hours	311
2016	H-ZSM-5, Zeolite, Extrudates	PBR	100% conversion for 72 hours, 1.5 kg converted	312
2017	HPA in water droplets of Pickering emulsion ^b	PBR	89 - 99% citronellal conversion for 1500 hours, 2460 TON	313
2019	H- β -25 / H- β -150 / H-Y-5.1, Zeolite, Extrudates	TBR	73% yield of isopulegols.	314
2019	H- β -25, Zeolite, Extrudates	TBR	66% conversion after 150 mins, $1.58 - 2.91 \times 10^{-7}$ mol g ⁻¹ s ⁻¹ reaction rate	315
2019	Ru/H- β -300 / Pt-/Ru-H- β -25, Zeolite, Extrudates	TBR ^a	Data for only cyclisation step not shown	316
2020	Fe/SCATs, Powder ^c	PBR ^a	Data for cyclisation step not shown. Prod of 0.0012 g hr ⁻¹ , TOF of 1.98 hr ⁻¹ ^d	317
2020	Ru-MCM-41, Zeolite, Extrudates	TBR ^a	Data for only cyclisation step not shown	263
2022	Clay materials, Extrudates	TBR	24% isopulegols yield, 61% selectivity to isopulegol, initial rate 10.3×10^{-7} mol g ⁻¹ s ⁻¹	318
2022	Ni/H- β -38, Zeolite, Extrudate	TBR ^a	Data for cyclisation step not shown.	319

^a TBR = trickle-bed reactor. Carried out cyclisation to produce isopulegols and then hydrogenation to menthols. ^b HPA = Heteropolyacid. ^c Iron oxide NP supported on ceramic core of scrap catalytic converters. ^d 'Prod' means productivity, the mass of isopulegols produced (g) per hour on stream. We

calculated these metrics with the data provided by the authors, and assumed a 100% yield of isopulegols.

When studied in continuous flow, the intramolecular cyclisation of citronellal is frequently carried out in combination with a subsequent hydrogenation step^{263, 311, 316, 317, 319} to produce menthols due to the industrial relevance of this compound and to showcase the capabilities of both the catalysts that were developed and/or the continuous mode of operation used. This has involved either carrying out both the cyclisation and hydrogenation step in the same reactor using a bi-functional catalyst,^{263, 316, 319} or the use of tandem reactor setups^{311, 317} which is an advantage of using continuous flow systems. Going forward, we can visualise the development of bi-functional catalysts in continuous flow systems somewhat analogous to the work carried out by Corma *et al.*²⁵⁴ In their work MIL-100(Cr) was functionalised with Pd nanoparticles and used to carry out a one-pot synthesis of menthols in batch. Due to the industrial relevance of hydrogenations, Pd NPs have previously been supported onto PBSAC spheres on a number of occasions.^{32, 186-188, 190, 191} MIL-100(Sc)@PBSAC composites could be functionalised with Pd NPs and used in a single continuous flow reactor, or alternatively a tandem reactor setup could be used where one reactor is filled with MIL-100(Sc)@PBSAC and another with Pd/PBSAC spheres.

The research efforts of Murzin *et al.*^{263, 314-316, 318, 319} are a feature of the current literature regarding the use of heterogeneous catalysts to catalyse this reaction in continuous flow. This has involved the fabrication of shaped catalysts (i.e. extrudates) which were either zeolite-^{263, 314-316, 319} or clay-³¹⁸ based. Additionally, metals (i.e. Ru, Pt, Ni) have been supported onto these materials for the one-pot synthesis of menthols.^{263, 316, 319} It is evident that these studies adopt a process chemistry perspective to studying this system as they consider not only the chemical properties of the catalyst (i.e catalytic activity, selectivity, turnover frequency), but also the physical properties (i.e size of the extrudates, mechanical strength), both of which must be considered when designing industrial catalytic processes. Typical flow reactions in these studies were between 2 - 5 hours long in which sufficient catalyst deactivation was frequently observed (Figure 90).^{263, 314, 316, 319} To temporarily alleviate this, solvent washes with cyclohexane were carried out in some cases.^{263, 316} These studies are promising and showcase the efforts that are being made to study this reaction in continuous flow with

heterogeneous systems but they also highlight the difficulties that can arise in attempting doing so.

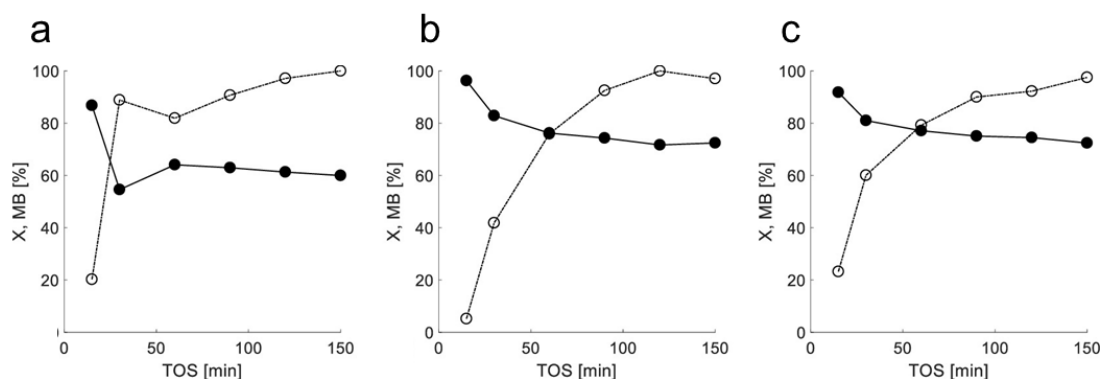


Figure 90: Continuous flow study carried out by Murzin and colleagues for the cyclisation of citronellal catalysed by different extrudates containing 30% wt. bentonite binder and zeolites a) H- β -25, b) H- β -150, and c) H-Y-5.1. Conversion of citronellal is shown by filled points whilst mass balance is shown by unfilled points over 150 minutes time-on-stream. Deactivation is visible in all three studies. Conditions: 35 °C, 10 bar argon, 0.4 mL/min, 0.086 M citronellal, 1 g catalyst. Figure a-c reproduced with permission.³¹⁵

Elsewhere, some of the most impressive results to date were published by Renz and Corma in 2004²⁵⁸ who investigated this reaction in continuous flow using a tin-supported zeolite catalyst, Sn- β . Following packing of this catalyst into a packed-bed reactor and subsequent heating of the reactor to 80 °C, a solution of citronellal in acetonitrile was flowed through the catalyst bed at a rate of 5 g hr⁻¹. Over the course of a 48 hour period, both the conversion and selectivity towards (-)-isopulegol remained constant at 99% and 83% respectively and no leaching of Sn from the support was observed. After 48 hours-on-stream, 118 g of citronellal was converted which translates to an average TON of 11,500.

Luque *et al.*³¹⁷ used a continuous-flow tandem system for the preparation of (\pm)-menthol from (\pm)-citronellal using scrap catalytic converters. The first reactor contained a Lewis acid catalyst consisting of iron oxide NPs supported on SCATs (the ceramic core of scrap catalytic converters), termed Fe/SCATs. The second reactor in the tandem system contained unfunctionalised SCATs for the hydrogenation of (\pm)-isopulegols to (\pm)-menthols. Under optimised conditions (20 mM citronellal in toluene, 0.1 mL min⁻¹, reactor 1 at 373 K and reactor 2 at 413 K, 5 bar H₂ pressure), menthols were obtained in \approx 77% yield for 7 hours of operation. After 72 hours, a slight decrease in the yield of (\pm)-menthols of about \approx 12% decrease was observed, which was restored back to the original activity

following a 20 minute washing step in toluene. This suggests that this was due to adsorption of material onto the catalyst rather than catalyst deactivation, this was also corroborated by the lack of iron present in the outlet solvent (following ICP-MS analysis).

This preceding work establishes an opportunity to extend work to MOF-based catalysts for flow-based intramolecular citronellal cyclisation. Due to the industrial importance of this reaction we therefore sought to explore the catalytic activity of novel MIL-100(Sc)@PBSAC heterogeneous catalyst composites in continuous flow. Many examples still exist regarding the catalysis of this reaction by MOFs in batch (Table 10 summarises some of the most popular examples to date) and thus the results obtained in flow would be compared with both these and the other catalysts that have previously been used in flow.

4.3.2.1 Studying at one flow rate

We first explored the catalytic activity of MIL-100(Sc)@PBSAC composites at a single flow rate with the aim of achieving a stable catalytic activity. A solution of (\pm)-citronellal (0.43 M) was flowed through the reactor at 0.25 mL/min. The catalytic activity, selectivity and efficiency was studied over the course of 9 hours-on-stream. Based on the liquid flow rate (0.25 mL/min) and volume of the packed reactor (8.5 mL), the residence time was calculated to be 34 minutes.

For this reaction, samples were taken on an hourly basis and the concentration of (\pm)-citronellal and the four (\pm)-isopulegol isomers were plotted over this time (Figure 91a). This data was also used to calculate the conversion and the selectivity of the reaction towards the formation of both (\pm)-isopulegols and (\pm)-isopulegol (Figure 91b) (see appendix 4.5.1 for a calculation of the reaction metrics). Average data values obtained across the 9 hours time-on-stream are shown in Table 34.

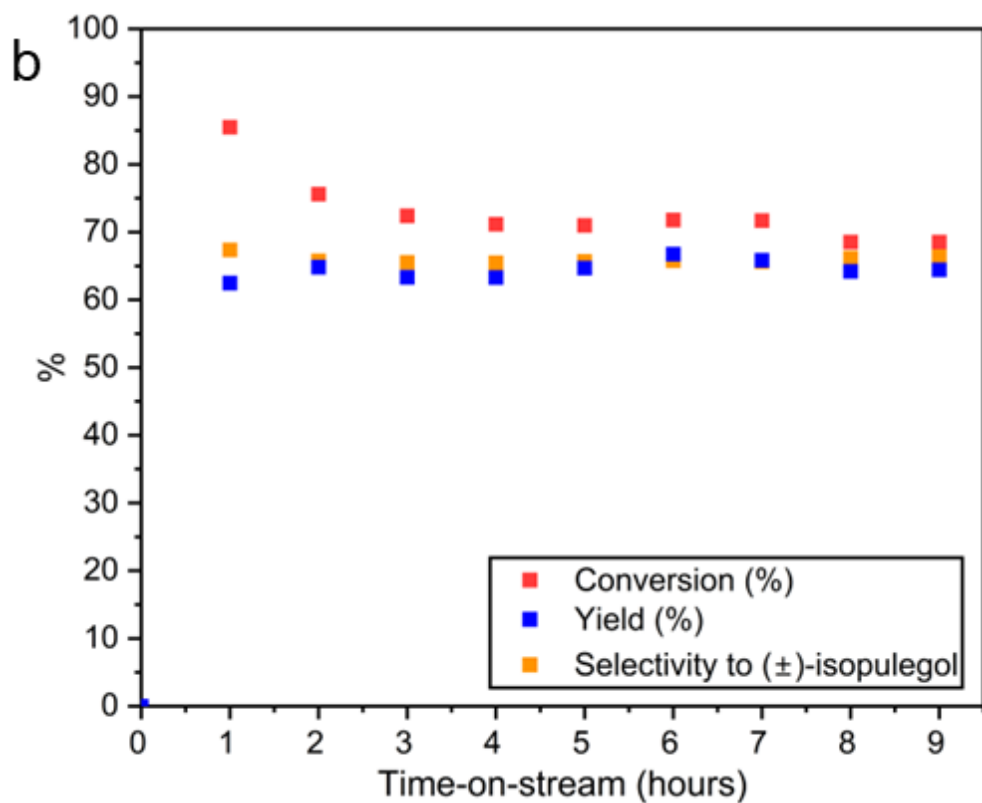
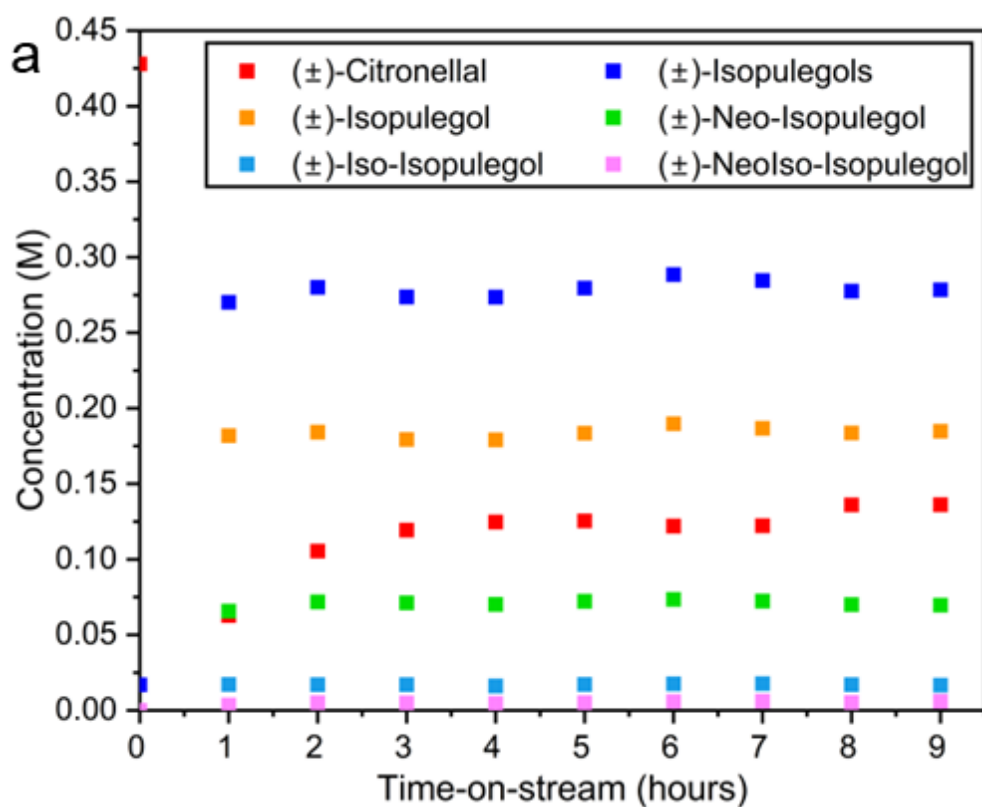


Figure 91: a) Concentration vs. time plots for (±)-citronellal and four (±)-isopulegol isomers that are produced in the reaction over the 9 hours time-on-stream at 0.25 mL/min. b) Conversion, yield and selectivity to (±)-isopulegol vs. time plot for the 9 hours time-on-stream.

Sampling was carried out using offline gas chromatography, with an initial spike in the conversion of (\pm)-citronellal (86%) after one hour observed when compared to the steady conversion value that was measured over the next 8 hours time-on-stream of between 69 - 76%. Conversion was determined by comparison of the initial (\pm)-citronellal concentration with the concentration that was present upon exiting the reactor; thus this initial spike may be indicative of phenomena such as (\pm)-citronellal adsorption onto the catalyst or the initial mass transfer of (\pm)-citronellal molecules into the pore network of the MIL-100(Sc)@PBSAC composites which, at the start of the reaction, were only filled with toluene and unoccupied by reactant molecules. Adsorption phenomena could be further explored by carrying out temperature programmed desorption analysis.⁵⁶

Table 34: Average productivity and TOF values obtained for the 9 hours time-on-stream and the productivity and TON after 9 hours.

Conversion (%)	Yield (%) ^a	Activity (mmol g _{cat} ⁻¹ hr ⁻¹) ^b	Selectivity to (\pm)-isopulegols (%)	Selectivity to (\pm)-isopulegol (%)
72.9 \pm 5.2	64.4 \pm 1.3	72.9 \pm 5.2 ^c	88.8 \pm 6.5	66.0 \pm 0.6

^a Of (\pm)-isopulegols. ^b Calculated as mmol of citronellal converted per gram of catalyst (MIL-100(Sc)) per hour. ^c Coincidentally conversion and activity values were identical for MIL-100(Sc)@PBSAC composites. Reported uncertainty values correspond to standard deviation between 1 - 9 hours.

The catalytic activity (i.e. the amount of (\pm)-citronellal converted per gram of catalyst per hour) was measured over the course of the 9 hours time on-stream and compared with the current literature regarding the use of MOFs to catalyst this reaction in batch (Table 34, column 3) (N.B. this data was previously presented in Table 10).

The activities of MIL-100(Sc)@PBSAC composites were greater than the activity of MIL-100(Sc) powder in batch (66.0 mmol g_{cat}⁻¹ hr⁻¹, Table 10) and was also found to be the second most active MOF-based species to catalyse this reaction (72.9 \pm 5.2 mmol g_{cat}⁻¹ hr⁻¹) to date after superacidic MOF-808-2.5SO₄ (83.1 mmol g_{cat}⁻¹ hr⁻¹).²⁵³ Overall, however, the research published by Renz and Corma²⁵⁸ using a Sn- β zeolite catalyst for this reaction was the most active overall (341.2 mmol g_{cat}⁻¹ hr⁻¹). In some cases, the catalytic activity of MIL-100(Sc)@PBSAC composites was found to be two orders of magnitude greater than other species (i.e. Cu₃(BTC)₂, MIL-100(Fe), MIL-101(Cr), Pd@MIL-100(Cr), Zr(Ti)-NDC).

For the duration of the 9 hours time-on-stream, the reactor demonstrated stable conversion and stable yield (62 - 67%) towards the formation of (\pm)-isopulegols (Figure 91a-b) meaning that, on average, 89% of the (\pm)-citronellal that was converted (conversion measured as difference in citronellal concentration at start and outlet of reactor) was forming (\pm)-isopulegols.

The selectivity towards the formation of (\pm)-isopulegol compared to other (\pm)-isopulegols also remained very consistent between 65 - 67% over the 9 hours-on-stream; the formation of all four (\pm)-isopulegols also remained stable over this time period. This selectivity value is in a similar range with selectivity values previously reported for other powdered, unsupported MOF catalysts in batch (Table 10) and, interestingly, was higher than the selectivity value obtained with MIL-100(Sc) powder in batch in section 2.4 (\approx 50% selectivity to (\pm)-isopulegol).

The fact that the diastereoselectivity remained constant over the course of the 9 hours means that consistent amounts of (\pm)-isopulegol were reliably synthesised, inviting potential for the introduction of downstream reaction modules to the system which is enabled intrinsically by the continuous mode of operation used. As discussed in section 4.3.2, a tandem hydrogenation step to produce (\pm)-menthols with Pd NPs supported on PBSAC spheres could be one approach to achieving this.

We also calculated other reaction metrics pertinent to industrial processes (i.e. productivity, TON, TOF, STY) (Table 35, Figure 92). A cumulative turnover number (TON) of 92.9 and turnover frequency (TOF) of 10.3 hr⁻¹ were determined. Higher TON values of 11,500 and 2460 were reported by Renz *et al.*²⁵⁸ and Yang *et al.*³¹³ when using a Sn- β zeolite catalyst or heteropolyacids (HPA) in the water droplets of a Pickering emulsion respectively. However, the operation times involved in their studies (48 hours for Sn- β and 1500 hours for the HPA catalyst) were much longer than those employing MIL-100(Sc)@PBSAC in this work (9 hours). Subsequent translation of the TON values into TOF values (by dividing the TON value by the total time-on-stream), therefore enabling greater comparison, indicated that MIL-100(Sc)@PBSAC showed greater catalytic efficiency than the HPA-based catalyst (1.64 hr⁻¹) but significantly less than the Sn- β catalyst (239.6 hr⁻¹). The TOF value obtained in this work was also calculated to be approximately 5-fold greater than what was obtained by

Luque *et al.*³¹⁷ when using Fe/SCATs for this reaction (1.98 hr^{-1}) (Table 33). Over the course of the 9 hours time-on-stream, a total amount of 5.7 g of (\pm)-isopulegols were produced with an average productivity of 0.64 g hr^{-1} .

Table 35: Average productivity and TOF values obtained for the 9 hours time-on-stream and the productivity and TON after 9 hours.

Productivity (g hr^{-1}) ^a	Productivity after 9 hours (g)	TON after 9 hours ^b	TOF (hr^{-1}) ^c	STY ($\text{g L}^{-1} \text{ hr}^{-1}$)
0.64 ± 0.01	5.7	95.6	10.6 ± 0.2	75.3

^a Productivity represents the average amount of (\pm)-isopulegols formed, in g, per hour over the 9 hours time-on-stream. ^b TON after 9 hours = Amount of (\pm)-isopulegols formed after 9 hours (in moles) / Amount of catalyst (in moles). ^c TOF (hr^{-1}) = TON per hour / time (in hours) for the 9 hours time-on-stream. Calculation of TON and TOF assumed that all scandium atoms in the MIL-100(Sc) framework participated in catalysis. STY ($\text{g L}^{-1} \text{ hr}^{-1}$) = average mass of (\pm)-isopulegols formed per residence volume (g) (for first 9 hours time-on-stream) / reactor volume (L) * residence time (hr). Uncertainty values correspond to standard deviation between 1 – 9 hours.

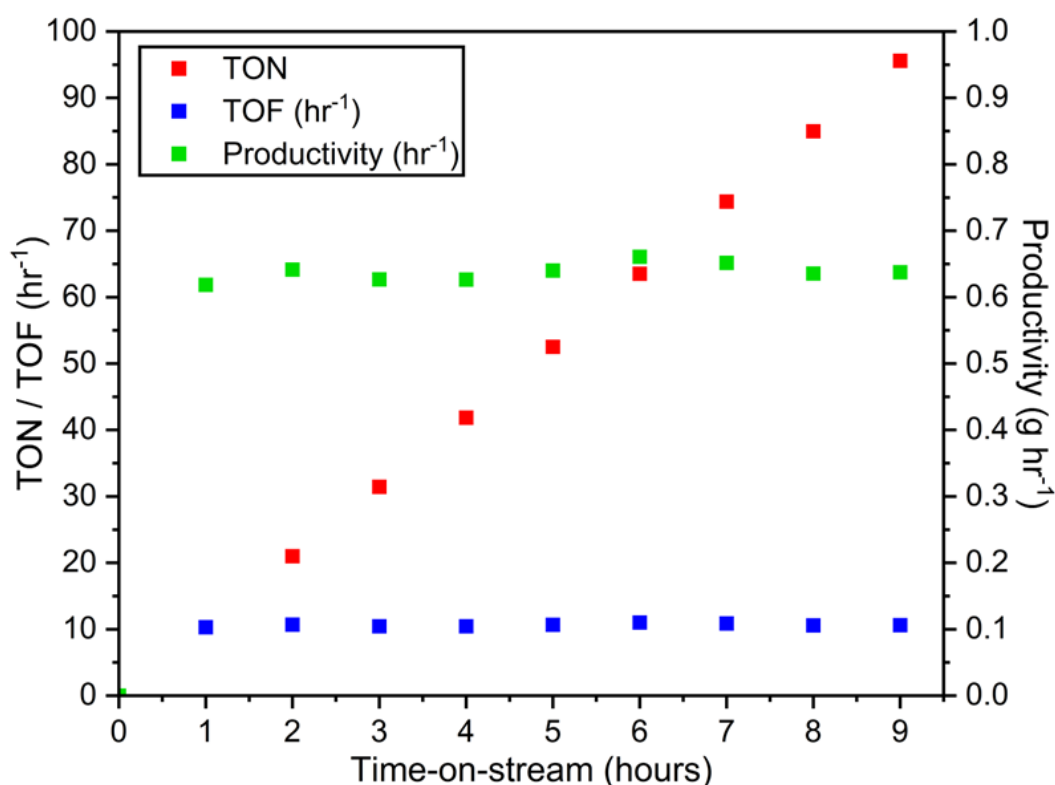


Figure 92: TON, TOF and productivity of the reaction for the formation of (\pm)-isopulegols vs. time over the 9 hours time-on-stream.

The space-time yield (STY) metric (see appendix 4.5.1 for calculation) is also of interest for many pharmaceutical processes due to the consideration of the size of the reactor, capacity of the equipment used and the economy of the reaction.

Based on this metric, a desirable outcome would be the production of large quantities of material in as little volume and in as short a time as possible.^{320, 321} For this flow reaction, this was calculated to be 75.01 g L⁻¹ hr⁻¹.

Over the 9 hours time-on-stream, the reaction ran smoothly with no reactor blockages or downtime. Additionally, no physical destruction of the catalyst (e.g. attrition, crushing) was observed following visual inspection after use. These positive results briefly showcase the high potential and robustness of this support material for use in continuous systems to exploit MOF-based catalysts in the future.

4.3.2.1.1 Studying the catalyst after the reaction

Building on the results after 9 hours-on-stream, after 26 hours of reaction, the conversion and yield were found to have decreased to 41% and 34% respectively. To investigate possible causes, we firstly analysed the scandium content of the catalyst by AAS after the reaction and compared it with that from before (Table 36). Over this amount of time a 7.5 - 13.6 % loss of scandium from the support material was measured which directly suggests that leaching was one of the causes of the loss in catalytic activity.

Table 36: Atomic absorption spectroscopy (AAS) data of before and after 26 hours time-on-stream. An average 10.6 % loss of scandium was measured to have leached over the course of the reaction.

Scandium loading before 26 hour reaction (% w/w)	Scandium loading after 26 hour reaction (% w/w)	% loss of scandium over course of reaction
1.68 ± 0.02	1.50 ± 0.03	7.5 – 13.6

The location of where the scandium was lost from the support material could have large implications on the resultant catalytic activity. For example, the MIL-100(Sc) located on the exterior of the PBSAC spheres, i.e. in the cracks on the surface (see section 3.3.4 for images), may contribute more to the overall reactivity of the catalyst than catalyst material located within the pore structure of the PBSAC support material due to the relative reduced mass transfer of the reactants. Because of this, the potential loss of MIL-100(Sc) from these cracks over the course of a reaction could cause the reactivity to drop proportionately more than the loss of MIL-100(Sc) from the pores of PBSAC spheres. We decided to examine the catalyst after the reaction by SEM to see if the outer surface of the

catalyst had changed (Figure 93). Upon inspection of the data, we did not subjectively observe any loss of scandium from the cracks of the PBSAC spheres. Consideration should be given to the small sample size ($\approx 1 - 5$ beads were inspected) relative to numbers used in a reaction (1000+ spheres), however.

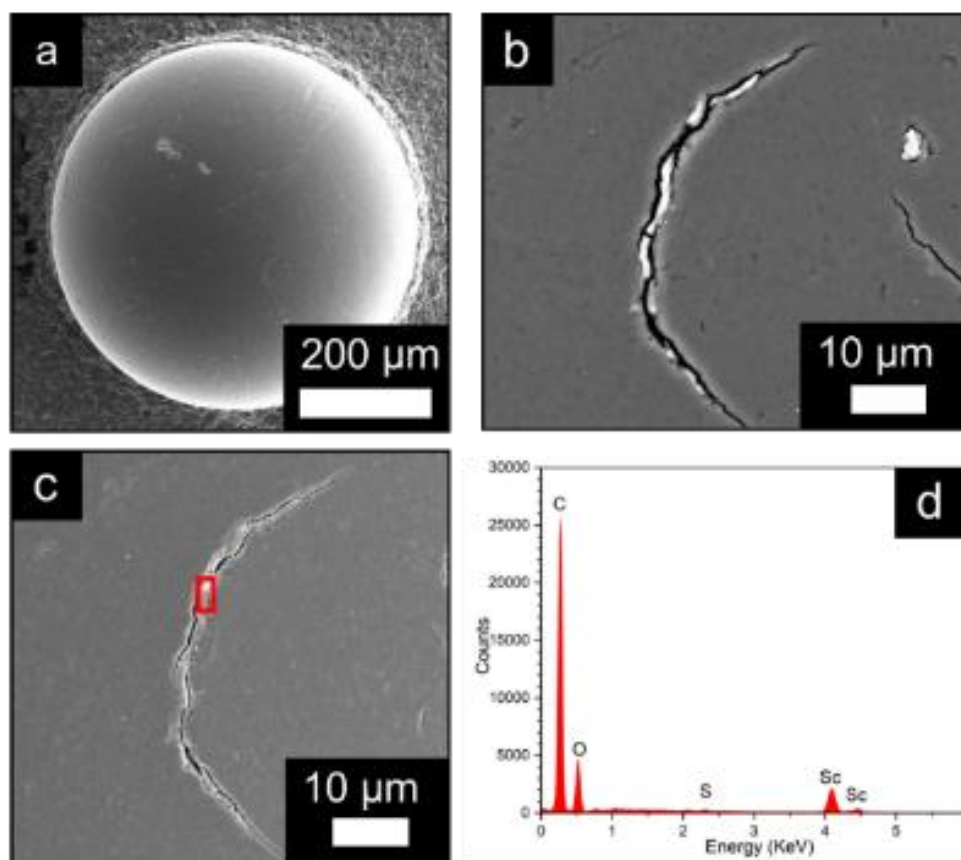


Figure 93: a-c) SEM image of MIL-100(Sc)@PBSAC composite sphere after 26 hours-on-stream. The surface of the particle appears unchanged to MIL-100(Sc)@PBSAC spheres that have not been used for a reaction. c) SEM image of a MIL-100(Sc)@PBSAC sphere with the region where EDX spectra was obtained highlighted. d) Resultant EDX spectra of this region. Figures reproduced with permission.³⁰⁰

As a third probe of the catalyst after the 26 hour reaction we used TGA to further characterise and compare with the material from before the analysis (Figure 94a-b). In the TGA profile of the sample after the reaction, there was a change in weight between 200 - 300 °C that was not observed in the profile in the corresponding sample but from before the 26 hour reaction (inspection of the first weight derivatives makes this clearer to see). This mass change that occurred during the TGA analysis may correspond to the removal of citronellal from the catalyst that accumulated over the course of the reaction, and, may partially be responsible for the loss in activity that was observed after 26 hours. This could

be explored by temperature programmed desorption analysis.⁵⁶ Further studies into decreasing catalytic activities observed over the course of flow reactions are detailed in section 4.3.2.3 and 4.3.2.4.

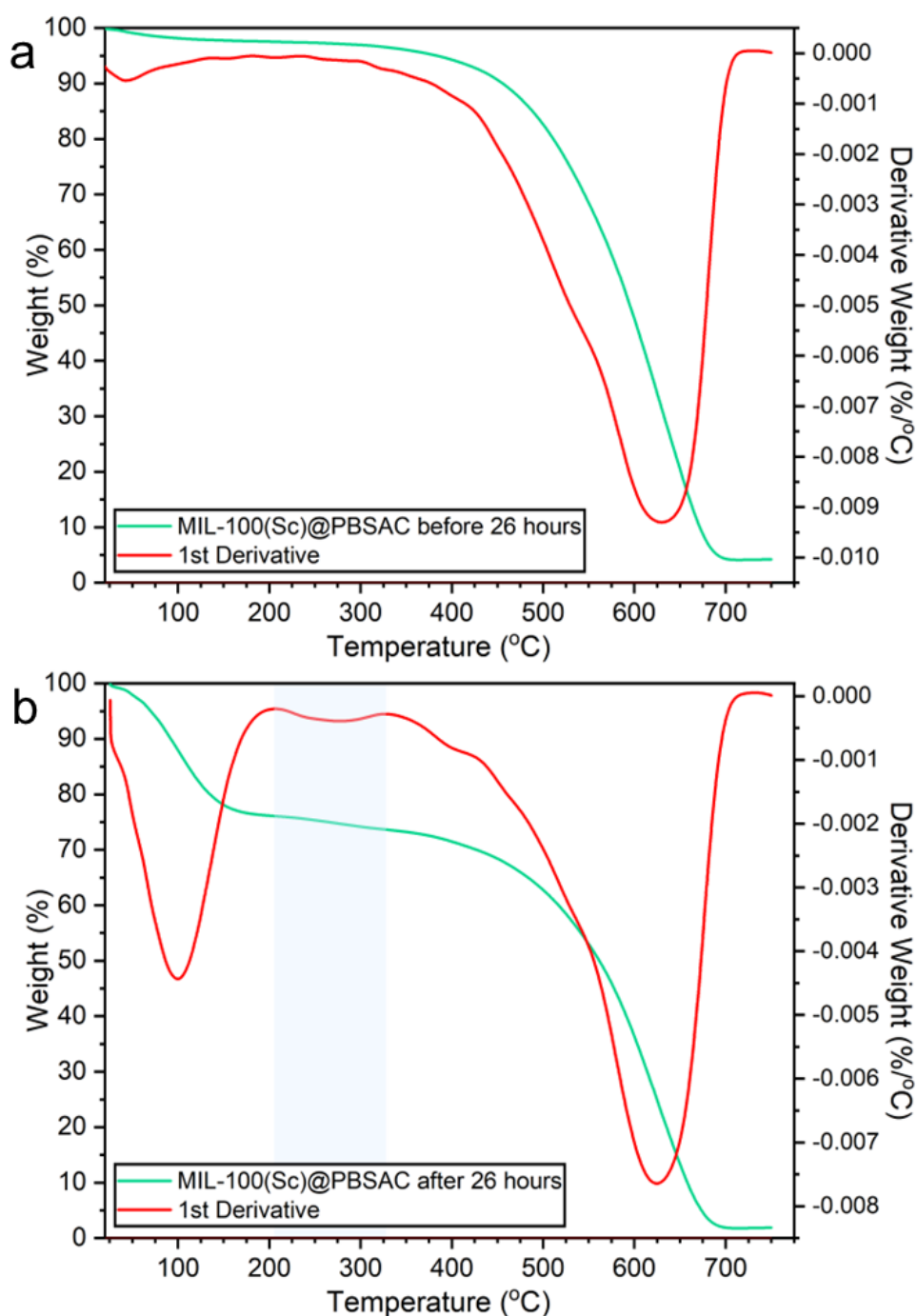


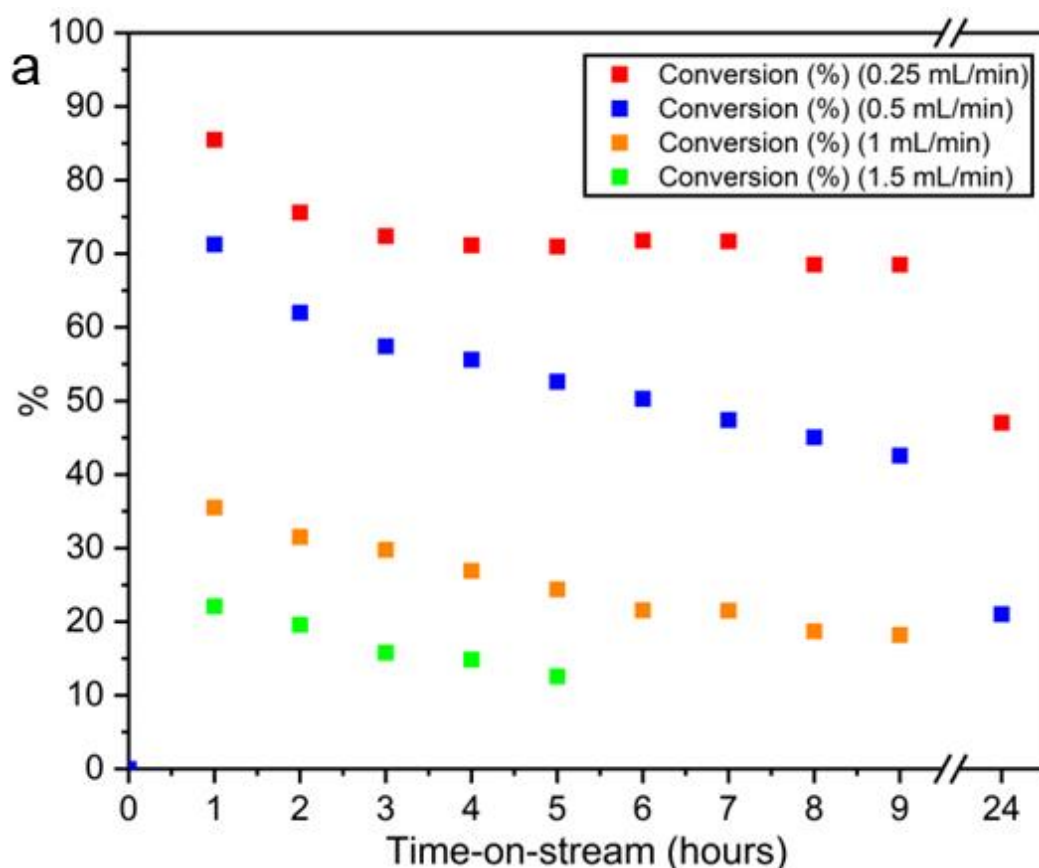
Figure 94: TGA profile and 1st derivative of MIL-100(Sc)@PBSAC composite a) before 26 hour reaction at 0.25 mL/min b) after 26 hour reaction at 0.25 mL/min.

4.3.2.2 Studying other flow rates

Due to the successful results obtained at 0.25 mL/min, we next decided to study the catalytic behaviour at a number of different flow rates (0.5, 1.0 and 1.5 mL/min) (with all other conditions identical to the experiment carried out at 0.25 mL/min). At each flow rate studied, the residence times are shown in Table 37. The resultant conversion and yield plots are shown in Figure 95a-b.

Table 37: Flow rate studied and the resultant residence times for the packed-bed reactor used in this work.

Flow rate (mL/min)	Residence time (mins)
0.25	34
0.5	17
1.0	8.5
1.5	5.7



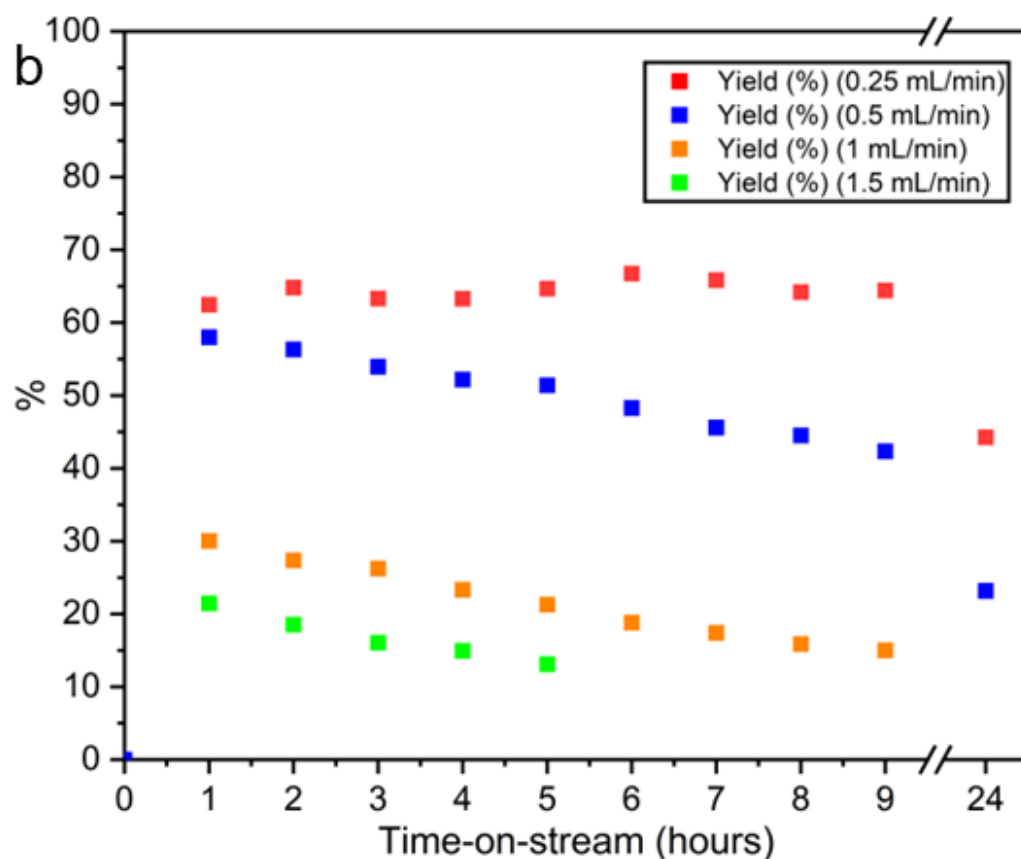


Figure 95: a) Conversion and b) Yield (of \pm -isopulegols) plots for flow experiments carried out at 0.25, 0.5, 1 and 1.5 mL/min. N.B. Data at 0.25 mL/min are same from section 4.3.2.1.

As the flow rate was increased, there was a decrease in both conversion and yield due to the shorter residence time inside of the reactor (Figure 95, Table 38). Unlike at 0.25 mL/min where stable values were obtained for the first 9 hours-on-stream, the conversion and yield were both found to decrease steadily as a function of time-on-stream. The cause of this behaviour is discussed in more detail in section 4.3.2.3 and section 4.3.2.4.

Despite the decreasing catalytic activity with increasing time-on-stream at the higher flow rates studied, averaged reaction metrics across the flow rates studied were still calculated to allow for comparison of the conditions (Table 38). The decrease in catalytic activity that was observed over time was accounted for by showing the standard deviation for each metric.

Table 38: Average conversion and yield values after first 9 hours time-on-stream (at 0.25, 0.5, 1.0 mL/min) and first 5 hours time-on-stream (at 1.5 mL/min).

Flow Rate (mL/min)	Residence time (mins)	Conversion (%)	Yield (%)
0.25	34	72.9 ± 5.2	64.4 ± 1.3
0.5	17	53.8 ± 9.0	50.3 ± 5.4
1.0	8.5	25.3 ± 6.0	21.7 ± 5.4
1.5	5.7	17.0 ± 3.8 ^a	16.9 ± 3.3

^a Of (±)-isopulegols. Uncertainty values correspond to standard deviation of conversion/yield value over first 9 hours time-on-stream (for 0.25, 0.5 and 1.0 mL/min) or 5 hours time-on-stream (for 1.5 mL/min).

Flow rates of 0.25, 0.5, 1.0 and 1.5 mL/min corresponded to average conversion values of 72.9, 53.8, 25.3 and 17.0% and average yield (of (±)-isopulegols) values of 64.4, 50.2, 21.7 and 16.9% respectively (Table 38). Based on these values, changing the flow rate between 0.5 - 1.5 mL/min resulted in an almost proportional change in the conversion/yield (e.g. doubling the flow rate (or halving the residence time) approximately halved the conversion/yield). This relationship was not observed upon lowering the flow rate to 0.25 mL/min, however, where (based on trend between 0.5 - 1.5 mL/min) approximately complete conversion/yield would be expected but was not obtained.

Further reaction metrics (i.e. productivity, TON, TOF, STY) across the different flow rates studied are shown in Table 39. Despite the decreasing conversion/yield over time at 0.5, 1 and 1.5 mL/min, the productivity of these reactions was still higher ($\approx 0.9 \text{ hr}^{-1}$) than at 0.25 mL/min (0.64 hr^{-1}) despite the stable conversion/yield values at this lower flow rate. The same trend was also observed for the TOF and STY values where similar values of $\approx 15 \text{ hr}^{-1}$ and $\approx 105 \text{ g L}^{-1} \text{ hr}^{-1}$ were calculated respectively for flow rates 0.5, 1.0 and 1.5 mL/min, greater than at 0.25 mL/min (TOF of 10.6 hr^{-1} and STY of $75.01 \text{ g L}^{-1} \text{ hr}^{-1}$). Thus for these metrics a stable catalytic activity is not necessarily a requirement for obtaining the highest values for this system.

Table 39: Average productivity, TOF and STY for first 9 hours time-on-stream (0.25, 0.5, 1.0 mL/min) or 5 hours time-on-stream (1.5 mL/min) and total productivity and TON after these times.

Flow Rate (mL/min)	Productivity (g hr ⁻¹) ^a	Productivity after 9 or 5 hours (g)	TON after 9 or 5 hours ^b	TOF (hr ⁻¹) ^c	STY (g L ⁻¹ hr ⁻¹) ^e
0.25	0.64 ± 0.01	5.7	95.6	10.6 ± 0.2	75.01
0.5	0.92 ± 0.10	8.2	137.4	15.3 ± 1.7	107.8
1.0	0.89 ± 0.22	8.0	133.0	14.8 ± 3.7	104.7
1.5	0.94 ± 0.18	4.7 ^d	78.2 ^d	15.6 ± 3.0	110.5

^a Productivity represents the average amount of (±)-isopulegols formed, in g, per hour over the 9 hours time-on-stream (at 0.25, 0.5 and 1.0 mL/min) or 5 hours time-on-stream (1.5 mL/min). ^b TON after 9 or 5 hours = Amount of (±)-isopulegols formed after 5 hours (for 1.5 mL/min) or 9 hours (0.25, 0.5 and 1.0 mL/min) (in moles) / Amount of catalyst (in moles). ^c TOF (hr⁻¹) = TON per hour for first 9 hours time-on-stream (at 0.25, 0.5 and 1.0 mL/min) or 5 hours time-on-stream (1.5 mL/min) / time (in hours). Calculation of TON and TOF assumed that all scandium atoms in the MIL-100(Sc) framework participated in catalysis. ^e STY (g L⁻¹ hr⁻¹) = average mass of (±)-isopulegols formed per residence volume (g) (for first 5 or 9 hours time-on-stream) / reactor volume (L) * residence time (hr).

4.3.2.3 Studying the loss in catalytic activity over time-on-stream

The first step that was taken to identify the causes of the activity loss over time-on-stream was to calculate the (±)-isopulegols mass balance at each flow rate (Eqn. 36), i.e. the amount of (±)-isopulegols produced relative to the amount of (±)-citronellal consumed after a certain amount of time. The (±)-isopulegols mass balance over the course of the reactions is shown by Figure 96.

$$\begin{aligned}
 & (\pm)\text{-Isopulegols MB (\%)} \\
 & = \frac{\text{mass } (\pm)\text{-isopulegols formed after time } t \text{ (g)}}{\text{mass } (\pm)\text{-citronellal reacted after time } t \text{ (g)}} \times 100
 \end{aligned}
 \tag{Eqn. 36}$$

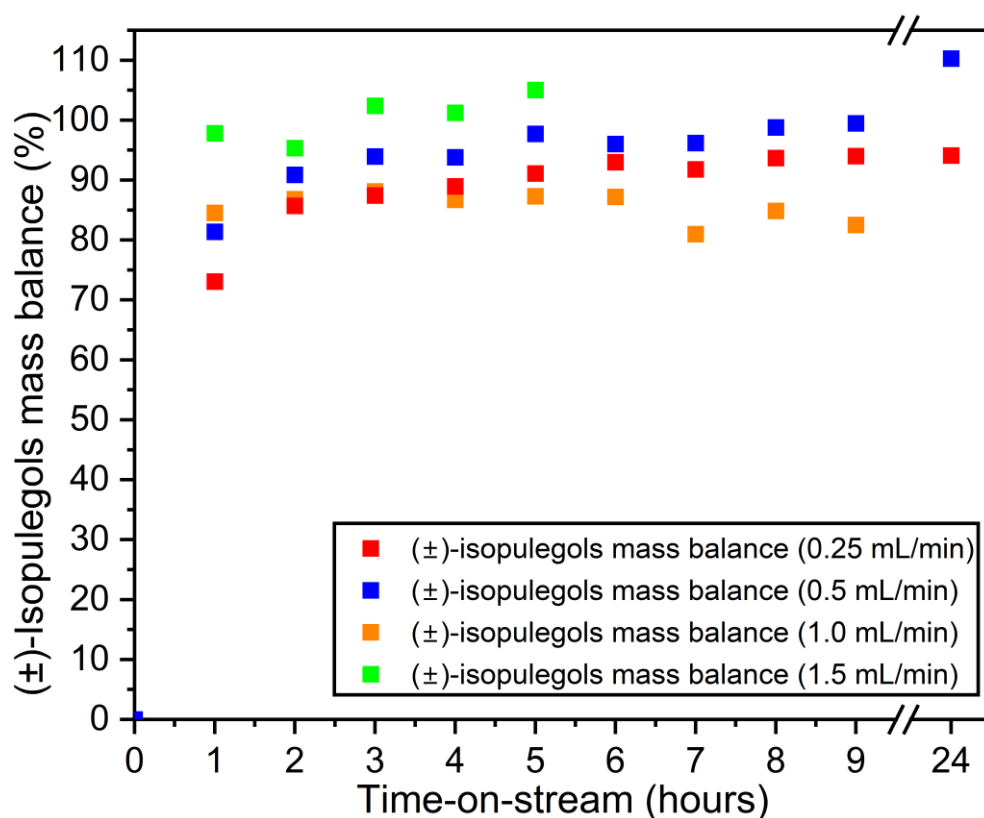


Figure 96: (±)-Isopulegols mass balance as a function of time in the flow experiments for the flow rate experiments conducted at 0.25, 0.5, 1.0 and 1.5 mL/min.

For the experiments conducted at 0.5 and 1.5 mL/min, there was an increase in the calculated (±)-isopulegols mass balance values increased over the course of the reaction which reached > 100%. Because the 'mass of (±)-citronellal reacted' in the (±)-isopulegols mass balance equation (Eqn. 36) was calculated as the difference between the mass at the start and end of the reactor, the increasing (and > 100%) (±)-isopulegols mass balance values suggest that (±)-citronellal was accumulating over time in the reactor. At 0.25 and 1 mL/min these values were observed to be more stable for the duration of the reaction.

Because of the increase in (±)-isopulegols mass balance values over time-on-stream, we postulate that the activity loss over time-on-stream should be a function of the amount of (±)-citronellal passed through the reactor (everything else being equal). We tested for this by plotting the data according to the number of residence volumes as this is a direct measure of the amount of material that had passed through the reactor. Because the conversion/yield values were a function of the residence time (and thus varied at the different flow rates), we

normalised the yield values obtained after 1 hour to enable better comparison. Figure 97 shows the data for this.

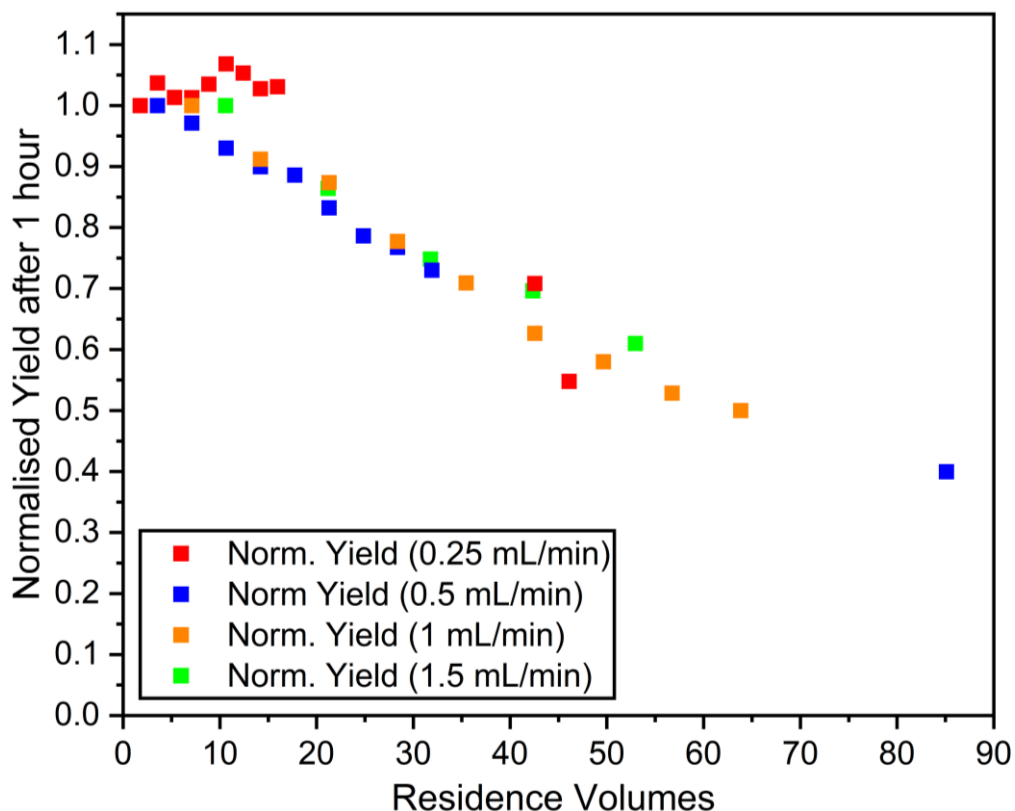


Figure 97: Normalised yield values after 1 hour of reaction versus the number of residence volumes for at the flow rates studied.

Interestingly, inspection of Figure 97 shows that the decrease in normalised yield as a function of the amount of material passed through the reactor (i.e. residence volumes) was similar for the reactions at 0.5, 1.0 and 1.5 mL/min. The similar decrease in normalised yield as a function of the residence volumes (and so amount of material passed through the reactor) at these flow rates further points to the hypothesis that (\pm)-citronellal was accumulating in the reactor over time. At 0.25 mL/min the plot does not follow the same trend with the normalised yield found not to decrease for the first 16.0 residence volumes (9 hours of reaction). This finding was unsurprising as changing the flow rate could have wider implications for the reaction beyond merely adjusting the amount of material passed through the reactor - for example the residence time distributions of different species and flow regimes. A decrease was observed after 42.6 and 46.1 residence volumes (24 and 26 hours of reaction) at 0.25 mL/min, however.

4.3.2.4 Regenerating catalytic activity

The results presented in section 4.3.2.3 show that (\pm)-citronellal accumulation in the reactor was occurring over time and may be one cause of the activity loss over time-on-stream.

During the same reactions we also we also observed the formation of a waxy material on the outside of the reactor (Figure 98). We identified an accumulation of this solid inside of the packed-bed reactor during the reaction as another potential reason for the loss in activity. To characterise the solid, we analysed the material by ^1H NMR. The solid immediately dissolved in CDCl_3 . ^1H NMR analysis of this material in CDCl_3 showed only broad peaks between 0.75 – 1.75 ppm which were assigned to $-\text{CH}_3$ and $-\text{CH}_2-$ environments (Figure 99).



Figure 98: Waxy material that was observed to form at the reactor connection.

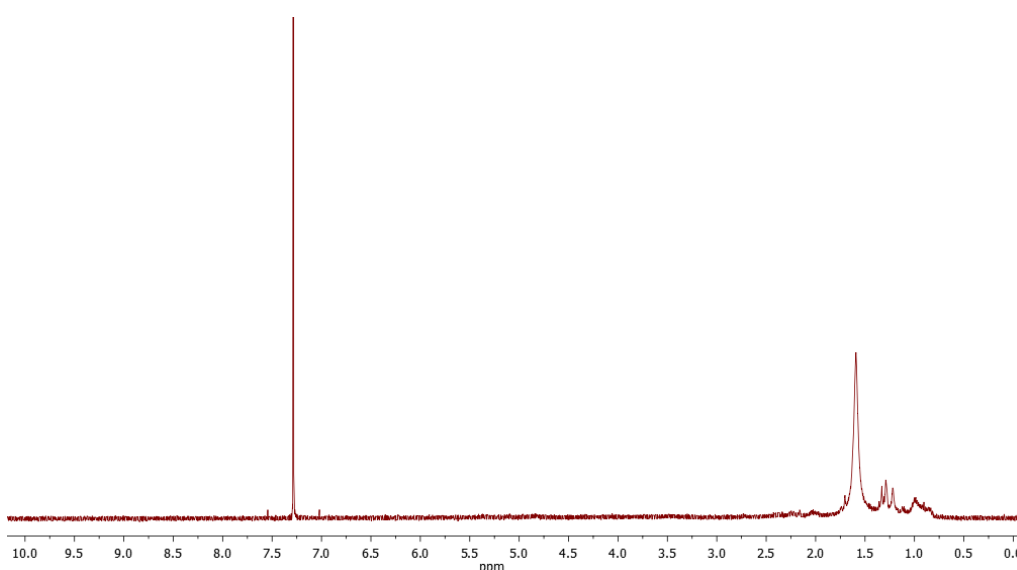


Figure 99: ^1H NMR (CDCl_3) of waxy material that was observed to form suggesting that it was hydrocarbon-based. Peak at 7.3 ppm corresponds to CHCl_3 solvent peak.

Solvent washes are commonly employed to regenerate the catalytic activity of heterogeneously catalysts when used in continuous flow reactions via the removal of adsorbed material to the catalyst. Upon studying the tandem cyclisation–hydrogenation of citronellal to menthol catalysed by scrap catalytic converters (SCATs) in continuous flow, Luque *et al.*³¹⁷ recovered catalytic activity to the original levels after they observed a decreased activity after 72 hours by washing with neat toluene for 20 minutes; the cause in activity loss was therefore attributed to the adsorption of organic species onto the catalyst.

Inspired by this, a toluene wash (2 mL/min, 2 hours, 110 °C) was first carried out after 24 hours-on-stream at 0.5 mL/min following the experiment detailed in section 4.3.2.2. Figure 100 shows the data. This washing step did not produce any improvements in the yield of conversion, however, with the yield and conversion still steadily decreasing over the next three hours.

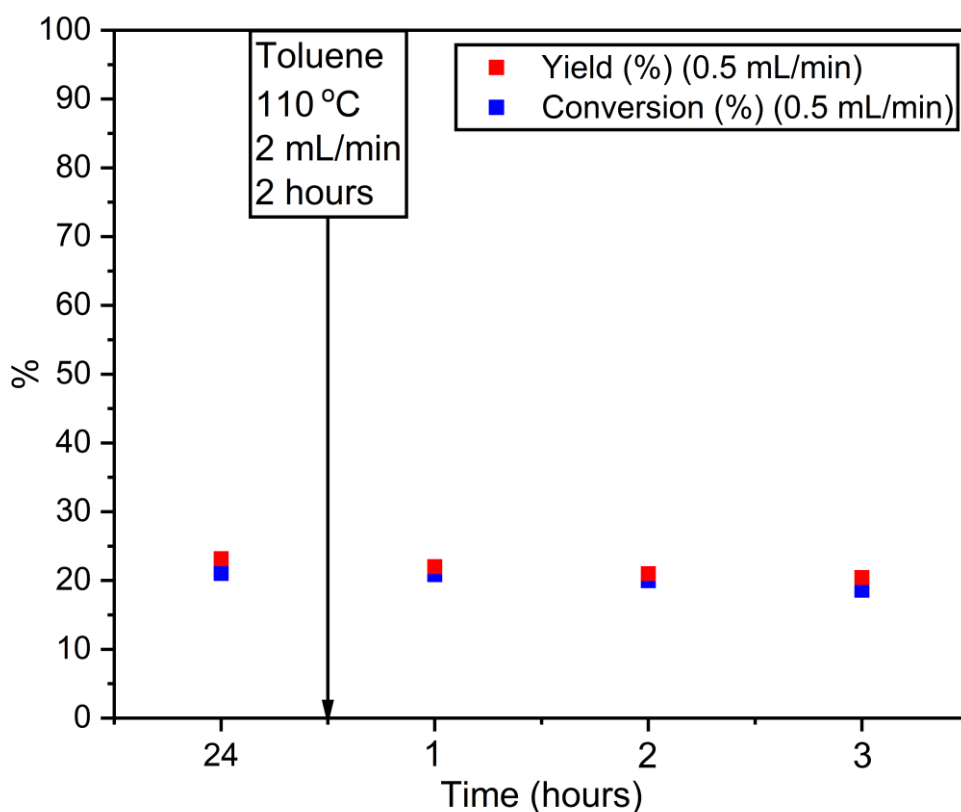


Figure 100: Toluene wash step after 24 hours in the flow reaction at 0.5 mL/min. Toluene was flowed through for 2 hours at 2 mL/min, 110 °C. No improvements in conversion or yield were observed.

With the lack of success in carrying out a washing step with toluene, we next designed a flow experiment that we theorised would be able to test for two causes of the observed activity loss: the formation of the waxy solid on the outside of the

packed-bed reactor (Figure 98) and the accumulation of (\pm)-citronellal onto the catalyst.

Firstly, because of the high solubility of the waxy solid in (deuterated) chloroform which we observed when preparing the sample for ^1H analysis, we decided to carry out a flow reaction with chloroform as the reaction solvent. We theorised that upon using chloroform as the reaction solvent, the waxy solid would remain dissolved rather accumulating in the reactor over time.

Secondly, we incorporated a washing step with methanol. Methanol has previously been used as a solvent to activate MIL-100(Sc) via replacement of material that is bound to the Sc^{3+} centres situated throughout the MIL-100(Sc) framework.^{119, 213} Thus, by carrying out a washing step with methanol, we theorised that there should be a replacement of any (\pm)-citronellal bound to Sc^{3+} sites in MIL-100(Sc) leading to a re-increase in the catalytic activity.

The experiment was run for 3.5 hours at 0.5 mL/min which would enable the identification of a stable catalytic activity before wash steps were subsequently carried out. Figure 101 shows the data from this experiment (N.B. the quantities of (\pm)-citronellal and MIL-100(Sc)@PBSAC used in this reaction were scaled-down to preserve materials). Advantageously, we were able to carry out the reaction at elevated temperatures (80 °C), above the boiling point of both chloroform and methanol, due to the use of a pressurised system.

Similar to the observed phenomenon when using toluene as the reaction solvent, the use of chloroform as the reaction solvent led to a decrease in the conversion and yield over 3.5 time-on-stream. At 3.5 hours the (\pm)-isopulegols mass balance exceeded 100% (due to the yield value being higher than the conversion, see Figure 101, 3.5 hours) suggesting that a build-up of (\pm)-citronellal was also still occurring when using chloroform as the reaction solvent. These results suggest that the waxy solid that was observed to form over the course of the reaction was likely not the primary cause of the activity loss over time. A further wash with neat chloroform at 80 °C and 3 mL/min, for which there were no improvements in the conversion/yield, further support this assessment.

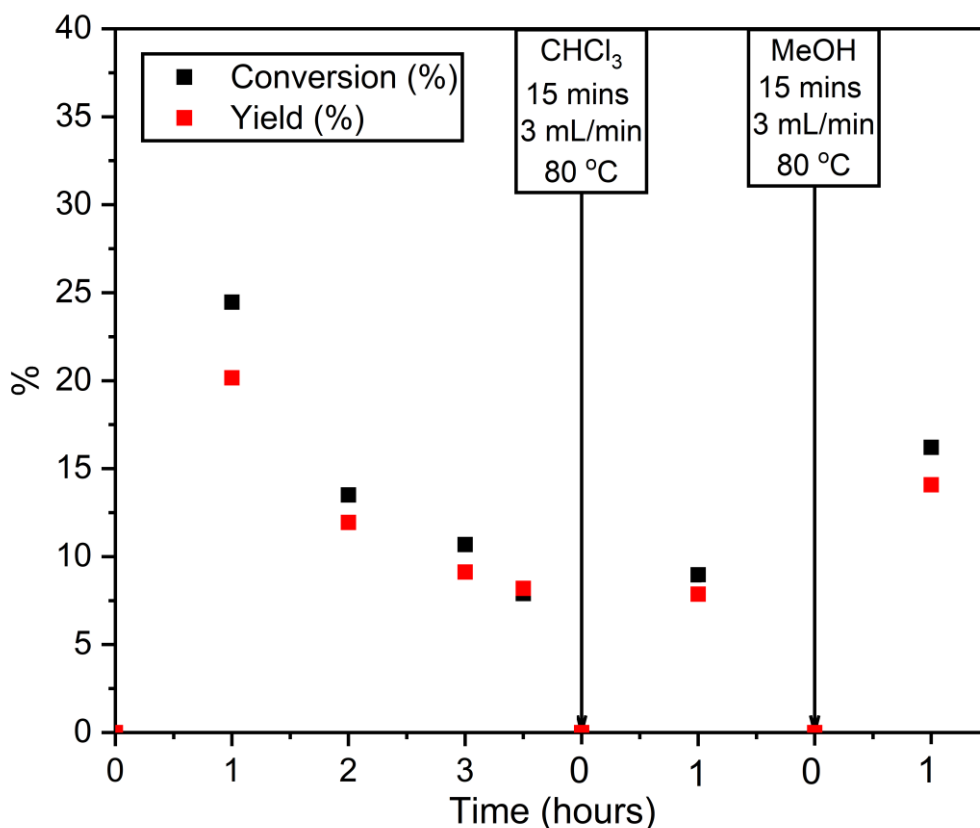


Figure 101: Conversion and yield vs. time data in the stability studies at 0.5 mL/min (0.23 M (\pm)-citronellal, 80 °C, CHCl₃, 0.5 mL/min) for 3.5 hours of time-on-stream then. NB: the quantities of (\pm)-citronellal and MIL-100(Sc)@PBSAC used in this reaction were scaled-down to preserve materials.

Following a solvent wash with neat methanol (3 mL/min, 80 °C), the conversion and yield were found to re-increase with the (\pm)-isopulegols mass balance decreasing to below 100% again. We postulate that this is due to the replacement of residual (\pm)-citronellal coordinated to the catalyst (Figure 102) and is further conclusive evidence that the loss in catalytic activity over time was due to a build-up of (\pm)-citronellal coordinated to the Sc³⁺ centres. This finding also suggests that the activity loss over time was not totally attributed to leaching of scandium from the support.

With some success in regenerating the catalytic activity via the use of a methanol wash, we decided to carry out another reaction in which methanol was used as the primary solvent. The reaction was carried out under identical conditions to the reaction carried out with chloroform (0.23 M (\pm)-citronellal, 80 °C, 500 mg MIL-100(Sc)@PBSAC) but using methanol as the solvent instead. We anticipated that the ability of methanol to strongly coordinate with the catalytically

active Sc³⁺ sites would enable more stable catalytic activity over longer reaction periods without significantly compromising the resultant catalytic activity.

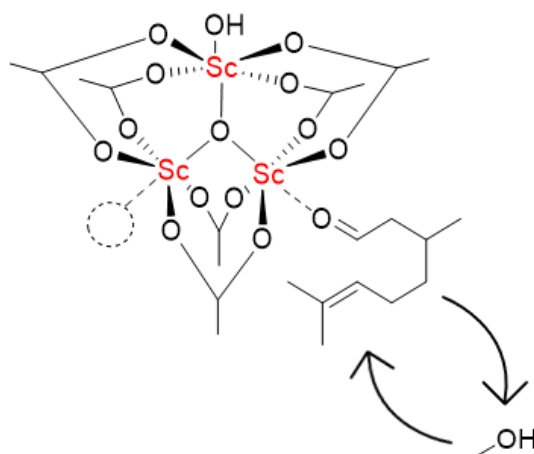


Figure 102: Depiction of replacement of (±)-citronellal molecule coordinated to Sc³⁺ site of MIL-100(Sc) node by methanol molecule.

Unfortunately, after one hour time-on-stream at 80 °C, the conversion and yield values were very low (5.7% and 0.7% in methanol compared to 24.5% and 20.2% in chloroform respectively) (Table 40, entry 1 and 2). This result confirms the coordinating (and competing) nature of methanol to the Sc³⁺ sites in MIL-100(Sc) resulting in a large decrease in the catalytic activity.

Table 40: Comparison of conversion and yield obtained after 1 hour on stream when using chloroform and methanol as the reaction solvents (0.2 M citronellal, 500 mg catalyst, 0.5 mL/min).

Entry	Solvent	Temperature (°C)	Conversion after 1 hour on stream (%)	Yield after 1 hour on stream (%)
1	Chloroform	80	24.5	20.2
2	Methanol	80	5.7	0.7
3	Methanol	100	12.3	2.1

We further increased the temperature to 100 °C (again which we were able to due to the use of a pressurised system) in an attempt to improve conversion and yields. After one hour time-on-stream at this temperature the conversion increased from 5.7% at 80 °C to 12.3% at 100 °C, with the yields increasing from 0.7% to 2.1% (Table 40, entry 3). We ran the reaction for a further three hours and noticed a decrease in the conversion to 9.1% whilst the yield remained more stable at approximately 2% (Figure 103). Based on this data, the conclusion was

reached that carrying out flow reactions in methanol was not appropriate for obtaining stable and sufficient conversions/yield values for this reaction.

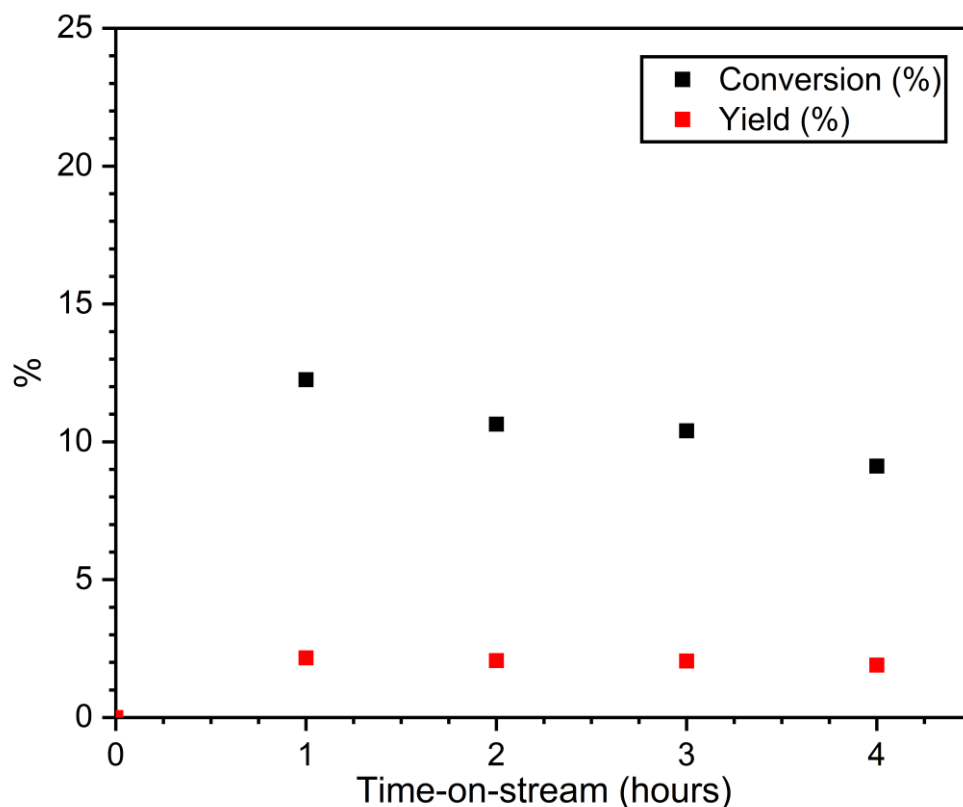


Figure 103: Conversion and yield vs. time data in the stability studies in methanol (0.5 mL/min, 0.2 M (\pm)-citronellal, 100 °C, 500 mg MIL-100(Sc)@PBSAC) for 4 hours.

To address the decreasing catalytic activity observed when reactions were carried out in toluene (Figure 95a-b), we devised a flow reaction that involved the use of toluene as the primary reaction solvent but where intermittent methanol washes (2 mL/min, 60 mins, 110 °C) would be carried out after every 4 hours in an attempt to restore the original levels of catalytic activity. In the experiment, a total of seven cycles of 4-hour long flow reactions were executed, taking the total reaction time to 28 hours (N.B. a total of 34 hours including methanol washes). The results are shown in Figure 104.

Figure 104 shows that the methanol washes were somewhat successful at regenerating the catalytic activity. However, the values did not return to the original values that were obtained in the first 4-hour long experiment. After each wash, the conversion re-increased due to the removal of (\pm)-citronellal from the catalyst which allowed for further adsorption of more upon restarting the reaction but generally the conversion/yield showed a downward trend. In some cases, the

yield increased after a methanol wash but not every single time. There was, however, seemingly a slowing down in the rate at which this value was decreasing.

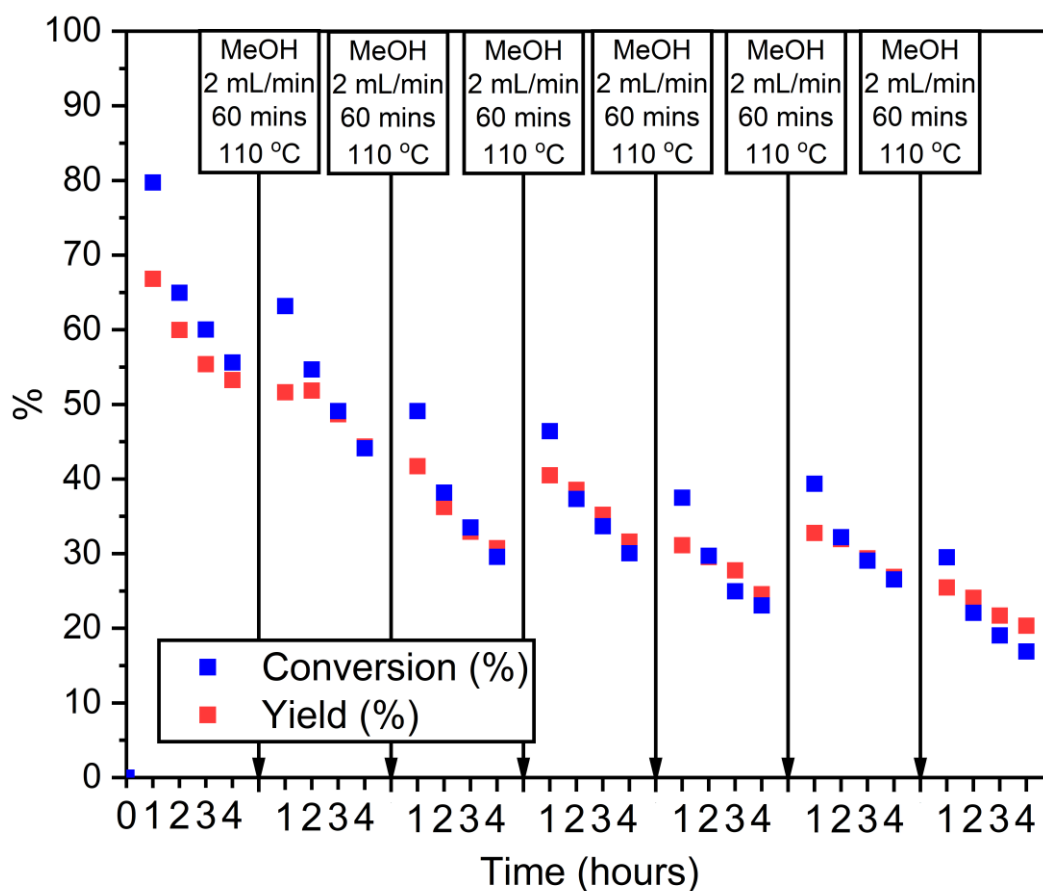


Figure 104: Methanol wash flow experiment that was carried out. After 4 hours of reaction (0.4 M (\pm)-citronellal, 1 g (\pm)-citronellal, 0.5 mL/min, 110 °C), the catalytic activity was partially regenerated by flowing methanol through the system (2 mL/min, 60 mins, 110 °C).

After the 28 hour (or 34 hours including methanol washes) reaction, we characterised the catalyst by AAS (Table 41) and TGA (Figure 105). There appeared to be a 2.2 – 5.6% loss of scandium over the course of the reaction, less than what was observed in the 26 hour experiment at 0.25 mL/min (7.5 - 13.6 % , section 4.3.2.1.1). The TGA profile of the catalyst after the methanol wash experiment (Figure 105) shows a mass loss between 200 - 300 °C, similar to after the 26 hour reaction at 0.25 mL/min, indicative of (\pm)-citronellal adsorption.

Table 41: Atomic absorption spectroscopy (AAS) data of before and after 26 hours time-on-stream. An average 3.9% loss of scandium was measured due leaching over the course of the reaction.

Scandium loading before MeOH wash experiment (% w/w)	Scandium loading after MeOH wash experiment (% w/w)	% loss of scandium over course of reaction
1.68 ± 0.02	1.61 ± 0.01	2.2 - 5.6

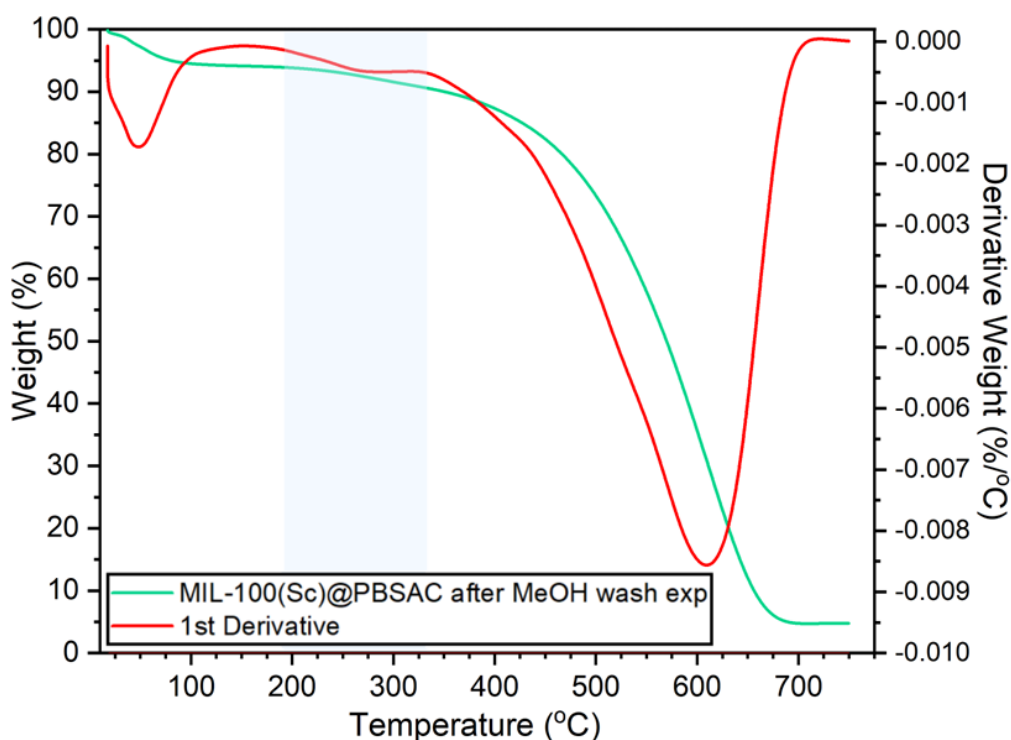


Figure 105: TGA profile and 1st derivative of MIL-100(Sc)@PBSAC composite a) after methanol wash experiment.

Whilst this experiment was somewhat successful at regenerating the catalytic activity of MIL-100(Sc), we would aim in the future to achieve more stable catalytic activities in different ways. Firstly, although carrying out a reaction in pure methanol was unable to give both suitable catalytic and stable catalytic activity, we would attempt as reaction involving the use of a mixture of methanol and toluene, for example a 1:9 v/v methanol/toluene solvent system in the hope that this would give a compromise between both a high enough catalytic activity and one that is stable over longer periods of time.

In a similar vein, we would also explore reactions using other, less polar substrates than (±)-citronellal which contains a polar aldehyde moiety thus implying a strong coordination to the Sc³⁺ sites throughout MIL-100(Sc).¹¹⁹

As the loss in catalytic activity was found to be a function of the amount of material passed through the reactor then, if we were aiming to simply maximise the amount of material produced in a given time, elevated temperatures could be employed due to the use of a pressurised flow system. Before doing this, however, the implications of elevated temperatures on MIL-100(Sc) crystallinity would also need to be evaluated.^{221, 322, 323}

4.3.2.5 Summary and future work

This work showcases the use of a MOF-based heterogeneous catalyst to catalyse the intramolecular cyclisation of (\pm)-citronellal in continuous flow. The results obtained in this mode of operation make this system one of the most active MOF-based system for citronellal cyclisation to date. The continuous mode of operation also showed greater activity than for reactions in batch with powdered MIL-100(Sc). At appropriate flow rates (0.25 mL/min), a stable catalytic activity could be obtained over extended reaction periods (9 hours) which briefly highlights the high potential of these materials for these applications in the future. At longer reaction times (≥ 24 hours) or higher flow rates (0.5, 1, 1.5 mL/min), however, the catalytic activity was found to decrease over time-on-stream. One cause of this was attributed to loss of scandium from the support material. Another cause was due to the accumulation of (\pm)-citronellal in the reactor over time; we found that a simple wash with methanol enabled some regeneration in the catalytic activity but not to the original levels.

Future work would seek to explore how this reduction in the loss of catalytic activity could be minimised, for e.g. by using a 10:90 v/v methanol/toluene solvent system to reduce the build-up of (\pm)-citronellal in the reactor or to greater understanding where catalyst leaching was occurring and the reaction conditions most conducive to causing this (i.e. higher pressures/flow rates). An understanding of the upper limits of usage (i.e. the most productive conditions that also maintain catalyst stability) would be ideal. We also envision the implementation of bi-functional/tandem catalysis to produce menthols, either through functionalisation of the catalyst to generate a bi-functional system (i.e. Pd NP deposition of MIL-100(Sc)@PBSAC composites) or the use of a tandem system (i.e. MIL-100(Sc)@PBSAC composites in one reactor, Pd/PBSAC catalyst in a second, downstream reactor).

4.3.3 Cannabidiol (CBD) and cannabidiol-methyl ester (CBD-ME) synthesis

Cannabinoids are a class of compounds derived from the *Cannabis sativa* plant (also known as the marijuana or hemp plant) for which more than 100 are known to exist. The use of herbal medicines containing cannabinoids containing plants extracts dates back > 2500 years ago to 500 BC,^{324, 325} Two of the most well-known cannabinoids are cannabidiol (CBD) and Δ^9 -tetrahydrocannabidiol (Δ^9 -THC) (Figure 106).^{324, 325} CBD finds use in a range of products such as food, beverages, cosmetics and pharmaceuticals. 2018 saw the first CBD-containing pharmaceutical, Epidiolex®, approved by the FDA for the treatment of epilepsy.³²⁶ In the same year the estimated global market value of \$4.6 billion, with projected CBD sales of \$20 billion is the USA alone by 2024.³²⁷

More broadly to cannabinoids, the FDA has also approved Marinol® or Syndros® which contains synthetic Δ^9 -THC as the active ingredient; such therapeutic uses include the treatment of AIDS-related anorexia.³²⁸ Cesamet® contains nabilone, a synthetic cannabinoid for chemotherapy-induced nausea.³²⁷

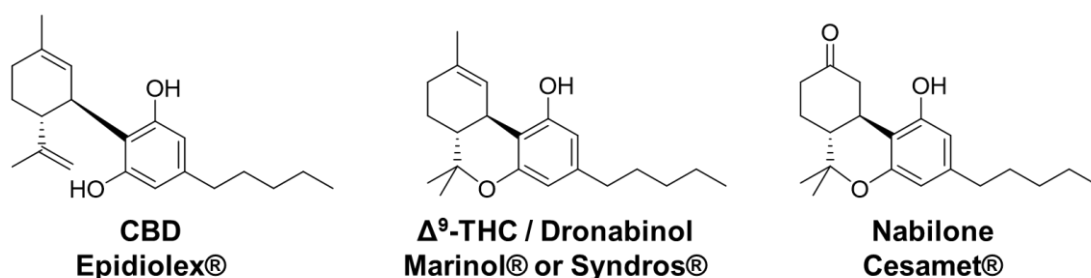
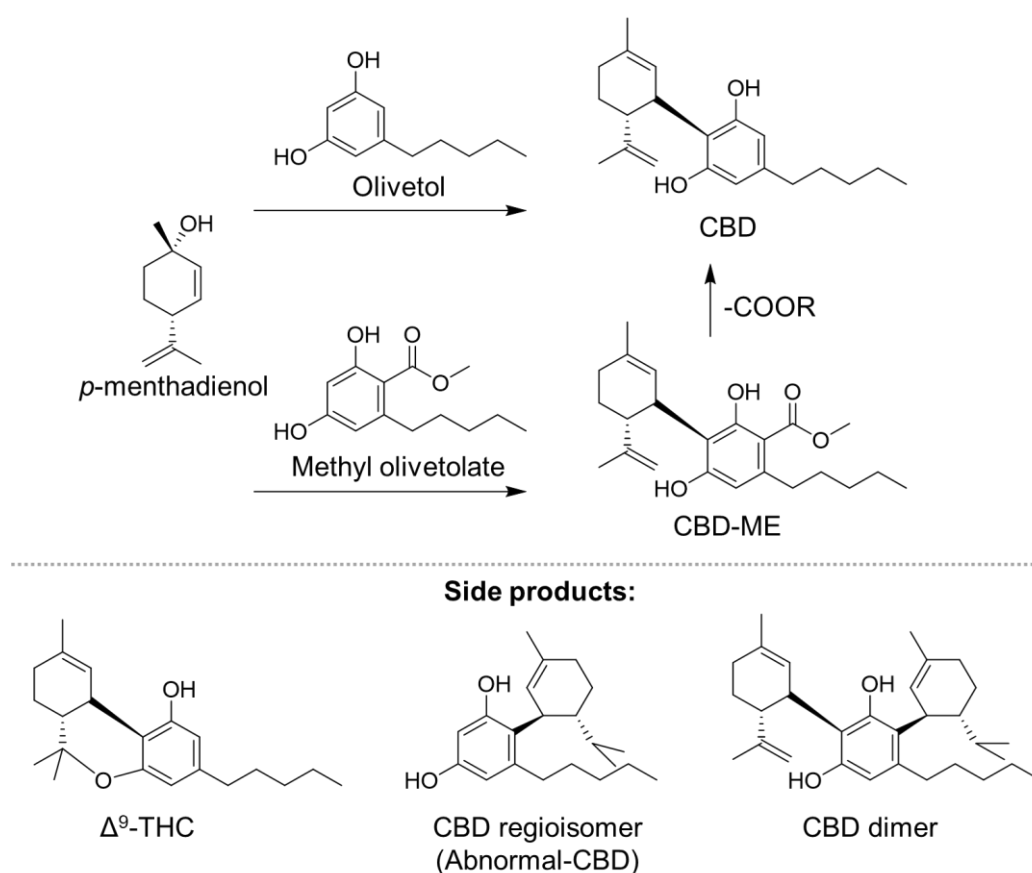


Figure 106: Left to right: Cannabidiol (CBD), the active ingredient in Epidiolex®, Δ^9 -THC, known as Dronabinol in a pharmaceutical context, the active ingredient in Marinol® and Syndros® and Nabilone, a synthetic cannabinoid and active ingredient in Cesamet®.

Given the enormous (and growing) interest in CBD and its derivatives for medicinal applications,³²⁹ it is unsurprising that pharmaceutical companies are directing research efforts into the development of new synthetic approaches to these compounds.

4.3.3.1 Synthetic approaches to CBD

Previous synthetic approaches to CBD and its derivatives were discussed in detail by Jagerovic *et al.*³³⁰ In their review article highlighting stereoselective synthetic strategies to CBD, Passarella *et al.*³³¹ classified synthetic approaches to CBD in three different categories: Friedel-Crafts reactions using olivetol and derivatives, nucleophilic addition/subtraction reactions, and intramolecular Ireland-Claisen rearrangements. The first of these approaches via a Friedel-Crafts reaction is the most common way to prepare CBD (Scheme 10). For the sake of brevity, this approach will only be discussed from this point forward.³³²



Scheme 10: Summary of reaction routes to CBD(-methyl ester) explored in this work into continuous flow. The reactions involve coupling of olivetol or methyl olivetolate with *p*-menthadienol in a Friedel-Crafts reaction.

The synthesis of CBD by a Friedel-Crafts reaction involves the reaction between olivetol or olivetolic alkyl esters (e.g. methyl olivetolate) and a terpene (e.g. *p*-menthadienol); this step may be catalysed by either Lewis or Brønsted acids and is still the most conventional production method to date (Scheme 10).^{331, 333} There are some additional issues associated with the production of

CBD via this approach, however. The acidity must be controlled so that the CBD can be produced while not promoting additional cyclisation into Δ^9 -THC. The reaction can also produce regioisomers (known as abnormal-CBD) and dimers. To prevent the formation of abnormal-CBD, the use of ester-groups such as a methyl-ester group can be added onto the olivetol moiety giving CBD-methyl ester (CBD-ME) upon reaction with *p*-menthadienol. The ester group is then subsequently removed.

Terpenes that have been used for the Friedel-Crafts reaction to CBD production include isopiperitenol, carene and menthadienol. This dates back to work carried out by Petrzilka and colleagues in the 1960s who used oxalic acid as the catalyst.^{334, 335} Since then, a number of different catalysts have been used, summarised by Passarella and colleagues³³¹. Catalysts for this reaction include BF₃-etherate supported on alumina,³³⁶ Ag(OTf)₃³³⁷ and Sc(OTf)₃.^{338, 339}

To date, a vast majority of these studies were conducted in batch. In recent times, some effort has been given to the production of CBD in continuous flow. In 2021, Palmieri *et al.*³²⁹ reported the first continuous flow synthesis of CBD whilst reducing the additional cyclisation to THC. The flow setup consisted of two reservoirs – one filled with olivetol and acetyl isoperitenol and the other with BF₃-etherate which met to react in a PTFE coil reactor. At the best conditions, CBD was obtained in 55% isolated yield. In 2021, Rutjús *et al.*³⁴⁰ explored the synthesis of CBD and THC in continuous flow using solid catalysts. For one of the reactions, *p*-menthadienol and olivetol were flowed through a column containing silica-supported boron trifluoride (Si-BF₃). A 20% yield of CBD (13% isolated yield) was achieved at a residence time of 5 seconds.

Metal-organic frameworks have not previously been used to catalyse this reaction. We first explored MIL-100(Sc)@PBSAC composites developed in this work as a catalyst for the Lewis acid catalysed Friedel-Crafts reaction between methyl olivetolate and *p*-menthadienol.

4.3.3.2 Methyl olivetolate and *p*-menthadienol coupling in continuous flow

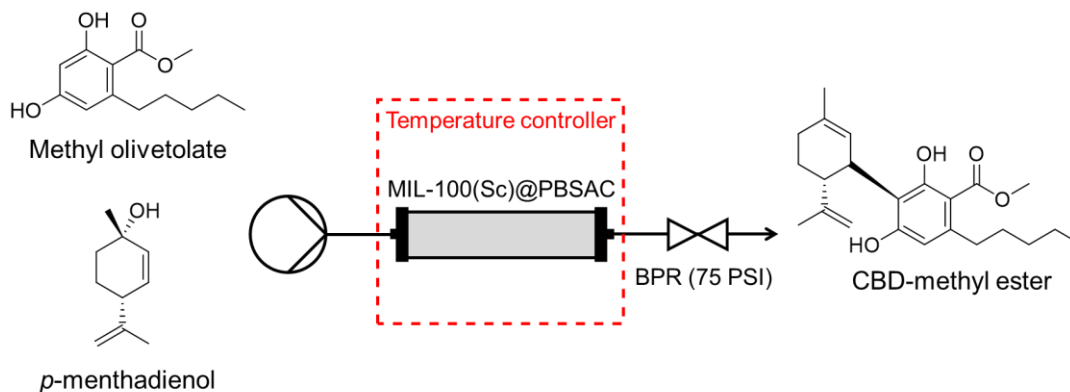


Figure 107: Coupling between methyl olivetolate and *p*-menthadienol to produce CBD-methyl ester catalysed by MIL-100(Sc)@PBSAC composites in continuous flow studied in this research.

Due to the presence of the methyl ester group on the olivetol moiety, this reaction was found to occur with greater regioselectivity than when using just olivetol.³⁴¹ High yields were reported previously for this reaction in batch (99%) when using BF₃OEt₂ as the catalyst with 80 - 85% yield after purification.^{342 343} Despite the improved regioselectivity, further steps are necessary to produce CBD via the removal of the ester group; the ester group removal is often conducted using a base which gives a final yield of between 50 - 70%.^{343, 344} Under optimised conditions, Crombie *et al.*³⁴⁵ attained an 89% selectivity to the CBD-methyl ester.

To the best of our knowledge, the reaction between methyl olivetolate and *p*-menthadienol to produce CBD-ME has not been studied in continuous flow. Given this, we decided to study this reaction in this mode of operation using MIL-100(Sc)@PBSAC as the catalyst. This also served as a test of the generalisability of this material towards other Lewis acid-catalysed reactions than those studied previously (i.e. the intramolecular cyclisation of citronellal).

We first explored the catalytic activity of MIL-100(Sc)@PBSAC towards this reaction in batch in an attempt to observe any formation of CBD-methyl ester. Chlorinated solvents are frequently used to catalyse this reaction,^{299, 337, 339, 340, 342, 343, 345} therefore dichloromethane and chloroform were used as the reaction solvents. A solution of methyl olivetolate (20 mM) and *p*-menthadienol (22 or 80 mM) (and thus in a ratio of 1:1.1 or 1:4 respectively) were refluxed (in dichloromethane or chloroform) with MIL-100(Sc)@PBSAC or Sc(OTf)₃ (0.5 mol % scandium loading relative to methyl olivetolate), the latter previously used to catalyse similar reactions (Table 42).^{338, 339} When MIL-100(Sc)@PBSAC was

used as the catalyst, no peak corresponding to CBD-ME was observed in the HPLC chromatogram after 24 hours of reaction. Conversely, peaks corresponding to the formation of CBD-ME were observed after just 4 hours when using Sc(OTf)₃.

Table 42: Batch testing of methyl olivetolate and *p*-menthadienol coupling in chlorinated solvents and using homogeneous species Sc(OTf)₃. Conditions: 20 mM methyl olivetolate and 22 mM or 40 mM of *p*-menthadienol, 0.5 mol % scandium loading (relative to methyl olivetolate).

Solvent	Catalyst	Molar ratio	Temp (°C)	Time (hrs)	CBD-ME? ^a
DCM	MIL-100(Sc)@PBSAC	1:1.1	40	24	N
DCM	MIL-100(Sc)@PBSAC	1:4	40	24	N
DCM	Sc(OTf) ₃	1:1.1	40	4	Y
Chloroform	MIL-100(Sc)@PBSAC	1:1.1	61	24	N
Chloroform	MIL-100(Sc)@PBSAC	1:4	61	24	N

^a Was CBD-methyl ester observed to have formed?

With this, we postulated that the reaction temperature was not high enough to enable any reaction to occur when using MIL-100(Sc)@PBSAC. We therefore decided to transfer the system to continuous flow and changed the reaction solvent to toluene as this would more easily enable the use of elevated temperatures. This solvent has also been used as the reaction solvent for the reaction between similar reactions (i.e. olivetol and *p*-menthadienol coupling) previously.³³⁷⁻³³⁹ The apparatus used to study this system in continuous flow was the same that used to study the intramolecular cyclisation of citronellal in continuous flow. See section 6.4.4 for a description of the system that was used.

The reaction temperature was increased to 140 °C and studied at a range of different flow rates and combinations of concentrations with *p*-menthadienol in excess (20 mM methyl olivetolate:40 mM or 80 mM *p*-menthadienol) (Table 43). At all conditions studied, the catalytic activity was low with the highest yield ≈ 2% when longer residence times (34 minutes) were employed.

Table 43: 20 mM methyl olivetolate, 80 mM *p*-menthadienol, 500 mg MIL-100(Sc)@PBSAC, toluene, 140 °C.

Entry	Flow rate (mL/min)	Residence time (mins)	Conc MO:Conc <i>p</i> -m	Conversion (%) ^a	Yield (%) ^a
1	2	4.25	20:80	≈ 1	0
2	1	8.5	20:80	≈ 0	0
3	0.5	17	20:80	≈ 1	≈ 1
4	0.25	34	20:80	6	≈ 2
5	2	4.25	20:40	≈ 1	≈ 0
6	1	8.5	20:40	≈ 1	≈ 0
7	0.5	17	20:40	6	≈ 1
8	0.25	34	20:40	17	≈ 1
9	2	4.25	40:80	2	≈ 0
10	1	8.5	40:80	3	≈ 1
11	0.5	17	40:80	6	≈ 1
12	0.25	34	40:80	13	≈ 2

^a Average of residence volumes 3 and 4.

We decided to further investigate the causes of the low catalytic activity that was observed in the flow reactions. In the HPLC chromatograms of samples the appearance of two peaks (at $t = 2.2$ and 2.7 minutes) was observed over the course of a reaction, the size of which appeared to be proportionate to the residence time (see appendix 4.5.2). The relative size of these peaks at $t = 2.2$ and 2.7 minutes also appeared to depend upon the concentration of *p*-menthadienol used for the reaction. For example, for different *p*-menthadienol concentrations (e.g. comparison of Table 43, entries 1 - 4 and 5 - 8 where 80 mM and 40 mM of *p*-menthadienol was used respectively) the size of the peaks at $t = 2.2$ and 2.7 minutes (following normalisation of these peaks by dividing by the internal standard peak area) appeared to be directly proportionate to the concentration of *p*-menthadienol used for the experiment. This is illustrated more clearly in Table 44. For example, in Table 44, entries 1 and 2 where 80 mM and 40 mM of *p*-menthadienol were used respectively, the ratio of the normalised peaks at $t = 2.2$ and 2.7 minutes was approximately 2. This relationship suggests that these peaks form as a result of *p*-menthadienol being consumed during the reaction. A similar trend is observed at 0.5 mL/min (Table 44, entry 3 and 4) but is less pronounced at flow rates of 1 mL/min and 2 mL/min (Table 44, entry 4 - 7) where residence times were shorter.

Analysis of reaction samples by ¹H NMR further supports the hypothesis that *p*-menthadienol was being fully consumed during the reaction at lower flow rates (appendix 4.5.3). The presence of peaks corresponding to *p*-menthadienol were

not observed in the ^1H NMR spectrum in the sample obtained at 0.25 mL/min (where the peaks at $t = 2.2$ and 2.7 minutes were largest) suggesting that the *p*-menthadienol was being fully consumed during the reaction. Peaks corresponding to *p*-menthadienol were present in the sample collected at 1.0 mL/min, however.

Table 44: Comparison of relative size of peaks at $t = 2.2$ and $t = 2.7$ minutes across experiments where different *p*-menthadienol concentrations (but identical methyl olivetolate concentrations) were employed. At lower flow rates (longer residence times), the size of these peaks appeared to depend linearly on the *p*-menthadienol concentration.

Entry	Ratio ^a	Flow Rate (mL/min)	Peak area ratio (t = 2.2 mins / IS) ^b	Ratio ^c	Peak area ratio (t = 2.7 mins / IS) ^d	Ratio ^c
1	20 mM:80 mM	0.25	0.64	1.7	1.73	2.0
2	20 mM:40 mM		0.38		0.88	
3	20 mM:80 mM	0.5	0.35	1.6	1.57	2.1
4	20 mM:40 mM		0.22		0.75	
5	20 mM:80 mM	1	0.10	3.7	0.65	3.1
6	20 mM:40 mM		0.03		0.21	
7	20 mM:80 mM	2	0.00	0.0	0.14	2.4
8	20 mM:40 mM		0.08		0.06	

^a Ratio of methyl olivetolate:*p*-menthadienol used in experiment. ^b Ratio of peak at $t = 2.2$ minutes and internal standard (biphenyl) peak. ^c Between peak area ratios for experiment employing 80 mM and 40 mM *p*-menthadienol. ^d Ratio of peak at $t = 2.7$ minutes and internal standard (biphenyl) peak.

Based on these findings, it seems plausible that *p*-menthadienol was being consumed before having the chance to react with methyl olivetolate. Future work would therefore seek to find a set of reaction conditions that give higher yields of CBD-ME which could be achieved by reducing the rate at which *p*-menthadienol is being consumed. One such approach could be by having *p*-menthadienol as the limiting reagent in the reaction. In this research, it was later established that the rate of *p*-menthadienol side reactions appears to be dependent upon the reaction temperature (section 4.3.3.3, Table 46), thus a compromise would need to be made between reaction temperatures that are too low such that no coupling between methyl olivetolate and *p*-menthadienol occurs but not too high that the *p*-menthadienol side reaction pre-dominates.

4.3.3.3 Olivetol and *p*-menthadienol coupling in continuous flow

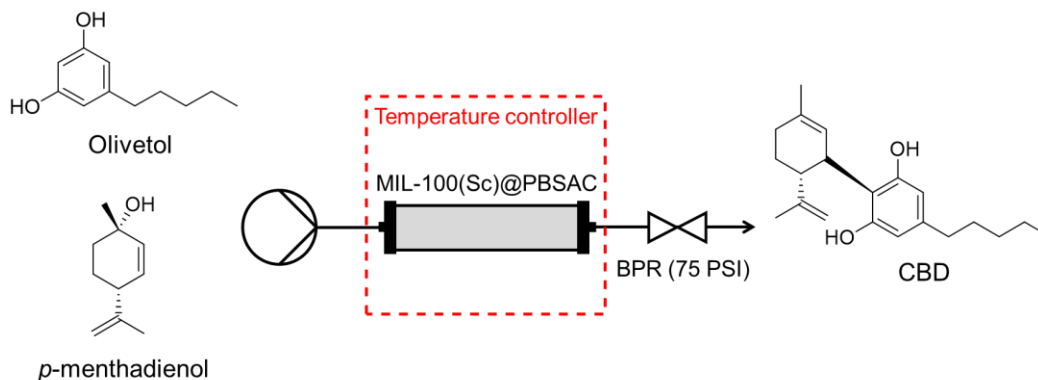


Figure 108: Coupling between olivetol and *p*-menthadienol to produce CBD catalysed by MIL-100(Sc)@PBSAC composites in continuous flow studied in this research.

Table 45 summarises the results that were obtained when studying the catalytic activity of MIL-100(Sc)@PBSAC composites for the coupling reaction between olivetol and *p*-menthadienol in continuous flow. This reaction differs from that studied in section 4.3.3.2 as the olivetol molecule does not contain a protecting methyl ester group. This coupling reaction directly leads to the formation of CBD (unlike when methyl olivetolate is used where the methyl ester group on CBD-methyl ester needs to be removed to give CBD) but may also produce abnormal-CBD and CBD dimers which are undesirable side-products. See section 4.5.2 for example chromatograms.

As described in more detail in section 6.4.7.3, the flow system used to study this reaction consisted of a vertically placed in an Omnifit glass column (length: 10 cm, 1 cm ID, empty volume: 7.85 cm³), PTFE tubing (1/16" OD, 1/32" ID), and an adjustable back pressure regulator. A Uniqsis FlowSyn System was used to both pump reagents through and heat the glass column. For a typical reaction, the glass column was filled with MIL-100(Sc)@PBSAC spheres (4.7 g) and a solution of olivetol (0.1 M) and *p*-menthadienol (0.4 M) were pumped through the bed from bottom to top at either 0.16 or 0.33 mL/min.

Table 45: Results obtained in this work for coupling of olivetol with *p*-menthadienol using MIL-100(Sc)@PBSAC composites in a packed-bed reactor in continuous flow. Comparison is done using HPLC peak areas for all olivetol-containing species. 100 mM Olivetol, 400 mM *p*-menthadienol, Omnifit glass column (10 cm x 0.88 cm) was filled with MIL-100(Sc)@PBSAC (4.7 g).

Entry	Flow rate (mL/min)	Residence Time (mins)	Temp (°C)	Solvent	Conv (%) ^a	CBD (%) ^a	CBD Regioisomer (%) ^a	Δ^9 -THC (%) ^a	CBD Dimer (%) ^a	Other (%) ^a
1	0.33	15	20	DCM	0.0	0.0	0.0	0.0	0.0	0.0
2	0.33	15	40	DCM	0.9 ± 0.1	0.4 ± 0.0	0.5 ± 0.1	0.0	0.0	0.0
3	0.33	15	80	DCM	27.2 ± 2.0	11.6 ± 0.3	10.9 ± 1.3	1.7 ± 0.1	0.0	3.2 ± 0.2
4	0.33	15	100	DCM	55.6 ± 0.1	23.4 ± 0.2	21.9 ± 0.3	3.5 ± 0.1	0.0	6.8 ± 0.2
5	0.16	30	100	DCM	28.6 ± 5.3	12.9 ± 2.6	10.4 ± 1.9	1.8 ± 0.3	0.0	3.5 ± 0.5
6	0.16	30	100	DCM ^b	15.5 ± 5.3	9.1 ± 3.5	5.0 ± 1.4	0.4 ± 0.1	0.0	1.0 ± 0.3
7	0.33	15	120	Toluene	94.5 ± 6.7	49.1 ± 7.9	30.8 ± 2.2	4.9 ± 0.3	5.3 ± 1.3	4.4 ± 0.1
8	0.33	15	140	Toluene	77.9 ± 0.2	35.8 ± 0.2	28.5 ± 0.4	4.0 ± 0.1	4.4 ± 0.1	5.2 ± 0.2
9	0.16	30	120	Toluene	77.4 ± 0.0	38.7 ± 0.3	26.9 ± 0.2	4.1 ± 0.0	3.5 ± 0.1	4.2 ± 0.0
10	0.16	30	140	Toluene	75.5 ± 0.2	34.5 ± 1.0	27.9 ± 0.9	3.8 ± 0.3	3.8 ± 0.1	5.5 ± 0.0

^a Standard deviations quoted as average of residence volumes 3 and 4. ^b Control sample with no catalyst, instead just PBSAC spheres were used.

We first explored the catalytic activity in DCM at a range of temperatures (20, 40, 80 and 100 °C). Between 20 - 40 °C minimal conversion was observed. Only at higher temperatures (≥ 80 °C), enabled by the elevated pressures of the flow system, were measurable conversions and products produced. The best results were obtained at 100 °C with a residence time of 15 minutes where a 55.6% conversion was obtained and the main product formed was CBD (23.4% peak area). Upon doubling the residence time to 30 minutes (by halving the flow rate to 0.16 mL/min), the conversion decreased to 28.6% which could be due to increased amounts of *p*-menthadienol side-reaction (also see section 4.3.3.2 for discussion of *p*-methadienol side reaction).

At ≥ 80 °C, the formation of the CBD regioisomer (abnormal-CBD) and THC were both observed with the former produced in almost identical quantities to CBD. This is an unfortunate result as this is not the isomer of CBD that we wanted to synthesise. Additionally, the formation of these species were also observed when no catalyst (just PBSAC spheres) was used, with CBD being produced in similar quantities in both instances (Table 45, entry 5 and 6). The use of MIL-100(Sc)@PBSAC led to greater conversions and greater amounts of CBD regioisomer and THC being produced relative to the control flow reaction. Based on these results, the role of both elevated temperatures and the catalyst support material in progressing this reaction cannot totally be ruled out.

There were also some other, unquantified impurities that were observed by HPLC to consistently form in small quantities (Table 45, column 11, 1.0 - 6.8% peak area) in both dichloromethane and toluene which is unsurprising given the diverse nature of this chemistry. We postulate that these could be different isomers of THC, as previously observed by Kappe *et al.*³⁴⁶ who investigated the formation of the synthesis of THC isomers in continuous flow using Lewis acid catalysts (Figure 109).

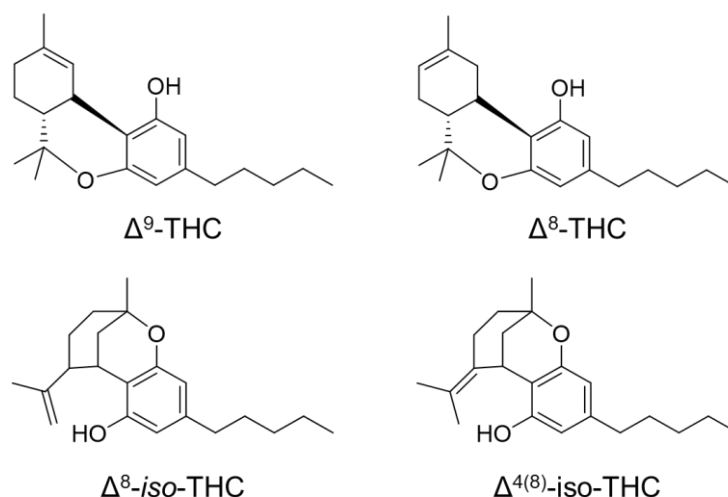


Figure 109: Δ^9 -THC and other THC isomers Δ^8 -THC, Δ^8 -iso-THC and $\Delta^{4(8)}$ -iso-THC that may have formed. These compounds were observed by Kappe *et al.*³⁴⁶ upon studying THC formation in continuous flow.

The reaction solvent was changed to toluene and elevated temperatures were also employed (120 and 140 °C). At 120 °C and a residence time of 15 minutes the a conversion of 94.5% was obtained. The conversion decreased to between 75 - 80% when either higher temperatures (140 °C) or longer residence times (30 minutes) were employed. We postulate that the increased reaction temperature or residence led to increased amounts of *p*-menthadienol side-reaction and lower amounts of reaction with olivetol. At the best conditions, CBD comprised approximately 50% of the product stream (with respect to olivetol-containing species) and forming in approximately a 1.6:1 ratio with CBD regioisomer. At these conditions, THC comprised approximately 5% of the HPLC peak area of olivetol-containing species. The formation of CBD-dimers was also observed at these conditions.

We also explored the consumption of *p*-menthadienol in a control reaction (i.e. no olivetol, 400 mM *p*-menthadienol, 140 °C, 30 minutes residence time) (Table 46, entry 11) and found that this compound contributed to the presence of three peaks in the HPLC chromatograms (at $t = 11.5$, 13.0 and 14.2 minutes) which were observed in the other experiments carried out using olivetol. The size of the peaks showed some dependency of the reaction temperature employed. For example in Table 46, entries 2, 3 and 4 where reaction temperatures of 40 °C, 80 °C and 100 °C were employed (15 minutes residence time, DCM), the peak areas % for the peak at $t = 14.2$ minutes were 0.3%, 12.6% to 21.5% respectively

showing an increase with reaction temperature. These peaks also constituted more of the % HPLC peak areas when toluene was used as the reaction solvent and higher temperatures (i.e. 120 °C, 140 °C) were employed. This is particularly true for the peaks at $t = 11.5$ and $t = 13.0$ minutes which only constituted 1.6 - 3.1% and 0.7% of the HPLC peak area when using DCM as the solvent but ranged from 18.9 - 25.0% and 5.3 - 9.6% when using toluene as the solvent respectively. These findings suggest that *p*-menthadienol was undergoing side-reactions which may occur faster when using higher temperatures or toluene as the reaction solvent. Such phenomena was also observed when studying the reaction between methyl olivetolate and *p*-menthadienol (section 4.3.3.2) where additional peaks were also observed in HPLC chromatograms.

Table 46: Percentage of HPLC peak areas for peaks at $t = 11.5$, 13.0 and 14.2 minutes as a percentage of all peaks in HPLC chromatogram (including olivetol-containing species) for experiments listed in Table 45.

Entry	Residence Time (mins)	Temp (°C)	Solvent	$t = 11.5$	$t = 13.0$	$t = 14.2$
1	15	20	DCM	0.0	0.0	0.0
2	15	40	DCM	0.0	0.0	0.3
3	15	80	DCM	3.1	0.0	12.6
4	15	100	DCM	1.7	0.0	21.5
5	30	100	DCM	1.9	0.0	11.6
6	30	100	DCM ^a	1.6	0.7	17.9
7	15	120	Toluene	19.4	7.0	34.3
8	15	140	Toluene	22.4	9.4	19.6
9	30	120	Toluene	18.9	5.3	27.8
10	30	140	Toluene	25.0	9.6	17.6
11	30	140	Toluene ^b	26.4	7.1	66.6

^a Control sample with no catalyst, instead just PBSAC spheres were used. ^b Control experiment using *p*-menthadienol (400 mM) and no olivetol used.

4.4 Conclusions of the chapter

The catalytic activity testing of MIL-100(Sc)@PBSAC composites in continuous flow in this chapter built upon the work carried out in Chapter 3 where these materials were fabricated and characterised. We studied the novel material, MIL-100(Sc)@PBSAC, as a catalyst for the intramolecular cyclisation of citronellal and for reactions pertinent to CBD production, i.e olivetol-containing species and *p*-menthadienol coupling, in continuous flow – the first time a MOF has been used to do this to date.

For citronellal cyclisation, a stable catalytic activity was obtained under appropriate conditions and no physical destruction of the catalyst was observed after extended usage (28 hours of reaction) which briefly showcases the high potential of these materials for use in continuous systems in the future. At different conditions, however, a loss in catalytic activity was observed over time indicative of catalyst deactivation; upon studying this we found that some leaching of catalyst from the support had indeed occurred and also attributed to a build-up of starting material in the reactor over time as another cause of activity loss. Further studies are required to greater quantify the upper limits of catalyst usage before the loss of activity becomes significant.

When studying the synthesis of CBD in continuous flow, for which only two examples in the literature exist to date, we found that low amounts of CBD-ME were produced which we attributed to the side-reaction of *p*-menthadienol before having the chance to react with methyl olivetolate. Larger amounts of CBD were observed to form in the reaction with olivetol, however. Impurities such as CBD-regioisomer, THC and CBD-dimer also formed during these studies, the prevention of which is desirable. Further research is required to establish the optimal conditions for CBD production.

This work shows that MIL-100(Sc) can successfully be immobilised onto PBSAC spheres and then applied to liquid phase Lewis acid heterogeneous catalysis in continuous flow for reactions that are pertinent to fine chemical production. MIL-100(Sc)@PBSAC composites gave the second highest reported activity for a MOF to date towards the intramolecular cyclisation of citronellal but also showed some deactivation (and loss in activity) over time. The generalisability with which MIL-100(Sc)@PBSAC can be applied towards other Lewis acid catalysed reactions, i.e. CBD synthesis, was also found not to be easy with side-reactions and impurity formation occurring over the main target reaction. These results show that PBSAC spheres can serve as a good vehicle for which to exploit the catalytic properties of MOFs in this mode of operation. This in turn provides a basis to exploit the catalytic properties of MOFs in continuous flow at pharmaceutically relevant scales, with the trend from batch to continuous manufacturing, where previously the powdered form of these materials would have hindered their application. The work carried out in this chapter is particularly exciting when coupled with the variety of MOF-based catalysts that have

previously been used in continuous flow for a range of organic transformations, as this work may provide the basis for a general approach to exploit the high versatility of MOF-based catalysts in continuous systems and improve their practicality due to the easier handling of these materials.

4.5 Appendices

4.5.1 Calculation of reaction metrics

$$\text{Conversion (\%)} = \frac{[(\pm) - \text{Citronellal}]_0 (M) - [(\pm) - \text{Citronellal}]_t (M)}{[(\pm) - \text{Citronellal}]_0 (M)} \times 100$$

$[(\pm) - \text{Citronellal}]_0 = (\pm) - \text{Citronellal}$ concentration at start of reaction

$[(\pm) - \text{Citronellal}]_t = (\pm) - \text{Citronellal}$ concentration at a given time t

$$\text{Yield (\%)} = \frac{[(\pm) - \text{Isopulegols}]_t (M)}{[(\pm) - \text{Citronellal}]_0 (M)} \times 100$$

$[(\pm) - \text{Isopulegols}]_t = (\pm) - \text{Isopulegols}$ concentration at a given time t

$[(\pm) - \text{Citronellal}]_0 = (\pm) - \text{Citronellal}$ concentration at start of reaction

$$\begin{aligned} \text{Selectivity to isopulegols (\%)} \\ = \frac{[(\pm) - \text{Isopulegols}]_t (M)}{[(\pm) - \text{Citronellal}]_0 (M) - [(\pm) - \text{Citronellal}]_t (M)} \times 100 \end{aligned}$$

$[(\pm) - \text{Isopulegols}]_t = (\pm) - \text{Isopulegols}$ concentration at a given time t

$[(\pm) - \text{Citronellal}]_0 = (\pm) - \text{Citronellal}$ concentration at start of reaction

$[(\pm) - \text{Citronellal}]_t = (\pm) - \text{Citronellal}$ concentration at given time t

$$\text{Selectivity to isopulegol (\%)} = \frac{[(\pm) - \text{Isopulegol}]_t}{[(\pm) - \text{Isopulegols}]_t} \times 100$$

$[(\pm) - \text{Isopulegol}]_t = (\pm) - \text{Isopulegol}$ concentration at a given time t

$[(\pm) - \text{Isopulegols}]_t = (\pm) - \text{Isopulegols}$ concentration at a given time t

$$\text{Turnover number (TON)} = \frac{\text{moles of } (\pm) - \text{Isopulegols produced after } x \text{ time}}{\text{moles of scandium used for reaction}}$$

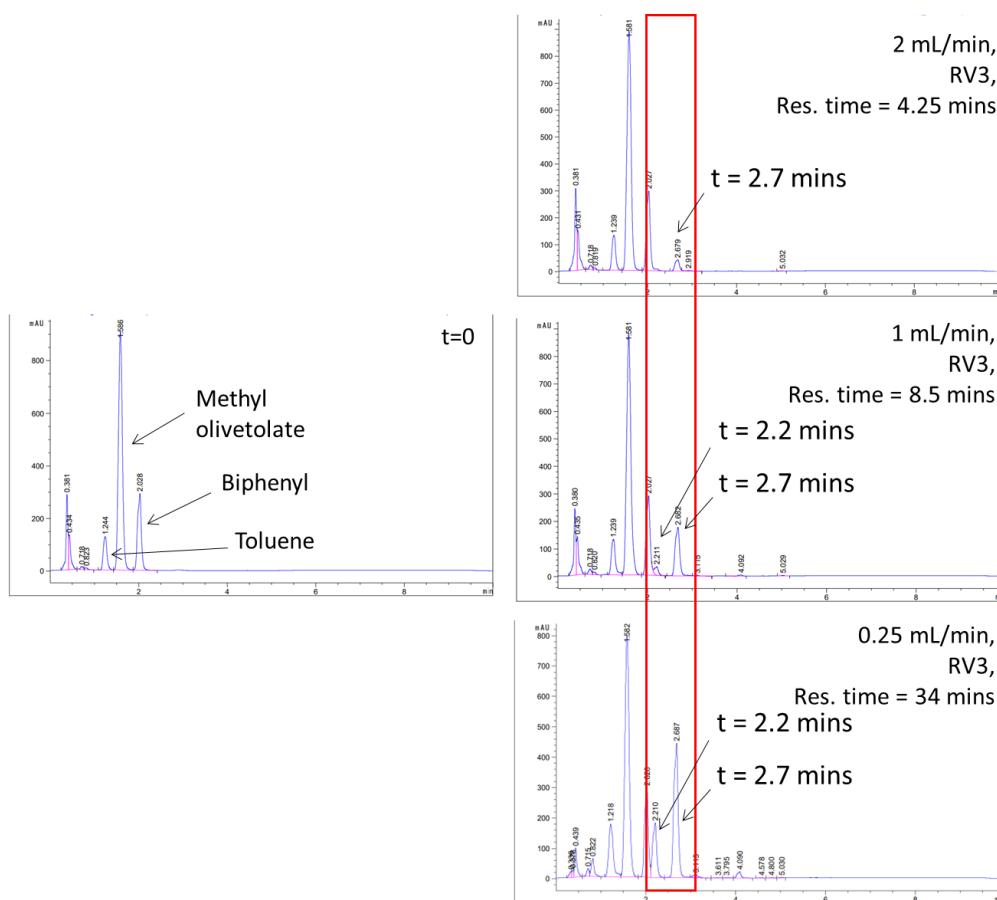
$$\text{Turnover Frequency (TOF)} (hr^{-1}) = \frac{TON}{\text{time (hr)}}$$

$$\text{Productivity (g hr}^{-1}\text{)} = \frac{\text{mass of } (\pm) \text{ - Isopulegols produced after 1 hour (g)}}{\text{time (hr)}}$$

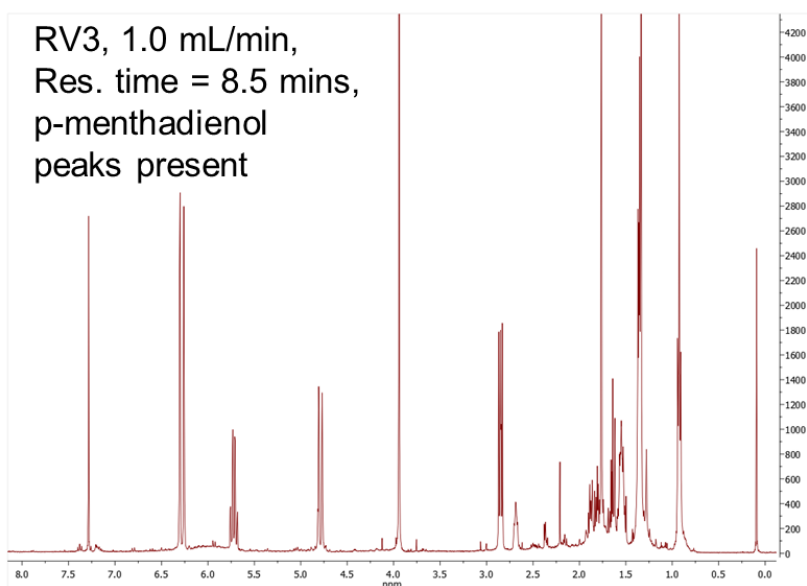
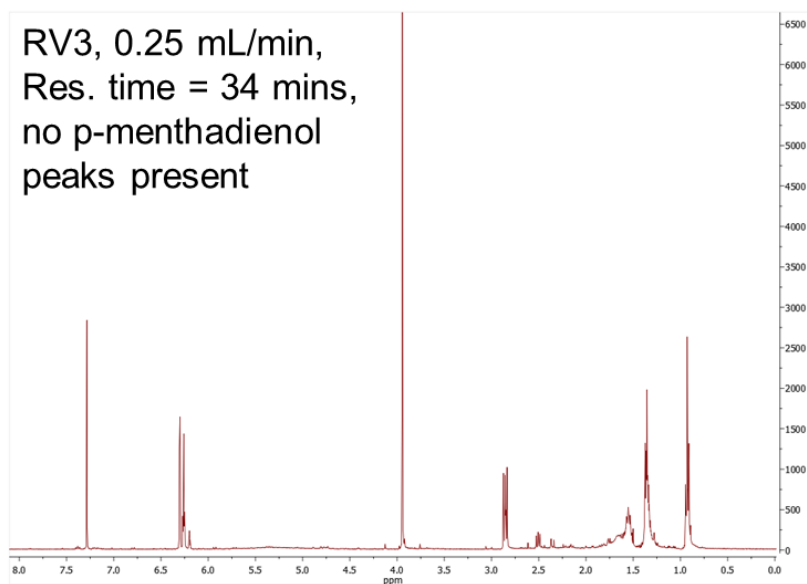
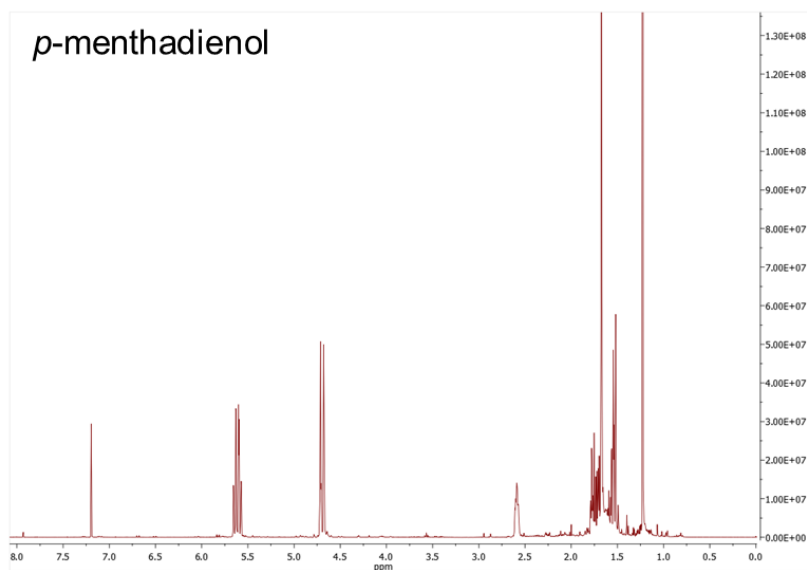
$$\text{STY (g L}^{-1}\text{ hr}^{-1}\text{)} = \frac{\text{mass } (\pm) \text{ - isopulegols produced per residence volume (g)}}{\text{reactor volume (L)} \times \text{residence time (hr)}}$$

$$\begin{aligned} \text{Activity (mmol } g_{\text{cat}}^{-1}\text{hr}^{-1}\text{)} \\ = \frac{\text{Average amount of } (\pm) \text{ - citronellal converted (mmol)}}{\text{hour - on - stream (hr)} \times \text{gram of catalyst (} g_{\text{cat}}\text{)}} \end{aligned}$$

4.5.2 HPLC chromatograms from methyl olivetolate and *p*-menthadienol coupling showing peaks at $t = 2.2$ mins and 2.7 mins (see section 4.3.3.2)



4.5.3 NMR of methyl olivetolate and *p*-menthadienol reaction (see section 4.3.3.2)



Chapter 5 Conclusions and Future Work

5.1 Conclusions

The aim of this research was to develop a novel heterogeneous Lewis acidic catalyst for fine chemical production in continuous flow by exploiting the favourable properties of polymer-based spherical activated carbon supports. A novel heterogeneous catalyst consisting of Lewis acidic catalytically active MOF, MIL-100(Sc), immobilised onto PBSAC spheres ideally shaped for use in packed-bed reactors was prepared and used in continuous flow for fine-chemical relevant organic transformations (i.e. specifically intramolecular cyclisation of citronellal and cannabidiol formation). The novel material was found to be the second most catalytically active Lewis acidic MOFs towards the intramolecular cyclisation of citronellal to date (activity of $72.9 \text{ mmol g}_{\text{cat}}^{-1} \text{ h}^{-1}$).

Before immobilising onto PBSAC spheres, the Lewis acidic catalytic properties of MIL-100(Sc) were studied in batch. This work was detailed in Chapter 2. MIL-100(Sc) powder was synthesised using conventional solvothermal approaches and characterised using a range of analytical techniques: PXRD, TGA, FT-IR, N_2 adsorption, SEM-EDX, DLS and XPS. This analysis also enabled calculations of properties pertinent to catalysis such as material stoichiometry (where the structure was found to be defective with a new formula accounting for this proposed) and estimations of the ratio of exterior to interior sites as a function of the particle size where a sharp increase in the ratio of sites located externally $< \approx 100 \text{ nm}$ was observed. Next, the Lewis acidic catalytic activity of MIL-100(Sc) towards the intramolecular cyclisation of citronellal, an industrially relevant reaction, was studied in batch. Following the use of molecular modelling to confirm that this reaction could feasibly occur within the pores of MIL-100(Sc), a combined DoE and kinetic modelling approach was conducted to explore this reaction further. For each experiment in the 2-level 3-factor full-factorial DoE conducted, time-series data was collected which enabled calculation of a range of metrics (i.e. initial rate, TOF, selectivity) over the course of each reaction. Good model fits were obtained for the initial rate and TOF and a trade-off between the initial rate and TOF was observed. The time-series data collected was also used to develop kinetic models of the reaction using DynoChem, where a Langmuir-Hinshelwood mechanism was unable to produce a good fit to the data.

This is the first time a DoE and kinetic modelling approach has been carried out for a MOF-based catalytic system. Overall, this work provided a good understanding of the catalytic properties of MIL-100(Sc) prior to immobilisation onto PBSAC spheres as preparation for use in continuous flow.

The work describing the fabrication of novel MIL-100(Sc)@PBSAC composites was detailed in Chapter 3. A facile synthesis of MIL-100(Sc)@PBSAC via reflux gave a material with consistent Lewis acidic catalytic properties over 24 batches (average isopulegols yield of $25.6\% \pm 4.6\%$ for cyclisation of citronellal after two hours). The novel material was characterised using FIB-SEM-EDX, PXRD, N_2 adsorption, TGA, AAS, XPS, light scattering and crush testing. MIL-100(Sc) was found to crystallise inside cracks $\approx 3 \mu\text{m}$ in diameter found on the outer surface of PBSAC spheres and inside the pores of the support too. Upon fabrication of MIL-100(Sc)@PBSAC, the support material was found to not lose any mechanical strength showcasing its suitability for continuous flow operations. A MIL-100(Sc) immobilisation efficiency onto PBSAC spheres was found to be approximately 50% with loose powdered MIL-100(Sc) also found to have formed independently of the spheres.

Chapter 4 described the catalytic activity studies of novel MIL-100(Sc)@PBSAC composites in batch and continuous flow. Following initial catalytic activity studies in batch towards the intramolecular cyclisation of citronellal, for which these materials were found to be highly reusable (no activity loss over 5 reaction runs), the reaction was then studied in continuous flow in a packed-bed reactor. A stable catalytic activity was obtained under appropriate conditions (over 9 hours time-on-stream at 0.25 mL/min) which briefly showcases the high potential of these materials for use in continuous systems in the future. Over longer reaction times (> 9 hours time-on-stream at 0.25 mL/min) and higher flow rates (0.5, 1.0, 1.5 mL/min), however, a loss in catalytic activity was observed over time which was attributed to some leaching of catalyst from the support (7 - 13%) and a build-up of citronellal in the reactor. It was found that the catalytic activity could partially be restored by carrying out methanol washes, however, the original catalytic activity could not be recovered and the catalytic activity decreased again when the reaction was restarted. Upon using MIL-100(Sc)@PBSAC as a catalyst in continuous flow for CBD synthesis via the coupling of olivetol and *p*-menthadienol, CBD was observed to form but also alongside other undesirable

impurities. This offered higher catalytic activity than when using methyl-olivetolate (to produce CBD-ME). Using methyl-olivetolate, poor yields of CBD-ME were obtained as a result of *p*-menthadienol self-reaction.

Overall, this research has demonstrated an approach to exploit Lewis acidic MOF-based heterogeneous catalysis in continuous flow for chemical synthesis in trend with the transition from batch to continuous manufacturing in the fine chemical industry. Additionally, this work may provide the basis for a general approach to exploit the high versatility of MOF-based catalysts in continuous systems and improve their practicality due to the easier handling of these materials.

5.2 Designing a new MOF@PBSAC system: preliminary work

The UiO- (University of Oslo) series of MOFs have garnered significant interest over the last decade due to their high thermal stability, large surface areas and tunable structures.^{228, 347-349} Now one of the most studied series of MOFs, the basic structure of UiO- MOFs consists of Zr-based clusters, $[Zr_6O_4(OH)_4]$, connected by aromatic dicarboxylate linkers with 12 extension points per node (Figure 110a).

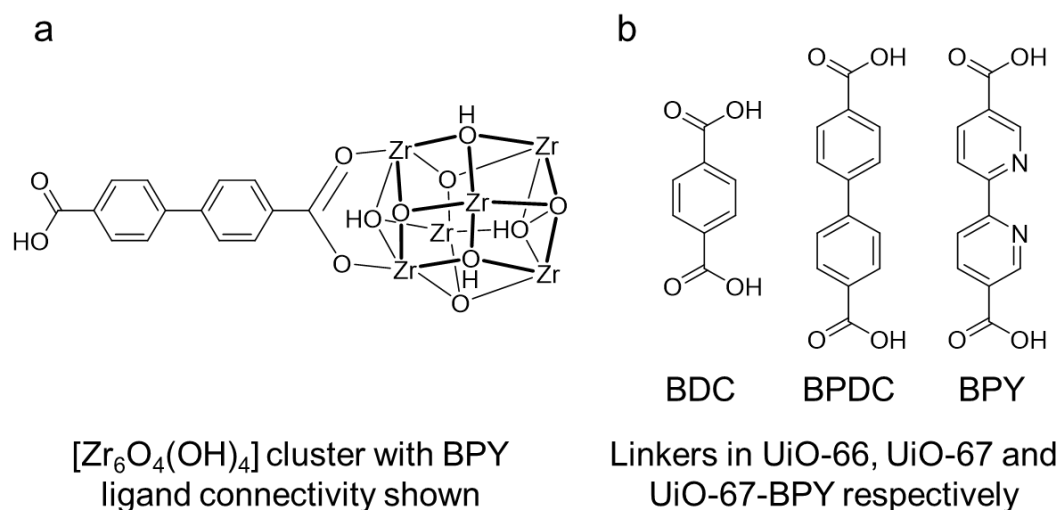


Figure 110: a) Zr₆ cluster in UiO- MOFs with connectivity to one 4,4-biphenyldicarboxylic acid linker in UiO-67 MOFs shown. b) Linkers in UiO-66, UiO-67 and UiO-67-BPY MOFs respectively. Left to right: 1,4-dicarboxylic acid, 4,4-biphenyldicarboxylic acid and 2,2'-bipyridine-5,5'-dicarboxylic acid.

UiO-66, the archetypal MOF of this series, contains 1,4-benzenedicarboxylate (BDC) linkers, whilst isorecticular derivative UiO-67 incorporates linear 4,4'-biphenyldicarboxylate (BPDC) linkers (Figure 110b).^{228, 347-349} Further, the BPDC linkers in UiO-67 may be replaced with 2,2-bipyridine-4,4'-dicarboxylate (BPY) linkers, giving UiO-67-BPY.²²⁶ Such functionalisation provides additional opportunities for catalysis applications via chelation of different metal ions such as copper,^{350, 351} palladium³⁵² and platinum³⁵³ to be used as the active species.

Luan *et al.*³⁵¹ synthesised Cu@UiO-67-BPY consisting of CuCl₂ ions chelated to the BPY ligands throughout the framework in two steps (i.e. MOF synthesis then post-synthetic modification with CuCl₂, see section 5.2.1 for more discussion of this) and used this as a catalyst for the aerobic epoxidation of olefins in batch (Figure 111a-b). For the aerobic epoxidation of olefins, a range of different olefin substrates were tested including cyclohexene. Molecular oxygen was supplied to the system thus making this reaction 3-phase (gas-liquid-solid). After 4 hours of reaction, > 99% yield of cyclohexene oxide was obtained.

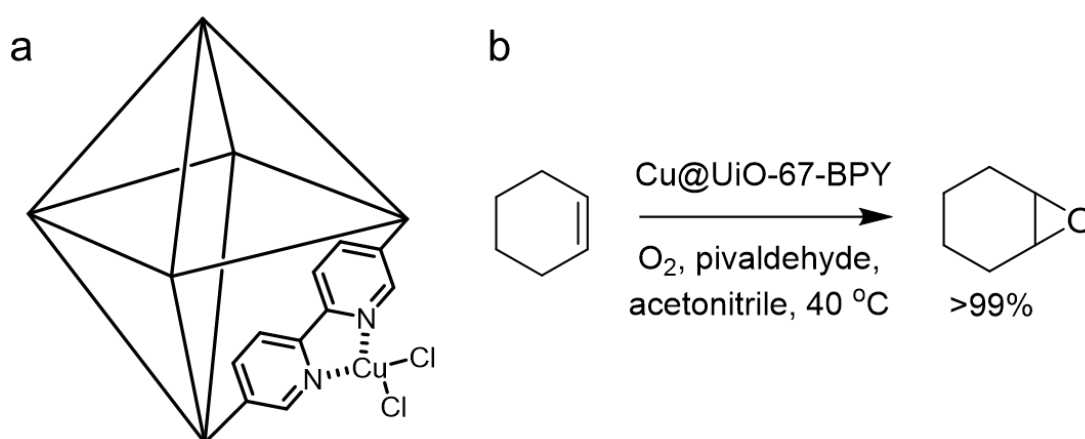


Figure 111: a) Cu@UiO-67-BPY prepared by Luan *et al.*³⁵¹ and used as a catalyst for the selective oxidation of alcohols and the aerobic epoxidation of alcohols. b) One reaction studied by Luan *et al.*³⁵¹ namely the aerobic epoxidation of cyclohexene catalysed by CuCl₂-UiO-67-BPY.

The different mode of catalysis of this system (via metal ion chelation to the linker), additional steps required in the design (i.e. post-synthetic modification) and different type of reaction studied (i.e. a three-phase solid-liquid-gas reaction) in comparison to MIL-100(Sc)@PBSAC (a pristine Lewis acid MOF catalyst prepared in one step used for a two-phase reaction) poses an exciting opportunity to develop a different, novel MOF@PBSAC system and study it in continuous flow. Thus, building upon the work conducted by Luan *et al.*,³⁵¹ we attempted to

prepare the novel material, Cu@UiO-67-BPY@PBSAC, and use this in continuous flow for the three-phase aerobic epoxidation of cyclohexene.

5.2.1 Synthesising Cu@UiO-67-BPY and Cu@UiO-67-BPY@PBSAC

Luan *et al.*³⁵¹ prepared Cu@UiO-67-BPY using solvothermal synthesis over two steps. Firstly, UiO-67-BPY was synthesised from an equimolar amount of ZrCl₄ and BPY ligand in DMF at 120 °C over 24 hours. Once the reaction vessel had cooled, CuCl₂.H₂O was added to the vessel and then heated to 40 °C (the authors did not specify for how long, although previous work involving the post-synthetic functionalisation of UiO-67-BPY with metals (including copper)^{352, 354} and similar materials (UiO-66-Sal)³⁵⁵ carried out the incubation step for 24 hours). Afterwards, the solution was filtered, washed with methanol at least three times and then dried at 80 °C for 12 hours.

A synthesis identical to that conducted by Luan *et al.*³⁵¹ including a 24 hour post-synthetic modification incubation step to incorporate CuCl₂ (similar to previous reports^{352, 354, 355}) was carried out to prepare Cu@UiO-67-BPY as well as a synthesis involving the in-situ addition of PBSAC spheres (an amount that would give a 50% w/w loading assuming 100% UiO-67-BPY yield) to the reaction vessel in an attempt to prepare Cu@UiO-67-BPY@PBSAC. For the latter, two samples were prepared: one without and one with the CuCl₂ incubation step giving UiO-67-BPY@PBSAC and Cu@UiO-67-BPY@PBSAC respectively. The appearance of the PBSAC-based materials was unchanged from the unfunctionalised PBSAC spheres.

To confirm if/how much zirconium immobilised onto the PBSAC spheres during the first step of the synthesis, a TGA of UiO-67-BPY@PBSAC was carried out (Figure 112a). The zirconium loading was calculated using the same equation used to determine the scandium loading on MIL-100(Sc)@PBSAC spheres (see section 3.3.3.1 for workings of this) where a zirconium loading of 1.14% on PBSAC was calculated, along with a UiO-67-BPY loading of 4.56% w/w. Based on the theoretical maximum 50% w/w UiO-67-BPY loading on PBSAC spheres for the synthesis, a loading efficiency of 9.12% was obtained.

Cu@UiO-67-BPY and Cu@UiO-67-BPY@PBSAC were analysed using PXRD (Figure 112b). Comparison of the PXRD patterns of these materials with the simulated pattern of Cu@UiO-67-BPY suggests that these materials were poorly

crystalline. In the PXRD pattern of Cu@UiO-67-BPY, a broad peak was observed between 5 - 8° 2theta (the region of the most intense peaks of crystalline Cu@UiO-67-BPY) as well as a sharper peak at approximately 7.2° 2theta which could be indicative of the formation of some crystalline Cu@UiO-67-BPY. This observation differs from Luan *et al.*,³⁵¹ who reported crystalline Cu@UiO-67-BPY phases in their work and instead more closely resembles PXRD patterns observed previously for UiO-67 MOFs where no/small amounts of modulator were employed in the synthesis.³⁵⁶ These findings are unsurprising given that a modulator was not used for the synthesis of these materials. There were also no peaks corresponding to crystalline UiO-67-BPY observed in the powder pattern of Cu@UiO-67-BPY@PBSAC. As well as employing an unmodulated synthesis, the lack of peaks corresponding to crystalline UiO-67-BPY in this composite material could also be due to a masking effect as a result of the broad amorphous scattering peak of the PBSAC spheres.

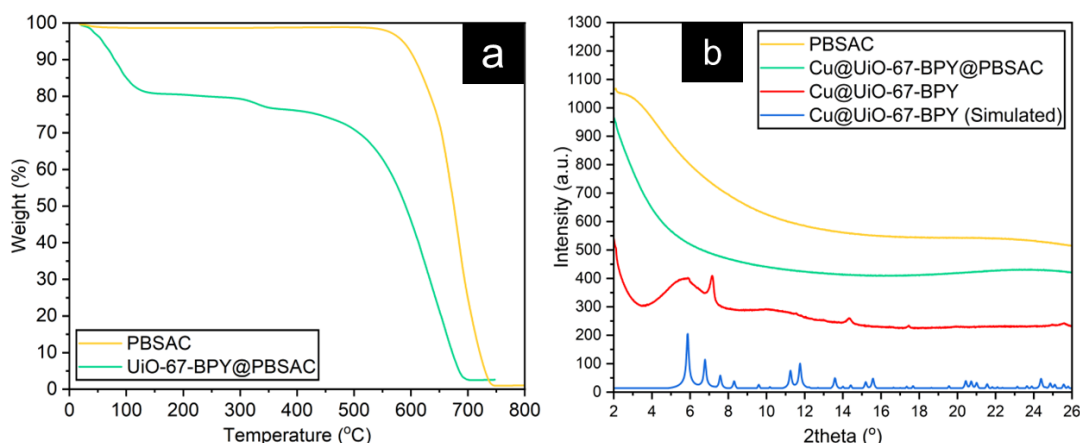


Figure 112: a) TGA of UiO-67-BPY@PBSAC (green) and PBSAC (yellow). b) PXRD of UiO-67-BPY (simulated) (blue), Cu@UiO-67-BPY (red), Cu@UiO-67-BPY@PBSAC (green) and PBSAC (yellow).

To further investigate whether any material had been immobilised onto the PBSAC spheres, SEM-EDX analysis was carried out. Similarly to MIL-100(Sc)@PBSAC composites, it appeared that material had formed inside the cracks of the PBSAC spheres (Figure 113a-d). An EDX spectra acquired of this material (Figure 113e-f) contained copper, chlorine and zirconium which are all constituent elements of the catalytic system.

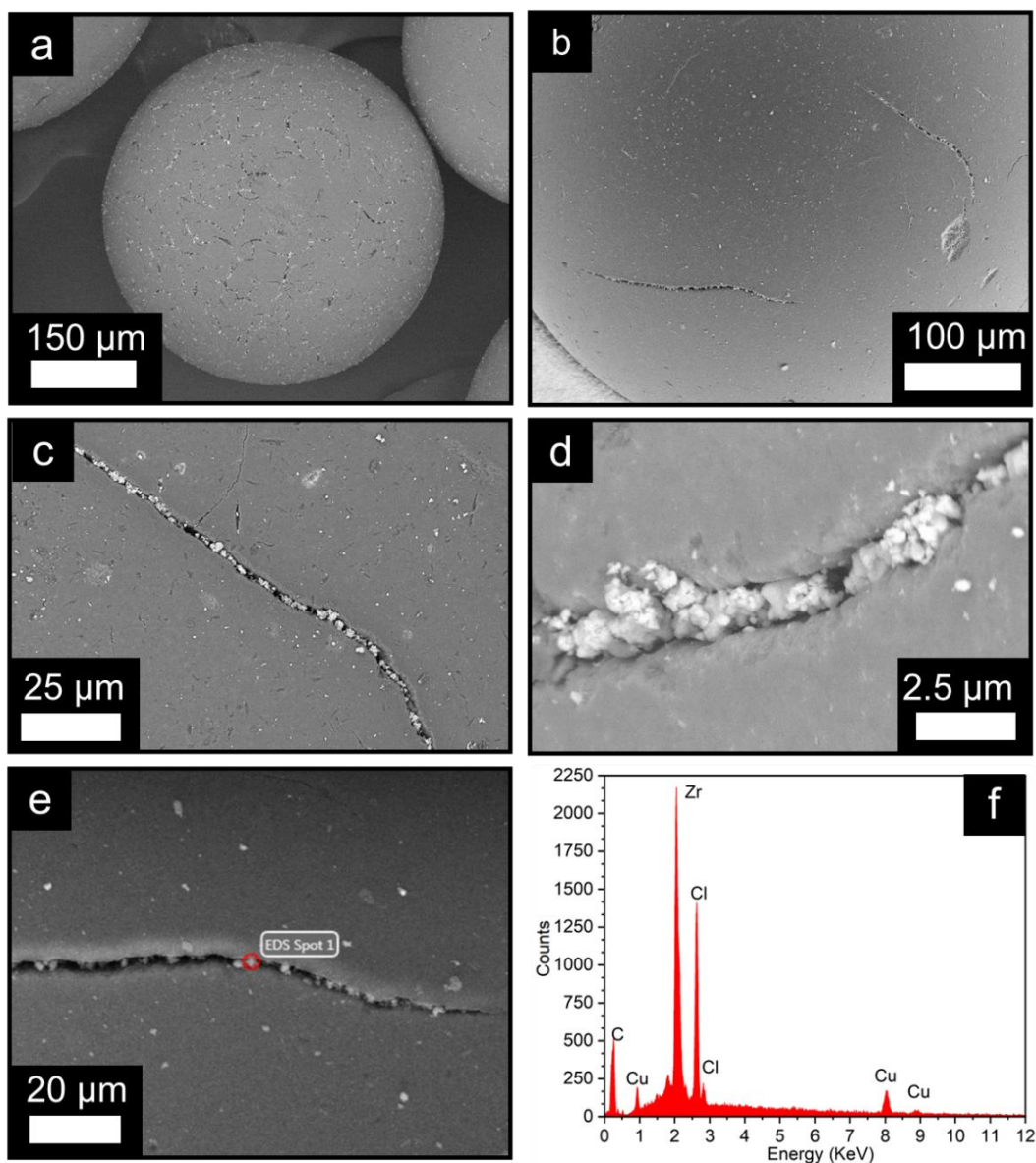


Figure 113: a-d) SEM images of Cu@UiO-67-BPY@PBSAC. e-f) EDX spot and subsequent spectrum obtained for Cu@UiO-67-BPY@PBSAC.

5.2.2 Preliminary catalytic activity testing

Although we could not confirm the presence of crystalline UiO-67-BPY formation onto the PBSAC spheres, we decided to carry out preliminary catalytic activity tests as SEM-EDX analysis confirmed that a material containing the constituent elements of the catalyst, (i.e. copper, zirconium, chlorine) was immobilised in the cracks of PBSAC spheres.

As noted in section 5.2, when using Cu@UiO-67-BPY as a catalyst for the aerobic epoxidation of cyclohexene Luan *et al.*³⁵¹ obtained a 99% yield of cyclohexene oxide after 4 hours of reaction (determined via GC-MS). For initial catalytic activity testing in this work, the effect of pivaldehyde, oxygen and PBSAC on the reaction

outcome was all studied (Table 47, entry 1 - 5). These tests found that cyclohexene reached complete conversion after 4 hours even without the use of Cu@UiO-67-BPY or Cu@UiO-67-BPY@PBSAC but there was no/minimal formation of cyclohexene oxide (Table 47, entry 2 - 4). The highest yield of cyclohexene oxide, $\approx 3\%$, was obtained when using Cu@UiO-67-BPY and Cu@UiO-67-BPY@PBSAC but this was still much below that obtained by Luan and colleagues (99%).³⁵¹ Thus, further studies are required to improve the selectivity of the reaction. The lower selectivity reported in this work could stem from the differences in crystallinity between the materials.

Table 47: Conversion of cyclohexene and yield of cyclohexene oxide after 4 hours of reaction. Conditions: 40 °C, acetonitrile (5 mL), 1 mmol cyclohexene, pivaldehyde (1.2 mmol) and 1 atm. compressed air balloon.

Entry	Piv	Cu@UiO-67-BPY	Cu@UiO-67-BPY@PBSAC	PBSAC	Conv (%)	Yield (%)
1	Y	Y			> 99	≈ 3
2	Y		Y		> 99	≈ 3
3	Y			Y	> 99	0
4					> 99	0
5	Y				> 99	0.1

Cyclohexene and compressed air used for all experiments. Molecular oxygen which was supplied via a balloon filled with compressed air. Piv = pivaldehyde.

5.2.3 Conclusion and next steps

These preliminary results have explored the fabrication of a novel catalytic system, Cu@UiO-67-BPY@PBSAC, incorporating additional complexity via post-synthetic modification of UiO-67-BPY (with CuCl₂) with the goal of exploring 3-phase (gas-liquid-solid) catalysis in continuous flow. By attempting to synthesise previously prepared (Cu@UiO-67-BPY) and novel (Cu@UiO-67-BPY@PBSAC) materials, the formation of crystalline UiO-67-BPY was not identified despite the immobilised material on the PBSAC spheres containing the constituent elements of Cu@UiO-67-BPY (i.e. copper, zirconium, chlorine). We postulate that one reason for this may be due to not using a modulated synthesis which is commonly employed for the preparation of crystalline UiO- MOFs.^{228, 248, 356, 357} The resultant catalytic activity of the materials towards the aerobic epoxidation of cyclohexene in batch was found to be low ($\approx 3\%$ yield) when compared to the results obtained by Luan *et al.*,³⁵¹ who obtained > 99% yield.

Future development work would seek to confirm the formation of crystalline UiO-67-BPY in powdered form and once immobilised on PBSAC spheres (via PXRD). A modulated synthesis would be employed as it has previously been noted that modulators play an important role in the formation of crystalline UiO-MOFs.^{228, 248, 356, 357} The lack of identification of UiO-MOF peaks in the PXRD pattern of Cu@UiO-67-BPY@PBSAC (section 5.2.1) could also be due to the loading being too low to measure. The most intense peaks in the powder pattern of UiO-67-BPY exist between 5 - 7° 2theta, where the intensity of the broad amorphous scattering peaks of the PBSAC support is the largest thus these peaks may be masked by this. Improvements in the loading of UiO-67-BPY on PBSAC spheres could therefore aid with the identification of crystalline phases via PXRD. This could be achieved through oxidation of the PBSAC surface via treatment with an acid/oxidizing agent, as was previously carried out by Navarro *et al.*¹⁹⁹ who treated PBSAC spheres with H₂O₂ prior to the immobilisation of UiO-66 on PBSAC spheres. This generates carboxylate group which can then bind to MOF metal centres.

Upon confirmation of crystalline UiO-67-BPY on PBSAC spheres, the copper loading following the postsynthetic modification step should be quantified, via AAS or ICP, to accurately determine the catalytic efficiency of the system. Further studies into improving the yield of cyclohexene oxide when using Cu@UiO-67-BPY@PBSAC as the catalyst are also required, with ≈ 3% yield obtained in preliminary catalytic activity studies where Luan and colleagues³⁵¹ obtained a > 99% yield. Upon obtaining a grasp of this reaction in batch, the reaction could then be studied in continuous flow in a 3-phase (gas-liquid-solid) system.

5.3 Future work

5.3.1 Routes to or requirements for scale-up

The application of MIL-100(Sc)@PBSAC composites in industrial flow reactors (i.e. scaled-up applications) is a logical next step for this research to realise industrial implementation. This requires consideration of both how these materials may be prepared more efficiently and on larger scales as well as obtaining deeper understanding of catalyst lifetime at a laboratory-scale and

subsequently plant scale. Thus, this section of future work concerns routes to or requirements for scaling-up these materials.

5.3.1.1 Optimise MIL-100(Sc)@PBSAC synthesis

For scale-up, the economic viability of the production of MIL-100(Sc)@PBSAC synthesis should be considered with scandium amongst the most expensive elements.²⁹⁷ In this research, the immobilisation of MIL-100(Sc) onto PBSAC spheres when prepared via reflux resulted in $\approx 50\%$ efficiency of immobilisation as loose powdered MIL-100(Sc) was also generated - thus the synthesis was wasteful. Optimising the immobilisation of MIL-100(Sc) onto PBSAC spheres to minimise the amount of scandium waste is therefore desirable. This may be achieved by adjusting the amount of MIL-100(Sc) precursors used in the synthesis according the loading that was achieved in this work (6.42 ± 1.93 % w/w) thus minimising the amount of scandium waste generated. Further, improvements in the loading on PBSAC spheres could be achieved via oxidation of the graphitic carbon surface where the oxygen functionalities generated could coordinate to scandium sites in MIL-100(Sc). This is frequently achieved through treatment with an acid¹⁸⁹⁻¹⁹¹ or oxidising agent¹⁹⁹. Such an approach was exploited by Navarro *et al.*¹⁹⁹ who immobilised UiO-66 onto PBSAC spheres following H₂O₂ treatment to generate oxygen functionalities on the graphitic carbon surface.

5.3.1.2 Explore scalability of MIL-100(Sc)@PBSAC synthesis

The implementation of MIL-100(Sc)@PBSAC composites, and, more generally speaking, other MOF@PBSAC catalytic systems into industrial flow reactors (i.e. larger than those used in this research) may require these materials to be produced in larger quantities. MIL-100(Sc)@PBSAC was synthesised in ≈ 1 g quantities in this research which was also the mass used for a typical flow reaction, thus the scalability of this synthesis should be assessed to produce quantities big enough to be implemented into industrial flow reactors (e.g. packed-bed reactor internal diameter used in this work: 0.94 cm, GSK's pilot plant reactor internal diameter range³²: 2.54 - 5.08 cm - based on reactor length used in this work (12 cm) GSK's pilot plant reactor volumes are ≈ 5.5 - 22x larger thus the use of tens to hundreds of grams of catalyst would be anticipated). A good

starting point for studying this could be through scaling up of the reflux conditions that were used.

There are many other preparation procedures that can be carried out to produce MOFs such as such as microwave-assisted, mechanochemical, electrochemical and continuous flow and thus these could be explored in greater detail as they could offer unique benefits.^{358, 359} For example, the synthesis of MOF in continuous flow offers reduced reaction times due to the improved mass and heat transfer as well as easier of scalability through parallelisation of reactors.^{358, 360} One approach to the synthesis of MIL-100(Sc)@PBSAC composites in continuous flow could be through the use of a fReactor continuous-stirred tank reactor (CSTR) platform, developed at the University of Leeds.³⁶¹ MIL-100(Sc) precursors could be continuously fed into a fReactor CSTR module containing PBSAC spheres to fabricate MIL-100(Sc)@PBSAC. The stirring rate should carefully be controlled, however, to minimise any attrition that may occur to the PBSAC spheres inside of the reactor.

5.3.1.3 Identifying poisoning/deactivation processes

The lifetime of a catalyst including factors such as the extent of leaching, poisoning resistance and mechanical and thermal stability should all be taken into account when used in an industrial setting.¹⁸ When studying MIL-100(Sc)@PBSAC composites in continuous flow, it was found that loss in activity was occurring over time-on-stream which was attributed to the accumulation of starting material (i.e. citronellal) in the reactor (which could partially be resolved by flowing methanol through the reactor) and also some leaching of MIL-100(Sc) from the support. Greater understanding of the conditions giving rise to these phenomena could be explored in greater detail. This could be done through mapping catalyst leaching (via ICP-MS or similar) as a function different variables (e.g. temperature, flow rate, reaction time) as well as exploring the highest reaction temperatures before significant losses in activity occur due to catalyst decomposition (as MIL-100(Sc) thermally decomposes at ≈ 380 °C). Comparison of the performance of MIL-100(Sc)@PBSAC with other catalysts over extended reaction periods via metrics such as TON would be useful in identifying the industrial feasibility of this material. Attempts at reducing or prolonging catalyst poisoning of MIL-100(Sc)@PBSAC composites should also be conducted, one such example could be through the use of methanol in

the reaction solvent (e.g. 10:90 v/v methanol/toluene solvent) as this was found to enable some regeneration in the catalytic activity. More detailed studies could be conducted to greater understanding the conditions that give rise to catalyst poisoning too.

5.3.2 Generalising to other reactions

The application of Lewis acid catalysis in organic chemistry is broad which provides ample opportunity to explore the utility of MIL-100(Sc)@PBSAC further. Furthermore, the favourable properties of PBSAC as a catalyst support in continuous flow provides a medium for the development of novel MOF@PBSAC systems to be exploited in this mode of operation. This section of future work discusses the potential application and optimisation of MIL-100(Sc)@PBSAC composites to other Lewis acid catalysed reactions as well as potential opportunities for the fabrication of different MOF@PBSAC systems to study other reaction chemistries.

5.3.2.1 Optimisation of CBD synthesis

Although the initial results were promising, further developmental work regarding the reactions concerning CBD synthesis (i.e. olivetol/methyl-olivetolate and *p*-menthadienol coupling) in continuous flow needs to be carried out. In the reaction between olivetol and *p*-menthadienol, the desired product CBD was obtained alongside other, undesirable impurities such as THC, CBD-regioisomer and CBD-dimer. A DoE would provide information about maximisation of CBD yield and minimisation of the formation of the impurities, particularly THC as this is a controlled substance. Furthermore, the stability of the catalytic activity of MIL-100(Sc)@PBSAC composites towards this reaction was not tested over extended periods of time-on-stream. A study like this would provide insight into the feasibility of using this catalyst for the industrial process, and would be compared with the trend observed for the intramolecular cyclisation of citronellal where a decrease in activity over time was observed.

5.3.2.2 Studying other chemistries with MIL-100(Sc)@PBSAC

A range of different reactions have previously been catalysed by MIL-100 MOFs as discussed in section 1.2.1.1, there is therefore a lot of scope to study different chemistries in continuous flow using MIL-100(Sc)@PBSAC composites. This

project focused on taking a careful progression from studying the intramolecular cyclisation of citronellal with MIL-100(Sc) powder in batch and then in flow with MIL-100(Sc)@PBSAC where it was found to be the second most active MOF reported to date. The time available for further exploration was applied to studying CBD chemistry. Comparison of the catalytic activity of MIL-100(Sc)@PBSAC with other MOFs towards other reactions not directly transferrable from the citronellal cyclisation system (e.g. employing different solvents, temperatures, molecule sizes) would provide further interesting insight into the catalytic nature of these systems.

The ease in which modules can be combined in continuous systems could also enable telescoped reactions to be exploited in similar fashion to recently reported work from the group.³⁶² For example, industrially, the intramolecular cyclisation of citronellal is followed by a hydrogenation step to produce final product menthol. The incorporation of a second reactor containing a material capable of catalysing hydrogenation reactions (e.g. Pd@PBSAC, which has also been used as a hydrogenation catalyst previously^{32, 191}), could serve as a way to develop this system further. The introduction of other modules downstream from the packed-bed reactor, such as purification via liquid-liquid separations could also be incorporated into the system to provide additional utility and harness the benefits of continuous systems.³⁶³

5.3.2.3 Different catalysts and different reaction chemistries

We postulated that the fabrication and application of MIL-100(Sc)@PBSAC composites in continuous flow in this work could provide the basis for a general approach to exploit the diversity of MOF-based catalysis in continuous flow systems. Thus, alongside varying the metal used for the synthesis of MIL-100(M)@PBSAC composites (e.g. M = Fe, Cr, Al), one logical next step is the design of different MOF@PBSAC catalysts to be used for different reaction chemistries.

The fabrication of novel material MIL-100(Sc)@PBSAC involved using this MOF in pristine form as a Lewis acid catalyst in 2-phase reactions (liquid-solid) in continuous flow. With this, we decided to attempt to develop a new MOF@PBSAC composite system with additional material complexity involving post synthetic modification (PSM) of the MOF following immobilisation onto the

PBSAC spheres and then applying this to a 3-phase (gas-liquid-solid) reaction in flow. See section 5.2 for preliminary work detailing this.

5.3.3 Further technique/method development across research

Further development into some of the studies conducted in this research would benefit the field more broadly, but remain outside the scope of the main thrust of this research (i.e. to develop novel heterogeneous Lewis acidic catalysts for fine chemical production in continuous flow). These areas pertain to studies that, if conducted, could enhance understanding of MOF-based heterogeneous catalysis and therefore serve as exciting areas for further development.

5.3.3.1 MIL-100(Sc) stoichiometry

Accurately describing the stoichiometry of MOFs can provide greater understanding into their catalytic properties. In this research, TGA was used to estimate the stoichiometry of MIL-100(Sc) (see section 2.2.3), however, further effort could be directed towards generating an even more accurate description. For example, previous work by Gates *et al.*²²² used NMR and IR spectroscopy to quantify the defect and structural vacancy sites on the Al₃O nodes of MIL-100(Al). Further, generating generalised formulae to describe the stoichiometry of MIL-100 MOFs, like the excellent work carried out by Lillerud *et al.*²⁰¹ with UiO-66 MOFs, who deduced the stoichiometry using TGA and ¹H NMR could help to build understanding of these materials.

5.3.3.2 Verification of external vs. internal catalytic site estimations

In Chapter 2, the amount of catalytic sites that are located on the exterior vs. interior as a function of the MIL-100(Sc) particle size was estimated (see section 2.2.6). These estimations were based on geometric principles and made use of experimentally obtained data (i.e. unit cell parameters, stoichiometry, BET surface area, particle size), however, they were not experimentally verified and assumed a monodisperse particle size range.

Verification of this estimation may arise from synthesising MIL-100(Sc) samples of different monodisperse sizes (and thus different exterior to interior site ratios) and correlating this to the resultant catalytic activity. Studies into the catalytic activity of MOFs as a function of particle size have previously been carried out on a number of occasions.^{152, 155, 364-369}

5.3.3.3 Kinetic modelling

The kinetic models used to describe the MIL-100(Sc)-catalysed intramolecular cyclisation of citronellal reactions could be developed further. A poor model fit was obtained using a LH kinetics mechanism to describe the reaction, which was generated using DynoChem. As discussed in section 1.2.2.3, one of the major challenges in understanding MOF-catalysed reactions is modelling the internal mass transfer within the pore network of MOFs - thus the development of more complex kinetic models that account for this would make them more accurate.^{102,}

148, 157

Chapter 6 Experimental

6.1 Characterisation

6.1.1 Powder X-ray diffraction (PXRD)

MIL-100(Sc) powder prepared via solvothermal synthesis (section 2.2.1) was analysed using a Bruker Phaser D2 using Cu K α radiation (1.54 Å) between 5 - 30° 2 θ with a typical step size of 0.01°. Measurements were carried out at room temperature (20 °C). MIL-100(Sc) powder was ground with a pestle and mortar before analysis.

MIL-100(Sc) powder prepared under reflux, MIL-100(Sc)@PBSAC composites, PBSAC spheres (section 3.3.1.3) and other preliminary materials (i.e. Cu@UiO-67-BPY, Cu@UiO-67-BPY@PBSAC) (section 5.2) were analysed using a Malvern PANalytical Empyrean diffractometer using Cu K α radiation (1.54 Å) between 2 - 30° 2 θ with a step size of 0.013°. Measurements were carried out at room temperature (20 °C). MIL-100(Sc)@PBSAC, Cu@UiO-67-BPY@PBSAC and PBSAC spheres were crushed into a powder whilst MIL-100(Sc) and Cu@UiO-67-BPY powder were ground using a pestle and mortar before analysis.

6.1.2 Thermogravimetric analysis (TGA)

Thermogravimetric analysis (TGA) was carried out on a Shimadzu TGA-50. A typical analysis involved heating approximately 10 mg of the sample from 20 °C to 750 - 900 °C at 10 °C min⁻¹ in flowing air (50 mL min⁻¹).

6.1.3 FT-IR spectroscopy

FT-IR spectroscopy analysis was carried out using a Bruker ALPHA FT-IR spectrometer between 500 - 4000 cm⁻¹. MIL-100(Sc) powder was placed on the sampling module and analysed.

6.1.4 N₂ adsorption (BET)

N₂ adsorption analysis was carried out at -196 °C using a Micrometrics Tristar 3000. Samples (\approx 50 mg) were activated prior to analysis by heating at 150 °C overnight under a flow of N₂. Brunauer–Emmett–Teller (BET) surface areas were

calculated using the BETSI method.²³² Pore volumes were obtained at $P/P_0 = 0.99$. Micropore volumes were extracted from t-plots.

6.1.5 Scanning electron microscopy-energy dispersive X-ray analysis (SEM-EDX)

MIL-100(Sc) powder and preliminary Cu@UiO-67-BPY@PBSAC materials were analysed by SEM-EDX using an FEI Nova 450 SEM. To prepare samples, MIL-100(Sc) was dispersed onto a silicon wafer using ethanol and attached to a stub whilst Cu@UiO-67-BPY@PBSAC materials were fixed onto a stub via carbon tape. Images were collected using a CBS (circular backscattered electron detector) detector at an electron beam voltage of 5 kV. EDX spectra were taken using EDAX TEAM software at a voltage of 18 kV.

6.1.5.1 MIL-100(Sc) particle size distribution

Powdered MIL-100(Sc) particle size distributions were obtained using Gatan Microscopy Suite (GMS) software version 3.4. The line profile tool was used to measure the diameter of 75 particles in which an average value was quoted when stating the diameter (Figure 114). Within the aggregates, the selection of particles for analysis was based on their ability to be individually identified. The width of the distribution was quoted as the standard deviation.

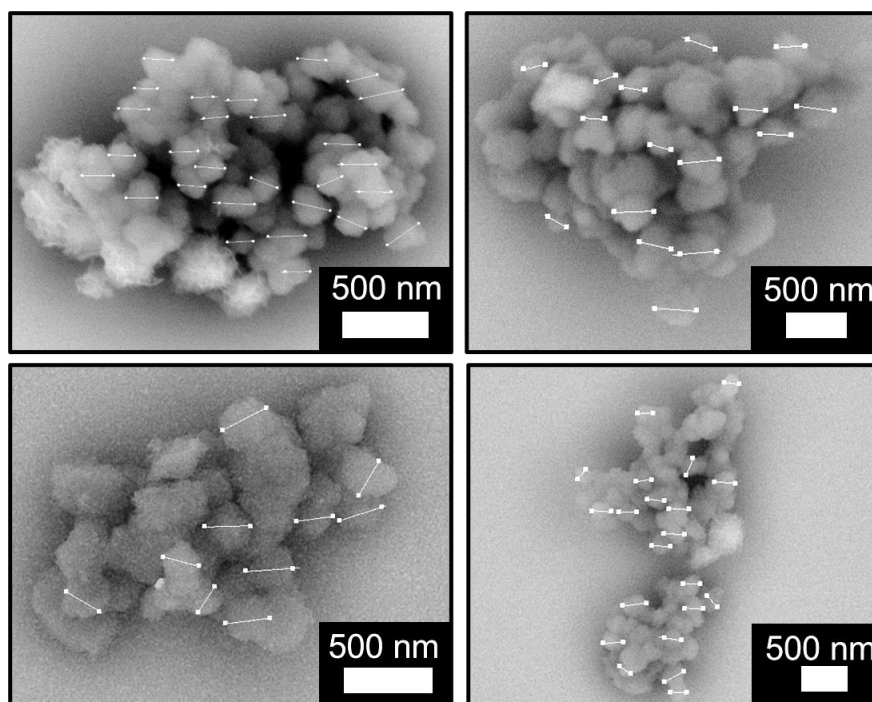


Figure 114: SEM images used to obtain particle size distribution with line profiles for each particle that was sized shown.

6.1.6 Focused ion beam-scanning electron microscopy-energy dispersive X-ray analysis (FIB-SEM-EDX)

MIL-100(Sc)@PBSAC and PBSAC spheres were analysed using Focused ion beam-scanning electron microscopy (FIB-SEM) and energy dispersive X-ray (EDX) analysis on an FEI Helios G4 CX DualBeam. Prior to imaging, 20 nm of carbon coating was evaporated onto the sample surface using a Quorum Q150TE coater to reduce charging. Images were collected using a standard ETD (Everhart–Thornley detector) in secondary electron mode or a CBS (circular backscattered electron detector) detector. The typical electron beam voltages used were 5 or 10 kV. EDX analysis was carried out using an Oxford instruments AZtec energy EDX system with a 150 mm X-Max SDD detector. The Ga source for the FIB was operated at 30 kV.

6.1.7 Dynamic light scattering (DLS)

Particle size distributions (of PBSAC or MIL-100(Sc) powder) were obtained using a Malvern Mastersizer 3000 laser diffraction system. The material being analysed was stirred in water using the Hydro MV automated wet dispersion unit at 3500 rpm, and was added until the laser obscuration reached between 10 - 20%. D10, D50, D90, and D[3,2] values were outputted by the software.

6.1.8 X-ray photoelectron spectroscopy (XPS)

XPS analysis of MIL-100(Sc), PBSAC and MIL-100(Sc)@PBSAC was carried out on a UHV-XPS module with a SPECS Phoibos 150 analyser with 1D-DLD detectors. Prior to analysis, samples were immobilised on carbon tape. The source was a monochromated Al anode (SPECS XR-50M) with an energy of 1486.7 eV, a power of 400 W and a voltage of 15 kV. The pass energy was 50 eV for the wide survey scans (1 eV step size) and 30 eV for the narrow elemental scans (0.1 eV step size) with a dwell time of 0.1 seconds per step. After collection of spectra, the data was processed using CasaXPS software. The spectra were calibrated against the adventitious C 1s peak, which was set to a binding energy of 284.8 eV and the intensity was calibrated using a transmission function calculated from a clean reference silver sample according to standard ISO 16243:2011. The spectra were fitted using the 'quantify' tool in CasaXPS. Tougaard-type backgrounds were applied to the elemental peaks, and peak

areas were then determined. Default RSF values for each element contained within the software were used to scale the peak areas.

6.1.9 Atomic absorption spectroscopy (AAS)

AAS was carried out using an Agilent 200 series AA system. Samples were prepared for analysis by heating, in air, a known amount of the activated material at 600 °C for 90 minutes with the resultant white solid dissolved in nitric acid (10 mL, 67%). Following dissolution the sample was then diluted to a known volume (30 ppm) for analysis.

6.1.10 Crush testing

Crush testing of PBSAC and MIL-100(Sc)@PBSAC spheres was done using an Instron 5566 according to a modified version of the ASTM D-4179 standard test for single pellet crush strength.³⁷⁰ Samples were heated to 250 °C under dynamic vacuum for 3 hours to remove water and then stored under nitrogen and in a desiccator until analysis. For measurements, increasing force at a uniform rate of 0.05 N s⁻¹ was applied until crushing of the particle occurred. For each sample 50 particles were crushed.

6.1.11 Nuclear magnetic resonance (NMR) spectroscopy

¹H NMR data was obtained using a Bruker AV3HD 400 MHz NMR Spectrometer. Prior to analysis, samples were typically prepared by dissolving sample in CDCl₃.

6.1.12 Gas chromatography (GC)

6.1.12.1 Intramolecular cyclisation of citronellal using MIL-100(Sc) and MIL-100(Sc)@PBSAC

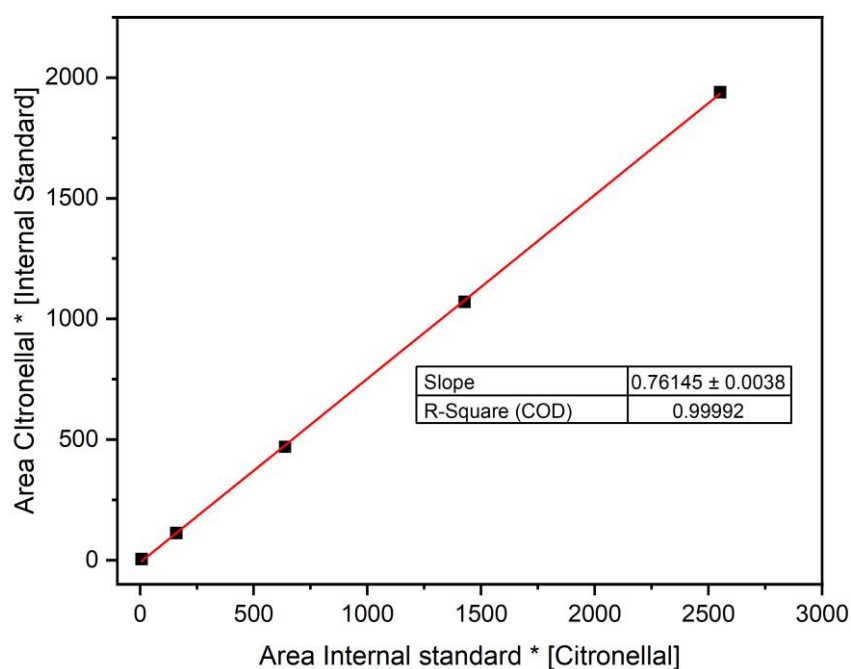
Gas chromatography (GC) analysis was carried out on a Hewlett Packard HP 6890 series GC system using a DB-624 column (length: 30 m, diameter: 0.25 m, film thickness: 1.40 µm) and FID detector at 300 °C. An internal standard (*n*-decane) was used to quantify the progress of the reactions. See Table 48 and Table 49 for more specific method information.

Table 48: GC method used for off-line experiment analysis

Column	DB-624 (Length: 30 m, Diameter: 0.25 m, Film Thickness: 1.40 μm)
Injection Volume	1 μL
Inlet Temperature	250 $^{\circ}\text{C}$
Detector Temperature	300 $^{\circ}\text{C}$
Split Ratio	25:1
Detection	FID

Table 49: Temperature program used for off-line GC chromatography.

Oven	Rate ($^{\circ}\text{C}/\text{min}$)	Value ($^{\circ}\text{C}$)	Hold Time (mins)	Run Time (mins)
Initial		40	1	1
Ramp 1	25	180	1	7.6
Ramp 2	2.5	190	1	12.6
Ramp 3	20	200	0	13.1

**Figure 115: Calibration curve of (\pm)-citronellal and response factor (slope). Internal standard used was n-decane. Figure reproduced with permission.³⁰⁰**

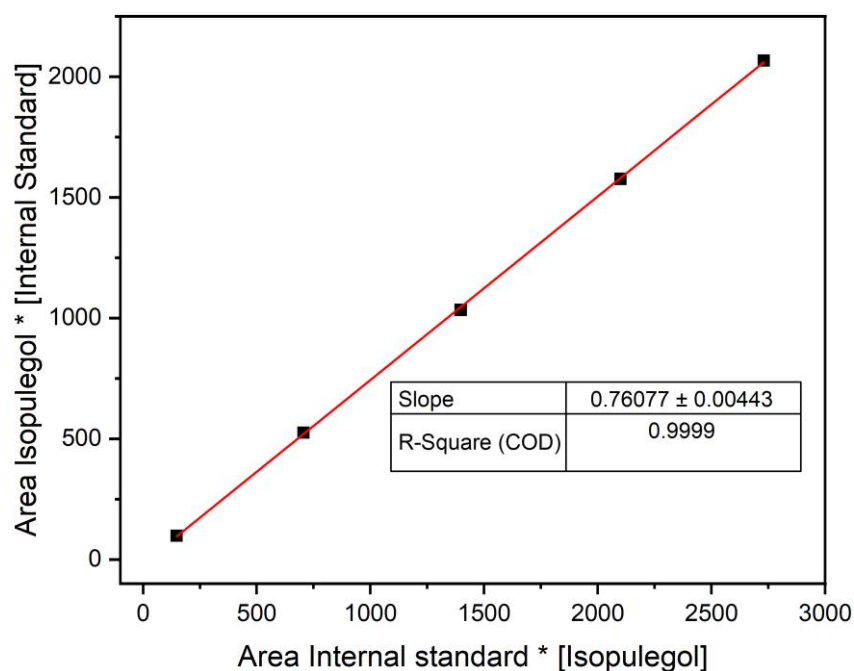


Figure 116: Calibration curve of isopulegol and response factor (slope). Internal standard used was n-decane. Figure reproduced with permission.³⁰⁰

6.1.12.2 For homogeneous kinetic model with scandium triflate

Gas chromatography (GC) analysis was carried out on a Agilent Technologies 7890B GC system using a HP-5 column (length: 30 m, diameter: 0.32 m, film thickness: 0.25 μm) and FID detector at 250 °C. An internal standard (biphenyl) was used to quantify the progress of the reactions. See Table 50 and Table 51 for more specific method information.

Table 50: GC method used for off-line experiment analysis

Column	HP-5 (Length: 30 m, Diameter: 0.32 mm, Film thickness: 0.25 μm)
Injection Volume	1 μL
Inlet Temperature	250 °C
Detector Temperature	250 °C
Split ratio	40:1
Detection	FID

Table 51: Temperature program used for off-line GC chromatography.

Oven	Rate (°C/min)	Value (°C)	Hold Time (mins)	Run Time (mins)
Initial		35	2	2
Ramp 1	4	37	0.5	3
Ramp 2	5	50	0	5.6
Ramp 3	30	180	0	9.93

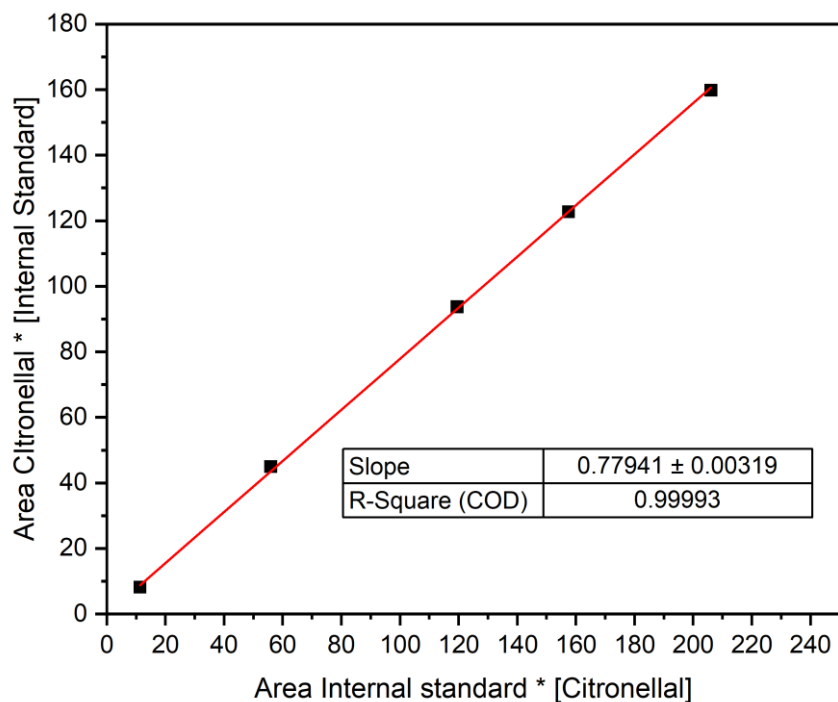


Figure 117: Calibration curve of (±)-citronellal and response factor (slope). Internal standard used was biphenyl.

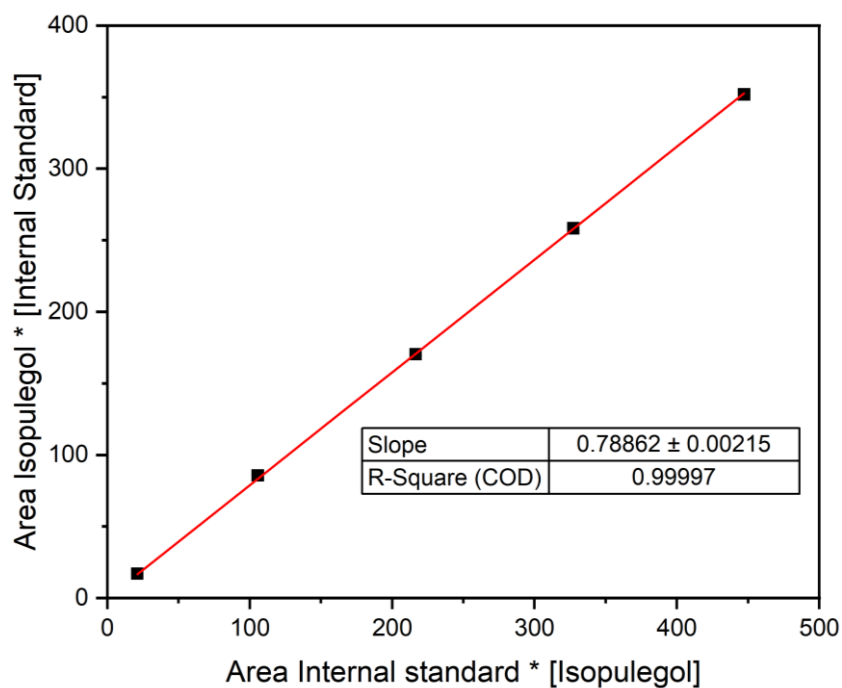


Figure 118: Calibration curve of isopulegol and response factor (slope). Internal standard used was biphenyl.

6.1.12.3 Aerobic epoxidation of cyclohexene

Gas chromatography (GC) analysis was carried out on a Agilent Technologies 7890B GC system using a HP-5 column (length: 30 m, diameter: 0.32 m, film

thickness: 0.25 μm) and FID detector at 250 $^{\circ}\text{C}$. An internal standard (biphenyl) was used to quantify the progress of the reactions. See Table 52 and Table 53 for more specific method information.

Table 52: GC method used for off-line experiment analysis

Column	HP-5 (Length: 30 m, Diameter: 0.32 mm, Film thickness: 0.25 μm)
Injection Volume	5 μL
Inlet Temperature	250 $^{\circ}\text{C}$
Detector Temperature	250 $^{\circ}\text{C}$
Split ratio	100:1
Detection	FID

Table 53: Temperature program used for off-line GC chromatography.

Oven	Rate ($^{\circ}\text{C}/\text{min}$)	Value ($^{\circ}\text{C}$)	Hold Time (mins)	Run Time (mins)
Initial		40	2	2
Ramp 1	20	300	2	17

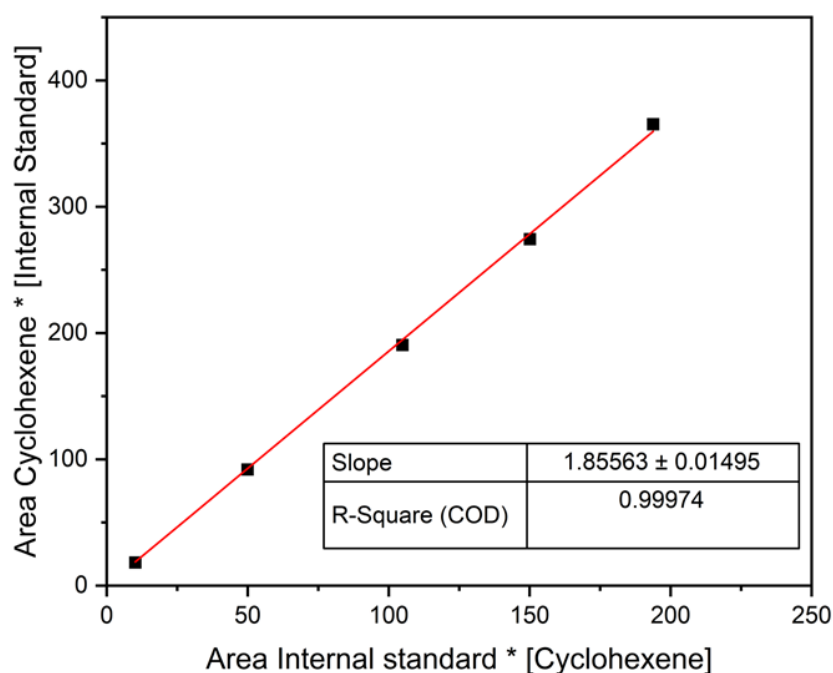


Figure 119: Calibration curve of cyclohexene and response factor (slope). Internal standard used was biphenyl.

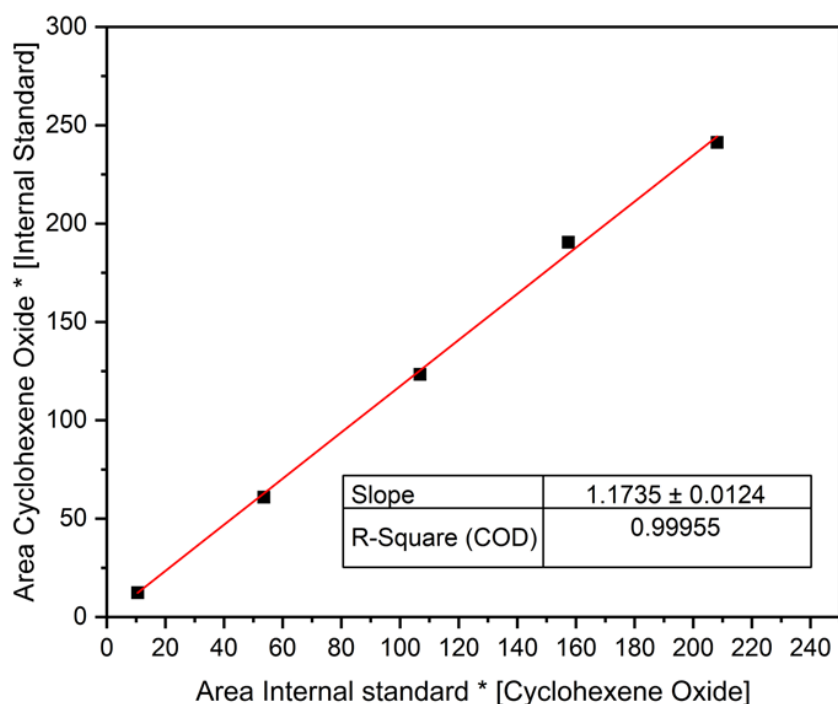


Figure 120: Calibration curve of cyclohexene oxide and response factor (slope). Internal standard used was biphenyl.

6.1.13 High-performance liquid chromatography (HPLC)

6.1.13.1 Methyl olivetolate and *p*-menthadienol coupling

HPLC analysis for this reaction was carried out using an Agilent 1290 Infinity II system with a diode array detector (UV). An internal standard (biphenyl) was used to quantify the progress of the reactions. See Table 54 and Table 55 for detailed information.

Table 54: Method parameters for HPLC analysis of methyl olivetolate and *p*-menthadienol coupling

Column	Agilent InfinityLab Poroshell 120 EC-C18 (Length: 50 mm x Diameter: 2.1 mm, Particle size: 1.9 μm)
Injection Volume	0.5 μL
Flow rate	0.5 mL/min
Column temperature	40 °C
Detection	UV
Diluent	Acetonitrile
Mobile Phase A	0.1 % TFA in water
Mobile Phase B	0.1 % TFA in acetonitrile

Table 55: Solvent composition for HPLC analysis of methyl olivetolate and *p*-menthadienol coupling.

Time (mins)	% mobile phase A	% mobile phase B
0	50	40
5	5	95
9	5	95
10	60	40

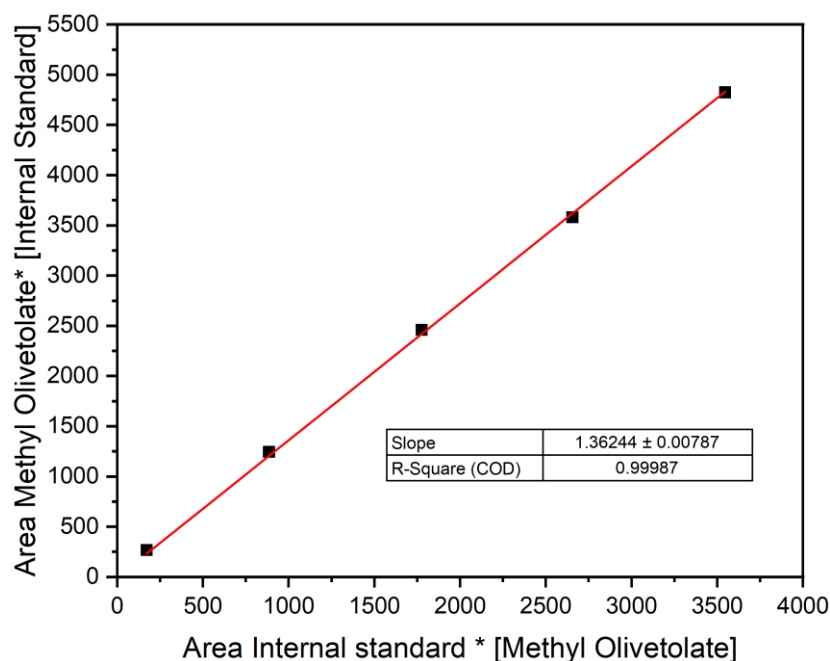


Figure 121: Calibration curve of methyl olivetolate and response factor (slope). Internal standard used was biphenyl.

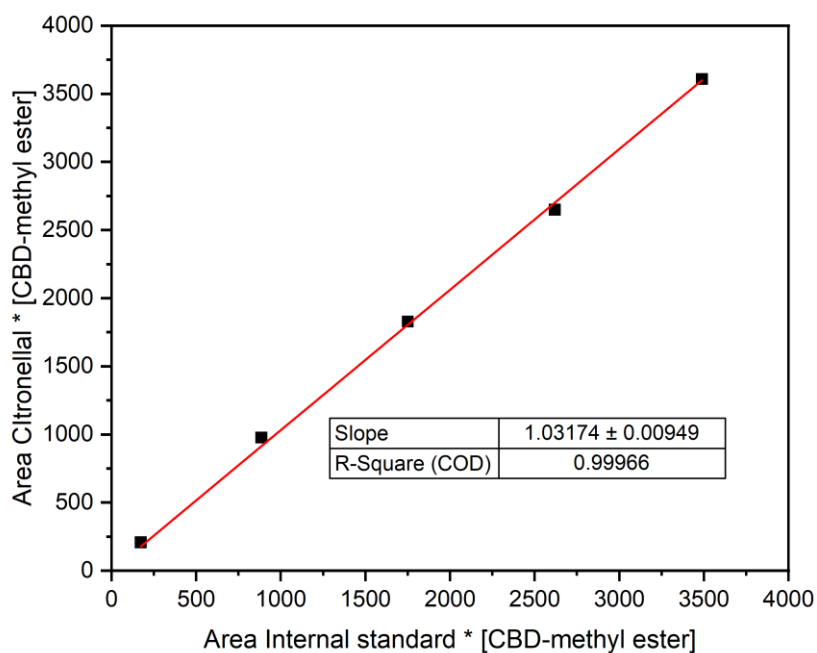


Figure 122: Calibration curve of CBD-methyl ester and response factor (slope). Internal standard used was biphenyl.

6.1.13.2 Olivetol and *p*-menthadienol coupling

Reaction analysis was carried out by comparison of % peak areas. See Table 56 and Table 57 for detailed information.

Table 56: Method parameters for HPLC analysis of olivetol and *p*-menthadienol coupling

Column	Waters Symmetry (Length: 150 mm x Diameter: 4.6 mm, Particle size: 3 μ m)
Injection Volume	10 μ L
Flow rate	1.0 mL/min
Column temperature	30 $^{\circ}$ C
Detection	UV (220 nm)
Diluent	Acetonitrile
Mobile Phase A	0.1 % TFA in water
Mobile Phase B	0.1 % TFA in acetonitrile

Table 57: Solvent composition for HPLC analysis of olivetol and *p*-menthadienol coupling.

Time (mins)	% mobile phase A	% mobile phase B
0	50	50
12	26	74
12.1	26	74
23	5	95
30	5	95
35	50	50
40	50	50

6.2 Chapter 2 procedures

6.2.1 Reagents and materials

For MIL-100(Sc) powder synthesis benzene-1,3,5-tricarboxylic acid (98%), scandium(III) nitrate hydrate (REacton, 99.9% (REO)), dimethylformamide (DMF) (\geq 99.5%), ethanol (absolute) and methanol (HPLC) were obtained from Fisher Scientific Ltd and used without further purification. Water (deionised, 15.0 M Ω cm $^{-1}$) was obtained from an Elga PURELAB Option purification system.

For catalytic activity testing, *n*-decane (99%) and biphenyl (99%) were purchased from Thermo Scientific, 2-propanol (99.9% for HPLC), acetone (\geq 99.5), (\pm)-citronellal (\geq 95% (GC)) and scandium(iii) triflate (99%) from Sigma-Aldrich. Dry toluene and dry dichloromethane were obtained from PureSolv MD5 Purification System.

6.2.2 Solvothermal synthesis of MIL-100(Sc)

The synthesis of MIL-100(Sc) composites was carried out according to a previously reported procedure by Wright *et al.*¹¹⁹ Benzene-1,3,5-tricarboxylic acid (905 mg, 0.43 mmol), scandium nitrate hydrate (245 mg, 0.86 mmol), and DMF (20 mL) were added to a Teflon-lined stainless steel autoclave and heated at 150 °C for 48 hours. Following synthesis, the white powder was washed with excess water (> 500 mL) and ethanol (> 500 mL) and then stirred in methanol for 24 hours. The powder was typically dried in an oven at 150 °C for 90 minutes.

6.2.3 Optimising MIL-100(Sc) drying temperature study

Samples that were dried at 150 °C for 1.5 hours were simply placed in a pre-heated oven at this temperature at ambient pressure for this amount of time. Samples dried under vacuum were heated, in a round bottomed flask, to the specified temperature (60, 100 or 200 °C) using an aluminium heating block filled with sand (to enhance contact with the reaction vessel) placed on a stirrer hotplate for the specified amount of time (3 hours or overnight) with dynamic high vacuum applied.

6.2.4 Molecular modelling

Molecular modelling was carried out using DS ViewerPro (version 6.0) software in which the distance between the atoms at the longest and widest parts of citronellal and isopulegol molecules was measured using the 'distance' tool. 3-D conformers of the molecules were obtained from PubChem3D.³⁷¹⁻³⁷³ As the value outputted by the software measured from the centre of the atoms selected, the van der Waals radius of the atoms (oxygen = 1.52 Å, carbon = 1.70 Å, hydrogen = 1.2 Å) was then added to the outputted software value to give the total size. These sizes were then compared to the literature reported pore sizes of MIL-100(Sc) to assess whether internal pore transport was feasible.¹¹⁹

6.2.5 Design-of-experiments (DoE)

The 2-level 3-factor FFD DoE was constructed, analysed and refined using Umetrics MODDE (version 13). Following model refinement, the software was also used to generate interaction and contour plots.

6.2.5.1 Typical DoE experiment

All of the reactions in the DoE were carried out using dry toluene as the solvent under an inert (N₂) atmosphere. The DoE reactions were performed in a dry microwave vial (10 mL) equipped with a suba-seal creating a sealed vessel. Prior to reaction, the sealed microwave vial was dried via vacuum/blowtorch/N₂ flushes (x3). This vessel was heated using an aluminium heating block filled with sand (to enhance contact with the reaction vessel) placed on a stirrer hotplate. To carry out a reaction, MIL-100(Sc) (35 mg) was introduced to a refluxing solution of (±)-citronellal (77 mg, 0.5 mmol, 0.1 M) and *n*-decane (internal standard) in toluene (5 mL) stirred by a magnetic stir bar at 1500 rpm. Aliquots (10 µL) were periodically taken from the reaction mixture, diluted to 1 mL with toluene, and analysed by GC to monitor the reaction progress. See section 6.1.12.1 for more information on the GC method that was used.

From the experimental data obtained in the DoE concentration profiles of (±)-citronellal consumption and (±)-isopulegols consumption was plotted and used to generate kinetic models using DynoChem (see section 2.5).

6.2.6 Kinetic experiments with scandium triflate for kinetic model

All of the reactions were carried out using dry DCM as the solvent under an inert (N₂) atmosphere. The reactions were performed in dry round-bottomed flasks (20 mL) equipped with a suba-seal creating a sealed vessel. Prior to reaction, the vessel was dried via vacuum/blowtorch/N₂ flushes (x3). Reactions temperatures of -20, -30 or -40 °C were obtained using a acetone/dry ice bath. For a typical experiment, a pre-cooled solution of scandium triflate (24.6 mg, 0.05 mmol, 5 mol %) dissolved in DCM (5 mL) was added to a pre-cooled round bottomed flask containing (±)-citronellal (154.2 mg, 1 mmol, 0.1 M) and biphenyl (internal standard) in DCM (5 mL) to initiate the reaction. After a specified amount of time an aliquot of reaction mixture was taken (0.5 mL), quenched with brine (1 cm³) and the organic layer analysed by gas chromatography. See section 6.1.12.2 for more information on the GC method that was used.

6.2.7 Kinetic modelling

The kinetic models in this work were generated using DynoChem (Scale-up Systems) (version 6). To build the model, all of the components in the reactions (e.g. reactants, products, catalyst, intermediates, solvent) were inputted

into the 'components' tab and individual steps for each model were inputted into the 'process' tab. Experimental data from reactions were then added with initial parameter values and reaction names listed in the 'scenarios' tab. To fit the kinetics, parameters were first manually fitted using the 'simulator' to ensure they were in the region of sensitivity thus providing an initial guess of the value for the model. The model were then generated using the 'fitting' tab. In DynoChem, the kinetic models are generated by minimising the sum of squares (SSQ) between inputted experimental data and model fit. For this work a Levenberg-Marquardt algorithm was used. Kinetic parameters were firstly obtained a single temperature before fitting at other temperatures and estimating other parameters such as the activation energy. To generate the plots showing experimental and modelled fitting data, the modelled data was extracted from DynoChem and plotted.

6.3 Chapter 3 procedures

6.3.1 Reagents and materials

For MIL-100(Sc)@PBSAC composite synthesis benzene-1,3,5-tricarboxylic acid (98%), scandium(iii) nitrate hydrate (REacton, 99.9% (REO)), dimethylformamide (DMF) ($\geq 99.5\%$), ethanol (absolute), and methanol (HPLC) were obtained from Fisher Scientific Ltd and used without further purification. Water (deionised, $15.0 \text{ M}\Omega \text{ cm}^{-1}$) was obtained from an Elga PURELAB Option purification system. Active carbon spheres ($500 \mu\text{m}$) were obtained from IBU-tec.

For catalytic activity testing, n-decane (99%) was purchased from Thermo Scientific and (\pm)-citronellal ($\geq 95\%$ (GC)) from Sigma-Aldrich. Dry toluene was obtained from a PureSolv MD5 Purification System.

6.3.2 Solvothermal synthesis of MIL-100(Sc)@PBSAC composites

The attempted synthesis of MIL-100(Sc)@PBSAC composites via solvothermal approaches was done identically to the synthesis of MIL-100(Sc) powder (see section 6.2.2) but with the addition of PBSAC spheres (150 mg) to the reaction vessel.

6.3.3 Reflux synthesis of MIL-100(Sc)@PBSAC composites

The synthesis of MIL-100(Sc)@PBSAC composites was based on previously reported procedures.^{119, 286} Benzene-1,3,5-tricarboxylic acid (90.5 mg, 0.043

mmol), PBSAC spheres (1.10 g) and DMF (20 mL) were stirred at 45 °C for 2 hours. Next, scandium nitrate hydrate (0.86 mmol, 245 mg) was added and the reaction mixture was stirred for another 2 hours at 45 °C. The reaction mixture was then refluxed with stirring overnight. All stirring was carried out at 500 rpm. MIL-100(Sc) powder was also observed to have formed inside of the reaction vessel independently of the PBSAC spheres. Following synthesis, the spheres were washed sequentially with excess water (> 500 mL) and ethanol (> 500 mL) and then stirred in methanol for 72 hours. The spheres were then filtered and dried at 65 °C under vacuum giving activated MIL-100(Sc)@PBSAC (1.18 g, ≈ 54.2% yield of MIL-100(Sc) immobilisation determined using TGA loading and maximum possible loading values). The appearance of the catalyst was identical to the unfunctionalised PBSAC spheres.

6.3.4 Testing MIL-100(Sc)@PBSAC catalytic activity

All of the reactions were carried out using dry toluene as the solvent under an inert (N₂) atmosphere. The reactions were performed in a dry microwave vial (10 mL) equipped with a suba-seal creating a sealed vessel. Prior to reaction, the sealed microwave vial was dried via vacuum/blowtorch/N₂ flushes (x3). This vessel was heated using an aluminum heating block filled with sand (to enhance contact with the reaction vessel) placed on a stirrer hotplate. To carry out a reaction, MIL-100(Sc)@PBSAC (65 mg) was introduced to a refluxing solution of (±)-citronellal (77 mg, 0.5 mmol, 0.1 M) and *n*-decane (internal standard) in toluene (5 mL) stirred by a magnetic stir bar at 1500 rpm. After 2 hours of reaction an aliquot (10 µL) was taken from the reaction mixture, diluted to 1 mL with toluene, and analysed by GC. See section 6.1.12.1 for more information on the GC method that was used.

6.3.5 Confirming trimesic acid adsorption

Benzene-1,3,5-tricarboxylic acid (90.5 mg, 0.043 mmol), PBSAC spheres (1.10 g) and DMF (20 mL) were stirred at 45 °C for 2 hours at 500 rpm. After this the PBSAC spheres were washed sequentially with excess water (> 500 mL) and ethanol (> 500 mL) and then stirred in methanol for 72 hours. The samples were then analysed using TGA. The appearance was identical to the unfunctionalised PBSAC spheres.

6.4 Chapter 4 procedures

6.4.1 Reagents and materials

For catalytic activity testing, *n*-decane (99%), and biphenyl (99%) was purchased from Thermo Scientific, toluene ($\geq 99.8\%$), methanol (HPLC) and chloroform (HPLC) from Fisher Scientific Ltd and dichloromethane (HPLC), 2-propanol (99.9% for HPLC), acetone (≥ 99.5), (\pm)-citronellal ($\geq 95\%$ (GC)), chloroform-d (99.8%), scandium(iii) triflate (99%) and glass spheres (500 μm diameter) from Sigma-Aldrich. Methyl olivetolate and olivetol were obtained from Carbosynth and *p*-menthadienol from Ark Pharm. Dry toluene was obtained from a PureSolv MD5 Purification System.

6.4.2 Reusability testing of MIL-100(Sc)@PBSAC composites

All reusability testing experiments were carried out using dry toluene as the solvent under an inert (N_2) atmosphere. Reactions were performed in a dry round bottomed flask (10 mL) equipped with a suba-seal creating a sealed vessel. Prior to reaction, the sealed microwave vial was dried via vacuum/blowtorch/ N_2 flushes (x3). This vessel was heated using an aluminium heating block filled with sand (to enhance contact with the reaction vessel) placed on a stirrer hotplate. For a typical reaction, MIL-100(Sc)@PBSAC (150 mg) was introduced to a refluxing solution of (\pm)-citronellal (70 mg, 0.45 mmol, 0.09 M) in toluene (5 mL) stirred by magnetic stir bar at 1500 rpm. After 1 hour of reaction, an aliquot (10 μL) of the reaction mixture was taken, diluted to 1 mL with toluene, and analysed by GC. After each reaction, the catalyst was soaked in methanol for 24 hours. Following this the solvent was decanted and the catalyst dried under nitrogen before being used again. See section 6.1.12.1 for more information on the GC method that was used.

6.4.3 Stirring rate experiment

All stirring rate experiments were carried out using dry toluene as the solvent under an inert (N_2) atmosphere. Reactions were performed in a dry round bottomed flask (10 mL) equipped with a suba-seal creating a sealed vessel. Prior to reaction, the sealed microwave vial was dried via vacuum/blowtorch/ N_2 flushes (x3). This vessel was heated using an aluminium heating block filled with sand (to enhance contact with the reaction vessel) placed on a stirrer hotplate. For a typical reaction, MIL-100(Sc)@PBSAC (150 mg) was introduced to a refluxing solution of (\pm)-citronellal (62 mg, 0.4 mmol, 0.08 M) in toluene (5 mL) at a given

stirring rate (120, 250, 500, 750, 1000 or 1500 rpm). Aliquots (10 μ L) were periodically taken from the reaction mixture, diluted to 1 mL with toluene, and analysed by GC to monitor the reaction progress. See section 6.1.12.1 for more information on the GC method that was used.

6.4.4 Flow system setup

The flow system used in this work to study the intramolecular cyclisation of (\pm)-citronellal and the synthesis of CBD-methyl ester (reaction between methyl olivetolate and *p*-menthadienol) consisted of a vertically placed stainless steel packed-bed reactor (1/2" OD, 0.065" wall thickness, length: 12 cm, empty volume with adapters: 11 mL) (Figure 123), PTFE tubing (1/16" OD, 1/32" ID), a cartridge back pressure regulator (BPR) (75 psi) and a Jasco HPLC pump (model PU-986) (Figure 124).

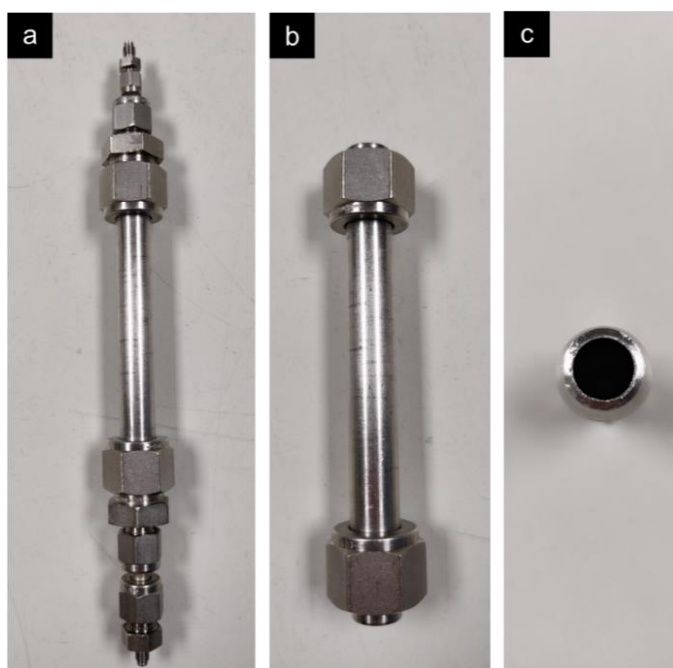


Figure 123: a) Packed-bed reactor used in this work with adapters connected. b) Packed-bed reactor used in this work without adapters connected. c) Top-view of packed-bed reactor used in this work. Figure reproduced with permission.³⁰⁰



Figure 124: Flow setup used in this work. Figure reproduced with permission.³⁰⁰

6.4.5 Residence time distribution (RTD) determination: pulse test

The residence time distribution of the flow system used in this work was measured by injecting a pulse of acetone (50 μL) into a pre-filled stream of toluene using a six-port valve and measuring the absorbance (at 290 nm) every second using online UV-Vis spectrometer (Jasco UV-2075 Plus) over time. The test was carried out at 0.5, 1, 2, 4 and 6 mL/min.

6.4.6 (\pm)-Citronellal cyclisation in continuous flow

6.4.6.1 Flow rate experiments at 0.25, 0.5, 1.0 and 1.5 mL/min

For a typical reaction, the packed-bed was plugged at both ends with two 1 cm wide cotton wool balls and filled with a homogeneous mixture of MIL-100(Sc)@PBSAC spheres (1 g) and glass spheres (9 g) (500 μm). The packed-bed reactor volume filled with the catalyst and with adapters attached was 8.5 mL. This was calculated by measuring the increase in mass of the reactor upon filling the packed reactor with 2-propanol and subsequently calculating the volume by dividing by the solvent density (0.786 g cm^{-3} at 20 $^{\circ}\text{C}$).

Before beginning the reaction, toluene was flowed through the solvent-less system at 1 mL min^{-1} until a continuous liquid phase was observed at the outlet

of the reactor and a stable pressure was achieved. The reactor, which was clamped vertically, was heated using an aluminium heating block which was connected to a Eurotherm temperature controller set to 110 °C. A solution of (±)-citronellal (0.43 M in toluene, n-decane internal standard) was pumped from bottom to top for ideal distribution throughout the packed-bed at either 0.25, 0.5, 1.0 or 1.5 mL/min. The resultant outlet stream was analysed offline by gas chromatography. For the preparation of GC samples, 10 µL of the outlet stream was diluted to a total volume of 1 mL with toluene. See section 6.1.12.1 for more information on the GC method that was used.

In the 0.5 mL/min experiment after 24 hours time-on-stream, a toluene wash was carried out by pumping neat toluene through the system at 2 mL/min for 2 hours at 100 °C.

The waxy solid that was observed was prepared for ¹H NMR analysis by dissolving in CDCl₃. The waxy solid dissolved immediately in CDCl₃.

6.4.6.2 Flow experiment in chloroform

The flow experiment in chloroform (0.5 mL/min) was carried out identically to the other flow rate reactions that were carried out in toluene (section 6.4.6.1) but using a lower concentration of (±)-citronellal (0.23 M), lower reaction temperature (80 °C) and lower MIL-100(Sc)@PBSAC loading (500 mg). The reaction was carried out at 0.5 mL/min. The washes with neat chloroform or methanol were carried out by pumping these solvents through the system at 3 mL/min for 15 minutes and 80 °C.

6.4.6.3 Flow experiment in methanol

The flow experiment in methanol (80 and 100 °C, 0.5 mL/min) was carried out identically to the flow rate reaction that was carried out in chloroform (section 6.4.6.2) but using methanol as the reaction solvent instead and higher temperatures (100 °C) for one of the reactions.

6.4.6.4 Methanol washing experiment

The methanol washing experiment (0.5 mL/min) was carried out identically to the other flow rate reactions that were carried out in toluene (section 6.4.6.1) but after 4 hours time-on-stream neat methanol was flowed through the system at 2 mL/min for 60 minutes at 110 °C (NB: this use of elevated temperatures above

the boiling point of methanol (at atmospheric pressure) was enabled by the use of a pressurised system). This was repeated for 7 cycles of reaction (or 6 methanol wash cycles).

6.4.7 Cannabidiol (CBD) and cannabidiol-methyl ester (CBD-ME) synthesis

6.4.7.1 Methyl olivetolate and *p*-menthadienol coupling in batch

The coupling reaction between methyl olivetolate and *p*-menthadienol was studied in batch using MIL-100(Sc)@PBSAC or Sc(OTf)₃ as catalysts and DCM or chloroform as solvents. MIL-100(Sc)@PBSAC (150 mg) or Sc(OTf)₃ (2.5 mg, 0.5 mol % relative to methyl olivetolate) was added to a refluxing solution of methyl olivetolate (20 mM) and *p*-menthadienol (22 mM or 40 mM) in DCM or chloroform (5 mL). The progress of the reaction was analysed offline HPLC. For the preparation of HPLC samples, 0.25 mL of the reaction mixture was diluted to a total volume of 1 mL with acetonitrile. See section 6.1.13.1 for method information.

6.4.7.2 Methyl olivetolate and *p*-menthadienol coupling in continuous flow

These experiments were conducted using the same flow apparatus as the (±)-citronellal cyclisation in continuous flow (see section 6.4.4).

In a typical reaction the packed-bed was plugged at both ends with two 1 cm wide cotton wool balls and filled with a homogeneous mixture of MIL-100(Sc)@PBSAC spheres (500 mg) and glass spheres (9 g) (500 µm). Before beginning the reaction, toluene was flowed through the solvent-less system at 1 mL min⁻¹ until a continuous liquid phase was observed at the outlet of the reactor and a stable pressure was achieved. The reactor, which was clamped vertically, was heated using an aluminium heating block which was connected to a Eurotherm temperature controller set to the reaction temperature (140 °C). A solution of methyl olivetolate (20 or 40 mM) and *p*-menthadienol (40 or 80 mM) in toluene (biphenyl internal standard) was pumped from bottom to top for ideal distribution throughout the packed-bed at either 0.25, 0.5, 1.0 or 2.0 mL/min, with residence volumes 3 and 4 analysed. The resultant outlet stream was analysed offline by HPLC. For the preparation of HPLC samples, 0.25 mL of the outlet stream was

diluted to a total volume of 1 mL with acetonitrile. See section 6.1.13.1 for method information.

Samples of the outlet stream were prepared for ^1H NMR analysis by removing the reaction solvent (toluene) under reduced pressure, resulting in a brown crude product. CDCl_3 (1 mL) was then then added to prepare the solutions for analysis.

6.4.7.3 Olivetol and *p*-menthadienol coupling in continuous flow

The flow system used in this work consisted of a vertically placed Omnifit glass column (length: 10 cm, 1 cm ID, empty volume: 7.85 cm), PTFE tubing (1/16" OD, 1/32" ID), and an adjustable back pressure regulator. A Uniqsis FlowSyn System was used to both pump reagents through and heat the glass column.

For a typical reaction, the glass column was filled with MIL-100(Sc)@PBSAC spheres (4.7 g). The reactor volume filled with the catalyst was 4.95 mL. This was calculated by measuring the increase in mass of the reactor upon filling the packed reactor with 2-propanol and subsequently calculating the volume by dividing by the solvent density (0.786 g cm^{-3} at $20 \text{ }^\circ\text{C}$).

Before beginning the reaction, neat reaction solvent (toluene or DCM) was flowed through the solvent-less system at 1 mL min^{-1} until a continuous liquid phase was observed at the outlet of the reactor and a stable pressure was achieved. The reactor, which was clamped vertically, was heated to the reaction temperature using the heating unit on the FlowSyn. A solution of olivetol (0.1 M) and *p*-menthadienol (0.4 M) in toluene was pumped from bottom to top for ideal distribution throughout the packed-bed at either 0.16 or 0.33 mL/min. The resultant outlet stream was analysed offline by HPLC. For the preparation of GC samples, $0.25 \text{ }\mu\text{L}$ of the outlet stream was diluted to a total volume of 1 mL with acetonitrile.

6.5 Future work procedures

6.5.1 Synthesis of Cu@UiO-67-BPY

The synthesis of Cu@UiO-67-BPY was based on previously reported procedures.^{351, 352, 354, 355} Zirconium chloride (ZrCl_4) (424 mg, 0.18 mmol), 2,2'-bipyridine-5,5'-dicarboxylic acid (BPY) (440 mg, 1.8 mmol) and DMF (70 mL) were added to a Teflon-lined stainless steel autoclave and heated at $120 \text{ }^\circ\text{C}$ for 24 hours. Next, the vessel was removed from the oven and allowed to cool to

room temperature. $\text{CuCl}_2 \cdot 2\text{H}_2\text{O}$ (340.0 mg, 2 mmol,) was added to the vessel, sonicated for a further 5 minutes, sealed and heated at 40 °C for 24 hours. After this, the reaction mixture was cooled, washed with methanol (3x) and the solids dried at 80 °C overnight under vacuum.

6.5.2 Synthesis of Cu@UiO-67-BPY@PBSAC

The synthesis of Cu@UiO-67-BPY@PBSAC was identical to the synthesis of Cu@UiO-67-BPY (section 6.5.1) but with the addition of PBSAC spheres (640 mg) in the first step when the other precursors were added to the vessel.

6.5.3 Epoxidation of cyclohexene with Cu@UiO-67-BPY@PBSAC

Cyclohexene (20.5 mg, 2.5 mmol), pivaldehyde (25.8 mg, 3 mmol), nitrobenzene (internal standard) and acetonitrile (5 mL) were added to a 2-neck round bottomed flask (25 mL). A condenser with a suba-seal in the top was placed in the middle neck of the flask to prevent solvent evaporation. Molecular oxygen was supplied to the vessel via a balloon filled with compressed air. The reaction was carried out at 40 °C. To start the reaction, $\text{CuCl}_2 \cdot 2\text{H}_2\text{O}$ (6.25 mg) or Cu@UiO-67-BPY@PBSAC (37.5 mg) were added to the reaction vessel. Reaction analysis was carried out via GC.

References

1. in *Fine Chemicals through Heterogeneous Catalysis*, 2000, DOI: <https://doi.org/10.1002/9783527612963.ch01>, pp. 1-11.
2. M. Lakshmi Kantam, R. Kishore, J. Yadav, S. K. Bhargava, L. A. Jones and A. Venugopal, in *Industrial Catalytic Processes for Fine and Specialty Chemicals*, eds. S. S. Joshi and V. V. Ranade, Elsevier, Amsterdam, 2016, DOI: <https://doi.org/10.1016/B978-0-12-801457-8.00010-0>, pp. 427-462.
3. *Global Fine Chemicals Market 2019 by Company, Regions, Type and Application, Forecast to 2024*, Absolute Reports, 2019.
4. J. Barlow and M. Hofer, *Sectoral Systems of Innovation and the UK's Competitiveness: The UK Biopharmaceutical Sector*, Imperial College London, Imperial College London, 2023.
5. C. Badman, C. L. Cooney, A. Florence, K. Konstantinov, M. Krumme, S. Mascia, M. Nasr and B. L. Trout, *Journal of Pharmaceutical Sciences*, 2019, **108**, 3521-3523.
6. FDA, *Quality Considerations for Continuous Manufacturing Guidance for Industry*, US, 2019.
7. S. K. Teoh, C. Rathi and P. Sharratt, *Organic Process Research & Development*, 2016, **20**, 414-431.
8. F. M. Akwi and P. Watts, *Chemical Communications*, 2018, **54**, 13894-13928.
9. G. S. Calabrese and S. Pissavini, *AIChE Journal*, 2011, **57**, 828-834.
10. C. L. Burcham, A. J. Florence and M. D. Johnson, *Annual Review of Chemical and Biomolecular Engineering*, 2018, **9**, 253-281.
11. B. Gutmann, D. Cantillo and C. O. Kappe, *Angewandte Chemie International Edition*, 2015, **54**, 6688-6728.
12. M. Baumann, T. S. Moody, M. Smyth and S. Wharry, *Organic Process Research & Development*, 2020, **24**, 1802-1813.
13. A. Hyer, D. Gregory, K. Kay, Q. Le, J. Turnage, F. Gupton and J. K. Ferri, *Advanced Synthesis & Catalysis*, **366**, 357-389.
14. T. O'Connor, *CDER's Perspective on the Continuous Manufacturing Journey*, US Food & Drug Administration 2023.
15. R. V. Chaudhari, in *Industrial Catalytic Processes for Fine and Specialty Chemicals*, eds. S. S. Joshi and V. V. Ranade, Elsevier, Amsterdam, 2016, DOI: <https://doi.org/10.1016/B978-0-12-801457-8.00002-1>, pp. 17-39.
16. S. Waclawek, V. V. T. Padil and M. Černík, *Ecological Chemistry and Engineering S*, 2018, **25**, 9-34.
17. V. V. Ranade and S. S. Joshi, in *Industrial Catalytic Processes for Fine and Specialty Chemicals*, eds. S. S. Joshi and V. V. Ranade, Elsevier, Amsterdam, 2016, DOI: <https://doi.org/10.1016/B978-0-12-801457-8.00001-X>, pp. 1-14.
18. P. Unnikrishnan and D. Srinivas, in *Industrial Catalytic Processes for Fine and Specialty Chemicals*, eds. S. S. Joshi and V. V. Ranade, Elsevier, Amsterdam, 2016, DOI: <https://doi.org/10.1016/B978-0-12-801457-8.00003-3>, pp. 41-111.
19. in *Fine Chemicals through Heterogeneous Catalysis*, 2000, DOI: <https://doi.org/10.1002/9783527612963.ch08>, pp. 351-471.
20. H. Witschi, *Toxicology*, 2000, **149**, 3-15.
21. in *Industrial Catalysis*, 2015, DOI: <https://doi.org/10.1002/9783527684625.ch8>, pp. 261-298.

22. in *Industrial Catalysis*, 2015, DOI: <https://doi.org/10.1002/9783527684625.ch9>, pp. 299-318.
23. M. Thommes, K. Kaneko, A. V. Neimark, J. P. Olivier, F. Rodriguez-Reinoso, J. Rouquerol and K. S. W. Sing, *Pure and Applied Chemistry*, 2015, **87**, 1051-1069.
24. R. Kopelent, J. A. van Bokhoven, J. Szlachetko, J. Edebeli, C. Paun, M. Nachtegaal and O. V. Safonova, *Angewandte Chemie International Edition*, 2015, **54**, 8728-8731.
25. H. Marsh and F. Rodríguez-Reinoso, in *Activated Carbon*, eds. H. Marsh and F. Rodríguez-Reinoso, Elsevier Science Ltd, Oxford, 2006, DOI: <https://doi.org/10.1016/B978-008044463-5/50022-4>, pp. 383-453.
26. P. McMorn and G. J. Hutchings, *Chemical Society Reviews*, 2004, **33**, 108-122.
27. W. Keim, *Green Chemistry*, 2003, **5**, 105-111.
28. J. Heveling, *Journal of Chemical Education*, 2012, **89**, 1530-1536.
29. S. S. Joshi, A. Bhatnagar and V. V. Ranade, in *Industrial Catalytic Processes for Fine and Specialty Chemicals*, eds. S. S. Joshi and V. V. Ranade, Elsevier, Amsterdam, 2016, DOI: <https://doi.org/10.1016/B978-0-12-801457-8.00008-2>, pp. 317-392.
30. S. Hübner, J. G. de Vries and V. Farina, *Advanced Synthesis & Catalysis*, 2016, **358**, 3-25.
31. R. Ciriminna, M. Pagliaro and R. Luque, *Green Energy & Environment*, 2021, **6**, 161-166.
32. E. Fernandez-Puertas, A. J. Robinson, H. Robinson, S. Sathiyalingam, H. Stubbs and L. J. Edwards, *Organic Process Research & Development*, 2020, **24**, 2147-2156.
33. A. Corma and H. García, *Chemical Reviews*, 2003, **103**, 4307-4366.
34. S. Kobayashi and K. Manabe, *Accounts of Chemical Research*, 2002, **35**, 209-217.
35. K. Wilson, D. J. Adams, G. Rothenberg and J. H. Clark, *Journal of Molecular Catalysis A: Chemical*, 2000, **159**, 309-314.
36. Z. Li, X. Ma, J. Liu, X. Feng, G. Tian and A. Zhu, *Journal of Molecular Catalysis A: Chemical*, 2007, **272**, 132-135.
37. D. C. Neckers, D. A. Kooistra and G. W. Green, *Journal of the American Chemical Society*, 1972, **94**, 9284-9285.
38. L. Wang and C. Cai, *Monatshefte für Chemie - Chemical Monthly*, 2009, **140**, 541-546.
39. M. Salavati-Niasari, J. Hasanalian and H. Najafian, *Journal of Molecular Catalysis A: Chemical*, 2004, **209**, 209-214.
40. T. M. Klapötke, F. McMonagle, R. R. Spence and J. M. Winfield, *Journal of Fluorine Chemistry*, 2006, **127**, 1446-1453.
41. U. Sridevi, B. K. Bhaskar Rao and N. C. Pradhan, *Chemical Engineering Journal*, 2001, **83**, 185-189.
42. J. Liu, D. Yin, D. Yin, Z. Fu, Q. Li and G. Lu, *Journal of Molecular Catalysis A: Chemical*, 2004, **209**, 171-177.
43. M. R. Gafurov, I. N. Mukhambetov, B. V. Yavkin, G. V. Mamin, A. A. Lamberov and S. B. Orlinskii, *The Journal of Physical Chemistry C*, 2015, **119**, 27410-27415.
44. M. Ravi, V. L. Sushkevich and J. A. van Bokhoven, *Nature Materials*, 2020, **19**, 1047-1056.
45. G. Li, C. Liu, R. Rohling, E. J. M. Hensen and E. A. Pidko, in *Modelling and Simulation in the Science of Micro- and Meso-Porous Materials*, eds.

- C. R. A. Catlow, V. Van Speybroeck and R. A. van Santen, Elsevier, 2018, DOI: <https://doi.org/10.1016/B978-0-12-805057-6.00007-7>, pp. 229-263.
46. Y. Li and J. Yu, *Nature Reviews Materials*, 2021, **6**, 1156-1174.
 47. A. Primo and H. Garcia, *Chemical Society Reviews*, 2014, **43**, 7548-7561.
 48. H. Furukawa, K. E. Cordova, M. O'Keeffe and O. M. Yaghi, *Science*, 2013, **341**, 1230444.
 49. K. Masuda, T. Ichitsuka, N. Koumura, K. Sato and S. Kobayashi, *Tetrahedron*, 2018, **74**, 1705-1730.
 50. A. Tanimu, S. Jaenicke and K. Alhooshani, *Chemical Engineering Journal*, 2017, **327**, 792-821.
 51. W.-J. Yoo, H. Ishitani, Y. Saito, B. Laroche and S. Kobayashi, *The Journal of Organic Chemistry*, 2020, **85**, 5132-5145.
 52. R. Porta, M. Benaglia and A. Puglisi, *Organic Process Research & Development*, 2016, **20**, 2-25.
 53. T. Tsubogo, H. Oyamada and S. Kobayashi, *Nature*, 2015, **520**, 329-332.
 54. P. Anastas and N. Eghbali, *Chemical Society Reviews*, 2010, **39**, 301-312.
 55. R. Munirathinam, J. Huskens and W. Verboom, *Advanced Synthesis & Catalysis*, 2015, **357**, 1093-1123.
 56. A. Basrur and D. Sabde, in *Industrial Catalytic Processes for Fine and Specialty Chemicals*, eds. S. S. Joshi and V. V. Ranade, Elsevier, Amsterdam, 2016, DOI: <https://doi.org/10.1016/B978-0-12-801457-8.00004-5>, pp. 113-186.
 57. M. Colella, C. Carlucci and R. Luisi, *Topics in Current Chemistry*, 2018, **376**, 46.
 58. S. A. Weissman and N. G. Anderson, *Organic Process Research & Development*, 2015, **19**, 1605-1633.
 59. S. N. Politis, P. Colombo, G. Colombo and D. M. Rekkas, *Drug Development and Industrial Pharmacy*, 2017, **43**, 889-901.
 60. C. J. Taylor, A. Pomberger, K. C. Felton, R. Grainger, M. Barecka, T. W. Chamberlain, R. A. Bourne, C. N. Johnson and A. A. Lapkin, *Chemical Reviews*, 2023, **123**, 3089-3126.
 61. I. M. Fukuda, C. F. F. Pinto, C. d. S. Moreira-, A. M. Saviano and F. R. Lourenço, *Brazilian Journal of Pharmaceutical Sciences*, 2018, **54**.
 62. G. Franceschini and S. Macchietto, *Chemical Engineering Science*, 2008, **63**, 4846-4872.
 63. C. J. Taylor, A. Baker, M. R. Chapman, W. R. Reynolds, K. E. Jolley, G. Clemens, G. E. Smith, A. J. Blacker, T. W. Chamberlain, S. D. R. Christie, B. A. Taylor and R. A. Bourne, *Journal of Flow Chemistry*, 2021, **11**, 75-86.
 64. V. K. Aggarwal, A. C. Staubitz and M. Owen, *Organic Process Research & Development*, 2006, **10**, 64-69.
 65. R. Leardi, *Analytica Chimica Acta*, 2009, **652**, 161-172.
 66. Sartorius, *MODDE 12 User Guide*, Sweden, 2017.
 67. F. Dedè, O. Piccolo and D. Vigo, *Organic Process Research & Development*, 2021, **25**, 292-299.
 68. F. Martínez, G. Morales, A. Martín and R. van Grieken, *Applied Catalysis A: General*, 2008, **347**, 169-178.
 69. H.-R. Bjørsvik, L. Liguori and F. Minisci, *Organic Process Research & Development*, 2000, **4**, 534-543.
 70. C. J. Taylor, H. Seki, F. M. Dannheim, M. J. Willis, G. Clemens, B. A. Taylor, T. W. Chamberlain and R. A. Bourne, *Reaction Chemistry & Engineering*, 2021, **6**, 1404-1411.

71. C. J. Taylor, M. Booth, J. A. Manson, M. J. Willis, G. Clemens, B. A. Taylor, T. W. Chamberlain and R. A. Bourne, *Chemical Engineering Journal*, 2021, **413**, 127017.
72. DynoChem; Scale-upSystemsLtd, 2023, (accessed 21/11/2023, DOI: <https://www.scale-up.com/dynochem>).
73. Compunetics (accessed 21/11/2023, DOI: <https://compunetics.net/>).
74. Berkeley Madonna, (accessed 21/11/2023, DOI: <https://berkeley-madonna.myshopify.com/>).
75. Z. Peng and J. L. Jimenez, *Journal of Chemical Education*, 2019, **96**, 806-811.
76. J. Plößer, M. Lucas, J. Wärnå, T. Salmi, D. Y. Murzin and P. Claus, *Organic Process Research & Development*, 2016, **20**, 1647-1653.
77. G. P. P. Kamatou, I. Vermaak, A. M. Viljoen and B. M. Lawrence, *Phytochemistry*, 2013, **96**, 15-25.
78. J. R. H. Ross, in *Heterogeneous Catalysis*, ed. J. R. H. Ross, Elsevier, Amsterdam, 2012, DOI: <https://doi.org/10.1016/B978-0-444-53363-0.10006-4>, pp. 123-142.
79. C. W. Mitchell, J. D. Strawser, A. Gottlieb, M. H. Millonig, F. A. Hicks and C. D. Papageorgiou, *Organic Process Research & Development*, 2014, **18**, 1828-1835.
80. J. I. Murray, M. V. Silva Elipe, A. Cosbie, K. Baucom, K. Quasdorf and S. Caille, *Organic Process Research & Development*, 2020, **24**, 1523-1530.
81. S. M. Changi and S.-W. Wong, *Organic Process Research & Development*, 2016, **20**, 525-539.
82. I. W. Ashworth, A. D. Campbell, J. H. Cherryman, J. Clark, A. Crampton, E. G. B. Eden-Rump, M. Evans, M. F. Jones, S. McKeever-Abbas, R. E. Meadows, K. Skilling, D. T. E. Whittaker, R. L. Woodward and P. A. Inglesby, *Organic Process Research & Development*, 2018, **22**, 1801-1808.
83. C. Yang, H. Feng and K. Stone, *Organic Process Research & Development*, 2021, **25**, 507-515.
84. R. Bright, D. J. Dale, P. J. Dunn, F. Hussain, Y. Kang, C. Mason, J. C. Mitchell and M. J. Snowden, *Organic Process Research & Development*, 2004, **8**, 1054-1058.
85. J. P. Guzowski, Jr., E. J. Delaney, M. J. Humora, E. Irdam, W. F. Kiesman, A. Kwok and A. D. Moran, *Organic Process Research & Development*, 2012, **16**, 232-239.
86. F. Susanne, D. S. Smith and A. Codina, *Organic Process Research & Development*, 2012, **16**, 61-64.
87. C. Nunn, A. DiPietro, N. Hodnett, P. Sun and K. M. Wells, *Organic Process Research & Development*, 2018, **22**, 54-61.
88. S. Schwolow, B. Heikenwälder, L. Abahmane, N. Kockmann and T. Röder, *Organic Process Research & Development*, 2014, **18**, 1535-1544.
89. D. M. Hallow, B. M. Mudryk, A. D. Braem, J. E. Tabora, O. K. Lyngberg, J. S. Bergum, L. T. Rossano and S. Tummala, *Journal of Pharmaceutical Innovation*, 2010, **5**, 193-203.
90. C. Waldron, A. Pankajakshan, M. Quaglio, E. Cao, F. Galvanin and A. Gavriilidis, *Industrial & Engineering Chemistry Research*, 2019, **58**, 22165-22177.
91. R. K. A. van Schendel, W. Yang, E. A. Uslamin and E. A. Pidko, *ChemCatChem*, 2021, **13**, 4886-4896.

92. F. Galvanin, E. Cao, N. Al-Rifai, A. Gavriilidis and V. Dua, in *Computer Aided Chemical Engineering*, eds. K. V. Gernaey, J. K. Huusom and R. Gani, Elsevier, 2015, vol. 37, pp. 323-328.
93. F. Galvanin, E. Cao, N. Al-Rifai, A. Gavriilidis and V. Dua, *Computers & Chemical Engineering*, 2016, **95**, 202-215.
94. G. Chakraborty, I.-H. Park, R. Medishetty and J. J. Vittal, *Chemical Reviews*, 2021, **121**, 3751-3891.
95. J. Fonseca, T. Gong, L. Jiao and H.-L. Jiang, *Journal of Materials Chemistry A*, 2021, **9**, 10562-10611.
96. D. Rani, K. K. Bhasin and M. Singh, *Dalton Transactions*, 2021, **50**, 13430-13437.
97. *Chemical Reviews*, 2012, **112**, 673-674.
98. H. Li, L. Li, R.-B. Lin, W. Zhou, Z. Zhang, S. Xiang and B. Chen, *EnergyChem*, 2019, **1**, 100006.
99. Z. Kang, L. Fan and D. Sun, *Journal of Materials Chemistry A*, 2017, **5**, 10073-10091.
100. R. F. Mendes, F. Figueira, J. P. Leite, L. Gales and F. A. Almeida Paz, *Chemical Society Reviews*, 2020, **49**, 9121-9153.
101. W. Xu and O. M. Yaghi, *ACS Central Science*, 2020, **6**, 1348-1354.
102. D. Yang and B. C. Gates, *ACS Catalysis*, 2019, **9**, 1779-1798.
103. M. Ding, R. W. Flaig, H.-L. Jiang and O. M. Yaghi, *Chemical Society Reviews*, 2019, **48**, 2783-2828.
104. L. T. Glasby, J. L. Cordiner, J. C. Cole and P. Z. Moghadam, *Chemistry of Materials*, 2024, DOI: 10.1021/acs.chemmater.4c00762.
105. P. Horcajada, S. Surblé, C. Serre, D.-Y. Hong, Y.-K. Seo, J.-S. Chang, J.-M. Grenèche, I. Margiolaki and G. Férey, *Chemical Communications*, 2007, DOI: 10.1039/B704325B, 2820-2822.
106. G. Férey, C. Serre, C. Mellot-Draznieks, F. Millange, S. Surblé, J. Dutour and I. Margiolaki, *Angewandte Chemie International Edition*, 2004, **43**, 6296-6301.
107. G. Zhong, D. Liu and J. Zhang, *Crystal Growth & Design*, 2018, **18**, 7730-7744.
108. D. Li, H.-Q. Xu, L. Jiao and H.-L. Jiang, *EnergyChem*, 2019, **1**, 100005.
109. Y. Fang, Z. Yang, H. Li and X. Liu, *Environmental Science and Pollution Research*, 2020, **27**, 4703-4724.
110. C. R. Quijia, C. Lima, C. Silva, R. C. Alves, R. Frem and M. Chorilli, *Journal of Drug Delivery Science and Technology*, 2021, **61**, 102217.
111. A. F. Sapnik, D. N. Johnstone, S. M. Collins, G. Divitini, A. M. Bumstead, C. W. Ashling, P. A. Chater, D. S. Keeble, T. Johnson, D. A. Keen and T. D. Bennett, *Dalton Transactions*, 2021, **50**, 5011-5022.
112. A. Vimont, J.-M. Goupil, J.-C. Lavalley, M. Daturi, S. Surblé, C. Serre, F. Millange, G. Férey and N. Audebrand, *Journal of the American Chemical Society*, 2006, **128**, 3218-3227.
113. J. N. Hall and P. Bollini, *ACS Catalysis*, 2020, **10**, 3750-3763.
114. F. Zhang, J. Shi, Y. Jin, Y. Fu, Y. Zhong and W. Zhu, *Chemical Engineering Journal*, 2015, **259**, 183-190.
115. A. Dhakshinamoorthy, M. Alvaro, P. Horcajada, E. Gibson, M. Vishnuvarthan, A. Vimont, J.-M. Grenèche, C. Serre, M. Daturi and H. Garcia, *ACS Catalysis*, 2012, **2**, 2060-2065.
116. L. Han, H. Qi, D. Zhang, G. Ye, W. Zhou, C. Hou, W. Xu and Y. Sun, *New Journal of Chemistry*, 2017, **41**, 13504-13509.

117. A. Dhakshinamoorthy, M. Alvaro, H. Chevreau, P. Horcajada, T. Devic, C. Serre and H. Garcia, *Catalysis Science & Technology*, 2012, **2**, 324-330.
118. F. Vermoortele, R. Ameloot, L. Alaerts, R. Matthessen, B. Carlier, E. V. R. Fernandez, J. Gascon, F. Kapteijn and D. E. De Vos, *Journal of Materials Chemistry*, 2012, **22**, 10313-10321.
119. L. Mitchell, B. Gonzalez-Santiago, J. P. S. Mowat, M. E. Gunn, P. Williamson, N. Acerbi, M. L. Clarke and P. A. Wright, *Catalysis Science & Technology*, 2013, **3**, 606-617.
120. L. Mitchell, P. Williamson, B. Ehrlichová, A. E. Anderson, V. R. Seymour, S. E. Ashbrook, N. Acerbi, L. M. Daniels, R. I. Walton, M. L. Clarke and P. A. Wright, *Chemistry – A European Journal*, 2014, **20**, 17185-17197.
121. L. Kurfiřtová, Y.-K. Seo, Y. K. Hwang, J.-S. Chang and J. Čejka, *Catalysis Today*, 2012, **179**, 85-90.
122. M. Giménez-Marqués, A. Santiago-Portillo, S. Navalón, M. Álvaro, V. Briois, F. Nouar, H. Garcia and C. Serre, *Journal of Materials Chemistry A*, 2019, **7**, 20285-20292.
123. G. Gómez-Pozuelo, C. P. Cabello, M. Opanasenko, M. Horáček and J. Čejka, *ChemPlusChem*, 2017, **82**, 152-159.
124. M. Taherimehr, B. Van de Voorde, L. H. Wee, J. A. Martens, D. E. De Vos and P. P. Pescarmona, *ChemSusChem*, 2017, **10**, 1283-1291.
125. B. R. James, J. A. Boissonault, A. G. Wong-Foy, A. J. Matzger and M. S. Sanford, *RSC Advances*, 2018, **8**, 2132-2137.
126. A. Bavykina, N. Kolobov, I. S. Khan, J. A. Bau, A. Ramirez and J. Gascon, *Chemical Reviews*, 2020, **120**, 8468-8535.
127. Y.-B. Huang, J. Liang, X.-S. Wang and R. Cao, *Chemical Society Reviews*, 2017, **46**, 126-157.
128. J. Guo, Y. Qin, Y. Zhu, X. Zhang, C. Long, M. Zhao and Z. Tang, *Chemical Society Reviews*, 2021, **50**, 5366-5396.
129. L. Jiao, Y. Wang, H.-L. Jiang and Q. Xu, *Advanced Materials*, 2018, **30**, 1703663.
130. L. Jiao and H.-L. Jiang, *Chinese Journal of Catalysis*, 2023, **45**, 1-5.
131. Q. Wang and D. Astruc, *Chemical Reviews*, 2020, **120**, 1438-1511.
132. C. V. Satyanarayana, D. Srikant and H. R. Gurav, in *Industrial Catalytic Processes for Fine and Specialty Chemicals*, eds. S. S. Joshi and V. V. Ranade, Elsevier, Amsterdam, 2016, DOI: <https://doi.org/10.1016/B978-0-12-801457-8.00005-7>, pp. 187-219.
133. C. Healy, K. M. Patil, B. H. Wilson, L. Hermanspahn, N. C. Harvey-Reid, B. I. Howard, C. Kleinjan, J. Koliën, F. Payet, S. G. Telfer, P. E. Kruger and T. D. Bennett, *Coordination Chemistry Reviews*, 2020, **419**, 213388.
134. H. Wan, C. Chen, Z. Wu, Y. Que, Y. Feng, W. Wang, L. Wang, G. Guan and X. Liu, *ChemCatChem*, 2015, **7**, 441-449.
135. N. K. Maghsoodi and M. H. Keshavarz, *Journal of Inorganic and Organometallic Polymers and Materials*, 2022, **32**, 4532-4539.
136. Q. Zhang, T. Yang, X. Liu, C. Yue, L. Ao, T. Deng and Y. Zhang, *RSC Advances*, 2019, **9**, 16357-16365.
137. C. Ye, Z. Qi, D. Cai and T. Qiu, *Industrial & Engineering Chemistry Research*, 2019, **58**, 1123-1132.
138. U. Jamil, A. Husain Khoja, R. Liaquat, S. Raza Naqvi, W. Nor Nadyaini Wan Omar and N. Aishah Saidina Amin, *Energy Conversion and Management*, 2020, **215**, 112934.

139. V. B. Lunardi, F. Gunawan, F. E. Soetaredjo, S. P. Santoso, C.-H. Chen, M. Yuliana, A. Kurniawan, J. Lie, A. E. Angkawijaya and S. Ismadji, *ACS Omega*, 2021, **6**, 1834-1845.
140. Z. Wu, C. Chen, H. Wan, L. Wang, Z. Li, B. Li, Q. Guo and G. Guan, *Energy & Fuels*, 2016, **30**, 10739-10746.
141. N. Sadeghi, S. Sharifnia and T.-O. Do, *Reaction Kinetics, Mechanisms and Catalysis*, 2018, **125**, 411-431.
142. M. Samy, M. G. Ibrahim, M. Fujii, K. E. Diab, M. ElKady and M. Gar Alalm, *Chemical Engineering Journal*, 2021, **406**, 127152.
143. G. A. Ortega-Moreno, S. C. Ayala-Durán, B. P. Barbero, G. E. Narda, M. C. Bernini and R. F. Pupo Nogueira, *Journal of Environmental Chemical Engineering*, 2022, **10**, 107678.
144. C. Gecgel, U. B. Simsek, B. Gozmen and M. Turabik, *Journal of the Iranian Chemical Society*, 2019, **16**, 1735-1748.
145. A. Khodkar, S. M. Khezri, A. R. Pendashteh, S. Khoramnejadian and L. Mamani, *International Journal of Environmental Science and Technology*, 2019, **16**, 5741-5756.
146. P. Hayati, Z. Mehrabadi, M. Karimi, J. Janczak, K. Mohammadi, G. Mahmoudi, F. Dadi, M. J. S. Fard, A. Hasanzadeh and S. Rostamnia, *New Journal of Chemistry*, 2021, **45**, 3408-3417.
147. V. N. Le, D.-P. Phan, S.-S. Kim, E. Y. Lee and J. Kim, *Fuel Processing Technology*, 2022, **238**, 107477.
148. B. A. Johnson and S. Ott, *Chemical Science*, 2020, **11**, 7468-7478.
149. G. Bauer, D. Ongari, D. Tiana, P. Gäumann, T. Rohrbach, G. Pareras, M. Tarik, B. Smit and M. Ranocchiari, *Nature Communications*, 2020, **11**, 1059.
150. D. Zhou, L. Wang, X. Chen, X. Wei, J. Liang, R. Tang and Y. Xu, *Chemical Engineering Journal*, 2020, **401**, 126024.
151. S. T. Dix, J. K. Scott, R. B. Getman and C. T. Campbell, *Faraday Discussions*, 2016, **188**, 21-38.
152. E. S. Gutterød, S. Øien-Ødegaard, K. Bossers, A.-E. Nieuwelink, M. Manzoli, L. Braglia, A. Lazzarini, E. Borfecchia, S. Ahmadigoltapeh, B. Bouchevreau, B. T. Lønstad-Bleken, R. Henry, C. Lamberti, S. Bordiga, B. M. Weckhuysen, K. P. Lillerud and U. Olsbye, *Industrial & Engineering Chemistry Research*, 2017, **56**, 13206-13218.
153. C. Wang, J.-L. Wang and W. Lin, *Journal of the American Chemical Society*, 2012, **134**, 19895-19908.
154. D. Yang, C. A. Gaggioli, D. Ray, M. Babucci, L. Gagliardi and B. C. Gates, *Journal of the American Chemical Society*, 2020, **142**, 8044-8056.
155. D. Yang, M. A. Ortuño, V. Bernales, C. J. Cramer, L. Gagliardi and B. C. Gates, *Journal of the American Chemical Society*, 2018, **140**, 3751-3759.
156. C. H. Sharp, B. C. Bukowski, H. Li, E. M. Johnson, S. Ilic, A. J. Morris, D. Gersappe, R. Q. Snurr and J. R. Morris, *Chemical Society Reviews*, 2021, **50**, 11530-11558.
157. B. A. Johnson, A. M. Beiler, B. D. McCarthy and S. Ott, *Journal of the American Chemical Society*, 2020, **142**, 11941-11956.
158. A. Dhakshinamoorthy, S. Navalon, A. M. Asiri and H. Garcia, *Chemical Communications*, 2020, **56**, 26-45.
159. V. Pascanu, P. R. Hansen, A. Bermejo Gómez, C. Ayats, A. E. Platero-Prats, M. J. Johansson, M. À. Pericàs and B. Martín-Matute, *ChemSusChem*, 2015, **8**, 123-130.

160. V. Pascanu, A. Bermejo Gómez, C. Ayats, A. E. Platero-Prats, F. Carson, J. Su, Q. Yao, M. À. Pericàs, X. Zou and B. Martín-Matute, *ACS Catalysis*, 2015, **5**, 472-479.
161. J. Li, F. Wu, L. Lin, Y. Guo, H. Liu and X. Zhang, *Chemical Engineering Journal*, 2018, **333**, 146-152.
162. W. Chen, P. Cai, P. Elumalai, P. Zhang, L. Feng, M. m. Al-Rawashdeh, S. T. Madrahimov and H.-C. Zhou, *ACS Applied Materials & Interfaces*, 2021, **13**, 51849-51854.
163. A. Swamy, K. S. Kanakikodi, V. R. Bakuru, B. B. Kulkarni, S. P. Maradur and S. B. Kalidindi, *ChemistrySelect*, 2023, **8**, e202203926.
164. L. Wan, M. Yuan, G. Xiong, S. Shi, W. Xiao, C. Chen and F. Ai, *Journal of Industrial and Engineering Chemistry*, 2023, **125**, 294-302.
165. H. Li, L. Ma, L. Zhou, J. Gao, Z. Huang, Y. He and Y. Jiang, *Chemical Communications*, 2018, **54**, 10754-10757.
166. D. Tian, X. Zhang, H. Shi, L. Liang, N. Xue, J.-H. Wang and H. Yang, *Journal of the American Chemical Society*, 2021, **143**, 16641-16652.
167. R. Greifenstein, T. Ballweg, T. Hashem, E. Gottwald, D. Achauer, F. Kirschhöfer, M. Nusser, G. Brenner-Weiß, E. Sedghamiz, W. Wenzel, E. Mittmann, K. S. Rabe, C. M. Niemeyer, M. Franzreb and C. Wöll, *Angewandte Chemie International Edition*, 2022, **61**, e202117144.
168. A. Chołuj, A. Zieliński, K. Grela and M. J. Chmielewski, *ACS Catalysis*, 2016, **6**, 6343-6349.
169. H. D. Park, M. Dincă and Y. Román-Leshkov, *Journal of the American Chemical Society*, 2018, **140**, 10669-10672.
170. A. Sachse, R. Ameloot, B. Coq, F. Fajula, B. Coasne, D. De Vos and A. Galarneau, *Chemical Communications*, 2012, **48**, 4749-4751.
171. C. G. Piscopo, M. Schwarzer, M. Herrmann, A. Affini, P. Pelagatti, G. Maestri, R. Maggi and S. Loebbecke, *ChemCatChem*, 2016, **8**, 1293-1297.
172. J. Hou, Y. Luan, X. Huang, H. Gao, M. Yang and Y. Lu, *New Journal of Chemistry*, 2017, **41**, 9123-9129.
173. J. Jia, C. Yang, F. Xu, S. Xu and X. Zhang, *Microchemical Journal*, 2021, **165**, 106113.
174. A. S. Shalygin, A. L. Nuzhdin, G. A. Bukhtiyarova and O. N. Martyanov, *Journal of Sol-Gel Science and Technology*, 2017, **84**, 446-452.
175. R. Oozeerally, S. D. K. Ramkhelawan, D. L. Burnett, C. H. L. Tempelman and V. Degirmenci, *Catalysts*, 2019, **9**, 812.
176. X. Chen, H. Jiang, B. Hou, W. Gong, Y. Liu and Y. Cui, *Journal of the American Chemical Society*, 2017, **139**, 13476-13482.
177. P. Ji, X. Feng, P. Oliveres, Z. Li, A. Murakami, C. Wang and W. Lin, *Journal of the American Chemical Society*, 2019, **141**, 14878-14888.
178. O. Singh, A. Agrawal, B. M. Abraham, R. Goyal, C. Pendem and B. Sarkar, *Materials Today Chemistry*, 2022, **24**, 100796.
179. B. Böhringer, O. Guerra Gonzalez, I. Eckle, M. Müller, J.-M. Giebelhausen, C. Schrage and S. Fichtner, *Chemie Ingenieur Technik*, 2011, **83**, 53-60.
180. J. Pallarés, A. González-Cencerrado and I. Arauzo, *Biomass and Bioenergy*, 2018, **115**, 64-73.
181. Z. Heidarinejad, M. H. Dehghani, M. Heidari, G. Javedan, I. Ali and M. Sillanpää, *Environmental Chemistry Letters*, 2020, **18**, 393-415.
182. R. C. Bansal and M. Goyal, *Activated Carbon Adsorption (1st ed.)*, CRC Press, 2005.

183. G. J. McDougall, *Journal of the Southern African Institute of Mining and Metallurgy*, 1991, **91**, 109-120.
184. H. F. Stoeckli, *Carbon*, 1990, **28**, 1-6.
185. S. Yenisoy-Karakaş, A. Aygün, M. Güneş and E. Tahtasakal, *Carbon*, 2004, **42**, 477-484.
186. A. Feiz, A. Bazgir, A. M. Balu and R. Luque, *Scientific Reports*, 2016, **6**, 32719.
187. G. Orsy, F. Fülöp and I. M. Mándity, *Green Chemistry*, 2019, **21**, 956-961.
188. A. J. Garcia-Olmo, A. Yopez, A. M. Balu, A. A. Romero, Y. Li and R. Luque, *Catalysis Science & Technology*, 2016, **6**, 4705-4711.
189. L. I. Godina, A. V. Tokarev, I. L. Simakova, P. Mäki-Arvela, E. Kortesmäki, J. Gläsel, L. Kronberg, B. Etzold and D. Y. Murzin, *Catalysis Today*, 2018, **301**, 78-89.
190. M. Munoz, V. Kolb, A. Lamolda, Z. M. de Pedro, A. Modrow, B. J. M. Etzold, J. J. Rodriguez and J. A. Casas, *Applied Catalysis B: Environmental*, 2017, **218**, 498-505.
191. H. Klefer, M. Munoz, A. Modrow, B. Böhringer, P. Wasserscheid and B. J. M. Etzold, *Chemical Engineering & Technology*, 2016, **39**, 276-284.
192. Y. W. Hsiao, X. Zong, J. Zhou, W. Zheng and D. G. Vlachos, *Applied Catalysis B: Environmental*, 2022, **317**, 121790.
193. M.-H. Baek, J.-W. Yoon, J.-S. Hong and J.-K. Suh, *Applied Catalysis A: General*, 2013, **450**, 222-229.
194. S. Fichtner, J. Hofmann, A. Möller, C. Schrage, J. M. Giebelhausen, B. Böhringer and R. Gläser, *Journal of Hazardous Materials*, 2013, **262**, 789-795.
195. P. C. With, N. Wilde, A. Modrow, S. Fichtner, B. Böhringer and R. Gläser, *Chemical Engineering & Technology*, 2015, **38**, 1671-1676.
196. R. Castro-Amoedo, Z. Csendes, J. Brünig, M. Sauer, A. Foelske-Schmitz, N. Yigit, G. Rupprechter, T. Gupta, A. M. Martins, K. Bica, H. Hoffmann and K. Kirchner, *Catalysis Science & Technology*, 2018, **8**, 4812-4820.
197. M. J. Schneider, M. Haumann, M. Stricker, J. Sundermeyer and P. Wasserscheid, *Journal of Catalysis*, 2014, **309**, 71-78.
198. W. Grähler, *Nanoporous Metal-Organic Frameworks for production (nanoMOF) - Project Final Report*.
199. R. Gil-San-Millan, P. Delgado, E. Lopez-Maya, J. D. Martin-Romera, E. Barea and J. A. R. Navarro, *ACS Applied Materials & Interfaces*, 2021, **13**, 50491-50496.
200. K. Wang, L. Han, J. Mustakis, B. Li, J. Magano, D. B. Damon, A. Dion, M. T. Maloney, R. Post and R. Li, *Industrial & Engineering Chemistry Research*, 2020, **59**, 2409-2421.
201. G. C. Shearer, S. Chavan, S. Bordiga, S. Svelle, U. Olsbye and K. P. Lillerud, *Chemistry of Materials*, 2016, **28**, 3749-3761.
202. M. Akbari, P. Asadi, M. K. Besharati Givi and G. Khodabandehlouie, in *Advances in Friction-Stir Welding and Processing*, eds. M. K. B. Givi and P. Asadi, Woodhead Publishing, 2014, DOI: <https://doi.org/10.1533/9780857094551.543>, pp. 543-599.
203. V. K. Aggarwal, G. P. Vennall, P. N. Davey and C. Newman, *Tetrahedron Letters*, 1998, **39**, 1997-2000.
204. J. Ren, X. Dyosiba, N. M. Musyoka, H. W. Langmi, M. Mathe and S. Liao, *Coordination Chemistry Reviews*, 2017, **352**, 187-219.

205. A. F. Sapnik, I. Bechis, S. M. Collins, D. N. Johnstone, G. Divitini, A. J. Smith, P. A. Chater, M. A. Addicoat, T. Johnson, D. A. Keen, K. E. Jelfs and T. D. Bennett, *Nature Communications*, 2021, **12**, 2062.
206. J. P. S. Mowat, S. R. Miller, A. M. Z. Slawin, V. R. Seymour, S. E. Ashbrook and P. A. Wright, *Microporous and Mesoporous Materials*, 2011, **142**, 322-333.
207. D. F. Sava Gallis, K. W. Chapman, M. A. Rodriguez, J. A. Greathouse, M. V. Parkes and T. M. Nenoff, *Chemistry of Materials*, 2016, **28**, 3327-3336.
208. C. P. Cabello, P. Rumori and G. T. Palomino, *Microporous and Mesoporous Materials*, 2014, **190**, 234-239.
209. M. Latroche, S. Surblé, C. Serre, C. Mellot-Draznieks, P. L. Llewellyn, J.-H. Lee, J.-S. Chang, S. H. Jung and G. Férey, *Angewandte Chemie International Edition*, 2006, **45**, 8227-8231.
210. S.-H. Huo and X.-P. Yan, *Journal of Materials Chemistry*, 2012, **22**, 7449-7455.
211. F. Jeremias, A. Khutia, S. K. Henninger and C. Janiak, *Journal of Materials Chemistry*, 2012, **22**, 10148-10151.
212. L. Zou, D. Feng, T.-F. Liu, Y.-P. Chen, S. Yuan, K. Wang, X. Wang, S. Fordham and H.-C. Zhou, *Chemical Science*, 2016, **7**, 1063-1069.
213. L. Mitchell, PhD Thesis, University of St Andrews 2014.
214. M. A. Simon, E. Anggraeni, F. E. Soetaredjo, S. P. Santoso, W. Irawaty, T. C. Thanh, S. B. Hartono, M. Yuliana and S. Ismadji, *Scientific Reports*, 2019, **9**, 16907.
215. H. Lv, H. Zhao, T. Cao, L. Qian, Y. Wang and G. Zhao, *Journal of Molecular Catalysis A: Chemical*, 2015, **400**, 81-89.
216. M. J. Cliffe, W. Wan, X. Zou, P. A. Chater, A. K. Kleppe, M. G. Tucker, H. Wilhelm, N. P. Funnell, F.-X. Coudert and A. L. Goodwin, *Nature Communications*, 2014, **5**, 4176.
217. D. N. Johnstone, F. C. N. Firth, C. P. Grey, P. A. Midgley, M. J. Cliffe and S. M. Collins, *Journal of the American Chemical Society*, 2020, **142**, 13081-13089.
218. X. Li, L. Lachmanski, S. Safi, S. Sene, C. Serre, J. M. Grenèche, J. Zhang and R. Gref, *Scientific Reports*, 2017, **7**, 13142.
219. S. Mustapha, J. O. Tijani, M. M. Ndamitso, S. A. Abdulkareem, S. D. Taye, A. K. Mohammed and A. T. Amigun, *Environmental Health Insights*, 2021, **15**, 11786302211036520.
220. P. L. Hanst, J. W. Spence and M. Miller, *Environmental Science & Technology*, 1977, **11**, 403-405.
221. M. Haouas, C. Volkringer, T. Loiseau, G. Férey and F. Taulelle, *The Journal of Physical Chemistry C*, 2011, **115**, 17934-17944.
222. S. Zhuang, H. Huang, Y. Xiao, Z. Zhang, J. Tang, B. C. Gates and D. Yang, *Journal of Catalysis*, 2021, **404**, 128-138.
223. J. Xu, J. Xu, S. Jiang, Y. Cao, K. Xu, Q. Zhang and L. Wang, *Environmental Science and Pollution Research*, 2020, **27**, 37839-37851.
224. S. Wuttke, P. Bazin, A. Vimont, C. Serre, Y.-K. Seo, Y. K. Hwang, J.-S. Chang, G. Férey and M. Daturi, *Chemistry – A European Journal*, 2012, **18**, 11959-11967.
225. H. Wu, Y. S. Chua, V. Krungleviciute, M. Tyagi, P. Chen, T. Yildirim and W. Zhou, *Journal of the American Chemical Society*, 2013, **135**, 10525-10532.
226. L. Xu, Y. Luo, L. Sun, S. Pu, M. Fang, R.-X. Yuan and H.-B. Du, *Dalton Transactions*, 2016, **45**, 8614-8621.

227. G. C. Shearer, S. Chavan, J. Ethiraj, J. G. Vitillo, S. Svelle, U. Olsbye, C. Lamberti, S. Bordiga and K. P. Lillerud, *Chemistry of Materials*, 2014, **26**, 4068-4071.
228. M. J. Katz, Z. J. Brown, Y. J. Colón, P. W. Siu, K. A. Scheidt, R. Q. Snurr, J. T. Hupp and O. K. Farha, *Chemical Communications*, 2013, **49**, 9449-9451.
229. C. Duan, Y. Yu, P. Yang, X. Zhang, F. Li, L. Li and H. Xi, *Industrial & Engineering Chemistry Research*, 2020, **59**, 774-782.
230. W. Xu, Y. Zhang, J. Wang, Y. Xu, L. Bian, Q. Ju, Y. Wang and Z. Fang, *Nature Communications*, 2022, **13**, 2068.
231. X.-Z. Guo, S.-S. Han, J.-M. Yang, X.-M. Wang, S.-S. Chen and S. Quan, *Industrial & Engineering Chemistry Research*, 2020, **59**, 2113-2122.
232. J. W. M. Osterrieth, J. Rampersad, D. Madden, N. Rampal, L. Skoric, B. Connolly, M. D. Allendorf, V. Stavila, J. L. Snider, R. Ameloot, J. Marreiros, C. Ania, D. Azevedo, E. Vilarrasa-Garcia, B. F. Santos, X.-H. Bu, Z. Chang, H. Bunzen, N. R. Champness, S. L. Griffin, B. Chen, R.-B. Lin, B. Coasne, S. Cohen, J. C. Moreton, Y. J. Colón, L. Chen, R. Clowes, F.-X. Coudert, Y. Cui, B. Hou, D. M. D'Alessandro, P. W. Doheny, M. Dincă, C. Sun, C. Doonan, M. T. Huxley, J. D. Evans, P. Falcaro, R. Ricco, O. Farha, K. B. Idrees, T. Islamoglu, P. Feng, H. Yang, R. S. Forgan, D. Bara, S. Furukawa, E. Sanchez, J. Gascon, S. Telalović, S. K. Ghosh, S. Mukherjee, M. R. Hill, M. M. Sadiq, P. Horcajada, P. Salcedo-Abraira, K. Kaneko, R. Kukobat, J. Kenvin, S. Keskin, S. Kitagawa, K.-i. Otake, R. P. Lively, S. J. A. DeWitt, P. Llewellyn, B. V. Lotsch, S. T. Emmerling, A. M. Pütz, C. Martí-Gastaldo, N. M. Padial, J. García-Martínez, N. Linares, D. Maspoch, J. A. Suárez del Pino, P. Moghadam, R. Oktavian, R. E. Morris, P. S. Wheatley, J. Navarro, C. Petit, D. Danaci, M. J. Rosseinsky, A. P. Katsoulidis, M. Schröder, X. Han, S. Yang, C. Serre, G. Mouchaham, D. S. Sholl, R. Thyagarajan, D. Siderius, R. Q. Snurr, R. B. Goncalves, S. Telfer, S. J. Lee, V. P. Ting, J. L. Rowlandson, T. Uemura, T. Iiyuka, M. A. van der Veen, D. Rega, V. Van Speybroeck, S. M. J. Rogge, A. Lamaire, K. S. Walton, L. W. Bingel, S. Wuttke, J. Andreo, O. Yaghi, B. Zhang, C. T. Yavuz, T. S. Nguyen, F. Zamora, C. Montoro, H. Zhou, A. Kirchon and D. Fairen-Jimenez, *Advanced Materials*, 2022, **34**, 2201502.
233. C. M. Maguire, M. Rösslein, P. Wick and A. Prina-Mello, *Sci Technol Adv Mater*, 2018, **19**, 732-745.
234. E. Roduner, *Chemical Society Reviews*, 2006, **35**, 583-592.
235. W. H. Qi, M. P. Wang and Q. H. Liu, *Journal of Materials Science*, 2005, **40**, 2737-2739.
236. S. Nanda and K. K. Nanda, *Journal of Chemical Education*, 2021, **98**, 1982-1987.
237. A. I. Frenkel, C. W. Hills and R. G. Nuzzo, *The Journal of Physical Chemistry B*, 2001, **105**, 12689-12703.
238. M. Shao, A. Peles and K. Shoemaker, *Nano Letters*, 2011, **11**, 3714-3719.
239. J. K. Gimzewski, D. J. Fabian, L. M. Watson and S. Affrossman, *Journal of Physics F: Metal Physics*, 1977, **7**, L305.
240. M. Emura and H. Matsuda, *Chemistry & Biodiversity*, 2014, **11**, 1688-1699.
241. D. Dylong, P. J. C. Hausoul, R. Palkovits and M. Eisenacher, *Flavour and Fragrance Journal*, 2022, **37**, 195-209.
242. E. J. Lenardão, G. V. Botteselle, F. de Azambuja, G. Perin and R. G. Jacob, *Tetrahedron*, 2007, **63**, 6671-6712.

243. H. Itoh, H. Maeda, S. Yamada, Y. Hori, T. Mino and M. Sakamoto, *RSC Advances*, 2014, **4**, 61619-61623.
244. *US Pat.*, US6774269B2, 2002.
245. L. Alaerts, E. Séguin, H. Poelman, F. Thibault-Starzyk, P. A. Jacobs and D. E. De Vos, *Chemistry – A European Journal*, 2006, **12**, 7353-7363.
246. M. Vandichel, F. Vermoortele, S. Cottenie, D. E. De Vos, M. Waroquier and V. Van Speybroeck, *Journal of Catalysis*, 2013, **305**, 118-129.
247. F. Vermoortele, M. Vandichel, B. Van de Voorde, R. Ameloot, M. Waroquier, V. Van Speybroeck and D. E. De Vos, *Angewandte Chemie International Edition*, 2012, **51**, 4887-4890.
248. F. Vermoortele, B. Bueken, G. Le Bars, B. Van de Voorde, M. Vandichel, K. Houthoofd, A. Vimont, M. Daturi, M. Waroquier, V. Van Speybroeck, C. Kirschhock and D. E. De Vos, *Journal of the American Chemical Society*, 2013, **135**, 11465-11468.
249. F. G. Cirujano and F. X. Llabrés i Xamena, *The Journal of Physical Chemistry Letters*, 2020, **11**, 4879-4890.
250. M. Vandichel, J. Hajek, F. Vermoortele, M. Waroquier, D. E. De Vos and V. Van Speybroeck, *CrystEngComm*, 2015, **17**, 395-406.
251. M. Ermer, J. Mehler, B. Rosenberger, M. Fischer, P. S. Schulz and M. Hartmann, *ChemistryOpen*, 2021, **10**, 233-242.
252. W.-L. Peng, F. Liu, X. Yi, S. Sun, H. Shi, Y. Hui, W. Chen, X. Yu, Z. Liu, Y. Qin, L. Song and A. Zheng, *The Journal of Physical Chemistry Letters*, 2022, **13**, 9295-9302.
253. J. Jiang, F. Gándara, Y.-B. Zhang, K. Na, O. M. Yaghi and W. G. Klemperer, *Journal of the American Chemical Society*, 2014, **136**, 12844-12847.
254. F. G. Cirujano, F. X. Llabrés i Xamena and A. Corma, *Dalton Transactions*, 2012, **41**, 4249-4254.
255. A. M. Rasero-Almansa, M. Iglesias and F. Sánchez, *RSC Advances*, 2016, **6**, 106790-106797.
256. X. Zhang, L. Chang, Z. Yang, Y. Shi, C. Long, J. Han, B. Zhang, X. Qiu, G. Li and Z. Tang, *Nano Research*, 2019, **12**, 437-440.
257. J. S. Hilliard and C. R. Wade, *Dalton Transactions*, 2023, **52**, 1608-1615.
258. A. Corma and M. Renz, *Chemical Communications*, 2004, 550-551.
259. F. Neațu, S. Coman, V. I. Pârvulescu, G. Poncelet, D. De Vos and P. Jacobs, *Topics in Catalysis*, 2009, **52**, 1292-1300.
260. A. Ramanathan, M. C. Castro Villalobos, C. Kwakernaak, S. Telalovic and U. Hanefeld, *Chemistry – A European Journal*, 2008, **14**, 961-972.
261. G. K. Chuah, S. H. Liu, S. Jaenicke and L. J. Harrison, *Journal of Catalysis*, 2001, **200**, 352-359.
262. P. J. Kropp, G. W. Breton, S. L. Craig, S. D. Crawford, W. F. Durland, Jr., J. E. Jones, III and J. S. Raleigh, *The Journal of Organic Chemistry*, 1995, **60**, 4146-4152.
263. Z. Vajglová, N. Kumar, M. Peurla, K. Eränen, P. Mäki-Arvela and D. Y. Murzin, *Catalysis Science & Technology*, 2020, **10**, 8108-8119.
264. *NL Pat.*, WO1999032422A1, 1998.
265. G. D. Yadav and J. J. Nair, *Langmuir*, 2000, **16**, 4072-4079.
266. D.-L. Shieh, C.-C. Tsai and A.-N. Ko, *Reaction Kinetics and Catalysis Letters*, 2003, **79**, 381-389.
267. X.-M. Liu, L.-H. Xie and Y. Wu, *Inorganic Chemistry Frontiers*, 2020, **7**, 2840-2866.
268. R. C. Bansal and M. Goyal, *Activated Carbon Adsorption*, 1st edn., 2005.

269. H. Marsh and F. Rodríguez-Reinoso, *Activated Carbon*, 2006.
270. F. T. U. Kohler, S. Popp, H. Klefer, I. Eckle, C. Schrage, B. Böhringer, D. Roth, M. Haumann and P. Wasserscheid, *Green Chemistry*, 2014, **16**, 3560-3568.
271. A. Weiß, M. Munoz, A. Haas, F. Rietzler, H.-P. Steinrück, M. Haumann, P. Wasserscheid and B. J. M. Etzold, *ACS Catalysis*, 2016, **6**, 2280-2286.
272. W. Xiang, S. Gebhardt, R. Gläser and C.-j. Liu, *Microporous and Mesoporous Materials*, 2020, **300**, 110152.
273. J. C. Muñoz-Senmache, S. Kim, R. R. Arrieta-Pérez, C. M. Park, Y. Yoon and A. J. Hernández-Maldonado, *ACS Applied Nano Materials*, 2020, **3**, 2928-2940.
274. O. Fleker, A. Borenstein, R. Lavi, L. Benisvy, S. Ruthstein and D. Aurbach, *Langmuir*, 2016, **32**, 4935-4944.
275. Z. Wang, L. Liu, Z. Li, N. Goyal, T. Du, J. He and G. K. Li, *Energy & Fuels*, 2022, **36**, 2927-2944.
276. Q. Ma, T. Zhang and B. Wang, *Matter*, 2022, **5**, 1070-1091.
277. S.-Y. Lee and S.-J. Park, *International Journal of Hydrogen Energy*, 2011, **36**, 8381-8387.
278. C. A. F. de Oliveira, F. F. da Silva, G. C. Jimenez, J. F. da S. Neto, D. M. B. de Souza, I. A. de Souza and S. A. Júnior, *Chemical Communications*, 2013, **49**, 6486-6488.
279. P. B. Somayajulu Rallapalli, M. C. Raj, D. V. Patil, K. P. Prasanth, R. S. Somani and H. C. Bajaj, *International Journal of Energy Research*, 2013, **37**, 746-753.
280. M. E. Casco, J. Fernández-Catalá, M. Martínez-Escandell, F. Rodríguez-Reinoso, E. V. Ramos-Fernández and J. Silvestre-Albero, *Chemical Communications*, 2015, **51**, 14191-14194.
281. F. N. Azad, M. Ghaedi, K. Dashtian, S. Hajati and V. Pezeshkpour, *Ultrasonics Sonochemistry*, 2016, **31**, 383-393.
282. R.-H. Shi, Z.-R. Zhang, H.-L. Fan, T. Zhen, J. Shangguan and J. Mi, *Applied Surface Science*, 2017, **394**, 394-402.
283. S. Kayal and A. Chakraborty, *Chemical Engineering Journal*, 2018, **334**, 780-788.
284. S. Gonen, O. Lori, G. Cohen-Taguri and L. Elbaz, *Nanoscale*, 2018, **10**, 9634-9641.
285. N. M. Mahmoodi, J. Abdi, M. Taghizadeh, A. Taghizadeh, B. Hayati, A. A. Shekarchi and M. Vossoughi, *Journal of Environmental Management*, 2019, **233**, 660-672.
286. L. N. McHugh, A. Terracina, P. S. Wheatley, G. Buscarino, M. W. Smith and R. E. Morris, *Angewandte Chemie International Edition*, 2019, **58**, 11747-11751.
287. N. M. Mahmoodi, M. Taghizadeh and A. Taghizadeh, *Journal of Molecular Liquids*, 2019, **277**, 310-322.
288. K. L. B. Solis, Y.-H. Kwon, M.-H. Kim, H.-R. An, C. Jeon and Y. Hong, *Chemosphere*, 2020, **238**, 124656.
289. B. Koo and S. P. Jung, *Chemical Engineering Journal*, 2021, **424**, 130388.
290. S. Soroush, N. M. Mahmoodi, B. Mohammadnezhad and A. Karimi, *Korean Journal of Chemical Engineering*, 2022, **39**, 2394-2404.
291. L. Luo, Y. Zhou, W. Yan, L. Luo, J. Deng, M. Fan and W. Zhao, *International Journal of Hydrogen Energy*, 2022, **47**, 39563-39571.
292. S. Gaikwad and S. Han, *Journal of Environmental Chemical Engineering*, 2023, **11**, 109593.

293. Z. Zhu, A. Li, S. Zhong, F. Liu and Q. Zhang, *Journal of Applied Polymer Science*, 2008, **109**, 1692-1698.
294. P. Silva, S. M. F. Vilela, J. P. C. Tomé and F. A. Almeida Paz, *Chemical Society Reviews*, 2015, **44**, 6774-6803.
295. H. U. Escobar-Hernandez, R. Shen, M. I. Papadaki, J. A. Powell, H.-C. Zhou and Q. Wang, *ACS Chemical Health & Safety*, 2021, **28**, 358-368.
296. An explosion occurred at the Institute of Chemistry, Chinese Academy of Sciences? Staff response: The deceased was not a researcher, <https://news.sina.cn/qn/2021-04-01/detail-ikmxzfmk0500184.d.html?from=wap>, (accessed 06/09/2023).
297. S. Phoung, E. Williams, G. Gaustad and A. Gupta, *Journal of Cleaner Production*, 2023, **401**, 136673.
298. L. McHugh, PhD Thesis, University of St Andrews, 2019.
299. *DE Pat.*, WO2001083368A1, 2007.
300. A. Griffiths, S. L. Boyall, P. Müller, J. P. Harrington, A. M. Sobolewska, W. R. Reynolds, R. A. Bourne, K. Wu, S. M. Collins, M. Muldowney and T. W. Chamberlain, *Nanoscale*, 2023, **15**, 17910-17921.
301. O. Abuzalat, D. Wong and M. A. Elsayed, *Journal of Inorganic and Organometallic Polymers and Materials*, 2022, **32**, 1924-1934.
302. Q. Wang, H. Gao, C. Zhao, H. Yue, G. Gao, J. Yu, Y.-U. Kwon and Y. Zhao, *Electrochimica Acta*, 2021, **369**, 137700.
303. S. Kim, K. Choi and S. Park, *Solid State Sciences*, 2016, **61**, 40-43.
304. R. Ramírez-Jiménez, M. Franco, E. Rodrigo, R. Sainz, R. Ferritto, A. M. Lamsabhi, J. L. Aceña and M. B. Cid, *Journal of Materials Chemistry A*, 2018, **6**, 12637-12646.
305. R. K. Reddy and J. B. Joshi, *Particuology*, 2010, **8**, 37-43.
306. H. Gao, Y. Luan, K. Chaikittikul, W. Dong, J. Li, X. Zhang, D. Jia, M. Yang and G. Wang, *ACS Applied Materials & Interfaces*, 2015, **7**, 4667-4674.
307. W. Ouyang, D. Zhao, Y. Wang, A. M. Balu, C. Len and R. Luque, *ACS Sustainable Chemistry & Engineering*, 2018, **6**, 6746-6752.
308. Y. Gao, F. J. Muzzio and M. G. Ierapetritou, *Powder Technology*, 2012, **228**, 416-423.
309. A. E. Rodrigues, *Chemical Engineering Science*, 2021, **230**, 116188.
310. Y. Kawakami, A. Borissova, M. R. Chapman, G. Goltz, E. Koltsova, I. Mitrichev and A. J. Blacker, *European Journal of Organic Chemistry*, 2019, **2019**, 7499-7505.
311. S. Chatterjee, V. Degirmenci and E. V. Rebrov, *Chemical Engineering Journal*, 2015, **281**, 884-891.
312. L. R. Mafu, PhD Thesis, Nelson Mandela Metropolitan University, 2016.
313. H. Chen, H. Zou, Y. Hao and H. Yang, *ChemSusChem*, 2017, **10**, 1989-1995.
314. Z. Vajglová, N. Kumar, P. Mäki-Arvela, K. Eränen, M. Peurla, L. Hupa, M. Nurmi, M. Toivakka and D. Y. Murzin, *Industrial & Engineering Chemistry Research*, 2019, **58**, 18084-18096.
315. Z. Vajglová, N. Kumar, P. Mäki-Arvela, K. Eränen, M. Peurla, L. Hupa and D. Y. Murzin, *Organic Process Research & Development*, 2019, **23**, 2456-2463.
316. M. Azkaar, P. Mäki-Arvela, Z. Vajglová, V. Fedorov, N. Kumar, L. Hupa, J. Hemming, M. Peurla, A. Aho and D. Y. Murzin, *Reaction Chemistry & Engineering*, 2019, **4**, 2156-2169.
317. A. Zuliani, C. M. Cova, R. Manno, V. Sebastian, A. A. Romero and R. Luque, *Green Chemistry*, 2020, **22**, 379-387.

318. Z. Vajglová, I. L. Simakova, K. Eränen, P. Mäki-Arvela, N. Kumar, M. Peurla, S. Tolvanen, A. Efimov, L. Hupa, J. Peltonen and D. Y. Murzin, *Applied Catalysis A: General*, 2022, **629**, 118426.
319. I. Simakova, P. Mäki-Arvela, M. Martinez-Klimov, J. Muller, Z. Vajglova, M. Peurla, K. Eränen and D. Y. Murzin, *Applied Catalysis A: General*, 2022, **636**, 118586.
320. C.-M. Wang, Y.-D. Wang, J.-W. Ge and Z.-K. Xie, *Chem*, 2019, **5**, 2736-2737.
321. C. A. Hone and C. O. Kappe, *Chemistry–Methods*, 2021, **1**, 454-467.
322. R. Giovine, C. Volkringer, S. E. Ashbrook, J. Trébosc, D. McKay, T. Loiseau, J.-P. Amoureux, O. Lafon and F. Pourpoint, *Chemistry – A European Journal*, 2017, **23**, 9525-9534.
323. J. W. Yoon, Y.-K. Seo, Y. K. Hwang, J.-S. Chang, H. Leclerc, S. Wuttke, P. Bazin, A. Vimont, M. Daturi, E. Bloch, P. L. Llewellyn, C. Serre, P. Horcajada, J.-M. Grenèche, A. E. Rodrigues and G. Férey, *Angewandte Chemie International Edition*, 2010, **49**, 5949-5952.
324. E. S. Seltzer, A. K. Watters, D. MacKenzie, L. M. Granat and D. Zhang, *Cancers*, 2020, **12**, 3203.
325. A. Kaba and S. D. Ray, in *Reference Module in Biomedical Sciences*, Elsevier, 2023, DOI: <https://doi.org/10.1016/B978-0-12-824315-2.00380-8>.
326. FDA Approves First Drug Comprised of an Active Ingredient Derived from Marijuana to Treat Rare, Severe Forms of Epilepsy, <https://www.fda.gov/news-events/press-announcements/fda-approves-first-drug-comprised-active-ingredient-derived-marijuana-treat-rare-severe-forms>, (accessed 13/09/2023).
327. K. M. Nelson, J. Bisson, G. Singh, J. G. Graham, S.-N. Chen, J. B. Friesen, J. L. Dahlin, M. Niemitz, M. A. Walters and G. F. Pauli, *Journal of Medicinal Chemistry*, 2020, **63**, 12137-12155.
328. M. E. Badowski and P. K. Yanful, *Therapeutics and Clinical Risk Management*, 2018, **14**, 643-651.
329. E. Chiurchiù, S. Sampaolesi, P. Allegrini, D. Ciceri, R. Ballini and A. Palmieri, *European Journal of Organic Chemistry*, 2021, **2021**, 1286-1289.
330. A. Lago-Fernandez, V. Redondo, L. Hernandez-Folgado, L. Figuerola-Asencio and N. Jagerovic, in *Methods in Enzymology*, ed. P. H. Reggio, Academic Press, 2017, vol. 593, pp. 237-257.
331. A. Maiocchi, J. Barbieri, V. Fasano and D. Passarella, *ChemistrySelect*, 2022, **7**, e202202400.
332. V. R. L. J. Bloemendal, J. C. M. van Hest and F. P. J. T. Rutjes, *Organic & Biomolecular Chemistry*, 2020, **18**, 3203-3215.
333. X. Gong, C. Sun, M. A. Abame, W. Shi, Y. Xie, W. Xu, F. Zhu, Y. Zhang, J. Shen and H. A. Aisa, *The Journal of Organic Chemistry*, 2020, **85**, 2704-2715.
334. T. Petrzilka, W. Haefliger, C. Sikemeier, G. Ohloff and A. Eschenmoser, *Helvetica Chimica Acta*, 1967, **50**, 719-723.
335. T. Petrzilka, W. Haefliger and C. Sikemeier, *Helvetica Chimica Acta*, 1969, **52**, 1102-1134.
336. S.-H. Baek, M. Srebnik and R. Mechoulam, *Tetrahedron Letters*, 1985, **26**, 1083-1086.
337. R. Anand, P. S. Cham, V. Gannedi, S. Sharma, M. Kumar, R. Singh, R. A. Vishwakarma and P. P. Singh, *The Journal of Organic Chemistry*, 2022, **87**, 4489-4498.

338. *WO Pat.*, Process for the production of cannabidiol and delta-9-tetrahydrocannabinol, WO2017011210A1, 2016.
339. *WO Pat.*, Synthetic cannabidiol compositions and methods of making the same, WO2019046806A1, 2019.
340. V. R. L. J. Bloemendal, B. Spierenburg, T. J. Boltje, J. C. M. van Hest and F. P. J. T. Rutjes, *Journal of Flow Chemistry*, 2021, **11**, 99-105.
341. *EU Pat.*, Process for the preparation of dibenzo b,d]Pyrans, EP0628037B1, 1993.
342. *US Pat.*, Process for preparing synthetic cannabinoids, US20100298579A1, 2010.
343. *US Pat.*, Method for preparing cannabinoids, US10981849B1, 2020.
344. *WO Pat.*, Synthesis of phytocannabinoids including a demethylation step, WO2019033164, 2019.
345. L. Crombie and W. M. L. Crombie, *Phytochemistry*, 1977, **16**, 1413-1420.
346. B. Bassetti, C. A. Hone and C. O. Kappe, *The Journal of Organic Chemistry*, 2023, **88**, 6227-6231.
347. M. Kandiah, M. H. Nilsen, S. Usseglio, S. Jakobsen, U. Olsbye, M. Tilset, C. Larabi, E. A. Quadrelli, F. Bonino and K. P. Lillerud, *Chemistry of Materials*, 2010, **22**, 6632-6640.
348. J. H. Cavka, S. Jakobsen, U. Olsbye, N. Guillou, C. Lamberti, S. Bordiga and K. P. Lillerud, *Journal of the American Chemical Society*, 2008, **130**, 13850-13851.
349. J. Winarta, B. Shan, S. M. McIntyre, L. Ye, C. Wang, J. Liu and B. Mu, *Crystal Growth & Design*, 2020, **20**, 1347-1362.
350. L. Braglia, E. Borfecchia, L. Maddalena, S. Øien, K. A. Lomachenko, A. L. Bugaev, S. Bordiga, A. V. Soldatov, K. P. Lillerud and C. Lamberti, *Catalysis Today*, 2017, **283**, 89-103.
351. R. Li, X. Li, D. Ramella, Y. Zhao and Y. Luan, *New Journal of Chemistry*, 2022, **46**, 5839-5847.
352. H. Fei and S. M. Cohen, *Chemical Communications*, 2014, **50**, 4810-4812.
353. S. Øien, G. Agostini, S. Svelle, E. Borfecchia, K. A. Lomachenko, L. Mino, E. Gallo, S. Bordiga, U. Olsbye, K. P. Lillerud and C. Lamberti, *Chemistry of Materials*, 2015, **27**, 1042-1056.
354. Y. Song, D. Yang, S. Yu, X. Teng, Z. Chang, F. Pan, X. Bu, Z. Jiang, B. Wang, S. Wang and X. Cao, *Separation and Purification Technology*, 2019, **210**, 258-267.
355. J. Hou, Y. Luan, J. Tang, A. M. Wensley, M. Yang and Y. Lu, *Journal of Molecular Catalysis A: Chemical*, 2015, **407**, 53-59.
356. A. Schaate, P. Roy, A. Godt, J. Lippke, F. Waltz, M. Wiebcke and P. Behrens, *Chemistry – A European Journal*, 2011, **17**, 6643-6651.
357. G. Kaur, S. Øien-Ødegaard, A. Lazzarini, S. M. Chavan, S. Bordiga, K. P. Lillerud and U. Olsbye, *Crystal Growth & Design*, 2019, **19**, 4246-4251.
358. C. Sun, M. Barton, C. M. Pask, M. Edokali, L. Yang, A. J. Britton, S. Micklethwaite, F. Iacoviello, A. Hassanpour, M. Besenhard, R. Drummond-Brydson, K.-J. Wu and S. M. Collins, *Chemical Engineering Journal*, 2023, **474**, 145892.
359. M. Rubio-Martinez, C. Avci-Camur, A. W. Thornton, I. Imaz, D. MasPOCH and M. R. Hill, *Chemical Society Reviews*, 2017, **46**, 3453-3480.
360. S. Bagi, S. Yuan, S. Rojas-Buzo, Y. Shao-Horn and Y. Román-Leshkov, *Green Chemistry*, 2021, **23**, 9982-9991.
361. M. R. Chapman, M. H. T. Kwan, G. King, K. E. Jolley, M. Hussain, S. Hussain, I. E. Salama, C. González Niño, L. A. Thompson, M. E. Bayana,

- A. D. Clayton, B. N. Nguyen, N. J. Turner, N. Kapur and A. J. Blacker, *Organic Process Research & Development*, 2017, **21**, 1294-1301.
362. A. D. Clayton, E. O. Pyzer-Knapp, M. Purdie, M. F. Jones, A. Barthelme, J. Pavey, N. Kapur, T. W. Chamberlain, A. J. Blacker and R. A. Bourne, *Angewandte Chemie International Edition*, 2023, **62**, e202214511.
363. Z. Lei, H. T. Ang and J. Wu, *Organic Process Research & Development*, 2023, DOI: 10.1021/acs.oprd.2c00374.
364. B. Wang, W. Liu, W. Zhang and J. Liu, *Nano Research*, 2017, **10**, 3826-3835.
365. A. Dhakshinamoorthy, M. Alvaro, Y. K. Hwang, Y.-K. Seo, A. Corma and H. Garcia, *Dalton Transactions*, 2011, **40**, 10719-10724.
366. R. R. Tuttle, S. J. Folkman, H. N. Rubin, R. G. Finke and M. M. Reynolds, *ACS Applied Materials & Interfaces*, 2020, **12**, 39043-39055.
367. O. M. Linder-Patton, T. J. de Prinse, S. Furukawa, S. G. Bell, K. Sumida, C. J. Doonan and C. J. Sumby, *CrystEngComm*, 2018, **20**, 4926-4934.
368. P. Li, R. C. Klet, S.-Y. Moon, T. C. Wang, P. Deria, A. W. Peters, B. M. Klahr, H.-J. Park, S. S. Al-Juaid, J. T. Hupp and O. K. Farha, *Chemical Communications*, 2015, **51**, 10925-10928.
369. T. Kiyonaga, M. Higuchi, T. Kajiwara, Y. Takashima, J. Duan, K. Nagashima and S. Kitagawa, *Chemical Communications*, 2015, **51**, 2728-2730.
370. *ASTM D4179-01: Standard Test Method for Single Pellet Crush Strength of Formed Catalyst Shapes*, ASTM International, US, 2001.
371. S. Kim, E. E. Bolton and S. H. Bryant, *Journal of Cheminformatics*, 2013, **5**, 1.
372. Citronellal (PubChem CID 7794), (accessed 26/11/2023, DOI: <https://pubchem.ncbi.nlm.nih.gov/compound/7794#section=3D-Conformer>).
373. Isopulegol (PubChem CID 24585), (accessed 26/11/2023, DOI: <https://pubchem.ncbi.nlm.nih.gov/compound/Isopulegol#section=3D-Conformer>).